Solar wind-magnetosphere coupling at Saturn

Thesis submitted for the degree of

Doctor of Philosophy

at the University of Leicester

Caitríona M. Jackman

Radio and Space Plasma Physics Group

Department of Physics and Astronomy

University of Leicester

June 2006

Abstract

Solar wind-magnetosphere coupling at Saturn

Caitríona M. Jackman

The studies contained within this thesis concern solar wind-magnetosphere coupling at Saturn. The first study uses data from the Cassini mission when it was upstream of Saturn to investigate the large-scale structure of the heliosphere and the interplanetary magnetic field (IMF) at 9 AU. The medium is found to be consistent with that expected during the declining phase of the solar cycle, structured by corotating interaction region (CIR) compressions and rarefactions. An empirical formula for open flux production at Saturn's magnetopause is presented. Estimates of open flux production associated with a period of strong solar activity indicate that major magnetospheric dynamics were excited by reconnection-mediated solar wind interaction during the interval.

The second study begins by examining concurrent IMF and Saturn kilometric radiation (SKR) data together with images from the Hubble Space Telescope from an interval in January of 2004, which show the effect of the arrival at Saturn of a CIR-related compression region. On examination of the IMF data surrounding the Saturn orbit insertion interval, it is suggested that a compression of similar character impinged on the magnetosphere at some point during the fly-through. Observations on the outbound pass show strong bursts of SKR extending to low frequencies, and provide evidence for the first specific link between SKR emission features and in situ dynamics inside Saturn's magnetosphere.

The third study comprises a theoretical model of the flows and currents in Saturn's polar ionosphere under conditions of strong Dungey-cycle driving. The flow pattern consists of components which are intended to represent plasma sub-corotation in the middle magnetosphere region, and the Vasyliunas- and Dungey-cycles of convection at higher latitudes. The model results indicate a strong dawn-dusk asymmetry in Saturn's main auroral oval under active Dungey-cycle conditions, and are in good agreement with observations.

<u>*Contents*</u>

Declarations

The research undertaken during the course of this doctoral programme has led to the submission and publication of the following scientific papers:

Jackman, C.M., N. Achilleos, E.J. Bunce, S.W.H. Cowley, M.K. Dougherty, G.H. Jones, S.E. Milan, and E.J. Smith: Interplanetary magnetic field at ~9 AU during the declining phase of the solar cycle and its implications for Saturn's magnetospheric dynamics, *J. Geophys. Res.*, 109, A11203,doi:10.1029/2004JA010614, 2004.

Jackman, C.M., N. Achilleos, E.J. Bunce, B. Cecconi, J.T. Clarke, S.W.H. Cowley, W.S. Kurth, and P. Zarka: Interplanetary conditions and magnetospheric dynamics during the Cassini orbit insertion fly-through of Saturn's magnetosphere, *J. Geophys. Res.*, 110, A10212, doi: 10.1029/2005JA011054, 2005a.

Jackman, C.M., N. Achilleos, E.J. Bunce, S.W.H. Cowley, and S.E. Milan: Structure of the interplanetary magnetic field during the interval spanning the first Cassini fly-through of Saturn's magnetosphere and its implications for Saturn's magnetospheric dynamics, *Adv. Space Res.*, 36, 2120-2126, 2005b.

Jackman, C.M., and S.W.H. Cowley: A model of the plasma flow and current in Saturn's polar ionosphere under conditions of strong Dungey cycle driving, *Ann. Geophysicae*, 24, 1029-1055, 2006.

Milan, S.E., E.J. Bunce, S.W.H. Cowley, and **C.M. Jackman:** Implications of rapid planetary rotation for the Dungey magnetotail of Saturn, *J. Geophys. Res.*, 110, A02201,doi:10.1029/2004JA010716RR, 2004.

Cowley, S.W.H., S.V. Badman, E.J. Bunce, J.T. Clarke, J.C. Gérard, D. Grodent, **C.M. Jackman,** S.E. Milan, T.K. Yeoman: Reconnection in a rotation-dominated

magnetosphere and its relation to Saturn's auroral dynamics, *J. Geophys. Res.*, 110, A02201,doi:10.1029/2004JA010796, 2005.

Bunce, E.J., S.W.H. Cowley, **C.M. Jackman**, J.T. Clarke, F.J. Crary, M.K. Dougherty: Cassini Observations of the Interplanetary Medium Upstream of Saturn and their relation of the Hubble Space Telescope Aurora Data, *Adv. Space Res.*, in press, 2004.

Achilleos, N. C.S. Arridge, **C.M. Jackman**, C. Bertucci, M.K. Dougherty, and C.T. Russell: Probabilistic modelling of Saturn's magnetopause boundary, *Geophys. Res. Lett.*, in preparation, 2006.

To him who made great lights, his love endures forever.
The sun to govern the day, his love endures forever.
The moon and stars to govern the night, his love endures forever.

Psalm 136:7-9

Acknowledgements

Firstly, I would like to thank Prof. Stan Cowley for being an excellent supervisor. I really appreciate his patience with my endless questions, his careful guidance, unfailing knowledge, and immense consideration and understanding during my frequent trips back to Ireland.

Next, a thank you to the British Federation of Women Graduates for funding me during my final year.

Thanks to Emma Bunce for all her help and friendship, to Steve Milan for being a cool second supervisor, and to Jonny Mopster who owes me a squash rematch!

I would like to thank all the members of RSPP who have been a great group to get to know. To my officemates, past and present: Thanks for putting up with my dodgy singing voice and *occasional* swearing (though I did in return have to endure some noxious gases – thanks boys!) To Sarah and Suzie in particular who have taught me to tolerate chilli, love chocolate brownie, and just been a really good laugh. Get awesome!

To Hannah for cooking for me countless times and always making time to listen/talk/take me shopping! To the lab ladies, Becks, Rhian and Gail, for providing many laughs and dramas, and let's not forget to mention Papillon! To all the subwardens of GMV for 3 years of good times and horrible dinners! And to all my friends at home, in particular Jenny, Mairead, Emily, Carol and Orla for a very welcome distraction from work!

Neil, grá mo chroí, go raibh míle maith agat as ucht do ghrá agus thacaíocht ar feadh trí mbliana. Tá mé ag súil go mór leis an lá a mbeimíd le chéile.

To Mom, who has been a source of strength and love, and a really good friend, not just during my PhD time. To Dad: I can't say how delighted I am that you are around to see this day. You have always supported and encouraged me and this work must in part be due to your enthusiasm.

Contents

Chapter 1

Introduction to solar-planetary physics

1.1 Introduction

This thesis concerns the large-scale structure of the heliosphere and the interplanetary magnetic field structure at distances of 9 AU, combined with both theoretical modelling and data analysis which serve to investigate Saturn's magnetospheric dynamics.

This preliminary chapter introduces the Sun, solar wind and interplanetary magnetic field, and the fundamentals of the interaction between the sun and magnetized planets. Chapter 2 goes on to address the kronian system in detail. It begins with a discussion of previous missions to Saturn, namely Pioneer 1 and Voyagers 1 and 2, and then includes the latest information on Saturn's magnetosphere obtained from the Cassini-Huygens mission, which has shed light on many previously unanswered questions. Chapter 3 discusses the instrumentation used to obtain the data presented in this thesis, namely from the magnetometer and radio and plasma wave science instruments on Cassini, along with the STIS camera on the Hubble Space Telescope, used to obtain images of the kronian aurora. A study of interplanetary conditions upstream of Saturn is presented in Chapter 4, which investigates the pattern of corotating interaction region compressions and rarefactions seen during the declining phase of the solar cycle. An empirical formula to estimate the rate of open flux production at Saturn's magnetopause is also presented. Chapter 5 looks at data from the January 2004 Hubble-Cassini campaign, correlating Saturn kilometric radiation emissions with interplanetary magnetic field data and auroral images. A similar method of analysis is used to infer magnetospheric conditions during Saturn orbit insertion. Finally, Chapter 6 presents a fully quantitative model of the flows and currents in Saturn's polar ionosphere under conditions of strong Dungey cycle driving.

1.2 The Sun and solar wind

The Sun is the most important celestial object to us on Earth. Our nearest star, it lies a distance of 1.5 x 10^8 km (1 AU – Astronomical Unit) away. It is a yellow dwarf of spectral type G2 V, and is held together and compressed under its own gravitational attraction. It is composed mainly of hydrogen (~90%) and helium (~10%) but with some heavier elements.

Figure 1.1 shows a schematic of the Sun's interior and atmosphere. The central core contains ~30% of the total mass and has a temperature of ~15 x 10^6 K. Here hydrogen nuclei fuse to form helium nuclei and energy is released in the form of photons which radiate outwards. The temperature drops with increasing distance from the core through the radiative zone until eventually convective motion takes over. Above this convective zone lies the photosphere, a region about 500 km thick that emits most of the Sun's light.

The photosphere is covered uniformly with a granular pattern outlining the convection cells beneath. It also has marks called sunspots, which have been observed from Earth by ancient Chinese astronomers for over 4000 years, and were then reported by Galileo Galilei in his 1610 work, the *Siderius Nuncius*. Sunspots are dark patches which usually appear in pairs consisting of a leading and trailing spot with respect to the solar rotation. All but the smallest have a dark inner region (the umbra) surrounded by a less dark edge (the penumbra). They mark the position of intense, localized magnetic fields. They follow a cyclic pattern, whereby successive sunspot minima (or maxima) occur every 11 years, a process termed the solar cycle, to be discussed below.

The Sun's atmosphere, defined as the region we can directly observe, begins at the photosphere, at a temperature of 5800 K, and has 3 further layers. Above the

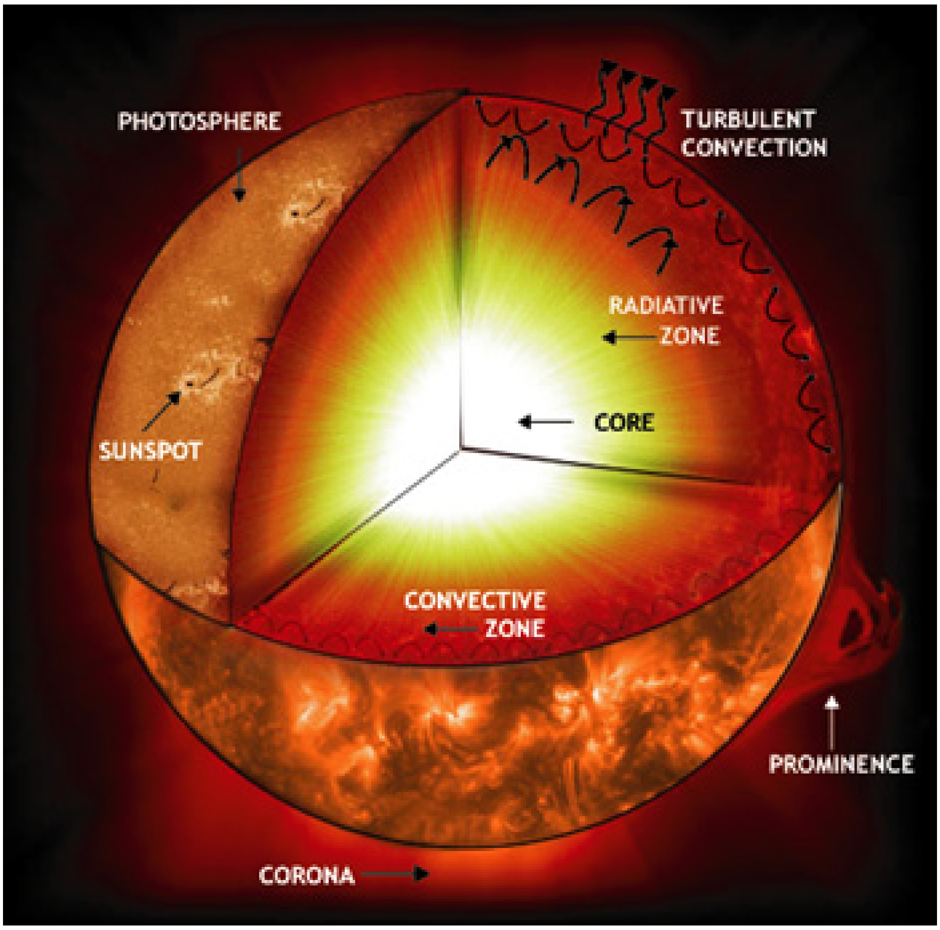

Figure 1.1: Schematic of the Sun's interior and atmosphere.
[Courtesy UC Berkeley].

photosphere lies the chromosphere where the temperature slowly decreases to ~4200 K, followed by a rapid increase in the transition region. The temperature then finally reaches $\sim 10^6$ K at the base of the solar corona.

If we assume the Sun's atmosphere to be in hydrostatic equilibrium, then on application of the equations of mass continuity and momentum, we find that the gas pressure in the corona falls off to a limiting value of $\sim 10^{-5}$ Pa. Now the region of space in which the Sun's influence is dominant is called the heliosphere, bounded at a distance of 100-150 AU by the local interstellar medium (LISM). If the gas pressure of the corona were less than that of the LISM, then the sun's atmosphere could be contained by the LISM in hydrostatic equilibrium. However, estimates put the pressure of the LISM to be $\sim 10^{-13}$ Pa. As a result, the coronal plasma is driven out at supersonic speeds into interplanetary space to form the solar wind. The existence of the solar wind was first postulated by Biermann in 1951 who observed that the ion tails of comets always point away from the Sun.

1.3 Solar and interplanetary magnetic fields

We know that the Sun's magnetic field direction reverses every 11 years as part of the solar cycle. This cycle can be tracked by the number of sunspots visible on the Sun. Figure 1.2 shows mean sunspot number plotted against time. At the start of the cycle, the sunspot number is low and they tend to be found at higher latitudes. Moving towards solar maximum, the field becomes disordered as the sunspots move to lower latitudes. This activity then dies away, at which point the field re-emerges with the opposite polarity at solar minimum. Thus, the whole cycle takes 22 years for the field to return to its original polarity. The prime cause of the solar cycle is a quasi-periodic oscillation of the solar magnetic field. Many solar properties vary with the solar cycle; the instance of coronal holes increases near solar minimum, while solar maximum sees over ten times more coronal mass ejections (CMEs) than minimum [Webb and Howard, 1994]. CMEs, which are huge bubbles of gas threaded with magnetic field lines, can nevertheless be

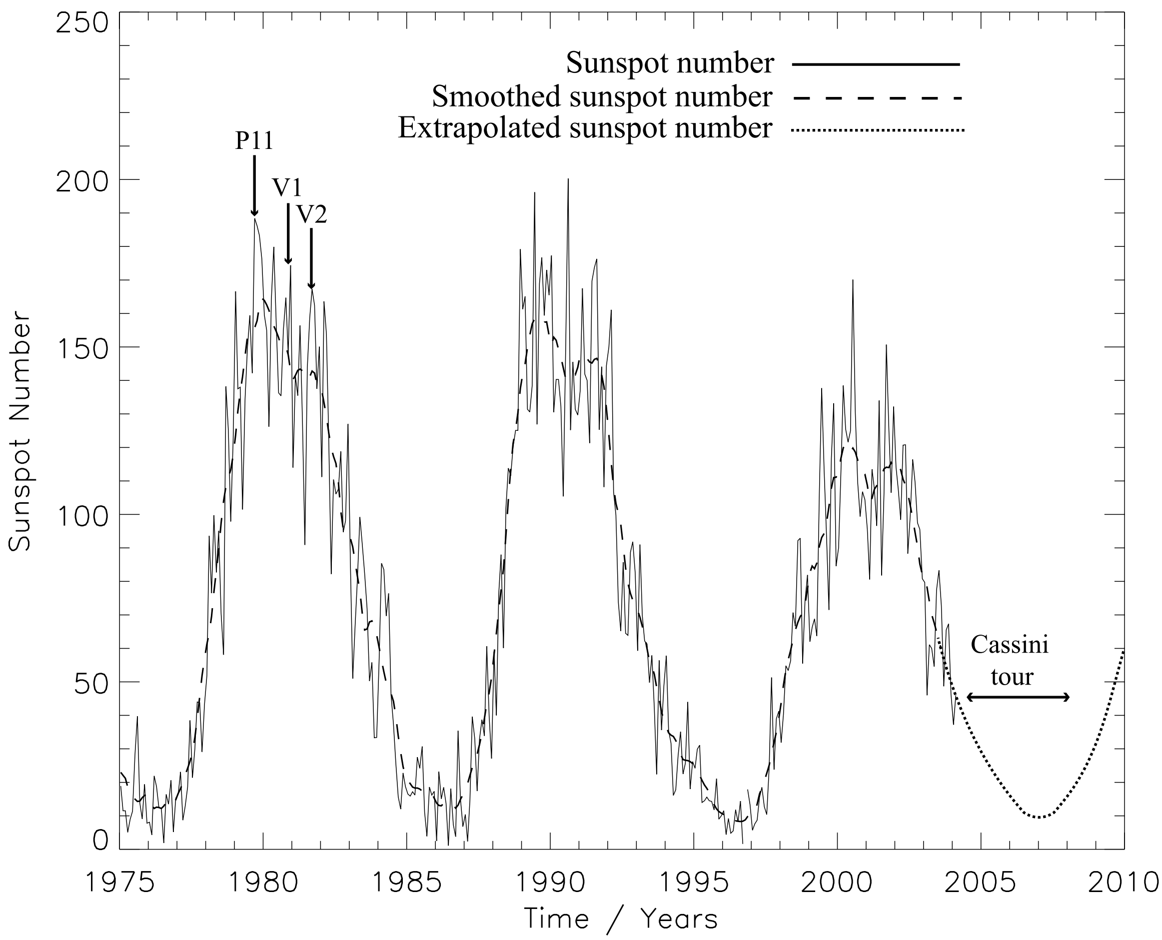

Figure 1.2: Plot of monthly (solid line) and monthly smoothed (dashed line) sunspot numbers since 1975, obtained from the Solar Influences Data analysis Centre (SIDC), Belgium, together with a simple extrapolation to 2010 (dotted line). The times of the previous Saturn fly-bys by Pioneer 11, Voyager 1, and Voyager 2 in 1979, 1980, and 1981, respectively, are marked by the vertical arrows. [From Jackman et al., 2004].

seen at all points in the solar cycle, disturbing the normal solar wind pattern, as mentioned in Chapter 4.

The solar wind carries with it a remnant of the coronal magnetic field, called the interplanetary magnetic field (IMF). In order to think about the transport of field lines and plasma, we must derive an 'equation of motion' of the magnetic field. Ohm's law for a plasma of conductivity σ is

$$\mathbf{E} + \mathbf{V} \times \mathbf{B} = \frac{\mathbf{j}}{\sigma} \tag{1.1}$$

where **E** is the electric field, **B** the magnetic field, **j** the electric current density, and **V** the plasma velocity. For the case of the collisionless solar wind, the conductivity is very large. Taking the curl of Eq. 1.1 and substituting it into Faraday's law

$$\frac{\partial \mathbf{B}}{\partial t} = -\operatorname{curl} \mathbf{E} \tag{1.2}$$

and using Ampère's law (neglecting the displacement current)

$$\operatorname{curl} \mathbf{B} = \mu_0 \mathbf{j} \tag{1.3}$$

where μ_0 is the permeability of free space, then yields the induction equation

$$\frac{\partial \mathbf{B}}{\partial t} = \operatorname{curl}(\mathbf{V} \times \mathbf{B}) + \frac{1}{\mu_0 \sigma} \nabla^2 \mathbf{B} \ . \tag{1.4}$$

Equation (1.4) describes the motion of the magnetic field with respect to the plasma in which it is embedded. The first term on the right-hand side is the convective transport term while the second is the magnetic diffusion term. The ratio of the terms is known as the magnetic Reynolds number, R_m

$$R_m = \mu_0 \sigma v L \quad , \tag{1.5}$$

where L is the characteristic length scale of the plasma and v the characteristic velocity. If $R_m >> 1$ the transport term dominates and the field and plasma are frozen together, as in the solar wind. When $R_m \leq 1$ the frozen-in approximation breaks down and the field can diffuse through the plasma, and a process called reconnection can occur, as will be discussed later.

We wish to examine the way in which the solar wind and interplanetary field propagate into interplanetary space, and as such, it is useful first to neglect the rotation of the Sun, and consider its field to be purely dipolar. Thus the outflow of solar wind is constantly radially outwards. After a long time the field near the Sun will point radially inwards or outwards, depending on the polarity of the dipole, and a thin current sheet will be set up in the dipole equator. The effect of the Sun's rotation on this picture was considered first by Parker in 1958, and is sketched in Fig. 1.3. The outflow of plasma is purely radial, and the IMF field lines are frozen to this flow. However, the foot of each field line is also frozen to the surface of the rotating Sun. Thus the streamline of interconnecting particles emerging from a fixed source takes the shape of a spiral, known as the Parker spiral, which is located along the locus of all plasma elements emitted from a given source region on the Sun's surface. The curvature is determined by both the flow speed and the distance from the Sun. The average Parker angle between the stream lines and the radial direction to the Sun at 1 AU is about 45º for a 400 km s^{-1} solar wind velocity. With increasing distance, the Parker spiral winds up further and further – at Jupiter's orbit, the angle is ~10º, while at Saturn it is ~6º.

The dipole axis of the solar magnetic field is not aligned parallel to the rotation axis, implying that the azimuthal current sheet does not lie in the equatorial plane. In practice the heliospheric current sheet (HCS) undulates like a ballerina's skirt, proposed first by Alfvén in 1977 and shown in Fig. 1.4. Thus, depending on the relative position of a planet to the current sheet, the IMF orientation and magnitude will vary between sectors of "toward" and "away" magnetic field. During solar maximum, the sector structure is

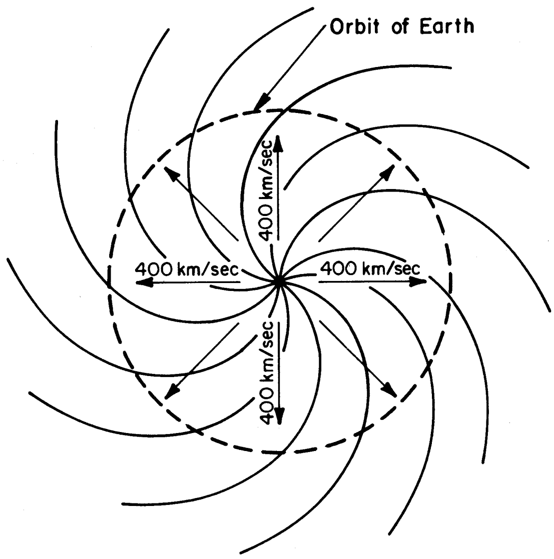

Figure 1.3. A sketch of the Parker spiral configuration of the interplanetary magnetic field (IMF). The foot of the field line remains attached to the Sun but due to the phenomenon of 'frozen in flow' the magnetic field lines are carried away from the Sun with the solar plasma, and are wound into a spiral by the Sun's rotation. [From Kivelson and Russell, 1995].

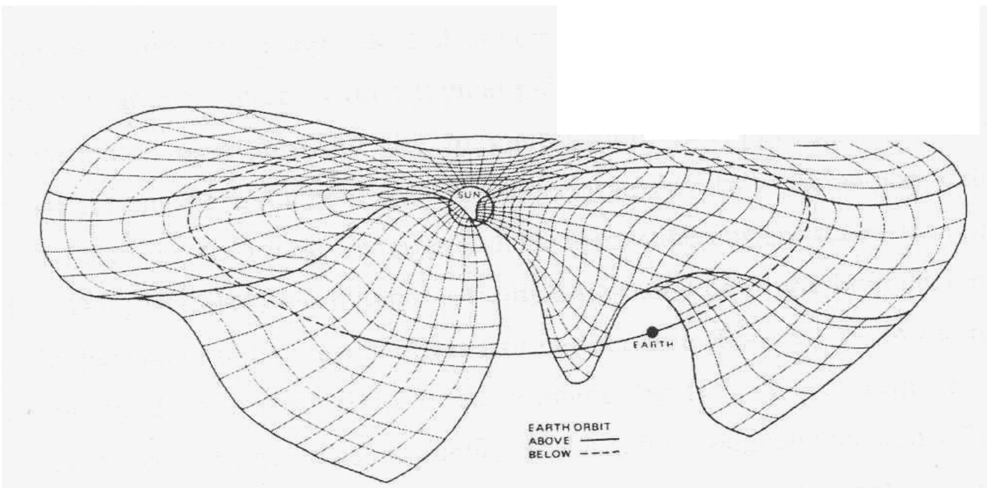

Figure 1.4. Current sheet in the inner heliosphere where the effect of the tilt of the solar magnetic axis with respect to the rotation axis produces the 'ballerina skirt' effect.
[From Kivelson and Russell, 1995].

complex and distorted by coronal mass ejections (CMEs) and magnetohydrodynamic (MHD) waves [Balogh et al., 1993]. At solar minimum, the field is more dipolar and so there is a clear two-sector structure, as discussed in more detail in Chapter 4.

1.4 Corotating Interaction Regions

It is well understood from theoretical studies, as well as from previous analysis of Ulysses data out to distances of ~5 AU, that the equatorial heliosphere at solar minimum will generally be highly structured by the compressions and rarefactions associated with recurrent 'corotating interaction regions' (CIRs) [e.g. Gosling and Pizzo, 1999; Crooker et al., 1999]. CIRs occur due to the emission into a given radial direction of solar wind plasma of strongly varying outward flow speed by varying source regions as the Sun rotates. When fast wind follows slow, a compression region is formed as the flow speed rises, while when slow wind follows fast, a rarefaction is formed as the flow speed falls. While each element of the solar wind plasma flows nearly radially outward from the Sun, the resulting pattern of compressed and rarefied plasma approximately corotates with the Sun, to the extent that the source pattern remains fixed with respect to the rotating Sun, as shown schematically in Fig. 1.5. The source pattern itself depends on the structure of the Sun's magnetic field, since slower (~400 km s^{-1}) denser wind originates from the regions immediately surrounding the closed field arcades which extend to heliocentric distances of about 2 solar radii, while the faster (~750 km s^{-1}) more tenuous wind originates from the open field coronal holes. The structure of the Sun's magnetic field, and hence the pattern of plasma outflow, then depends significantly on the phase of the solar activity cycle.

During the declining phase of the solar cycle, the Sun's magnetic field takes the form of a dipole tilted with respect to the spin axis [see e.g. Gosling and Pizzo, 1999, and references therein]. The angle of the tilt generally decreases with decreasing solar activity, such that the dipole tends to align with the spin axis near solar minimum. In this configuration the closed field line arcades generally straddle the magnetic equator, thus

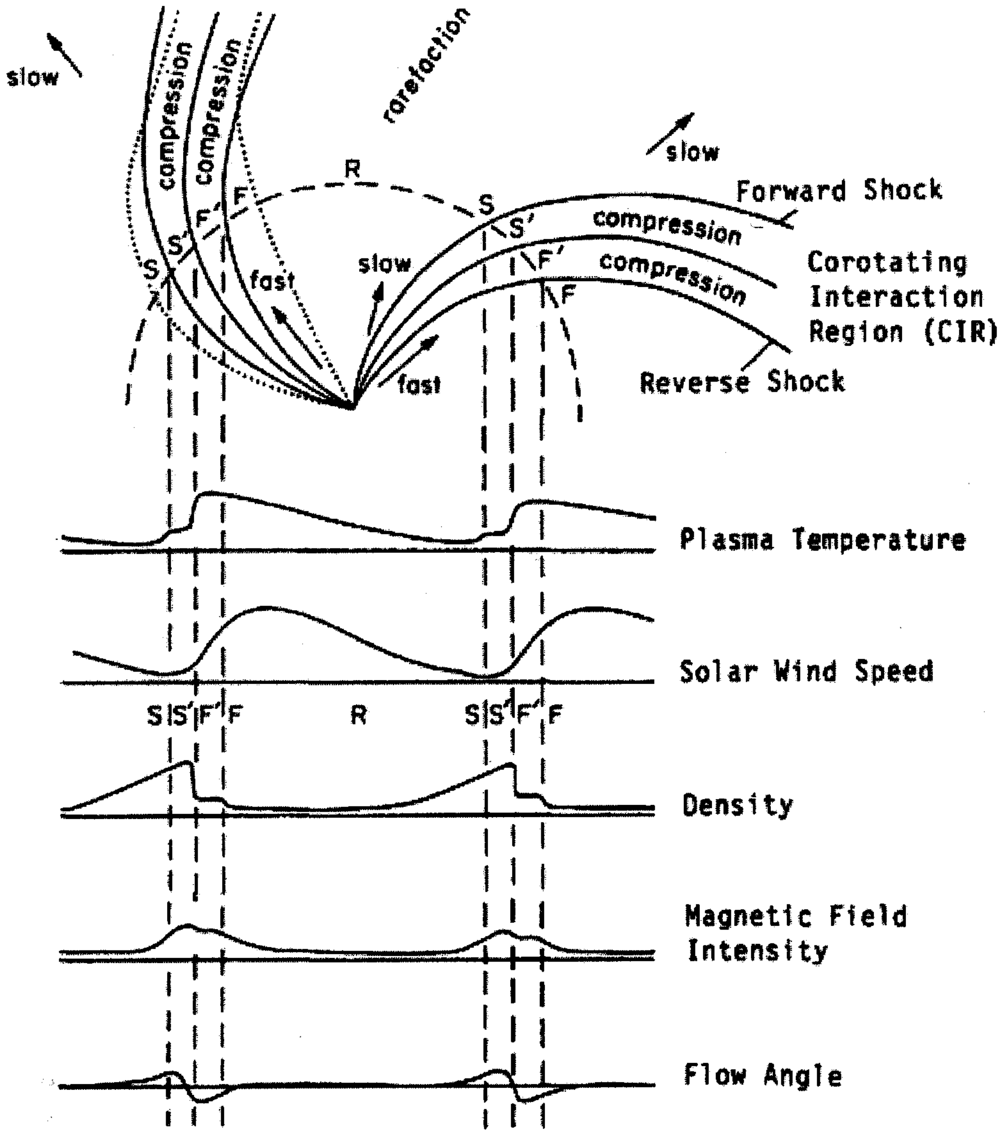

Figure 1.5: Schematic diagram of two CIRs corotating with the Sun, along with the associated solar wind and magnetic field signatures at 1 AU. [From Kunow, 2001].

defining a magnetic equatorial band of slower solar wind outflow. Fast wind then emerges from the coronal holes at higher magnetic latitudes. The heliospheric structures to which this configuration gives rise are illustrated schematically in Fig. 1.6, adapted from Gosling [1996]. This shows a plot in heliographic latitude and longitude, fixed to the rotating Sun, of the regions of slow (shaded) and fast (unshaded) solar wind outflow, at a distance of (say) a few solar radii, beyond the closed field regions, where the magnetic field is nearly radial. The diagram is specifically for the case of a tilted solar dipole appropriate to the declining phase of the solar cycle. The dashed line shows the boundary between fields that point radially outward from the Sun, and those that point radially inward, thus marking the location of the heliospheric current sheet (HCS). For the present solar cycle, the field points outward south of the line, and inward north of the line. The HCS thus lies centrally within the region of slow plasma outflow. The maximum heliographic latitude reached by the HCS in the north and south indicates the tilt angle of the dipole relative to the Sun's spin axis. The solid lines then mark the northern and southern boundaries of the slow and fast outflows, and thus the slow-fast solar wind stream interfaces (SI), as also indicated in the figure.

The compression regions associated with CIRs occur when fast wind follows slow into a given radial direction, as indicated above. Given that the slow-fast pattern shown in Fig. 1.6 rotates from left to right with respect to a fixed observer, these occur where the latitude of the northern SI increases with heliographic longitude (between longitudes of 0° and 180° in the figure), and where the latitude of the southern SI decreases with longitude (between 180° and 360° in the figure). On the other segments of the SIs, slow wind follows fast into a given radial direction, and a rarefaction region occurs. Focusing now on the compression regions, the slow wind ahead of the fast is compressed and accelerated, while the fast behind the slow is similarly compressed and slowed. The compressive effects propagate as waves moving away from the SIs into the respective solar wind streams, the wave propagating into the slow wind moving outward from the Sun with respect to the plasma and forming the 'forward wave' (shown by the dot-dashed lines marked FW in the figure), while the wave propagating into the fast wind moves backward towards the Sun with respect to the plasma (though still outward overall) and

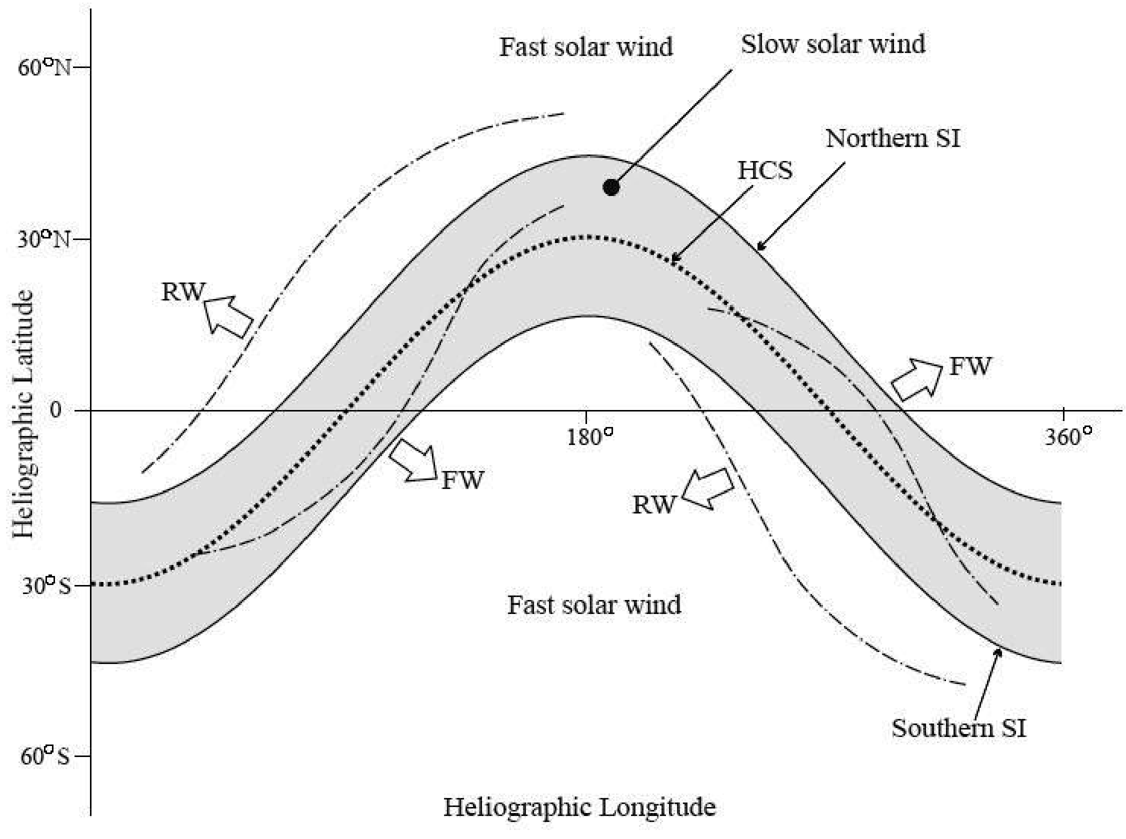

Figure 1.6: Sketch of the source regions of slow and fast solar wind flow in heliographic co-ordinates fixed in the rotating Sun, for tilted dipole solar field conditions appropriate to the declining phase of the solar cycle. [Adapted from Gosling, 1996].

forms the 'reverse wave' (shown by the dot-dashed lines marked RW in the figure). As the interaction region propagates away from the Sun, these waves steepen into forward and reverse shocks which bound the region of compression, shock formation typically occurring within a few AU (~2-3 AU) of the Sun [Gosling and Pizzo, 1999, and references therein]. In addition, at such distances (and beyond), it is found that the forward wave has generally overtaken the HCS in the equatorial region, as shown in Fig. 1.6, such that the latter is incorporated within the compression region.

We thus consider the plasma and magnetic field structures that are expected to be observed on this basis at a given near-stationary, near-equatorial, observing point as the Sun rotates, such that the observer moves from right to left within the diagram. Suppose for sake of argument we start at 180° heliographic longitude in the region of fast solar wind emerging from the southern coronal hole, then initially we will be located in a rarefaction region of low solar wind density and field strength as the solar wind speed falls with increasing time at the observer. The field direction in this region will correspond to an 'away' sector during the present solar cycle. The observer will then pass across the southern SI into the slower solar wind, before encountering the forward shock propagating away from the northern SI. We note, however, that the computations of Pizzo [1994a, b] indicate that by ~10 AU, near Saturn's orbit, this forward shock may have encompassed much of the equatorial slow solar wind plasma, as indicated in the figure, after which it will start to propagate into the trailing edge of the fast wind from the southern hemisphere. Across the forward shock the plasma velocity, density, and field strength will all abruptly increase. This will then be followed by a crossing of the HCS into a 'toward' field sector, and then the northern SI (though generally SIs do not have a very obvious magnetic signature). Finally we cross the trailing edge of the reverse wave associated with the northern SI, where the plasma density and field strength will abruptly drop, while the velocity will increase to reach its peak value during the solar rotation. This will then be followed by a rarefaction region where the plasma velocity and density slowly drop with time before the compression region associated with the southern SI is encountered. Overall, it can be seen that for the declining phase of the solar cycle we anticipate an IMF consisting of two sectors per solar rotation, where the sector boundaries (HCS crossings) are embedded within two CIR compression regions, separated by plasma and field rarefactions

1.5 Planetary Magnetospheres

A magnetosphere is the cavity which contains the planet's internal magnetic field and is confined by the impinging solar wind and IMF. There are six magnetized planets in our solar system and the relative size of their magnetospheres is shown in Fig 1.7. Saturn has the second largest magnetosphere in the solar system, and its structure and dynamics will be discussed in detail in Chapter 2.

In 1931, Chapman and Ferraro considered the case of a planet with a purely dipolar magnetic field and plasma originating in the ionosphere. According to the theory of frozen-in-flux, the solar wind plasma remains frozen to the IMF and planetary plasma remains frozen to the planetary magnetic field. When the plasma populations meet each other, they cannot mix, and a thin current sheet is set up between the two, forming a closed magnetosphere, as shown in Fig. 1.8. This current sheet is called the magnetopause, and across it the magnetic field undergoes a sharp change of strength and direction. The magnetosphere is compressed on the dayside by the pressure of the impinging solar wind, while on the nightside the magnetosphere extends into a long magnetotail consisting of two anti-parallel lobes of magnetic flux connected to the poles of the planet. Upstream of the dayside magnetopause lies the bow shock, which forms as a consequence of the supersonic solar wind flow. Across the shock, plasma is slowed, compressed and heated, forming a layer of turbulent plasma called the magnetosheath. Inside the cavity, the magnetospheric magnetic field lines extend down into the ionosphere and upper atmosphere (thermosphere) of the planet, such that the magnetosphere, ionosphere, and thermosphere are strongly coupled together. In the case where there are no other forces acting on the magnetospheric plasma, it would rotate with the same angular velocity as the planet. This "corotation" is a result of angular momentum being transferred from the atmospheric neutral atoms to the plasma ions via

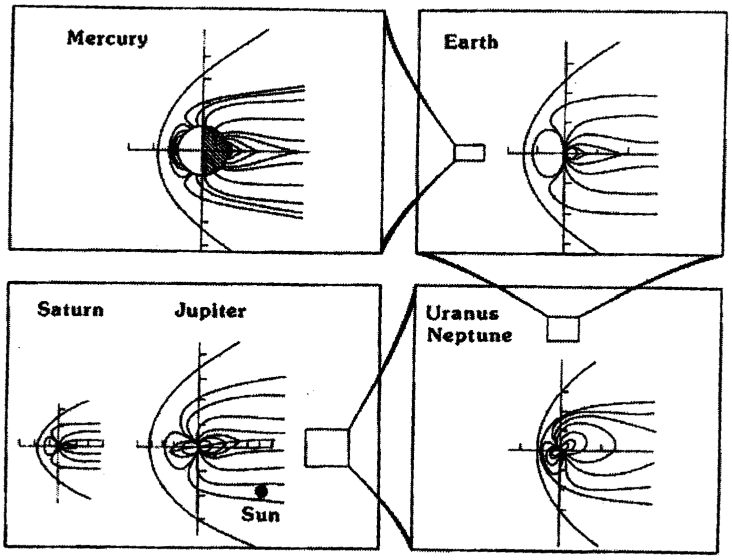

Figure 1.7: Relative sizes of planetary magnetospheres. [From Kivelson and Russell, 1995].

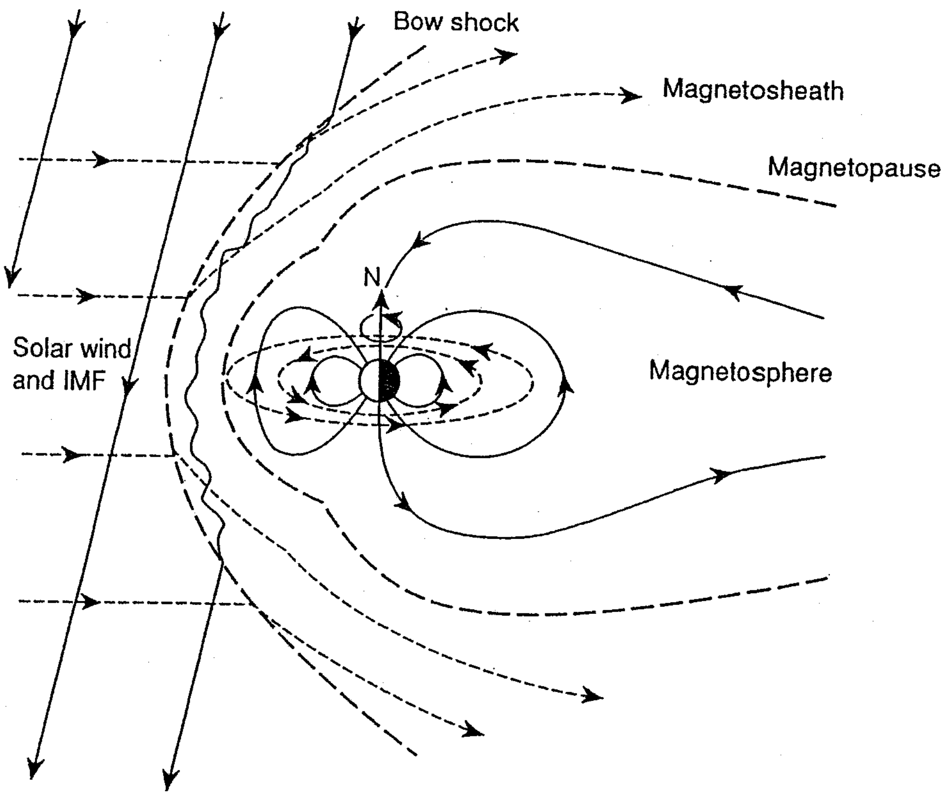

Figure 1.8: Sketch of the Chapman-Ferraro closed magnetosphere in the noon-midnight meridian plane, based on the strict application of the frozen-in-flow approximation. The arrowed dashed lines represent plasma streamlines, and the heavy long-dashed lines the bow shock and magnetopause boundaries. [From Cowley, 1991].

collisions in the lower ionosphere. The torque is communicated to the magnetospheric plasma by the planetary field, such that in the steady state rigid corotation will prevail. Let us now consider the effect of solar wind and IMF interaction with the magnetosphere.

1.5.1 The Dungey Cycle

In 1961 James Dungey suggested that this frozen-in-flux approximation could break down in some regions. For the case of the dayside current sheet boundary layer, when there are anti-parallel magnetic fields and the scale size is small enough, the plasma can become diffusion dominated. In terms of the induction equation (Eq. 1.4), we note that a plasma is diffusion dominated if the second term on the right-hand side is much larger than the first, yielding $R_m \leq 1$. Thus, the field lines are allowed to diffuse through the plasma and "reconnect", as illustrated in Fig. 1.9. Magnetic tension will cause the newly reconnected field lines to retreat along the current sheet, away from the reconnection site, allowing further field lines from the two original populations to diffuse into the current sheet and undergo reconnection.

The implications of reconnection and the breakdown of the frozen-in approximation for the magnetosphere are significant. There is now a mechanism by which plasma from the solar wind can mix with planetary plasma. The process by which reconnection occurs at the dayside magnetopause, initiating a cyclical flow pattern within the magnetosphere is illustrated in Fig. 1.10. Reconnection on the dayside produces planetary field lines that are 'open' to the IMF, thus allowing the transfer of mass, momentum and energy from the solar wind to the planetary magnetosphere. These newly reconnected field lines (1 and 1' in Fig. 1.10), are connected at one end to the Sun and at the other end to the planet. They are then pulled anti-sunward by the solar wind flow, thus flowing across the polar cap, and are stretched out into a long magnetotail where energy and magnetic flux are stored. On the nightside, the near-planet portion of the field sinks toward the centre of the magnetotail and eventually reconnects via another X-type field arrangement. In the region tailward of this reconnection region the disconnected flux tubes flow back into the

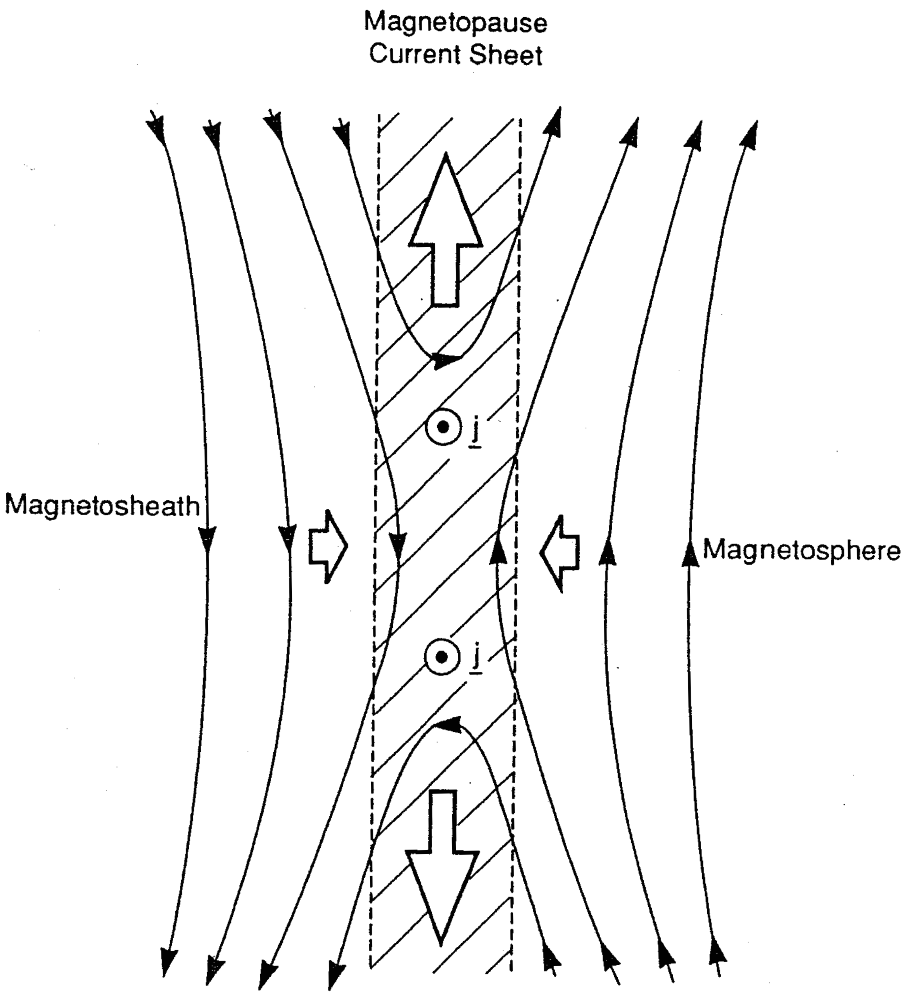

Figure 1.9: Sketch showing magnetic reconnection in the magnetopause current sheet. In the current sheet (hatched region), the current density points out of the plane of the diagram. Solid arrowed lines represent magnetic field lines and the large arrows show the direction of plasma motion. [From Cowley, 1991].

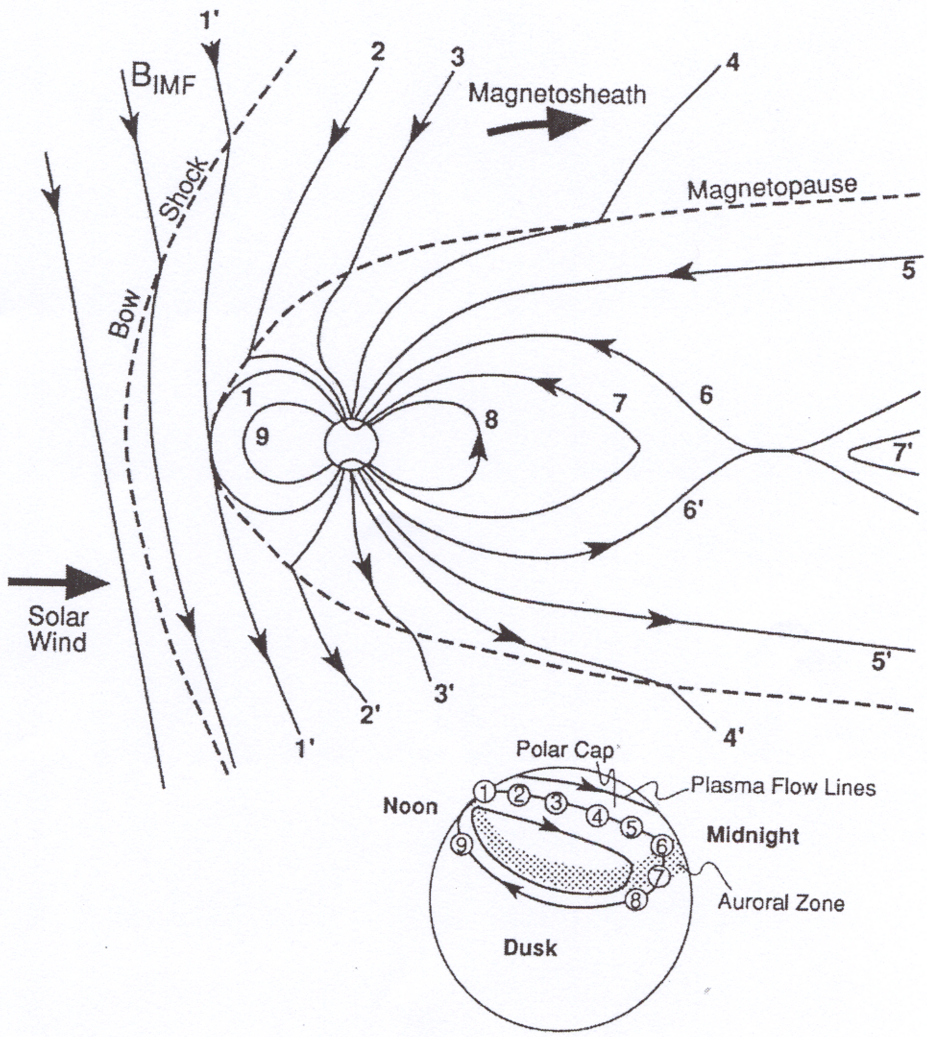

Figure 1.10: Cross-section of Dungey's 'open' magnetosphere in the noon midnight meridian plane (for the case of the Earth). The numbered field lines indicate the evolution of a newly reconnected field line (1') as it is transported tailward before undergoing tail reconnection. The inset indicates the position of the foot of the field line in the ionosphere as it moves through the Dungey cycle. [From Hughes, 1995].

solar wind, while close to the planet the newly closed field lines convect around the flanks of the inner magnetosphere towards the dayside magnetopause, where the cycle then repeats itself. However, not all of the flux tubes take part in the solar-wind driven convection cycle. There is a region extending into the equatorial plane (to a distance of ~4 R_E for the Earth's magnetosphere), where the flux tubes approximately corotate with the planet. Further out from the planet, the effect of the solar wind interaction takes over. The Dungey cycle and the relative importance of corotation will be described for Saturn in Chapter 2, while the timescales for transport of open field lines downtail will be discussed in Chapter 4.

1.6 Summary

This chapter has provided a background discussion of the origins and nature of the solar wind and IMF, and the interactions that occur with planetary magnetospheres. Chapter 2 will go on to discuss the kronian system in particular detail.

Chapter 2

Review of the global structure and dynamics of the kronian magnetosphere

2.1 Introduction

In this chapter we now focus more closely on the kronian magnetosphere. Saturn is the sixth planet from the Sun at a distance of 9.5 AU, and the second largest, after Jupiter. Saturn was observed by Galileo in 1610, while in 1655 Christiaan Huygens correctly inferred the geometry of the spectacular rings. Saturn is a gas giant planet, and composed of about 75% hydrogen and 25% helium, with other trace elements. The planet's interior is believed to be similar to Jupiter's, consisting of a rocky core, a liquid metallic hydrogen layer and a molecular hydrogen layer. Saturn is a fast rotator, with a period of ~10.75 hours (to be discussed in more detail in Section 2.7), and this rotation generates a centrifugal force, causing the equatorial regions to bulge and the poles to flatten. The speedy rotation, combined with its metallic hydrogen layer, generates a very large planetary magnetic field, the properties of which will be discussed in some detail in Section 2.2.

Saturn's magnetosphere, sketched in Figure 2.1, is the cavity which contains and is controlled by Saturn's magnetic field. This cavity is compressed on the dayside by the pressure of the impinging solar wind, and is stretched out into a long magnetotail on the nightside. The position of the magnetopause boundary is defined by the condition of pressure balance between the magnetosheath plasma and field on one side, and the magnetospheric field and plasma on the other. Typically the magnetopause extends to ~20 R_S on the dayside [Behannon et al., 1983], (one Saturn radius, R_S, is taken

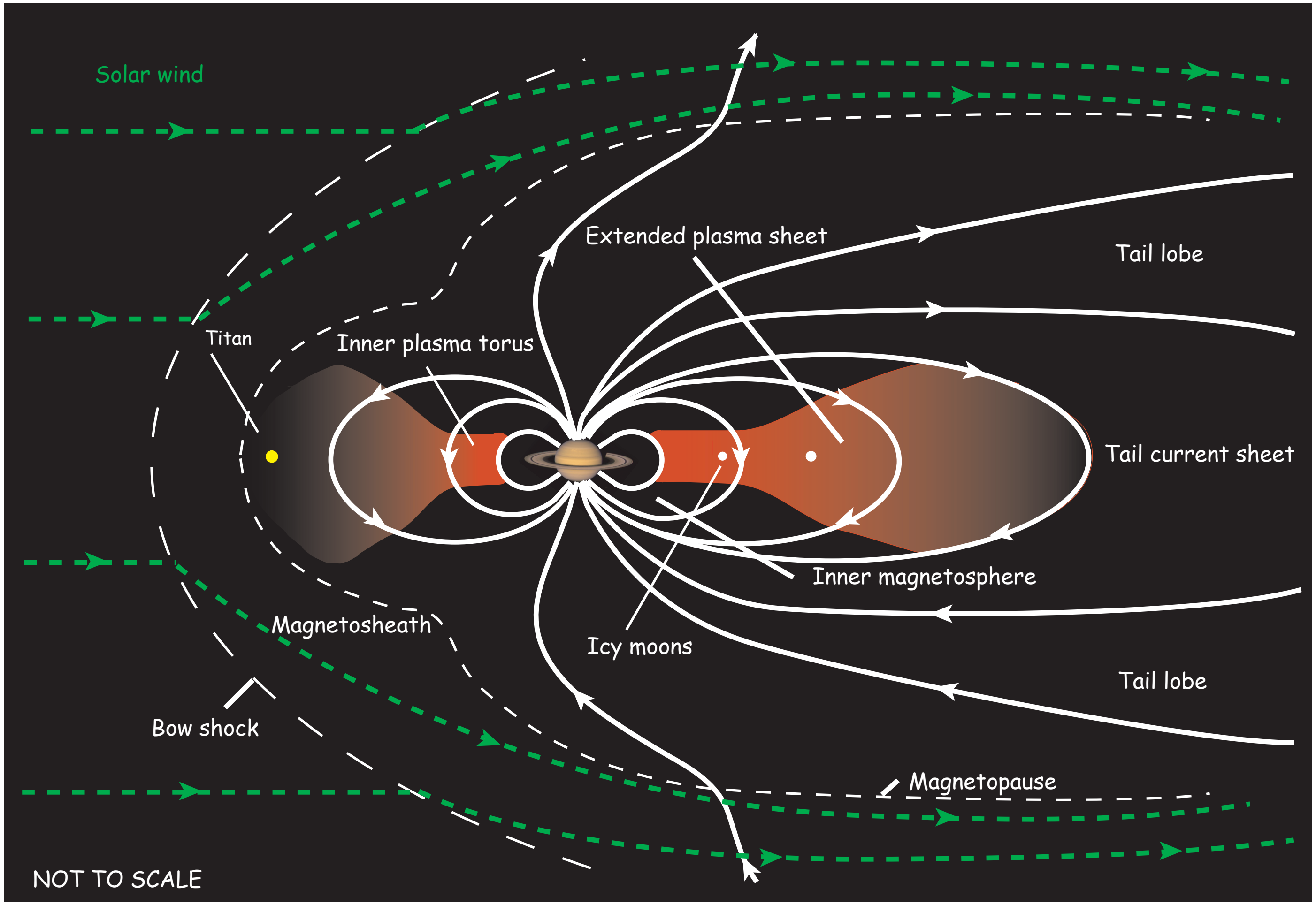

Figure 2.1 Sketch of Saturn's magnetosphere in the noon-midnight meridian plane, with the Sun to the left and the solar wind blowing from left to right. The arrowed solid lines are the magnetic field lines, while the dashed lines are the magnetopause and bow shock [Courtesy Dr. Emma Bunce].

throughout this thesis to be 63,330 km), though statistical studies of multiple Cassini orbits are currently aiming to refine this value for the standoff distance [Achilleos et al., 2006]. Because the solar wind is supermagnetosonic in the rest frame of the planet, a bow shock stands upstream of the dayside magnetopause. The magnetosphere, ionosphere and upper atmosphere are coupled together, and as such angular momentum is transferred between the three, via the magnetic field.

2.2 Saturn's magnetic field

2.2.1 In situ measurements

The first *in situ* measurements of the kronian system were made by the Pioneer-11 spacecraft in 1979, followed by Voyager-1 and Voyager-2 in 1980 and 1981 respectively. The trajectories of these spacecraft are shown in Figure 2.2. All three spacecraft entered the planet's magnetosphere in the vicinity of the noon meridian, with Pioneer-11 and Voyager-2 exiting nearly along the dawn meridian, while Voyager-1 exited further down the tail [e.g. Smith et al., 1980; Ness et al., 1981, 1982]. Cassini's successful orbit insertion on 1 July 2004 provided the first examination of Saturn's magnetosphere in 23 years, with periapsis at ~1.33 R_S. The inbound trajectory of Cassini was at an earlier local time than previous missions, but the outbound passage was similar to that of Voyager-2, exiting at high southern latitudes [Dougherty et al., 2005]. The Cassini inbound crossings occurred further from Saturn than their average expected locations, revealing an expanded magnetosphere at the time of the inbound encounter. On the outbound pass, there is evidence to suggest a compressed magnetosphere, as will be presented in some detail in Chapters 4 and 5.

2.2.2 Internal field

The planetary field is primarily that of a dipole with a magnetic moment of 0.21 R_S^3 G [Acuña et al., 1980; Ness et al., 1981]. However, the magnetometer

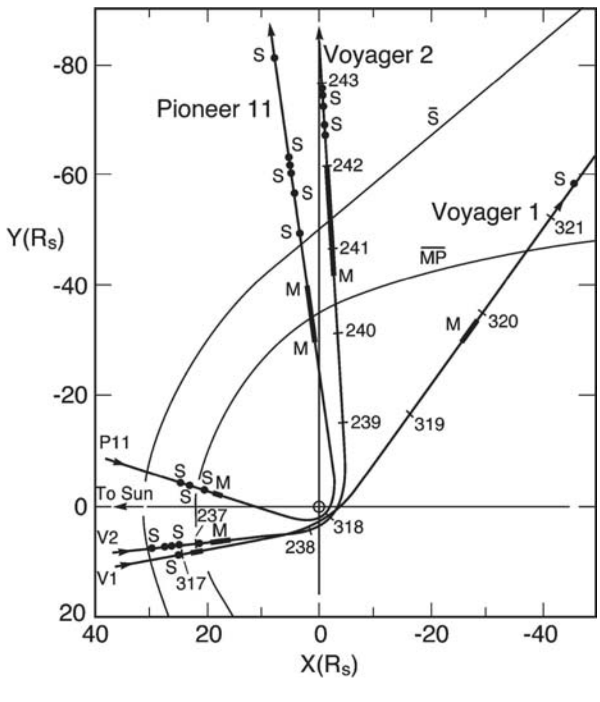

Figure 2.2: Equatorial view of the three spacecraft flybys of Saturn. On the trajectories the black dots labelled S show observed bow shock crossings, and black rectangles labelled M show observed magnetopause crossings [From Dougherty et al., 2004].

observations from Pioneer-11, Voyager-1 and Voyager-2 revealed axially aligned quadrupole and octupole terms also, and these can be expected to have a significant role in charged-particle motion in Saturn's magnetosphere [e.g. Connerney et al., 1981]. The magnetic field shows a remarkable symmetry about the rotation axis of the planet with there being a less than 0.7º tilt between the dipole and rotational axes, a unique feature in our solar system. The polarity of the field is opposite to that of the Earth, and thus is directed positive from north geographic pole to south geographic pole.

Several models of Saturn's field have been proposed, including the Z3 zonal harmonic model, derived from Voyager 1 and 2 flux gate magnetometer observations [Connerney 1982], and the SPV (Saturn Pioneer Voyager) model which is based on all available pre-Cassini data [Davis and Smith, 1990]. The Z3 and SPV models showed that only the axially symmetric dipole, quadrupole, and octupole terms were significant in the modelling of the field due to internal sources. Cowling [1934] demonstrated that if the magnetic field is generated by electrical currents produced by the circulation of conducting fluids inside the planet, the model must include non-axisymmetric coefficients. The absence of these coefficients in these new models, as Stevensen [1982] pointed out, is probably due to a highly conducting shell outside the dynamo region and rotating about Saturn's polar axis.

2.2.3 The size of the kronian magnetosphere

In order to estimate the size of the magnetospheric cavity of Saturn in the solar wind, the above value of the dipole moment may be used (as a good approximation) along with a simple consideration of pressure balance across the magnetopause [e.g. Baumjohann and Treumann, 1997]. Neglecting magnetic pressure in the solar wind and gas pressure in the magnetosphere, we find that the distance to the subsolar magnetopause R_{mp} is given approximately by

$$\left(\frac{R_{mp}}{R_S}\right) = \left(\frac{B_{eq}{}^2}{\mu_0 \rho v^2}\right)^{\frac{1}{6}} \tag{2.1}$$

where B_{eq} is the planet's equatorial surface magnetic field strength, v is the solar wind bulk velocity, ρ is the solar wind mass density, and the result is normalized to the planet's radius R_S. This equation gives the position of the sub-solar magnetopause at ~20 R_S, in reasonable accord with spacecraft observations.

2.2.4 The ring current

Initial observations from Pioneer-11, later confirmed by Voyager-1 and 2, have shown that Saturn is surrounded by an eastward-flowing ring current which extends from ~8 to ~16 R_S in the equatorial plane and with a total thickness of ~5 R_S, similar in form to the ring current that flows westward around the Earth. The current is generated by the relative drift of ions and electrons in opposite directions around the planet. Current flow in a plasma generates magnetic fields, and the ring current results in the dipole-like magnetic field lines of the planetary field being stretched outwards in a radial direction, as will be described in Section 2.4.

2.3 Saturn's plasma environment

The nature of the plasma dynamics in a planetary magnetosphere depends on the nature of the plasma sources and sinks, and the nature of the transport processes which convey the plasma from the former to the latter. Saturn has numerous possible sources of thermal plasma, including the solar wind at the outer boundary, the ionosphere at the inner boundary, the rings, inner icy moons, and Titan's atmosphere. Cassini has recently probed the plasma environment and found the magnetosphere to be composed primarily of a complex mixture of water-derived molecular and atomic ions [Young et al., 2005].

The behaviour of the plasma in the magnetosphere can be separated into three distinct regions as are shown in Fig. 2.3. The left-hand side of the figure shows the magnetosphere at noon local time whereas the right-hand side reveals the behaviour in the dawn magnetosphere [from Sittler et al., 1983].

The **inner plasma torus** is characterized by the presence of dense low-energy ions and electrons with low temperatures and high densities. Inside of 4 R_S the torus is thin about the equatorial plane, of the order of 0.4 R_S. Between 4 and 8 R_S, the plasma sheet thickens out to about 2 R_S, and Frank et al. [1980] suggest the rings and to a lesser extent the satellites Dione and Tethys as sources of plasma in this region. Sputtering from these sources produces neutrals, which are then ionized to form H+ and O+ [Richardson 1986]. Instruments on Cassini have also detected low energy N+ ions within 8 R_S, most likely from a minor constituent of the icy satellite surfaces or the E-ring, or locally ionized nitrogen from Titan [Young et al., 2005].

Outside of the inner plasma torus lies an **extended equatorial plasma sheet** with enhanced levels of cold plasma [Connerney et al., 1981]. This plasma sheet extends out to about 15 R_S and has a thickness of ~5 R_S around the equatorial plane [Sittler et al., 1983]. The mass loading in this region is sufficient to cause the magnetosphere to subcorotate, and thus may be indicative of the existence of a meridional current system [e.g. Richardson, 1986; Richardson and Sittler, 1990; Saur et al., 2004], as will be discussed further in Section 2.4. The inner edge of the extended plasma sheet coincides with a vast cloud of neutral hydrogen that extends from there to beyond 25 R_S, and was first observed by the Voyager UVS experiment [Broadfoot et al., 1981]. This neutral hydrogen probably escaped from Titan and the other satellites.

Beyond the extended plasma sheet lies the **hot outer magnetosphere.** In this region, plasma has been thought to come primarily from the solar wind and Titan's atmosphere. Titan is a direct source of nitrogen ions, which stream away from the moon in the local corotation direction, thereby generating a plume of plasma. However, new data from Cassini has pointed to the moon Enceladus as a major source of ions for the

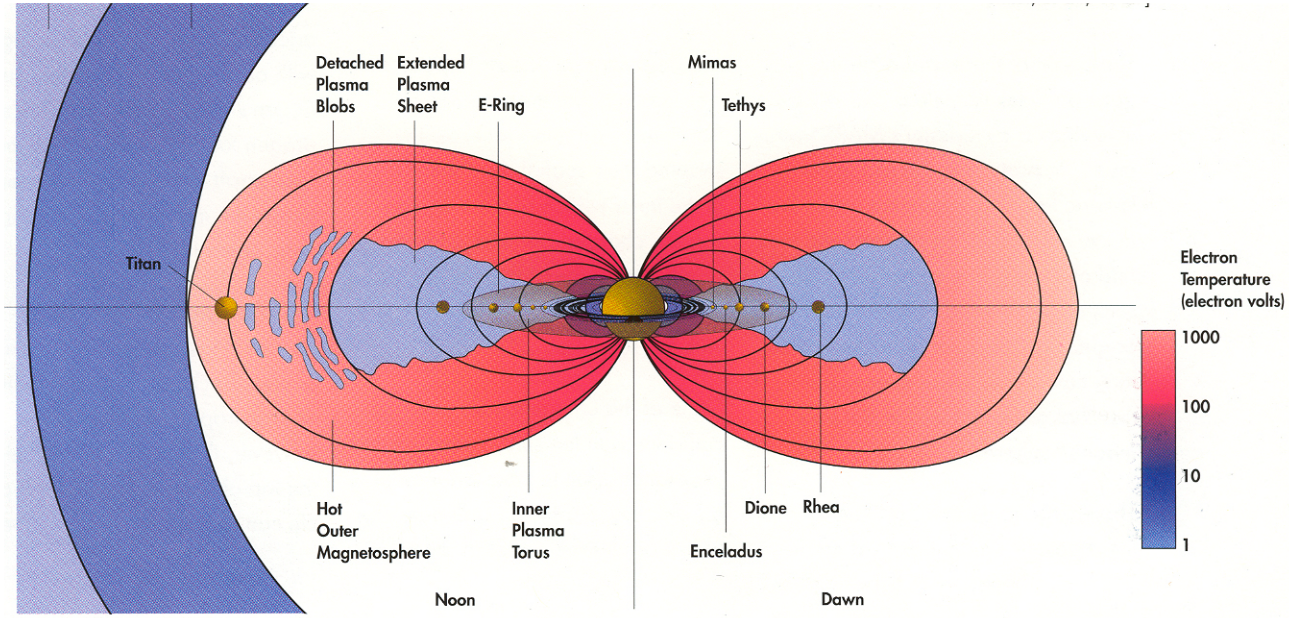

Figure 2.3: The different plasma regions of Saturn's magnetosphere, where the noon meridian is shown on the left of the figure and the dawn meridian on the right. The inner plamsa torus, extended plasma sheet and hot outer magnetosphere are all shown with respect to the position of the rings and some of the inner satellies. [From Sittler et al., 1983].

magnetospheric plasma. At the time of writing, the specific role of this source is yet to be determined and quantified.

2.4 Magnetosphere-ionosphere coupling

Planets which possess both atmospheres and magnetospheres are observed, as expected, to exhibit the phenomenon of corotation. Rigid corotation implies that the planetary plasma rotates with the same angular velocity as the planet itself. Angular momentum is transferred from the rotating planet up into the ionosphere, where collisions between ions and neutrals speed up the plasma toward corotation.

However, corotation cannot extend to arbitrarily large distances from the planet, and must ultimately break down as the result of either external forces or of the inertia of the corotating plasma. There are several mechanisms by which corotation can break down. Firstly, if plasma is produced, e.g. by ionization of neutral gas, then these newly-ionized particles will take up angular momentum from the plasma, causing it to slow below rigid corotation [e.g. Pontius and Hill, 1982]. Secondly, if ions are transported radially outwards from an internal source, the angular velocity of the plasma will drop as ρ^{-2} if there is no torque on the plasma, such that angular momentum is conserved.

These processes of plasma production and radial transport thus cause the plasma to subcorotate relative to the planet [Richardson, 1992, Richardson et al., 1998; Richardson and Sittler, 1990; Saur et al., 2004]. Corotation-enforcement currents, as first discussed by Hill [1979] and Vasyliunas [1983] in the Jovian context, must therefore also flow at Saturn [Cowley and Bunce, 2003a]. These currents communicate torque to the equatorial plasma and flow along essentially resistance-free field lines [Hill, 1979; Connerney, 1981; Vasyliunas, 1983; Khurana and Kivelson, 1993]. The azimuthal fields observed in the inner part of the magnetosphere on both Voyager fly-bys can be reasonably well accounted for by this magnetosphere-ionosphere coupling mechanism, given an effective value of the ionospheric Pedersen conductivity of ~1-2 mho [Bunce et al., 2003]. The magnetopause-tail current system contributes only small fields within this region.

The magnetosphere-ionosphere coupling current system is illustrated in Figure 2.4, which is a sketch of a meridian cross section through Saturn's quasi-axisymmetric inner and middle magnetosphere, extending to distances of ~15-20 R_S in the equatorial plane. The magnetic field lines, indicated by arrowed solid lines, are modestly distended outward from the planet by azimuthal currents (the 'ring current') flowing in the near-equatorial plasma. The rotating plasma, shown by the dotted region, consists mainly of protons and oxygen ions and associated electrons, which derive from water ice originating from ring grains and moon surfaces. Three angular velocities are indicated. These are the angular velocity of a particular shell of field lines ω, the angular velocity of the planet Ω_S, and the angular velocity of the neutral upper atmosphere in the Pedersen layer of the ionosphere, Ω_S^*. The value of Ω_S^* is expected to lie between ω and Ω_S because of the frictional torque on the atmosphere due to ion-neutral collisions. The oppositely-directed frictional torque on the magnetospheric flux tubes is communicated to the equatorial plasma by the current system indicated by the arrowed dashed lines, shown here for the case of subcorotation of the plasma (i.e. $\omega < \Omega_S$) [Bunce et al., 2003]. In this system, Pedersen currents flow equatorward in the ionosphere, driven by the equatorward-directed electric field of the sub-corotating flow in the neutral atmosphere rest frame, and close via field-aligned currents which flow radially outward in the magnetospheric plasma. The **j**x**B** force in the equatorial plane is directed into the diagram and acts to increase the speed of the sub-corotating equatorial plasma, while the **j**x**B** force of the closure currents in the ionosphere acts in the opposite direction as a drag force on the rotation of the thermosphere [Bunce, 2001]. Overall, angular momentum is transferred from the planet's atmosphere to the magnetospheric plasma.

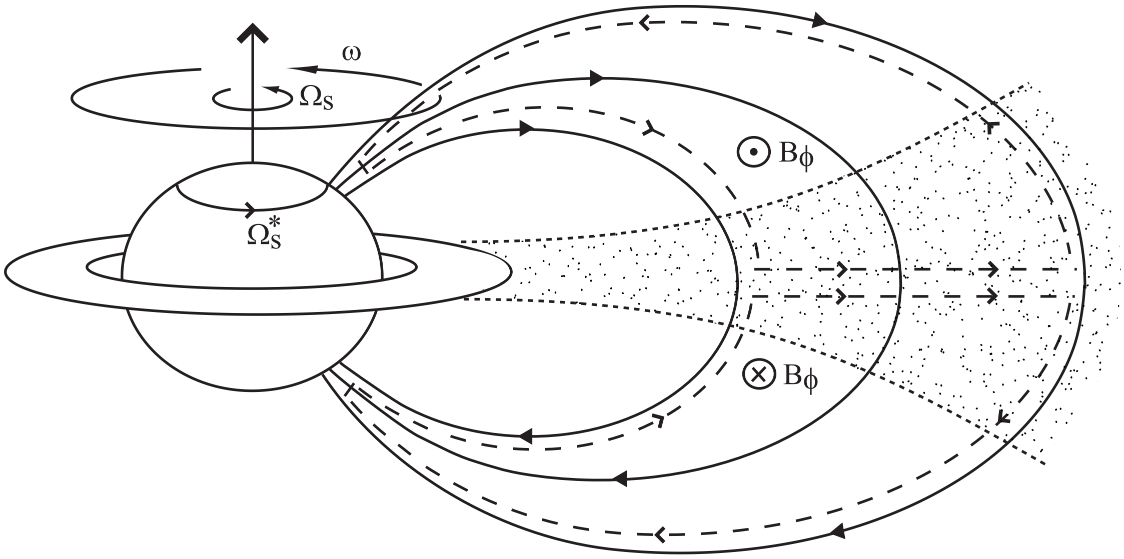

Figure 2.4: Sketch of a meridian cross-section through Saturn's quasi-axisymmetric inner and central magnetosphere, extending to distances of ~15-20 R_S in the equatorial plane. The arrowed solid lines indicate magnetic field lines. The rotating plasma is shown by the dotted region. Three separate angular velocities are indicated. These are the angular velocity of a particular shell of field lines, ω, the angular velocity of the planet, Ω_S, and the angular velocity of the neutral upper atmosphere in the Pedersen layer of the ionosphere, Ω_S*. The magnetosphere-ionosphere coupling current system is indicated by the arrowed dashed lines [From Bunce et al., 2003].

2.4.1 Bending of field lines

The above current system bends the field lines out of meridian planes, into a 'lagging' configuration, associated with the azimuthal field components B_{φ} shown. For the case of Saturn, where the field is directed southward at the equator, the sense of the associated azimuthal field is negative north of the equator, reversing to positive south of the equator.

The sense of field bending due to this "lagging" effect is shown in Fig 2.5, which looks down onto the north pole of the planet. The inner field lines from low latitudes are bent out of the meridian planes. There is also a second effect associated with the day-night asymmetric confinement of the planetary field by the solar wind, i.e. the effect of the magnetopause and tail currents system. The sense of the field bending associated with these currents is shown by the outer field lines in the figure, which are bent away from noon and towards the tail on either side. On the dawn side, the "lagging" effect has the same sense as the bending effects induced by the solar wind, so it is not simple to separate them in this sector. However, on the dusk side, the effects are opposite, and "lagging" fields at smaller distances have been found to give way to "leading" tail-like fields at larger distances. Thus, in the north, the perturbation fields are eastwards on the dusk side of the magnetosphere and westward on the dawn side. "Leading" and "lagging" fields as described here have indeed been observed by spacecraft. The observed "lagging" fields are consistent in magnitude with the sub-corotation effect with an effective ionospheric conductivity of ~1-2 mho. However, the magnitude of the observed "leading" fields is found to be significantly larger than those calculated from scaled terrestrial models, and appears indicative of the presence of another dynamical process.

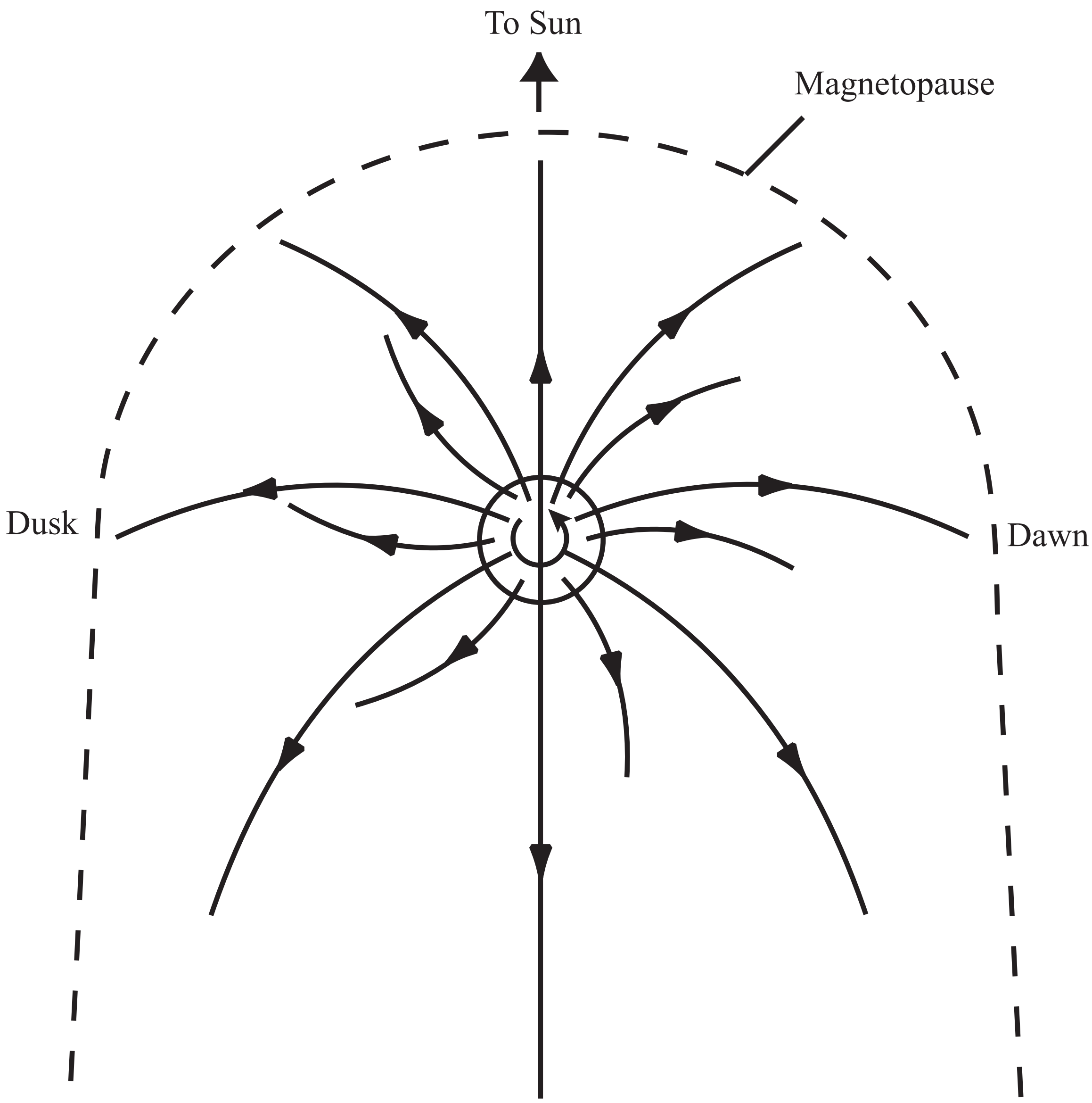

Figure 2.5: Sketch looking down onto the northern pole of Saturn, showing field lines (arrowed solid lines) projected onto the equatorial plane. The sense of planetary rotation is anti-clockwise, as indicated. The inner field lines are shown bent into a 'lagging' configuration associated with angular momentum transfer from the atmosphere to the magnetosphere due to sub-corotation of the magnetospheric plasma. The outer field lines are shown bent away from noon, due to the effect of the magnetopause (dashed line) and tail current system. [From Bunce et al., 2003].

2.5 Equatorial and ionospheric flows – weak reconnection

With the knowledge of the planetary magnetic field, plasma sources, and magnetosphere-ionosphere coupling system, we now consider the large-scale flow in Saturn's magnetosphere. Cowley et al. [2004a] have proposed a physical picture of Saturn's magnetospheric flow and currents which contains co-existing features associated both with internally-driven processes and with the solar wind interaction. Here, however, we first focus on the internal dynamics, supposing initially that while open flux is present in the system, mapping to the tail lobes, ongoing reconnection (and thus the Dungey cycle, as described in Chapter 1) is weak both at the magnetopause and in the tail.

2.5.1 Equatorial flows

The flow in the magnetospheric equatorial plane under these circumstances is depicted schematically in Fig. 2.6, in which the direction toward the Sun is at the bottom of the diagram, dusk is to the right, and dawn to the left. The outer boundary of the diagram is the planetary magnetopause, extending to ~20 R_S in the sunward direction, while the arrowed solid lines within the boundary show plasma streamlines. With increasing radial distance from the planet, the regimes of plasma flow are characterised as follows. First, in the inner part of the magnetosphere the plasma to a first approximation corotates with the planet, due to the torque imposed by ion-neutral collisions at the feet of the field lines in the ionosphere. Voyager observations show that the rotation is near-rigid out to equatorial radial distances of ~5 R_S, after which the plasma angular velocity falls to about half of rigid rotation within several R_S of the dayside magnetopause [Richardson, 1986, 1995; Richardson and Sittler, 1990]. The fall in angular velocity is believed to be due to the production and pick-up of plasma from internal sources as mentioned above, together with subsequent diffusive radial transport and loss [e.g. Richardson et al., 1998; Saur et al., 2004]. Here we term the near-rigidly rotating inner region the 'inner magnetosphere', and the sub-corotating region the 'middle magnetosphere' respectively. The latter region is then surrounded by an 'outer' layer, bounded by the arrowed dashed streamline and

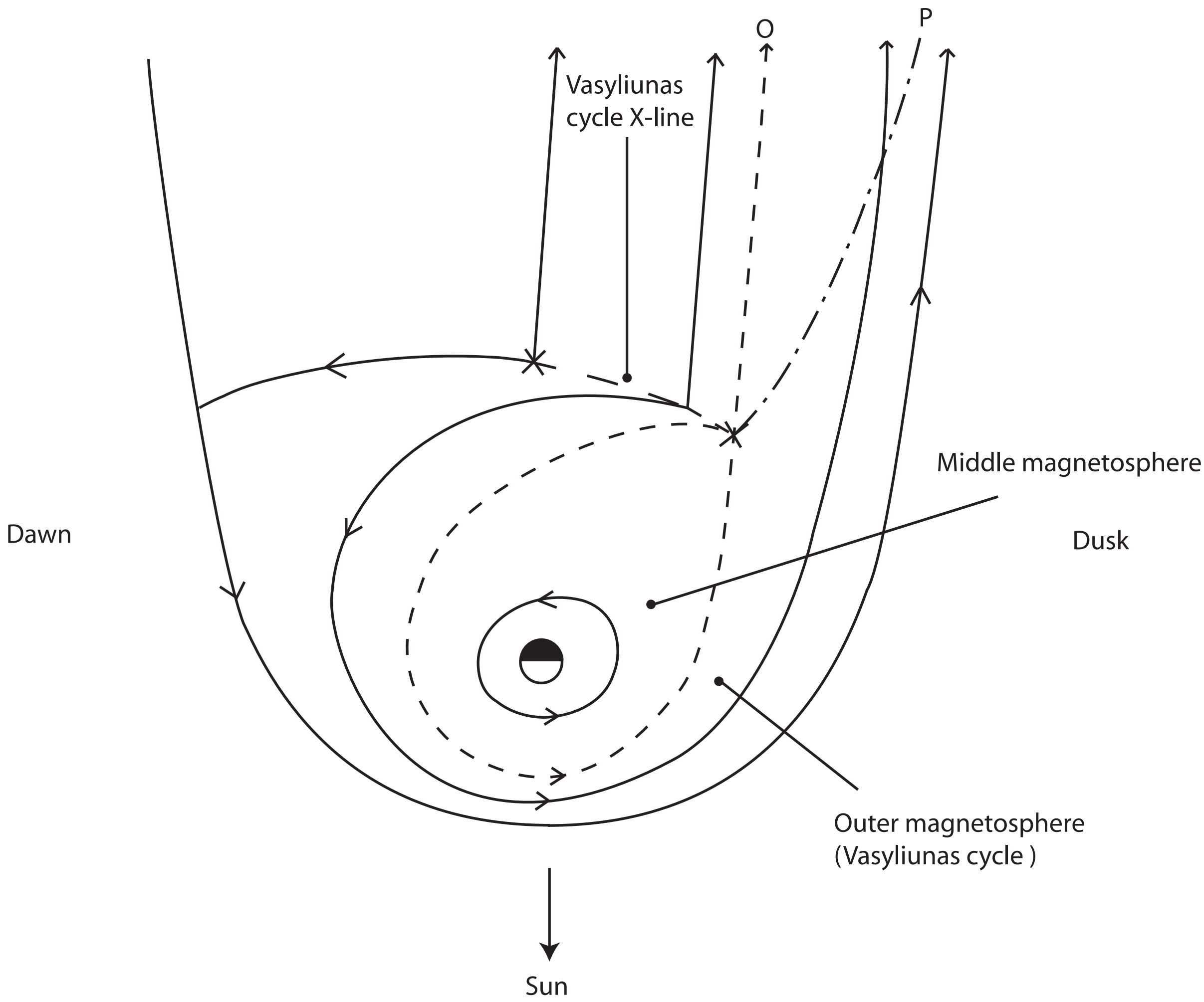

Figure 2.6: Sketch of the plasma flow in the equatorial plane of Saturn's magnetosphere for the case in which steady-state Vasyliunas-cycle flow is active, but not Dungey-cycle flow. The direction to the Sun is at the bottom of the diagram, dusk is to the right, and dawn is to the left. The outer boundary of the diagram represents the planet's magnetopause (at a subsolar distance of ~20 R_S). Arrowed solid lines (including the magnetopause) show plasma streamlines, while the arrowed short dashed line (also a streamline) shows the boundary between the sub-corotating middle magnetosphere and the outer magnetosphere continaing the Vasyliunas-cycle flow. The dashed line with Xs shows the tail reconnection line associated with the Vasyliunas cycle, while in the tailward region the dashed line marked 'O' shows the path of a plasmoid O-line formed by the reconnection (also a streamline), and 'P' marks the outer limit of the plasmoid field lines (not a streamline) which eventually asymptotes to the dusk tail magnetopause. The solid line contiguous to the reconnection X-line in the tail (also a streamline) shows schematically the outer boundary of closed field lines in the dusk sector, beyond which lies the (steady state) lobes of the magnetic tail. [From Jackman et al., 2006].

extending (in this case) to the magnetopause, in which dynamical mass-loss of internal plasma takes place. In this region, the mass-loaded closed field lines which are rotating towards midnight from dusk extend into the tail and then pinch off to form a tailward-moving plasmoid, as first described by Vasyliunas [1983] in the jovian context. (Similar flows were also discussed by Carbary et al. [1976]). The 'X'-line of the plasmoid is shown by the dashed line marked by Xs in the dusk-sector tail, while the 'O'-line at its centre (a streamline) is indicated by the arrowed dashed line marked 'O'. The outer boundary of the plasmoid is indicated by the dot-dashed line marked 'P' (not a streamline), which eventually asymptotes to the dusk magnetopause. After reconnection, the mass-reduced closed flux tubes contract back toward the planet at higher speeds, and rotate around into the dayside via dawn under the action of the ionospheric torque. As they do so, they become slowed and re-loaded with planetary plasma due to cross-field diffusion from the middle-magnetosphere, such that the process then repeats as the flux tubes rotate toward the tail via dusk. This flow is termed the 'Vasyliunas cycle', and is conceived here for simplicity as a steady-state process. It also seems possible, however, that the process may be episodic, involving intervals of plasma accumulation in the sub-corotating outer magnetosphere region, followed by intervals of plasmoid-formation and mass-loss down the dusk tail flank.

2.5.2 Ionospheric flows and currents

The region of open flux mapping to the tail lobes, which could not be depicted in the previous figure occupies the central region in the ionospheric diagram in Figure 2.7 which is in the same format as Fig. 2.6. This figure shows the corresponding flow in Saturn's northern polar ionosphere. The outer boundary of this diagram corresponds to a co-latitude from the northern pole of ~30°, mapping magnetically into the near-rigidly corotating equatorial flow of the inner magnetosphere at a radial distance of ~3 R_S. The plasma angular velocity then falls with increasing latitude in the region mapping to the middle magnetosphere, reaching about half of rigid co-rotation at the boundary of the outer magnetosphere containing the Vasyliunas cycle flow, indicated by the outer

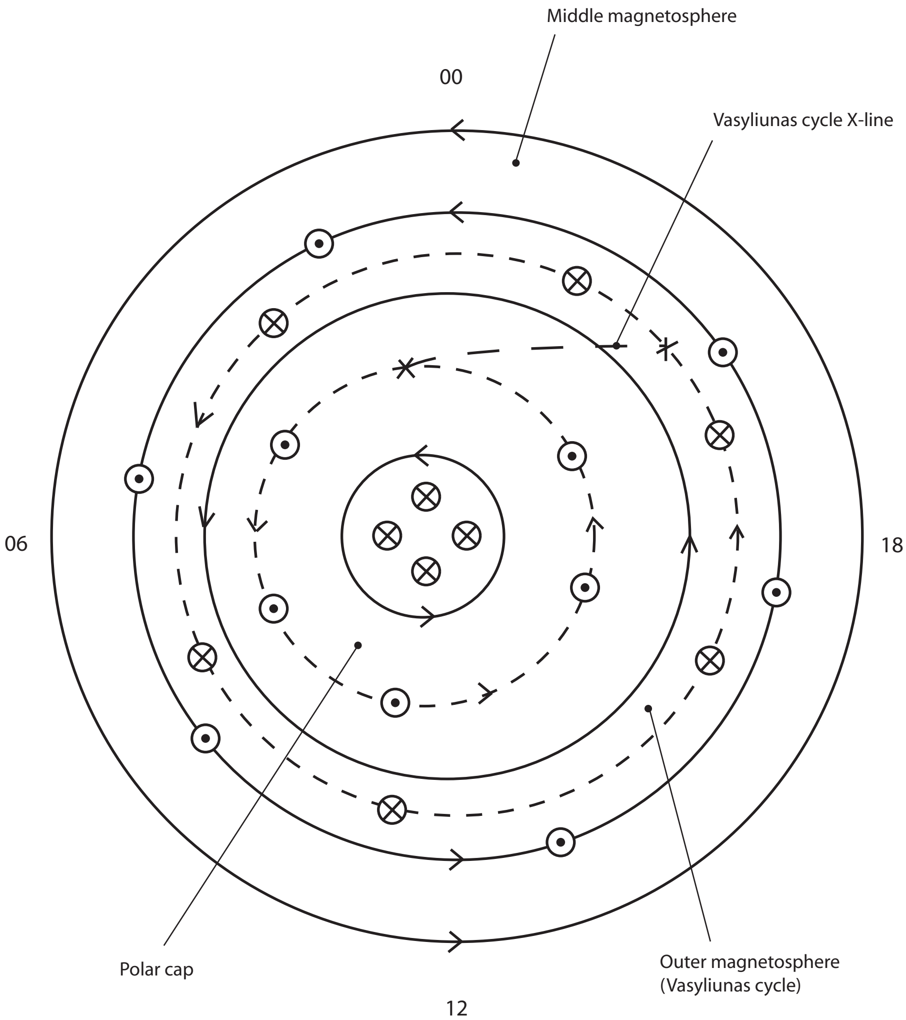

Figure 2.7: Sketch of the plasma flow in Saturn's northern ionosphere for the case in which steady-state Vasyliunas-cycle flow is active, but not Dungey-cycle flow, as in Fig. 2.6, following the format of that figure. The direction to the Sun is again at the bottom of the figure, dusk to the right, and dawn to the left. The outermost circle corresponds to a co-latitude of ~30^{o} from the pole, which maps to the equatorial plane in the inner magnetosphere at a radial distance of ~3 R_S, poleward of which lies the sub-corotating flow of the middle magnetosphere. The outer magnetosphere region containing the Vasyliunas-cycle flow then forms an asymmetric ring bounded by the dashed streamline at lower latitudes, and the dashed-line boundary of open field lines at highest latitudes, which is correspondingly displaced towards dawn. The circled dots and crosses indicate regions of upward and downward field-aligned current, respectively, as indicated by the divergence of the horizontal ionospheric current. Hall currents flow generally anti-clockwise round the pole and close in the ionosphere, while Pedersen currents flow generally equatorward and close in the field-aligned current systems shown. [From Jackman et al., 2006].

arrowed dashed streamline. The outer magnetosphere region then forms a narrow ring of closed field lines surrounding the central region of open flux mapping to the tail. On the dawn side, the flow speed in the outer magnetosphere ring is expected to be higher than that in the adjacent middle magnetosphere, due to the loss of planetary plasma downtail following plasmoid pinch-off as mentioned above, but will slow to a comparable speed to the middle magnetosphere in the dusk sector due to subsequent diffusive mass-loading. The Vasyliunas-cycle ring is thus wider at dusk than at dawn as shown, reflecting this difference in the flow speed and the consequent greater accumulation of flux in the dusk sector compared with dawn. The central region of open flux, which could not be represented in the equatorial diagram in Fig. 2.6, and which extends to a typical co-latitude of ~15° according to Voyager magnetic field estimates [Ness et al., 1981; Cowley et al., 2004b], is thus correspondingly displaced toward dawn. In the absence of on-going reconnection, the flow in this region is expected to consist of a rotational circulation driven by ion-neutral collisions in the ionosphere which twists the open tail field lines [Isbell et al., 1984]. The plasma angular velocity to which this process gives rise depends on the poorly-known value of the effective ionospheric Pedersen conductivity. Recent ground-based Doppler observations of ionospheric IR emissions by Stallard et al. [2004] indicate plasma angular velocities of about a third of rigid corotation in this region, this value implying an effective Pedersen conductance of the polar ionosphere of ~0.5-1 mho. Values of ~1-2 mho have also been derived for the middle magnetosphere region by Bunce et al. [2003], based on Voyager plasma angular velocity profiles and the observed sweep-back of middle magnetosphere magnetic field lines, and as described in Section 2.4.

2.6 Equatorial and ionospheric flows – steady reconnection

The flows in both the equatorial plane and the ionosphere alter significantly as a consequence of the solar wind interaction, specifically due to steady reconnection at the magnetopause and in the tail, as first described by Dungey [1961] in the terrestrial context, and outlined in Section 1.5 of Chapter 1.

2.6.1 Equatorial flows

The combined flows in the equatorial plane are shown in Figure 2.8, in the same format as Figure 2.6. Reconnection at the magnetopause X-line, shown by the dashed line with Xs on the dayside boundary, now produces open field lines which move poleward out of the plane of the diagram, and are stretched into a long magnetic tail on the nightside by the solar wind flow. This process occurs principally when the interplanetary magnetic field (IMF) points north, opposite to the southward-directed near-equatorial planetary field. The open tubes then reconnect again in the centre plane of the tail, principally on the dawn side as shown in Fig. 2.6, due to the presence of the Vasyliunas-cycle outflow at dusk. The closed field line segments then flow back to the dayside again via dawn, acted on by the planetary ionospheric torque, where the process repeats. This flow is termed the 'Dungey cycle' and is outlined more generally in Chapter 1. Comparing equatorial flows between Figs. 2.6 and 2.8, it can be seen that a layer of sunward-flowing closed flux tubes is now added to the dawn side outer magnetosphere, flowing between the active tail reconnection site and the dayside magnetopause. The flow speed in this layer is likely to be comparable to that in the adjacent dawn-side Vasyliunas cycle, since both regions of closed flux will not be strongly mass-loaded with planetary plasma. As a consequence we consider the Dungey-cycle 'return' flow and the Vasyliunas-cycle flow to form a combined 'outer magnetosphere' region in this case, located between the sub-corotating flow of the middle magnetosphere and the magnetopause.

2.6.2 Ionospheric flows and currents

The combined flows in the ionosphere are shown in Figure 2.9, again in similar format to Figure 2.7. Here, a narrow layer of sunward-flowing closed field lines correspondingly lies immediately poleward of the Vasyliunas-cycle ring in the dawn sector 'outer magnetosphere', flowing from the nightside to the dayside reconnection

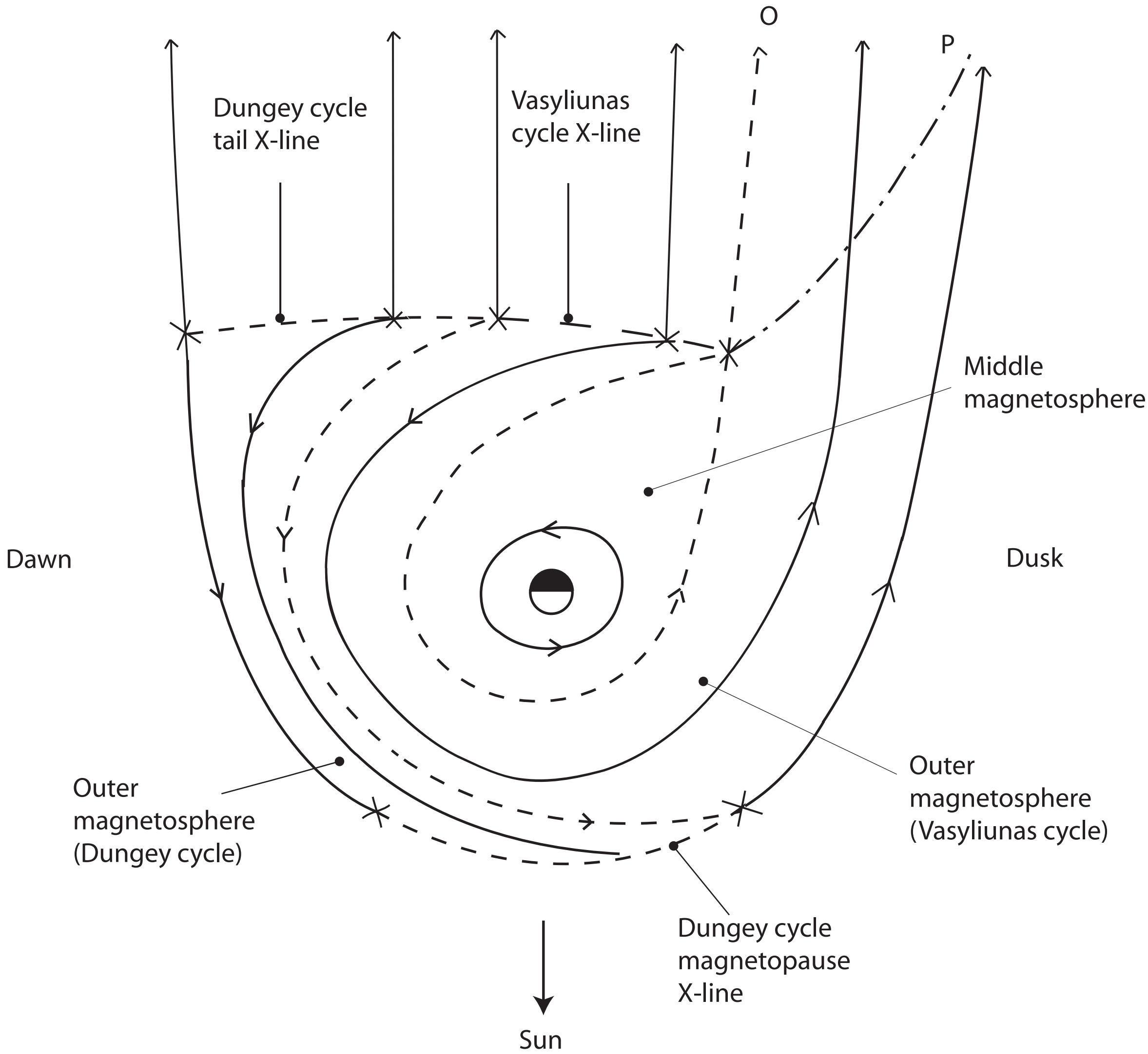

Figure 2.8: Sketch of the plasma flow in the equatorial plane of Saturn's magnetosphere in the same format as Figure 2.6, where now both steady-state Vasyliunas-cycle flow and Dungey-cycle flow are active. The new feature compared with Figure 2.6 is the appearance of an additional plasma layer in the outer dawn-side magnetosphere, in which closed field lines from an active tail reconnection region (dashed line with Xs in the dawn sector) flow sunward toward an active magnetopause reconnection region in the noon sector (dashed line with Xs in the dayside sector). The boundary between the Dungey-cycle flow and the Vasyliunas-cycle flow in the dawn sector is indicated by a dashed-line streamline. The corresponding tail reconnection lines are shown as being contiguous, though this is not necessarily the case [From Jackman et al., 2006].

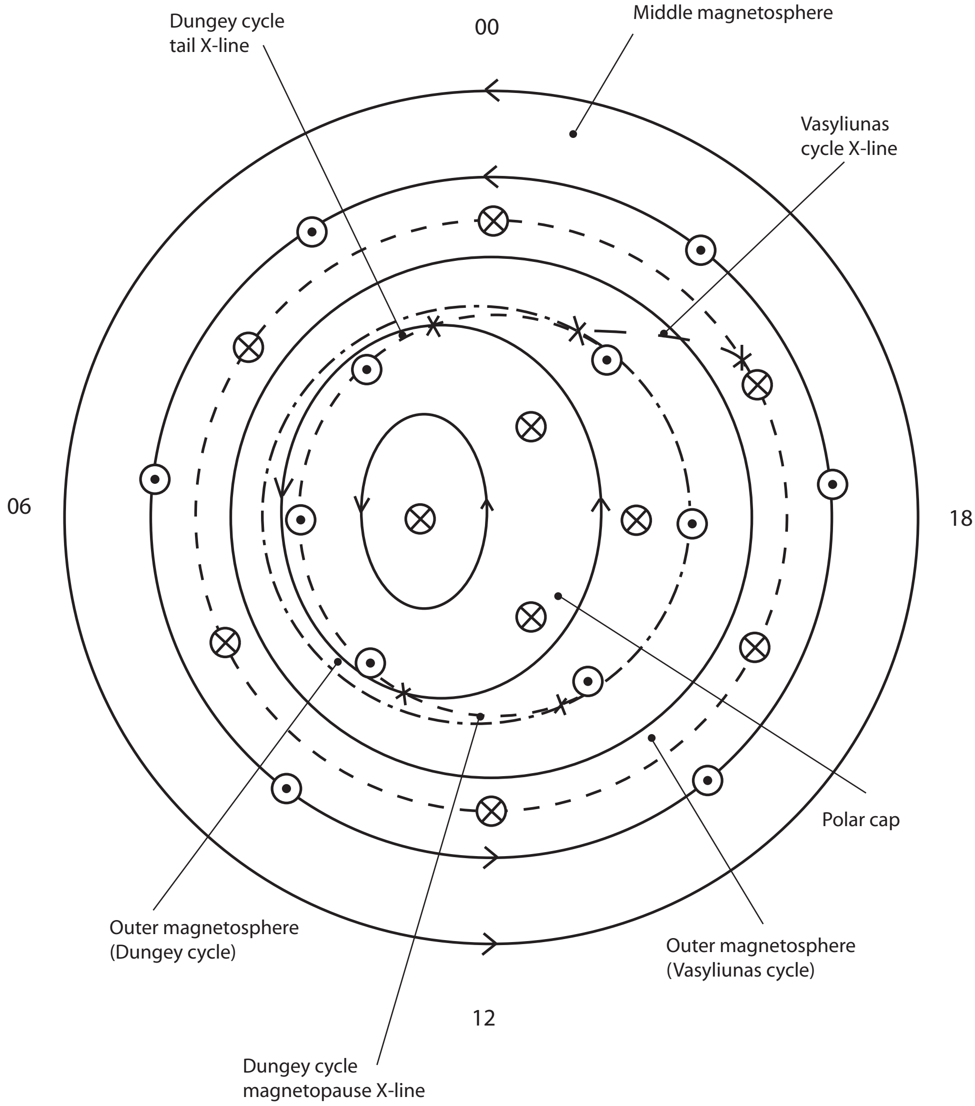

Figure 2.9: Sketch of the plasma flow in Saturn's northern ionosphere in the same format as Figure 2.7, where now both steady-state Vasyliunas-cycle flow and Dungey-cycle flow are active, as in Figure 2.8. A new feature compared with Figure 2.7 is the appearance of an additional plasma layer poleward of the Vasyliunas-cycle ring in the dawn sector, in which closed field lines from the active tail reconnection region (or 'merging gap') on the nightside open-closed field line boundary (dashed line with Xs) flow sunward toward the active magnetopause reconnection region on the dayside open-closed field line boundary (also dashed line with Xs). A component of anti-sunward flow also correspondingly appears across the central region of open field lines, adding to the weak rotational flow already present in Figure 2.7 [From Jackman et al., 2006].

regions (or 'merging gaps') lying on the open-closed field line boundary (dashed lines with Xs). The additional presence of this Dungey-cycle return flow layer results in the open field line region now being more centrally located than in Fig. 2.7. In the central open field polar cap, anti-sunward flow between the 'merging gaps' closes the Dungey cycle flow, adding to the sub-corotational flow driven by ion-neutral collisions shown in Fig. 2.9. Some closed streamlines may continue to be present in the polar cap as shown, however, where open flux circulates between more major intervals of tail reconnection. It is an overall flow of this nature, and the associated ionospheric and field-aligned current system, that is quantitatively modeled and described in detail in Chapter 6 of this thesis.

2.7 The Kronian Aurora

The kronian auroral emissions provide a means of remote sensing the dynamics occurring within the magnetosphere.

2.7.1 First Observations

The kronian aurora was first unambiguously detected by the Voyager UV spectrometer (UVS) during the flybys of Saturn in 1980-81 [Broadfoot et al., 1981; Sandel and Broadfoot, 1981; Sandel et al., 1982; Shemansky and Ajello, 1983]. Prior to that, polar limb brightenings were detected by the Pioneer 11 longwave photometer [Judge et al., 1980], and spatially resolved images of Saturn obtained by the International Ultraviolet Explorer (IUE) satellite showed enhancements in H Ly-α emissions which could have come from Saturn's polar atmosphere [Clarke et al., 1981]. With the limited viewing geometry of the Voyager observations the kronian aurora appeared as a narrow circumpolar region with no apparent emission present in the polar cap.

Subsequently, a number of individual images of Saturn's polar aurorae have been obtained using the Hubble Space Telescope (HST) [Gérard et al., 1995; Trauger et al., 1998; Cowley et al., 2004a] which have shown a highly variable morphology. Overall, the aurora typically takes the form of narrow bands around the poles, often brighter at dawn than at dusk, lying at a typical co-latitude of ~15º for the southern aurora, and ~12º for the north. Auroral intensities vary between ~1 kR (the minimum observable limit) and ~100 kR, peaking in the pre-noon sector, a feature which could be related to the location of the Saturn kilometric radiation source regions (see Section 2.8.2). In the absence of upstream data, it had not been possible to relate these images to concurrent interplanetary conditions. However, Prangé et al. [2004] have discussed a HST image showing a polar disturbance that they infer was triggered by the passage of an interplanetary shock associated with a coronal mass ejection, tracked from the Sun via Earth and Jupiter.

2.7.2 Theories on auroral formation

Concurrent with observations, theoretical work has centred on the origins of the aurorae at Saturn, and their implications for magnetospheric dynamics. Due to the 'discrete' nature of the aurora it is generally accepted that the UV emissions are associated with regions of upward field-aligned current (i.e. downgoing electrons). Essentially, there are two basic sources of such large-scale field-aligned current which transfer momentum and energy in the solar wind-magnetosphere-ionosphere system.

The first is that which is associated with the transfer of angular momentum from the atmosphere of the rapidly rotating planet to the sub-corotating equatorial plasma [Hill, 1979; Vasyliunas, 1983]. As discussed in Section 2.4, the radial outflow of plasma at Saturn is sufficient to cause the breakdown of corotation [Richardson, 1986, 1995; Richardson and Sittler, 1990], and hence the generation of the magnetosphere-ionosphere coupling current system depicted in Figure 2.4. Cowley and Bunce [2003b] have considered the properties of this current system at Saturn, and their results suggest that the region of upward field-aligned current illustrated in Figure 2.7, and associated with magnetosphere-ionosphere coupling, is both too weak in magnitude and flows at too large a co-latitude (~20º) to reasonably account for the implied auroral currents associated with Saturn's main auroral oval emissions, unlike the corresponding situation at Jupiter [Bunce and Cowley, 2001; Cowley and Bunce, 2001; Hill, 2001; Nichols and Cowley, 2004].

The second possibility is that the aurora is related to field-aligned currents and hot plasma precipitation associated with the interaction between the solar wind and its embedded IMF, with the magnetosphere. This process functions principally via magnetic reconnection at the magnetopause and the Dungey cycle [Dungey, 1961]. As such, Cowley et al. [2004a] have suggested that Saturn's aurorae are associated with a ring of upward current along the open-closed field line boundary, as illustrated in Figure 2.9. However, these currents will also be significantly modulated by the solar wind and IMF, as at Earth. Under active Dungey cycle conditions, bright aurorae will be produced at the open-closed field line boundary, with stronger currents at dawn relative to dusk. In addition, hot plasma production in tail reconnection events, followed by rotation around the outer magnetosphere due to ionospheric coupling, should also result in the formation of 'diffuse' auroral forms which spiral around the open closed field line boundary from midnight via dawn [Cowley et al., 2005a].

2.7.3 Cassini-HST Campaign

Based on the above observations and other spacecraft data, it is often stated that Saturn's magnetosphere and aurora are intermediate between the case of the Earth, where the dominant processes are solar wind driven, and the case of Jupiter, where processes are driven by a large source of internal plasma [Clarke et al., 2005; Grodent et al., 2005]. This theory was tested in January of 2004, when a major campaign of simultaneous HST UV images of Saturn's aurora and Cassini spacecraft measurements of the interplanetary medium upstream of Saturn was undertaken. This included concurrent measurements of the solar wind and IMF, together with observations of SKR emissions. A series of 5 HST orbits on 8 Jan. 2004 provided measurements of the local time variations of the auroral emissions over 70% of a Saturn rotation, while single orbit observations on 12 other days were obtained to compare the auroral activity with varying solar wind conditions.

Observations during the January Cassini-HST campaign show the effect of varying solar wind conditions on the auroral forms, and some of the images are shown in Figure 2.10. For example, during extended solar wind rarefaction intervals in which the IMF is very weak, the aurorae are also typically weak, and consist of irregular patches which sub-corotate around the polar cap boundary.

However, results have also demonstrated that both UV aurora and SKR emissions respond strongly to the shock compressions that are associated with interplanetary corotating interaction regions (CIRs), as discussed in Chapter 5, and by Clarke et al. [2005], Crary et al. [2005], Grodent et al. [2005], and Kurth et al. [2005]. Following a compression, the aurorae are observed to brighten, to contract poleward, and to exhibit strong local-time asymmetry, with brightest aurorae occurring in the dawn sector.

Over time the aurorae are found to evolve into spiral forms [Gérard et al., 2004, and Grodent et al. 2005]. Cowley et al. [2005a] have suggested that these phenomena are associated with reconnection-related dynamics in Saturn's magnetosphere, in which intervals of rapid open flux closure in the tail are stimulated by sudden solar wind compressions, as is also sometimes observed to occur at Earth [e.g. Petrinec and Russell, 1996; Sigwarth et al., 2000; Chua et al., 2001; Boudouridis et al., 2003, 2004; Milan et al., 2004; Meurant et al., 2004]. Reconnection in the tail plasma sheet leads to the injection of newly-closed flux tubes and hot plasma into the nightside magnetosphere, thus producing an auroral 'bulge' in the polar cap, which is then transported by sub-corotation with the planet around the outer magnetosphere via dawn, leading to the 'spiral' auroral emission. That compression-induced tail reconnection appears to be a dominant effect at Saturn, as opposed to the primarily substorm-related reconnection at Earth, is taken to be related to the long time scales typically required at Saturn for

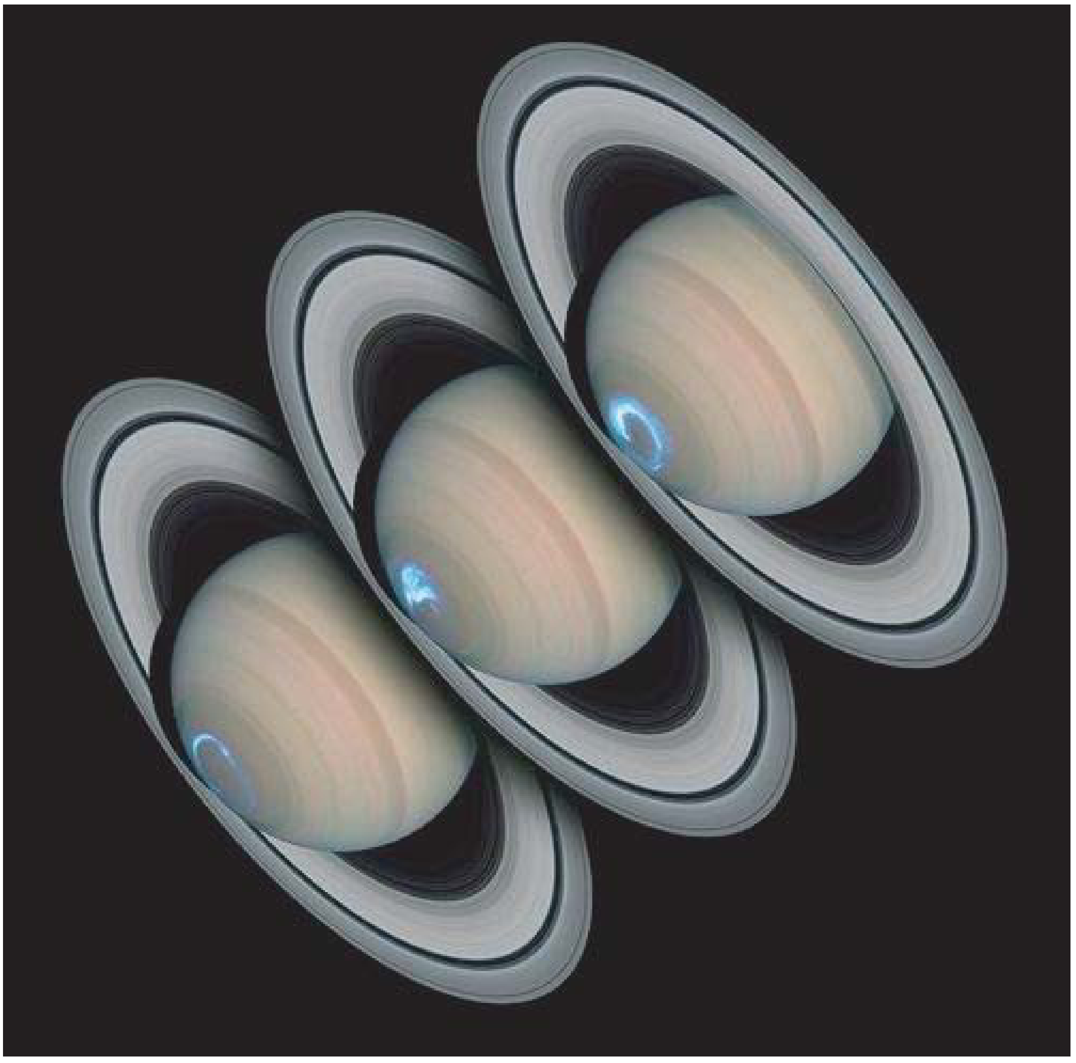

Figure 2.10: Images of Saturn's UV aurora taken by the Hubble Space Telescope during the January 2004 Cassini-HST campaign and superimposed on visible images of the planet. The images show the large variability in the auroral morphology. [Courtesy of John Clarke]

inflation of the tail with open flux. At Saturn this time-scale is typically a week or more (as described in detail in Chapter 4), which is thus comparable with the interval between interplanetary compression regions, as opposed to several tens of minutes for a typical substorm 'growth phase' at Earth.

Corresponding dynamic behaviour has also been observed by Cassini directly in Saturn's nightside outer magnetosphere [e.g. Bunce et al., 2005a, and described in Chapter 5]. Bursts of SKR were also shown to be associated with these compression-induced auroral effects [Kurth et al., 2005], thus corresponding to the solar wind dynamic pressure modulation found previously by Desch [1982] and Desch and Rucker [1983].

This January 2004 Cassini-HST campaign has told us more about Saturn's aurora than all the other images taken to date. The observations demonstrate that rather than being intermediate between the Earth and Jupiter, the different conditions at Saturn lead to auroral emissions whose behaviour is fundamentally different from those at other planets. Further study is warranted, and, at the time of writing, images from campaigns in February and October/November of 2005 are being analysed.

2.8 Saturn Kilometric Radiation

Studies of planetary wave emission started with the discovery by Burke and Franklin [1955] of Jupiter's decametric radio emission. It is now known that the magnetospheres of five magnetized planets, Earth, Jupiter, Saturn, Uranus and Neptune, are sources of non-thermal radio emissions [Kaiser, 1989; Zarka, 1998]. These emissions are an interesting remote sensing tool of magnetospheric plasmas: they can travel far from their source region, and carry imprints of both their source region characteristics (through their generation mechanism) and of the plasma they traversed (through various propagation effects) [Zarka and Kurth, 2005].

Much of our present knowledge of radio emissions from Saturn's magnetosphere comes from the Voyager-1 and Voyager-2 spacecraft [Warwick et al., 1981, 1982; Gurnett et al., 1981; Scarf et al., 1982]. In January 1980, the Planetary Radio Astronomy (PRA) experiment on Voyager-1 detected Saturn Kilometric Radiation (SKR), the primary component of the emission [Kaiser et al., 1980]. SKR is an intense radio emission, analogous to auroral kilometric radiation (AKR) at Earth, and is thought to originate from Saturn's auroral zones. Saturn's radio emission spectrum spreads from about 3 kHz to more than 1.2 MHz, with the broad SKR peak generally located between 100 and 400 kHz [Kaiser et al., 1984].

2.8.1 Planetary rotation period

The sidereal rotation period of giant planets cannot be deduced from optical measurements because of the superimposed motion of the atmosphere. However, since the charged particles responsible for the radio emissions are controlled by the large-scale magnetic field, the modulation of the SKR emission intensity provides a direct link with the deep interior, and up until very recently, has been widely adopted as the rotation period of Saturn [Gurnett et al., 2004, 2005].

During the Voyager flybys of Saturn in 1980-81, the SKR modulation period was found to be 10 hr 39 min 24 ±7 sec [Kaiser et al., 1984]. The Unified Radio and Plasma Wave (URAP) experiment on the interplanetary spacecraft Ulysses detected SKR 18 years later and found that the period differed by 1% [Galopeau and Lecacheux, 2000], and is variable in time over timescales (from months to years) much larger than the rotation period. Most recently, Cassini found a radio rotational period of 10 hr 45 min ±36 sec, approximately 6 minutes longer than that first measured by Voyager [Gurnett et al., 2005].

Figure 2.11, taken from Gurnett et al. [2005], shows a normalized power spectrum of the fluctuations in the SKR intensity obtained over an interval of a little more than one year,

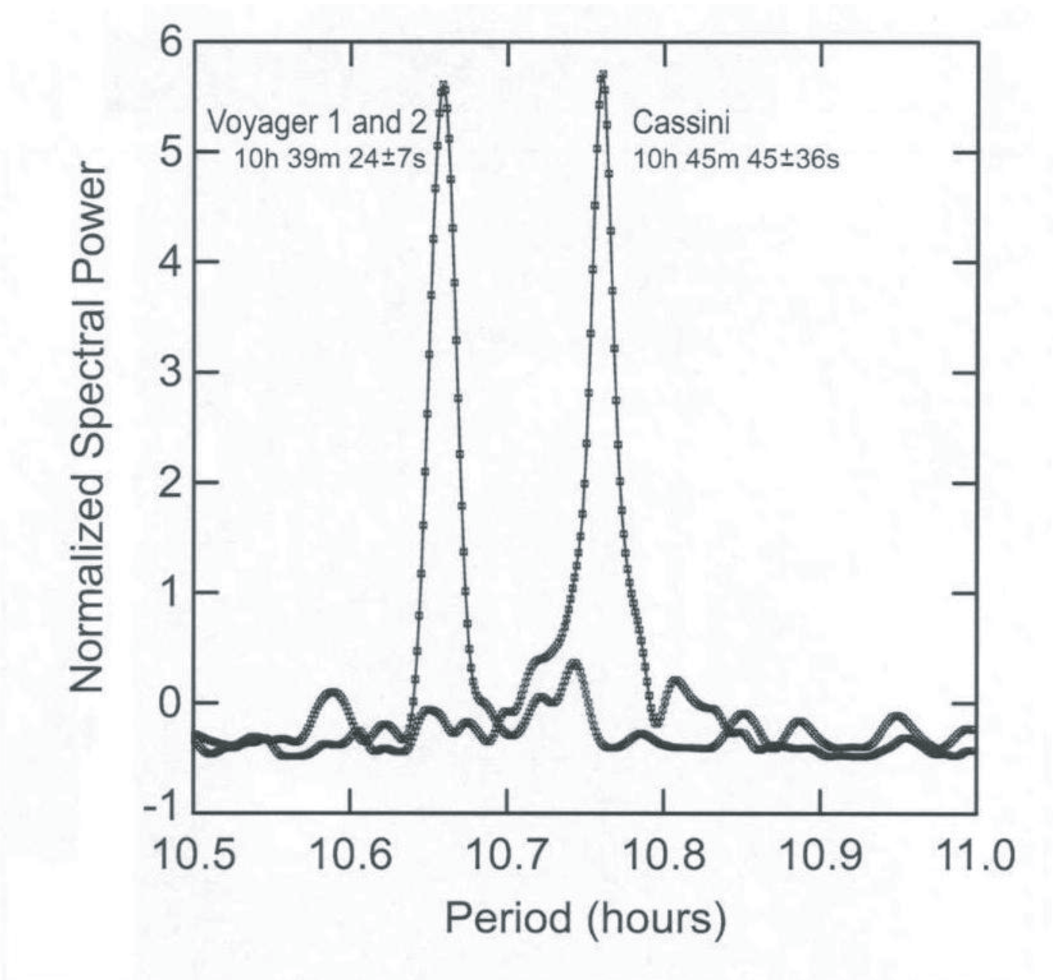

Figure 2.11: A comparison of the power spectrum of variations in the intensity of Saturn kilometric radiation (SKR) as measured by Voyager and Cassini. Clearly the radio modulation period of Saturn has shifted substantially from the Voyager era in 1980-81 to the Cassini era in 2003-04. [From Gurnett et al., 2005].

during Cassini's approach to Saturn in 2003-04. The sharp peak in the power spectrum denotes the rotation period as found by Cassini, while for comparison, the Voyager power spectrum is also shown. The reason for this shift in period is at present poorly understood. In light of new data from Cassini, several theories have been put forward, and these will be discussed briefly in Section 2.8.4.

2.8.2 Source location

Knowing the source of the radiation is necessary for having a good understanding of the SKR periodicity. Two main SKR sources were discovered from Voyager's observations [Kaiser et al., 1981; Kaiser and Desch, 1982; Lecacheux and Genova, 1983]: a northern source emitting a 100% right-handed circular polarization and a southern source emitting a 100% left-handed circular polarization. The sources were thought to be confined to the high-latitude (≥ 60º) dayside auroral zone, on field lines that pass through or near to the dayside polar cusps [Behannon et al., 1981]. The inferred source field lines are projected down to the cloud tops of Saturn and shown in Figure 2.12. These source locations were for many years thought to be in good agreement with the location of Saturn's aurora, as determined from ultraviolet images taken by the HST [e.g. Trauger et al., 1998]. However, recent theories, as described in Section 2.8.5, suggest a revised view of the source regions.

If indeed the sources are near the dayside polar cusps, a solar wind driven radio source seems a likely possibility. Certainly, Desch and Rucker [1983] have found strong correlations between SKR emission and solar wind dynamic pressure. Furthermore, during the Voyager-2 encounter, a total disappearance of the SKR for about 2 days coincided with a possible immersion of Saturn in Jupiter's magnetic tail [Warwick et al., 1982; Scarf et al., 1982]. A dropout in the SKR would be the expected response since Saturn's magnetosphere would have been shielded from direct solar wind interaction and the associated current system. Chapter 5 contains a study of a similar dropout in SKR,

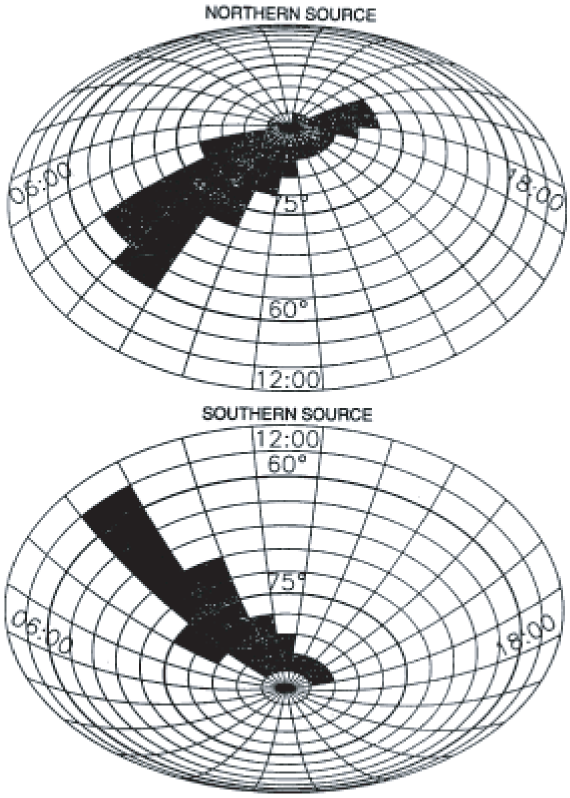

Figure 2.12: SKR source locations inferred from pre-Cassini data projected down Saturn's magnetic field lines to the cloud tops [From Galopeau et al., 1995]. This theory on SKR source locations has since been challenged.

however this time following a strong solar wind compression during the Cassini Saturn Orbit Insertion (SOI) pass.

2.8.3 Generation mechanism

Figure 2.13 shows a sketch of the suggested SKR source regions, illustrating two possible generation mechanisms [Cecconi and Zarka, 2005]. When studying the variations of the measured polarization along the Voyager-1 and Voyager-2 flybys, Galopeau et al. [1995] found that the SKR sources had a broad extent towards the morningside at lower latitudes. Thus, a Kelvin-Helmholtz instability at the magnetopause was suggested as the source of accelerated electrons responsible for the auroral radio and UV emissions. As an alternative, Cowley et al. [2004a] gave arguments in favour of upwards field-aligned currents at the boundary between open and closed field lines (described in Section 2.6) as the primary source of Saturn's UV aurora and, as a consequence, of SKR.

We have discussed possible locations for the emission source, along with possible drivers for SKR. Next, it is useful to consider the physical mechanism by which the emission is actually produced. The most likely candidate for this is the **cyclotron maser mechanism** [Wu and Lee, 1979]. Cyclotron maser radiation is produced by a coherent electromagnetic plasma instability and is generated at frequencies very close to the electron cyclotron frequency. Since the coupling in the cyclotron maser mechanism is with the electrons, the radiation is primarily right-hand polarized with respect to the magnetic field (i.e. the electric field vector rotates in the same sense as the cyclotron motion of an electron).

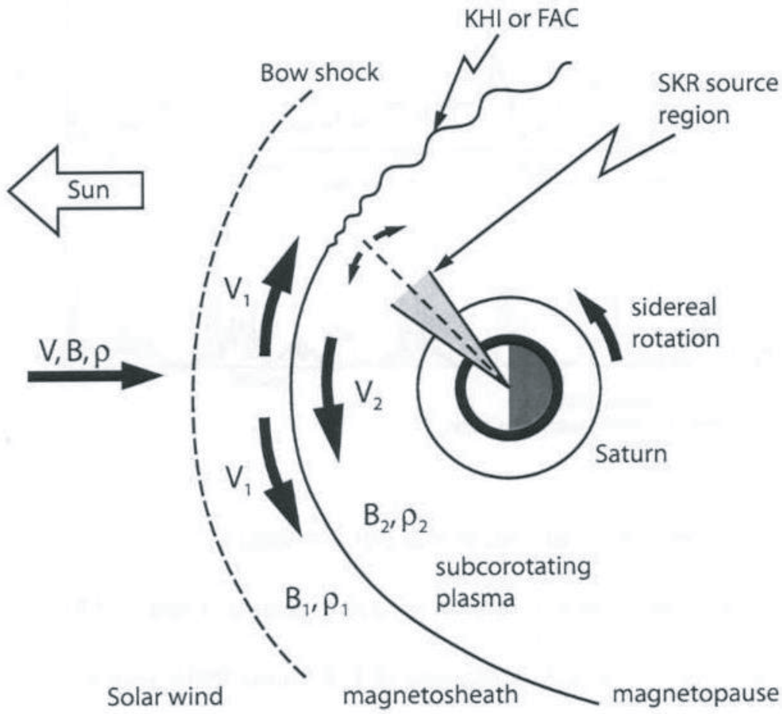

Figure 2.13: Sketch of the SKR source region as seen from the north magnetospheric pole. V, B and ρ stand for the unperturbed solar wind velocity, magnetic field, and mass density. V_1, B_1 and ρ_1 represent the same quantities in the magnetosheath, which vary with the local time. V_2, B_2 and ρ_2 characterize the subcorotating kronian magneto-plasma. The main average SKR source location as derived by Galopeau et al. [1995] is represented by the grey cone. Its LT position coincides with the locus of maximum algebraic difference between V_1 and V_2 consistent with both the KHI and FAC [Cowley et al., 2004] theories. Solar wind variations imply variations of V_1, B_1 and ρ_1, leading to back and forth motions of the SKR source versus LT, as analyzed by Cecconi and Zarka [2005]. [Adapted from Galopeau and Lecacheux, 2000].

2.8.4 Reasons for rotation period shift

As stated above, the observed shift in the SKR period is currently a topic of intense debate. Several authors attribute the modulation to a magnetic anomaly at high latitudes sweeping by a restricted local time region where electron precipitations are present [Galopeau et al., 1981; Galopeau and Zarka, 1992; Ladreiter et al., 1994].

Solar wind variations may also play a part in shifting the rotation period. As the solar wind fluctuates (on timescales of e.g. a solar rotation), the position of the magnetopause and magnetohydrodynamic flow around it are modified so that the zone of Kelvin-Helmholtz instability slowly moves, causing the radio sources to drift in local time. This can in turn account for the observed variations in the SKR period [Galopeau and Lecacheux, 2000].

2.8.5 New theories

The above descriptions show the view of SKR production that has been held for 25 years. However, since the arrival of Cassini at Saturn there have been a number of new developments in this area of thought, as will be briefly outlined here.

Several studies have suggested that the actual SKR source is not absolutely fixed in local time as previously thought. Kurth et al. [2005] put forward the theory that SKR sources may move with bright auroral features through a restricted range of local times. Further observational evidence of this is put forward by Farrell et al. [2005] who show that during Cassini's Saturn Orbit Insertion manoeuvre, SKR was detected on the nightside of the planet. If the previous theories of SKR originating from a high-latitude dayside source are to be believed, radio beams from such a source would not be viewable in this nearplanet night-side location. However, their observations suggest the presence of a source possibly near the outer edge of the icy-moon created plasma torus surrounding the planet. The implication is that some of the SKR is driven by an internal energy source that may also account for recent UV aurora observations. Images taken by Clarke et al. [2005], and studied by Grodent et al. [2005], reveal a set of longitudinally-elongated active auroral regions or "hot spots" that were not fixed in local time, but instead rotated about the pole at about half the corotation rate. As these active regions rotated in view of Cassini, the SKR proceeded to "turn on".

Other authors go a step further and refute the very claim that the SKR period represents Saturn's real sidereal rotation period. Work by Cecconi and Zarka [2005] says that the dominant peak in the harmonic analysis of SKR variations seen by Voyager may be different from Saturn's sidereal rotation period. Their results suggest that the velocity shear between magnetospheric subcorotating plasma and magnetosheath flowing plasma plays a major role in the process leading to electron precipitation. If the results are confirmed by other studies, they would imply that either the Kelvin-Helmholtz Instability source model requires deep modifications, or that another SKR generation model is to be preferred, as for instance, the field-aligned currents model of Cowley et al. [2004a]. Giampieri et al. [2006] have also looked at other methods of determining the sidereal rotation period. They have analysed the periodic modulation in the magnetic field to infer the rotation rate of the planetary source directly from magnetic field measurements. They found oscillatory variations in the field with a well-defined period of 10hr 47min 6sec, almost 8 minutes longer than some previous measurements.

Clearly, there is much to learn about SKR, its source regions, generation mechanisms, and periodicity. It is expected that multiple traversals of the magnetosphere by Cassini will enable us to decipher further secrets of this emission.

Chapter 3
Instrumentation

3.1 Introduction

The data used in this thesis were obtained primarily from the magnetometer (MAG) and radio and plasma wave science instruments (RPWS) on the Cassini-Huygens mission to Saturn and Titan. Chapter 5 also includes images taken with the Space Telescope Imaging Spectrograph (STIS) on the Hubble Space Telescope (HST). Here, an overview of the Cassini-Huygens mission and its scientific objectives is presented, followed by a description of the working principles of the above instruments.

3.2 The Cassini-Huygens mission

3.2.1 Mission Introduction

The Cassini-Huygens mission to Saturn consists of a two-part spacecraft. Its formal beginning was in June 1982, the project being a joint undertaking by the National Aeronautics and Space Administration (NASA) in the United States who supplied the Saturn orbiter, and the European Space Agency (ESA) who supplied the Titan probe. The orbiter is named after the French/Italian astronomer Giovanni Domenico Cassini, who discovered several Saturnian satellites and ring features (including the famous Cassini division) in the period 1671-1685. The probe is named after the Dutch astronomer Christiaan Huygens who discovered Titan in 1655.

The Italian space agency (Agenzia Spaziale Italiana, or ASI) provided hardware systems for the orbiter as well as instruments for both the orbiter and the probe. The overall mission is managed by the Jet Propulsion Laboratory (JPL), Pasadena, California.

Huygens operations were carried out by ESA from its European Space Operations Center (ESOC) in Darmstadt, Germany.

3.2.2 The Cassini Orbiter

As shown in Figure 3.1, Cassini consists of several sections, all stacked vertically on top of each other. Most of the orbiter's scientific instruments are installed on one of two body-fixed platforms. These are called the *remote-sensing pallet*, and the *particles and fields pallet*. An 11-metre long boom supports sensors for the Dual-Technique Magnetometer (described in more detail in Section 3.3). At the top of the stack is the large, 4-metre-diameter *high-gain antenna*. Centered and at the very top of this antenna is a relatively small *low-gain antenna*. Another *low-gain antenna* is located near the bottom of the spacecraft. These antennae are used for two-way communication through the Deep Space Network (DSN) via an X-band radio link.

Electrical power for the Cassini spacecraft and instruments is provided by three Radioisotope Thermoelectric Generators (RTGs). RTGs provide power through the natural radioactive decay of plutonium (Pu-238). The heat generated by this process is then changed into electricity by solid-state thermoelectric converters.

Cassini is a three-axis stabilized spacecraft. Either reaction wheels or the set of 0.5 N (Newton) thrusters can change the attitude of the spacecraft. Attitude changes will be done frequently because the instruments are body-fixed and the whole spacecraft must be turned in order to point them. Consequently, most of the spacecraft activities are made without a real-time communication link to Earth. All data are recorded on two solid-state recorders, each of which has a storage capacity of about two gigabits.

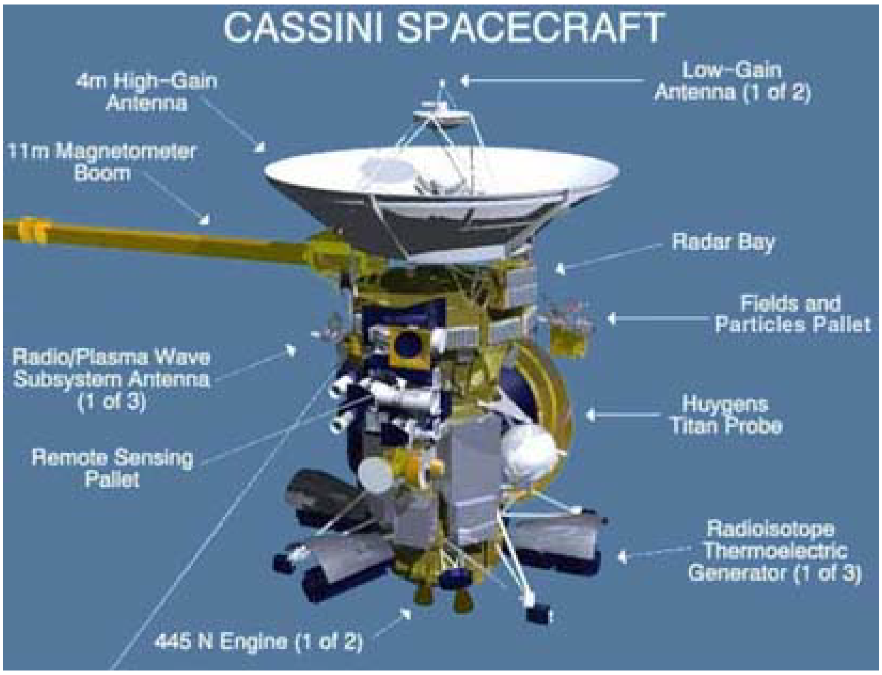

Figure 3.1: Diagram showing the main components of the Cassini spacecraft along with several of the instruments.
[From http://saturn.jpl.nasa.gov/home/index.cfm]

3.2.3 Launch and Journey to Saturn

Cassini-Huygens was launched on 15 October 1997 from Cape Canaveral on its 7-year journey to Saturn, and the interplanetary trajectory is shown in Figure 3.2. Due to the vast distances involved and its large mass, the spacecraft could not be directly flown to Saturn. Consequently, two Venus swingbys, plus Earth and Jupiter gravity assists were necessary to accelerate the spacecraft toward Saturn, ~1.3 billion km from Earth. During the various flybys, calibration and testing of the instruments were undertaken. There were also opportunities for science investigations. For example, the Jupiter flyby provided the opportunity for a solar wind-Jupiter magnetosphere-aurora investigation involving Cassini, Galileo, and the Hubble Space Telescope [Hanlon et al., 2004; Grodent et al., 2003].

3.2.4 Arrival and Saturn Orbit Insertion

On 30 June 2004, Cassini approached Saturn from below the ring plane, crossing through the large gap between the F and G rings. The main engine burn began at 01:12 Coordinated Universal Time (UTC) on 1 July 2004, shortly after Cassini had crossed above the rings, the burn continuing for 96 minutes. Closest approach was at a distance of 1.33 R_S, the closest Cassini will ever come during its four-year tour. Figure 3.3 shows the arrival trajectory in more detail.

3.2.5 Orbital Tour

Following the successful Saturn Orbit Insertion (SOI) manoeuvre, Cassini began its four-year orbital tour of the kronian system, exploring the planet itself, the icy satellites, the magnetosphere, the atmosphere and the rings. Cassini uses close flybys of

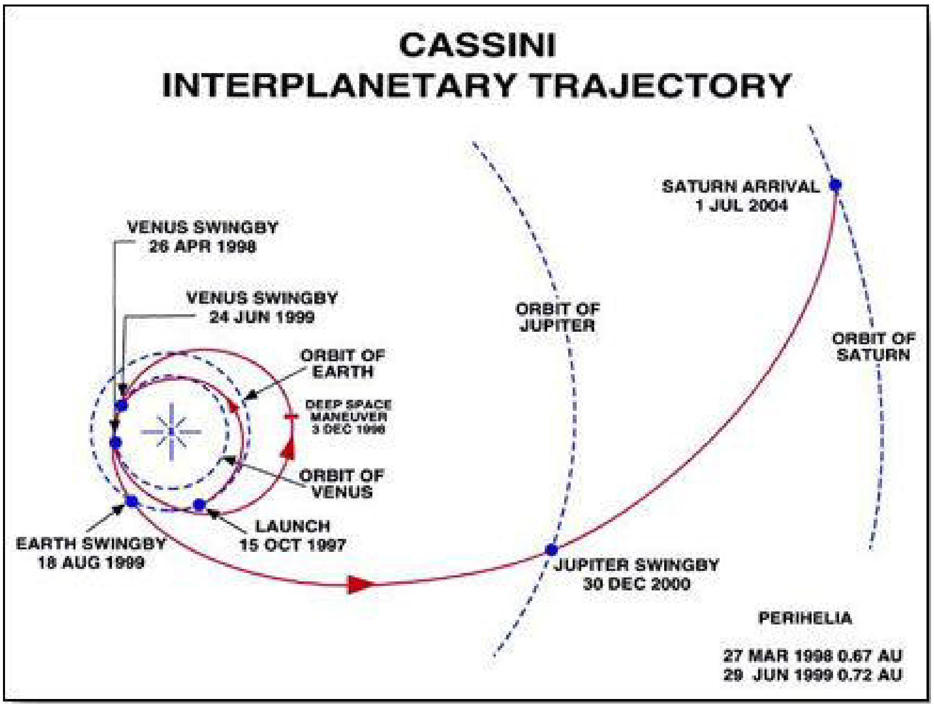

Figure 3.2: The interplanetary trajectory of Cassini-Huygens, including two Venus swingbys, one Earth gravity assist and a further Jupiter gravity assist before orbit insertion at Saturn on July 1st 2004.
[From http://saturn.jpl.nasa.gov/home/index.cfm]

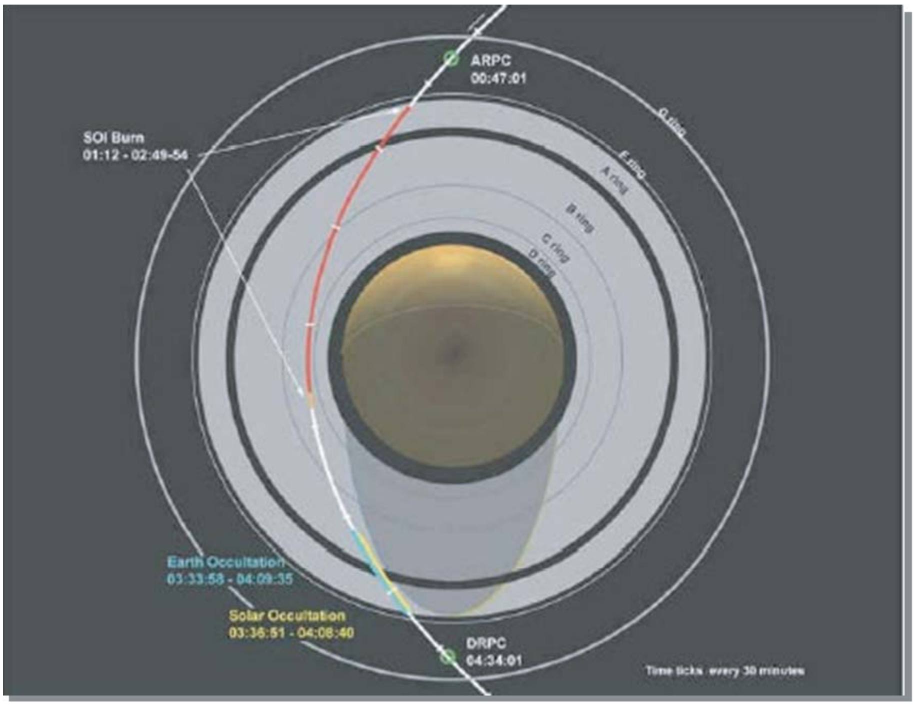

Figure 3.3: Diagram showing the Saturn Orbit Insertion trajectory including the rocket burn.
[From http://saturn.jpl.nasa.gov/home/index.cfm]

Titan both to study the moon itself and to obtain gravitationally assisted orbit changes. The tour consists of 76 Saturn-centered orbits in total, navigated using propulsive maneuvers and 45 Titan-gravity-assist flybys. The main phases of the orbital tour are illustrated in Figure 3.4.

3.2.6 The Huygens Probe

Although not discussed in the science sections of this work, any thesis on Saturn would be incomplete without at least a mention of the hugely successful Huygens probe, which was attached to the side of the main Cassini stack before being ejected towards Titan in December 2004. On 14 January 2005, the cone-shaped probe descended into Titan's cloudy atmosphere. Three sets of parachutes were deployed to slow the probe and to provide a stable platform for scientific measurements. Instruments on board collected information about the chemical composition of the atmosphere and the clouds surrounding Titan. The data were radioed to the Cassini orbiter, and then relayed back to Earth. Two hours twenty-seven minutes after entering Titan's atmosphere, the probe landed near the moon's equator and was able to communicate with the spacecraft for a few minutes. Huygens is now the furthest human-made object ever to land on a celestial body. For a detailed description of the instrumentation on the Huygens probe see Lebreton et al. [2002], and for a summary of the initial results see Lebreton et al. [2005].

3.2.7 Science Objectives

Cassini-Huygens accommodates some twenty seven different scientific investigations which are supported by eighteen specially designed instruments, twelve on the orbiter and six on the Huygens probe. The list of science objectives for the mission is extensive, but can be categorized under five main headings: the planet itself, the rings, Titan, the icy satellites and the magnetosphere. This thesis primarily concerns Saturn’s magnetosphere

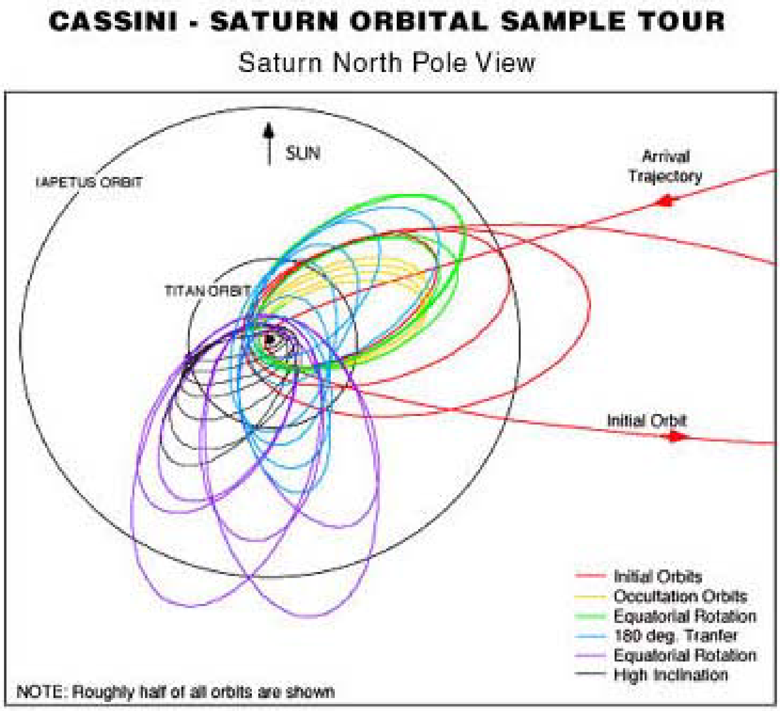

Figure 3.4: Petal diagram showing the various stages of Saturn's 4-year orbital tour, projected onto Saturn's equatorial plane, with the Sun to the top of the diagram. The coloured petals indicate the various stages of the tour, starting with orbit insertion, and finishing with the set of high inclination orbits.
[From http://saturn.jpl.nasa.gov/home/index.cfm]

and its dynamics and as such, the science objectives directly related to the magnetosphere are listed below:

- Determine the configuration of the nearly axially symmetric magnetic field and its relation to the modulation of Saturn Kilometric Radiation (SKR).
- Determine current systems, composition, sources, and sinks of magnetospheric charged particles.
- Investigate wave-particle interactions and dynamics of the dayside magnetosphere and the magnetotail of Saturn and their interactions with the solar wind, the satellites, and the rings.
- Study the effect of Titan's interaction with the solar wind and magnetospheric plasma.
- Investigate interactions of Titan's atmosphere and exosphere with the surrounding plasma.

3.3 Cassini Magnetometer

3.3.1 Science Objectives

A key tool for studying the magnetosphere, and the source of much of the data in this thesis, is the Cassini dual technique magnetometer [Dougherty et al., 2004], situated on the 11 m boom. The main scientific objectives of the Cassini magnetic field investigation are shown schematically in Figure 3.5. Due to the orbital nature of the mission, a very comprehensive three-dimensional sampling of the magnetic field measurements over a wide range of latitudes, longitudes and radial distance is possible. This will enable a more complete characterization of the planetary field than previous missions have allowed, and a determination of the internal magnetic field of Saturn to at least fourth order spherical harmonic terms. The close flybys of Titan will be used to determine possible internal magnetic field sources of the moon, as well as investigate

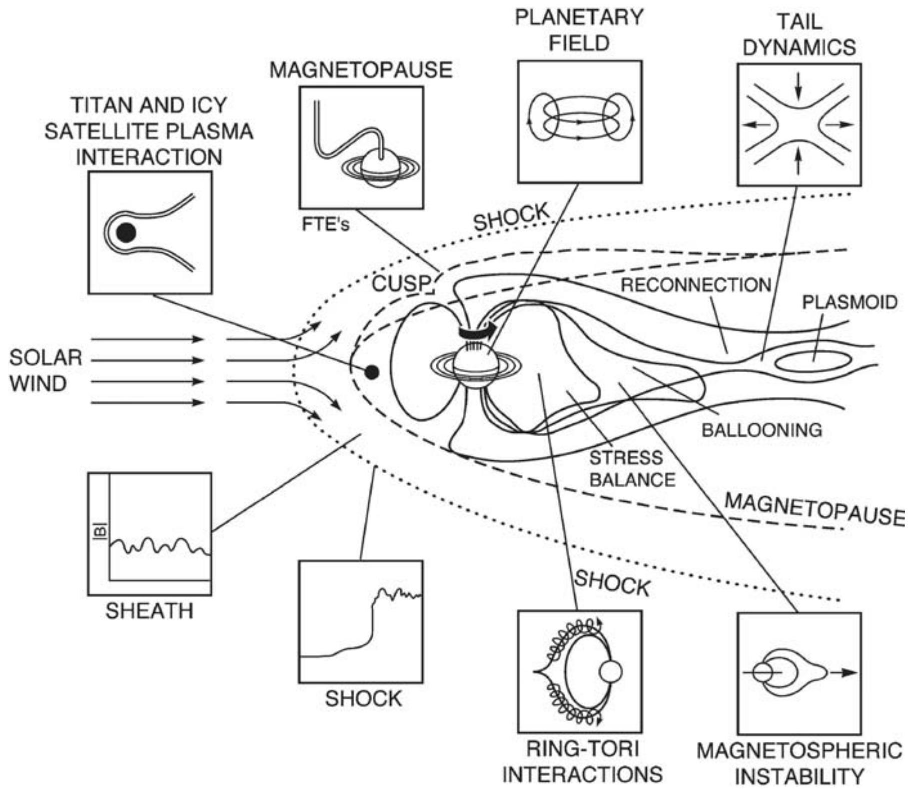

Figure 3.5: Schematic of Saturn's magnetosphere and magnetometer science objectives. [From Dougherty et al., 2002].

external sources such as ionospheric and plasma currents. In addition there are 12 targeted (close) flybys of some of the icy satellites, as well as 28 untargeted (and therefore more distant) flybys as well.

3.3.2 Instrument Requirements

The design of the instrument has been driven by a range of requirements, in particular the long mission duration which requires high reliability and survivability. To conform to practical limits, the mission makes use of onboard data storage. The science aims require measurements with high sensitivity over a wide dynamic range (from tens of thousands of nT during Earth flyby, through to the extremely low field strengths in the solar wind, and the intermediate values inside Saturn's magnetosphere. The dual technique magnetometer (similar to that flown on Ulysses, Balogh et al. [1992]), meets all of the above requirements, and consists of a vector helium magnetometer (VHM) and a fluxgate magnetometer (FGM), plus the option to operate the VHM in scalar mode (SHM). Simultaneous operation of the VHM and FGM will assure maximum sensitivity over the broad range of frequencies from 0 to 20 Hz.

3.3.3 Instrument Details

In total, the instrument consists of the two boom-mounted sensors, subchassis No. 1 (an assembly containing electronics for the FGM, VHM and SHM, the heater control electronics, the power supplies and power management system) and subchassis No. 2 (an assembly containing the data processing unit). Both subchassis are mounted in bay 4 of the Orbiter upper equipment module (UEM). Figure 3.6 shows the location of the magnetometer hardware on the spacecraft together with the spacecraft and sensor axes. The V/SHM sensor is mounted on the end of the 11m spacecraft boom, while the FGM is halfway along it. The boom distances the sensors from the stray magnetic field associated with the spacecraft and its subsystems, and spacing the sensors at different

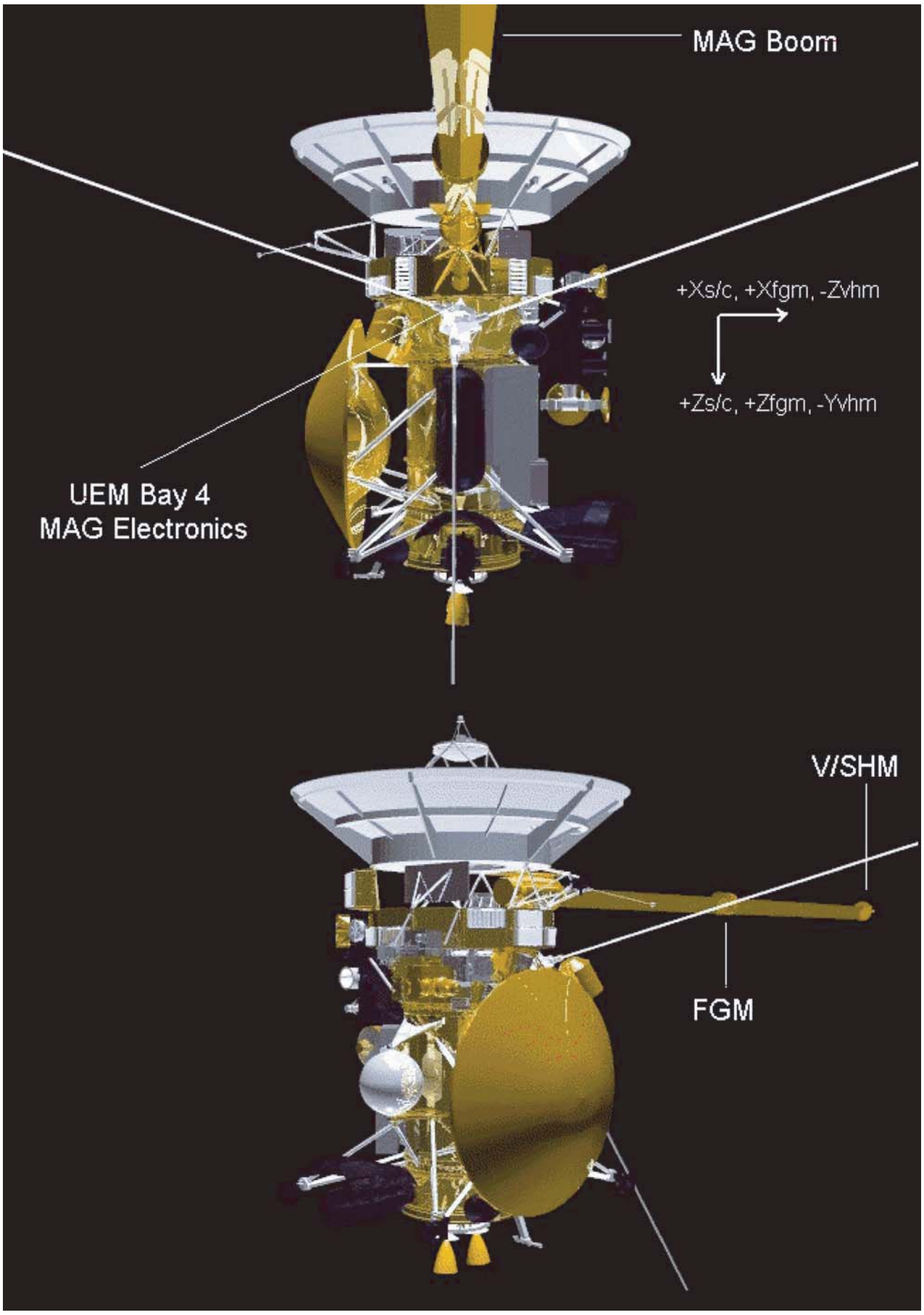

Figure 3.6: The placement of magnetometer hardware on the spacecraft is shown as well as the axes of the sensors [From Dougherty et al., 2004].

distances along the boom allows this field to be better characterized and removed from the observations.

The magnetometer boom was deployed on 14 August 1999, 4 days prior to the Earth swingby. Deployment in the inner heliosphere (less than 0.85 AU from the Sun) was prohibited because the boom would become too warm and exceed its temperature tolerance. It also could not be deployed until after the trajectory correction manoeuvre (TCM) which optimized the spacecraft trajectory for Earth flyby, due to the additional attitude control uncertainties during TCM induced by the 11 metre boom. However, the magnetometers needed to be operational during the Earth swingby to obtain data in Earth's magnetosphere that would be critical for their calibration.

3.3.4 The FGM

The fluxgate magnetometer (FGM), mounted halfway along the boom, is best for measurements at high frequency and it operates over an extremely wide dynamic range from very low fields ranging up to measurements in Earth's high field. A photograph of the instrument with its case removed, showing the location of the single-axis sensors on the sensor block, together with its associated electronics, is shown in Figure 3.7.

The FGM is based on three single-axis core flux-gate sensors mounted orthogonally on a machinable glass ceramic block. Ceramic is chosen for its low thermal expansion coefficient, minimizing misalignments between sensors due to temperature changes. In each sensor, a drive coil is wound around a high permeability ring core which is completely enclosed in a sense winding. The drive coil is driven by a crystal-controlled 15.625 kHz square wave which is used to generate a magnetic field driving the core into saturation twice per cycle. The three drive coils are connected in series to simplify the cabling and circuitry. The presence of an ambient magnetic field component parallel to the axis of the sense coil causes the saturation of the core to become asymmetrical. This induces a second harmonic of the drive frequency in the sense coil which is proportional

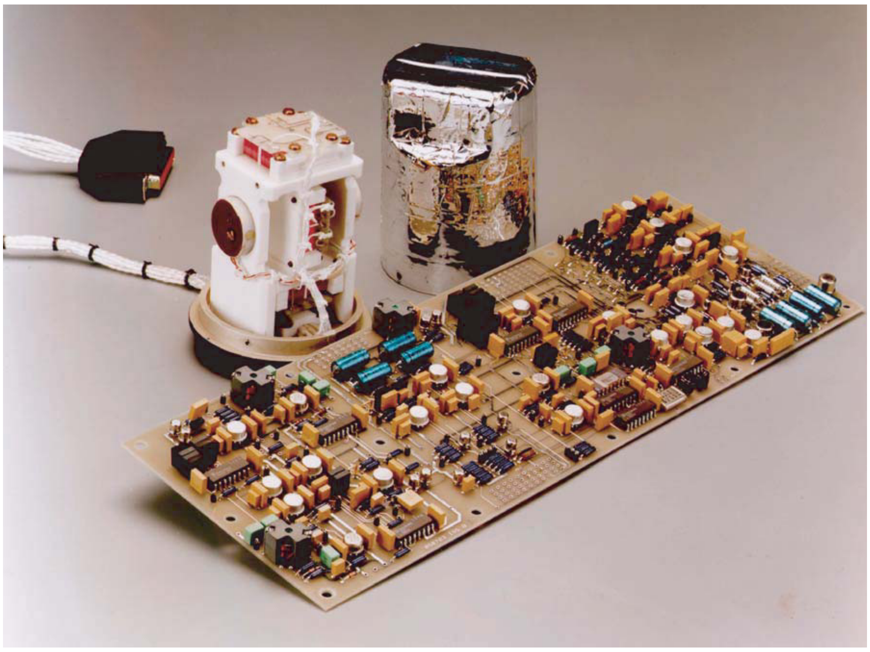

Figure 3.7: Ultra Electronics photograph of the FGM (with cover off) and electronics board. [From Dougherty et al., 2004].

to the magnitude of the magnetic field component along that axis. The signal is processed through a narrow band amplifier tuned to the second harmonic of the drive frequency, which attenuates harmonics other than the second. The result is integrated, converted to a current and fed back to the sensor coil to null the ambient field. The integrated output voltage, amplified and corrected for scale factor and alignment errors, is proportional to the ambient field. The three analogue vector components are passed to the DPU for analogue to digital conversion and data processing.

Changing the electronics feedback path and the output amplification allows the sensor to be operated in one of four different full scale magnetic field ranges (± 40 nT; ± 400 nT; 10,000 nT; ± 40,000 nT). Switching between ranges in normal operations is automatic, controlled by the DPU, but all parameters are also modifiable by command. A 1 W heater has been provided to maintain the FGM within its operating temperature range of -30 to +50º C.

3.3.5 The VHM

The V/SHM sensor, mounted at the end of the 11 metre magnetometer boom, optimizes low frequency vector measurements in low fields. A photograph of the V/SHM sensor and the VHM electronics is shown in Figure 3.8. A set of cables running the length of the boom connect it to the VHM and SHM electronics on Subchassis No. 1. The flight sensor is actually the flight spare Ulysses vector helium magnetometer sensor, with the addition of a small pair of coils nested inside a pair of the larger Helmholtz coils used in the vector mode and a coaxial cable carrying the signal from the voltage controlled oscillator (VCO) to that cable. Similarly, the VHM electronics box is the Ulysses flight spare unit with small modifications to change the sensor operating ranges and to compensate for the different boom cable lengths. A new electronics board has been added to Subchassis No. 1 containing the electronics to operate in the scalar mode.

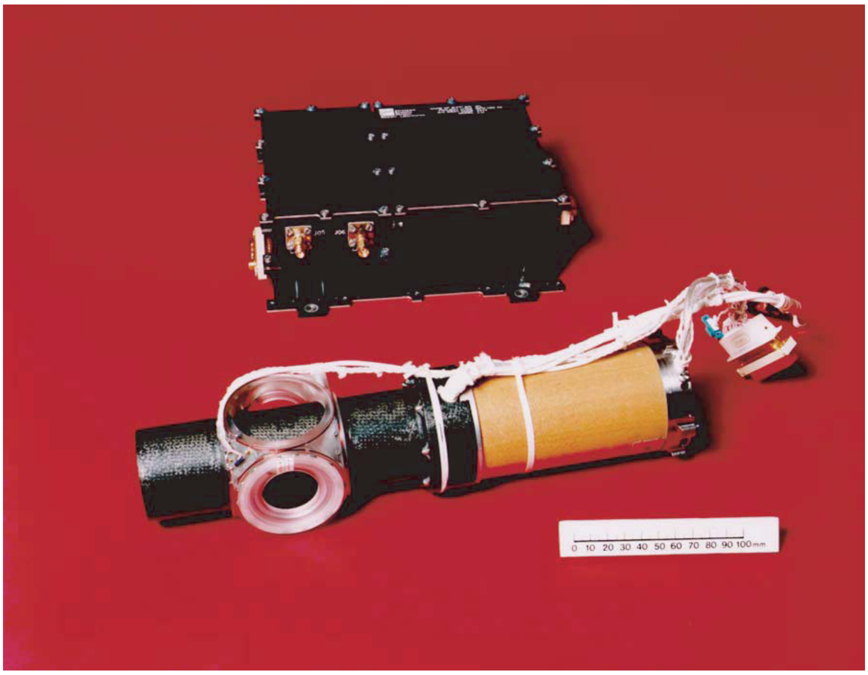

Figure 3.8: V/SHM sensor and VHM electronics.
[From Dougherty et al., 2004].

The operation of the vector helium magnetometer is based on field dependent light absorption (the Zeeman effect) and optical pumping to sense the magnetic field. Helium in an absorption cell is excited by a radio frequency (RF) discharge to maintain a population of metastable long-lived atoms. Infrared radiation at 1083 nm from a helium lamp, also generated by RF excitation, passes through a circular polarizer and the cell to an infrared detector. The absorption (pumping efficiency) of the helium in the cell is dependent on the ambient magnetic field direction. The optical pumping efficiency is proportional to $\cos^2\Theta$ where Θ is the angle between the optical axis and the direction of the magnetic field. This directional dependence is utilized in the vector mode by applying low frequency sweep fields rotating about the cell, which allow the extraction of the three orthogonal ambient field components. These fields are fed back using a set of triaxial Helmholtz coils mounted on the sensor housing around the cell.

In the scalar mode, a weak AC field at the Larmor frequency is applied to the cell, which opposes the optical pumping. The decrease is detected by the IR detector as a decrease in transmitted light from the lamp. The Larmor frequency which is proportional to the ambient magnetic field is measured. In order to track the ambient field the applied field is frequency modulated so that the detector output contains a signal component harmonically related to the modulation frequency. The proportionality constant is the gyromagnetic ratio which for helium is 28.023561 Hz/nT. Detection and measurement of the Larmor frequency lead to a very accurate measurement of the ambient field magnitude. In this mode, the directional dependence results in a "field of view" restricted to a cone with half angle approximately 45 º, centred on the optical axis detector.

Changing the VHM sweep field allows the sensor to operate in different ranges. Two VHM ranges have been selected for Cassini (± 32 nT; ± 256 nT, 31.2 pT). As for the FGM, automatic ranging has been implemented in the DPU. A single range has been implemented for the SHM. Injection of known currents into the Helmholtz coil system provides an in-flight calibration (IFC) capability. A non-magnetic proportional heater using up to 2 W is incorporated into the V/SHM sensor and is controlled from electronics built into the VHM electronics box on Subchassis No. 1. The operating temperature range of the sensor is -10 to +40º C.

3.4 The Radio and Plasma Wave Science Investigation

3.4.1 Introduction

An overview of the current knowledge of Saturn's radio emissions is presented in Chapter 2. It is clear that our knowledge is incomplete. Much more observing time and spatial coverage in the vicinity of Saturn are needed to fully understand the modulation effects imposed by planetary rotation, solar wind pressure variations, and interactions with Saturn's moons and rings. Direction-finding and polarization measurements are needed to constrain the generation mechanisms and to compare the source locations with other in-situ and remote sensing observations. High-time resolution measurements are needed to study the fine structure of Saturn Kilometric Radiation. The Cassini mission with its four years of in-orbit observations provides an ideal opportunity to carry out these studies.

Data from the Cassini radio and plasma wave investigation is used in Chapter 5 to study Saturn's radio emissions as a remote diagnostic of Saturn's magnetospheric dynamics. Compared with Voyagers 1 and 2, which are the only spacecraft that have made radio and plasma wave measurements in the vicinity of Saturn, the Cassini radio and plasma wave science instrument [Gurnett et al., 2002] has several new capabilities. These include (1) greatly improved sensitivity and dynamic range, (2) the ability to perform direction-finding measurements of remotely generated radio emissions and wave normal measurements of plasma waves, (3) both active and passive measurements of plasma resonances in order to give precise measurements of the local electron density, and (4) Langmuir probe measurements of the local electron density and temperature. With these new capabilities, it will be possible to perform a broad range of studies of radio emissions, wave-particle interactions, thermal plasmas and dust in the vicinity of Saturn.

3.4.2 Instrument Description

A simplified block diagram of the RPWS instrument is shown in Figure 3.9. Three nearly orthogonal monopole electric field antennas, labeled E_u, E_v and E_w, are used to detect electric fields over a frequency range from 1 Hz to 16 MHz. The orientations of these three antennas relative to the x, y and z axes of the spacecraft are shown in Figure 3.10. By electronically taking the difference between the voltages of the E_u and E_v monopoles, these two antennas can be used as a dipole, E_x, aligned along the x-axis of the spacecraft. The E_u and E_v antennas can also be used to sound the local plasma by transmitting short pulses. In an alternative mode of operation, they can be biased and used as Langmuir probes to measure the phase velocity of density structures in the plasma.

The tri-axial search coil magnetic antennas, labeled B_x, B_y, and B_Z in Figure 3.9, are used to detect three orthogonal magnetic components of electromagnetic waves over a frequency range from 1 Hz to 12 kHz. The search coil axes are aligned along the x, y and z axes of the spacecraft. The spherical Langmuir probe, shown at the bottom of the block diagram, is used for electron density and temperature measurements. Both the electric antennas and the Langmuir probe can be used to detect dust impacts.

Signals from the electric and magnetic antennas are processed by five receiver systems shown in the middle column of the block diagram: a high frequency receiver that covers the range from 3.5 kHz to 16 MHz for high frequency spectral, polarization, and direction-finding measurements, and which provides simultaneous auto- and cross-correlation measurements from two selected antennas; a medium frequency receiver that covers the range from 24 Hz to 12 kHz for medium frequency spectral measurements; a low frequency receiver that covers the range from 1 Hz to 26 Hz for low-frequency spectral measurements; a five-channel waveform receiver that covers the range from 1 Hz to 2.5 kHz in two bands, 1 Hz to 26 Hz and 3 Hz to 2.5 kHz, to perform wave normal and fine-scale plasma structure measurements; and a wideband receiver that has two frequency bands, 60 Hz to 10.5 kHz and 800 Hz to 75 kHz to provide high-resolution

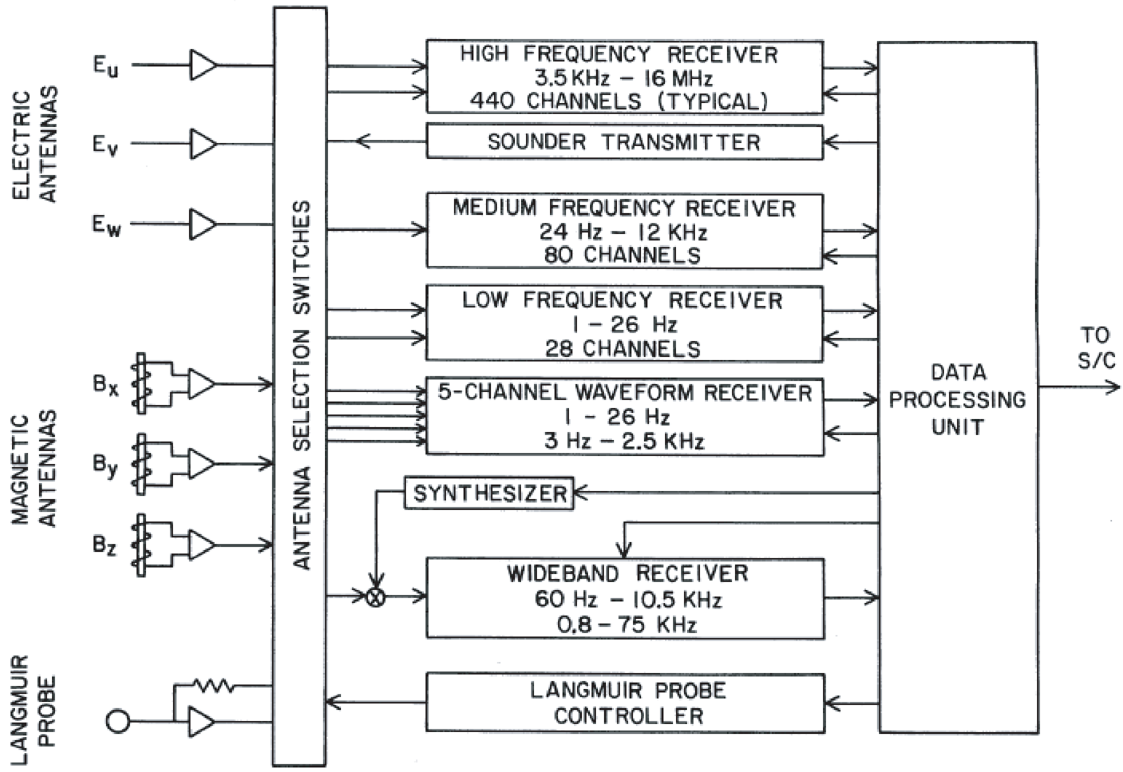

Figure 3.9: A functional block diagram of the RPWS instrument. The seven sensors, three electric, three magnetic and the Langmuir probe are shown on the left side. In the middle, the several receivers which the instrument uses to analyse the signals are shown. The data management and control functions, as well as the interface with the spacecraft are shown as the data processing unit on the right side. [From Gurnett et al., 2004].

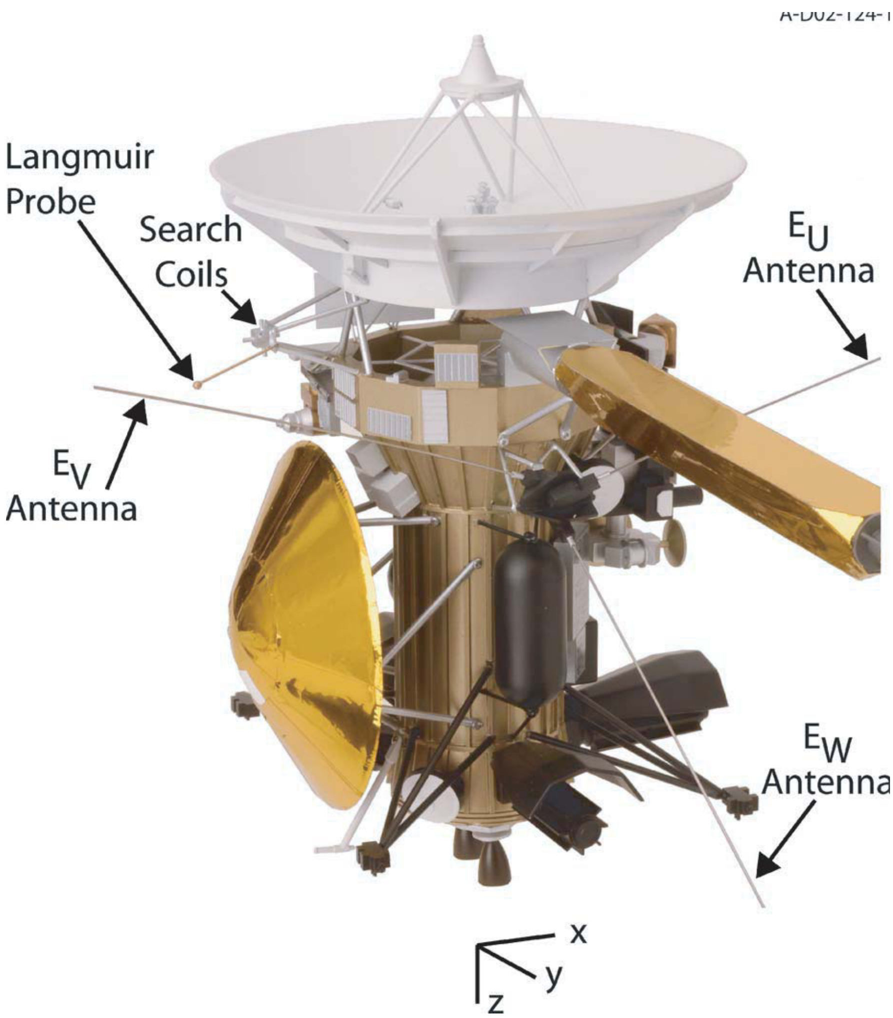

Figure 3.10: The Cassini spacecraft showing the locations of the RPWS sensors and their relationship with other structures on the spacecraft. [From Gurnett et al., 2004].

frequency-time spectrograms. In addition, a sounder transmitter can be used to stimulate plasma resonances over a frequency range from 3.6 kHz to 115.2 kHz. Each receiver determines the power per Hertz in that frequency band (i.e. the total power in that filter divided by the filter width in Hz), and that is what is plotted in the spectrograms.

3.5 The Hubble Space Telescope

Saturn's dynamic aurora is described in Chapter 2, and some observations are discussed in Chapter 5. All the images in this thesis were obtained using the Hubble Space Telescope (HST), a cooperative programme of ESA and NASA to operate a long-lived space-based observatory. HST is a 2.4-metre reflecting telescope which was deployed in low-Earth orbit (600 kilometres) by the crew of the space shuttle Discovery (STS-31) on 25 April 1990 (See Figure 3.11).

HST's current complement of science instruments includes three cameras, two spectrographs, and fine guidance sensors (primarily used for astrometric observations). Because of HST's location above the Earth's atmosphere, these science instruments can produce high resolution images of astronomical objects. Ground-based telescopes can seldom provide resolution better than 1.0 arc-seconds, while HST's resolution is about 10 times better, or 0.1 arc-seconds.

3.5.1: Aurora

Saturn's aurora (as discussed in detail in Chapter 2) is produced as charged particles precipitating from the magnetosphere collide with atmospheric gases – molecular and atomic hydrogen in Saturn's case. As a result of this, the gases from Saturn's main auroral oval glow at far-UV wavelengths (110-160 nm) which are absorbed by the Earth's atmosphere, and so can only be observed from space-based telescopes like HST. It should be noted that there are other emissions from Saturn,

Figure 3.11: The Hubble Space Telescope in orbit about the Earth.
[Image courtesy of NASA].

namely in the EUV and x-ray wavelength bands; however, it is the discrete FUV aurora that is of prime interest here.

Atomic hydrogen has its Lyman series, with the strongest Lyman-alpha line at 121.6 nm, and the weaker lines spanning down to 91.1 nm at the hydrogen ionization continuum. Molecular hydrogen, H_2, has the prominent Lyman and Werner bands from ~80 to ~167 nm. The reflected sunlight from the planet also shows atmospheric compositional properties, such as from the absorption signatures of simple and complex hydrocarbons present in the stratosphere, and also from the scattering properties of molecules and hazes.

Saturn's aurora has been studied in detail since 1994 when the first FUV image was obtained using Hubble's Wide Field and Planetary Camera 2 (WFPC2) [Gérard et al., 1995]. More recently, the Space Telescope Imaging Spectrograph (STIS) [e.g. Woodgate et al., 1998] has been used to image the aurora as its far-UV imaging mode has about 10 times better sensitivity than a typical WFPC2 exposure, and about 4 times the spatial resolution (e.g., the Cassini division of the rings is now clearly visible).

3.5.2 STIS

The Space Telescope Imaging Spectrograph was installed on HST during the second servicing mission in February 1997 [Woodgate et al., 1998]. A spectrograph spreads out the light gathered by a telescope so that it can be analyzed to determine such properties of celestial objects as chemical composition and abundances, temperature, radial velocity, rotational velocity, and magnetic fields. STIS can study these objects across a spectral range from the UV (115 nanometers) through the visible red and the near-IR (1000 nanometers). Correction for HST's spherical aberration and astigmatism is also included.

3.5.3 Optics

The optical design is illustrated in Figure 3.12. The STIS optics have been configured into two basic subassemblies. The first is a two-element reflecting corrector, which eliminates the spherical aberration and the off-axis aberrations present. The corrector is followed by the imaging spectrograph: collimator, grating and camera elements to provide high-resolution and high-efficiency spectroscopy and imaging capability in order to satisfy the science requirements.

3.5.4 Detectors

STIS uses three detectors to optimize performance over the instrument wavelength range: a cesium iodide (CsI) photocathode Multi-Anode Microchannel Array (MAMA) for 115 to 170 nm (Far UltraViolet), a cesium telluride (Cs_2Te) MAMA for 165 to 310 nm (Near UltraViolet), and a Charge Coupled Device (CCD) for 305 to 1000 nm. The detectors have a format of 1024x1024 pixels.

The use of CCDs in the UV is difficult at best and as such, the MAMA arrays are selected for imaging of Saturn's aurora. The MAMA arrays have a linear size of 0.0243 arcsec, thus providing a field of view for each MAMA of 24.7 x 24.7 arcsec^2 with a 0.08 arcsec full width at half maximum point spread function. In the UV, the spatial resolution is limited by the telescope point-spread function.

The STIS MAMA detectors are solar-blind photon-counting devices which process events serially, and they have several modes of operation. In MAMA ACCUM mode, which is the standard integration mode, photons are accumulated into a 2048x2048 array in the STIS data buffer memory as they are received. Alternatively, in TIMETAG mode, the time and location of each photon event can be recorded explicitly. As such, the MAMA produces an event stream of data points with a time resolution of 125 microseconds.

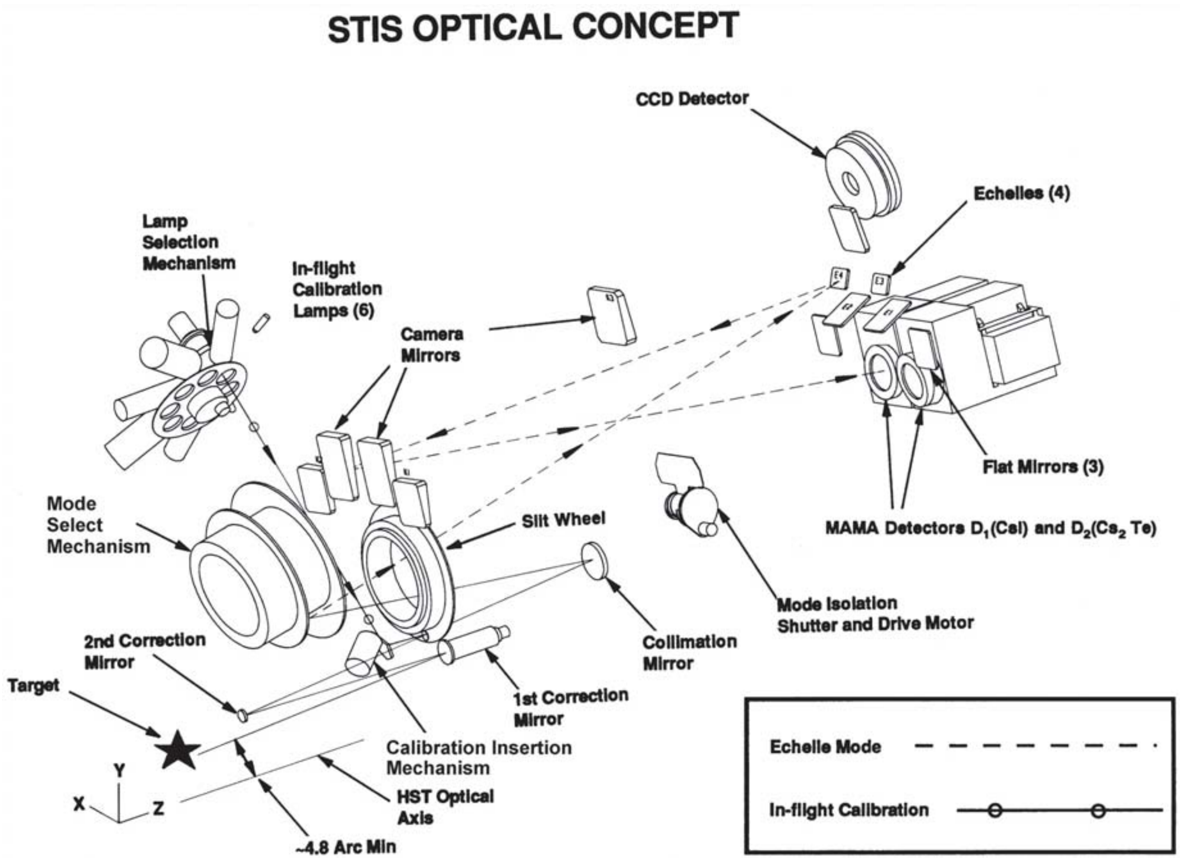

Figure 3.12: Optical layout of STIS. The beam path is common up to the mode select mechanism, the position of which selects the remaining beam path, determining the spectral or imaging mode being used. (Note the filter wheel shown near the lamps was descoped and not built. Some filters were moved to the slit wheel) [From Woodgate et al., 1998]

3.5.5 STIS imaging of Saturn's aurora

For the purposes of this thesis, we wish to examine the operation of STIS for imaging of Saturn's aurora. In particular, we focus on the operating conditions during the January 2004 Hubble-Cassini campaign discussed in Chapters 2 and 5. The 24.7x24.7 arcsec^2 field of view of STIS includes Saturn's full disk and a fraction of the ring system. The distance subtended by 1 pixel on the field of view projected at Saturn is then approximately 150 km. At this distance, a resolution element corresponds to ~500 km on the planet. There are a number of imaging modes available on the instrument, two of which are used in the January data set and thus will be described here.

<u>Clear mode:</u>
In the "clear" (no filter) mode, the passband extends from 115 to 180 nm and is sensitive to the H_2 Lyman and Werner bands as well as the strong H Lyman-α line. This mode is often used during "dark time", i.e. the 25-min period during which HST is in the shadow of the Earth and therefore when minimal contamination is expected from the geocoronal Lyman-alpha emission.

<u>Filtered mode:</u>
In the "filtered" mode, the F25-SrF_2 filter is added in the optical path in order to reject the emission shortward of 125 nm, including the (contaminated) H Lyman-alpha line. This mode is generally used for images taken immediately before and after the "dark time".

3.5.6 Target tracking

Even though the target tracking stability of HST is about one hundredth of an arcsec over the exposure time, the actual pointing precision is limited by the accuracy of the onboard guide star catalogue. Consequently, the centre position of the planet deduced from the observation log is only known within ~160 pixels. This imprecision is far too large to allow a reliable mapping of the auroral emission in Saturnian coordinates. As a result, a limb fitting procedure has been developed to aid in the determination of the centre position of the planet [Gérard et al., 2004; Grodent et al., 2005]. The method provides a centre position with an accuracy comparable to the size of a resolution element, i.e. less than ~3 pixels.

Subsequently, each pixel of the initial image is assigned a planetocentric latitude and a S3 longitude. The latitudes and longitudes were calculated assuming an oblate spheroid with a radius corresponding to an average height of the auroral emission of 1000 km above the 1 bar level. This procedure makes it possible to generate polar (orthographic) projections as if the observer was located above the pole.

Chapter 4
Interplanetary magnetic field at ~9 AU during the declining phase of the solar cycle and its implications for Saturn's magnetospheric dynamics

4.1. Introduction

As discussed in Chapter 2, the large magnetic fields generated by the internal dynamos of the gas giant planets Jupiter and Saturn, combined with their rapid rotation, indicate that corotation of the plasma with the planet will be the dominant flow within their magnetospheric cavities [Brice and Ioannidis, 1970]. This scenario implies that the dominant physics of these magnetospheres will concern the nature of the plasma sources from the atmospheres and surfaces of interior moons, ring grain material, and the planet's ionosphere, combined with radial transport and loss processes [e.g., Hill et al., 1983; Vasyliunas, 1983; Barbosa, 1987; Pontius, 1997; Richardson et al., 1998; Delamere and Bagenal, 2003; Saur et al., 2004]. This picture nevertheless does not preclude significant interactions taking place between the magnetosphere and the solar wind. Two distinct types of interaction may be envisaged. The first is the compressions and expansions of the magnetosphere due to changes in solar wind dynamic pressure, [e.g., Southwood and Kivelson, 2001; Cowley and Bunce, 2003a], while the second is the excitation of magnetospheric convection by momentum coupling at the magnetopause boundary, as discussed in some detail in Chapter 2.

The principal purpose of this chapter is to investigate the reconnection-driven interaction of the solar wind with Saturn's magnetosphere, with particular reference to the consequences for magnetospheric dynamics during the four-year orbital tour of the Cassini spacecraft which began on 1 July 2004 with Cassini orbit insertion around the planet. To this end we study the IMF data obtained by Cassini during a ~6.5 month interval when the spacecraft was approaching Saturn at heliospheric radial distances between ~8.5 and ~8.9 AU, this interval encompassing eight solar rotations during the declining phase of the solar cycle. These data are employed to estimate the dayside reconnection voltage produced at Saturn's magnetopause associated with the production of open magnetic flux, based on an adaptation of understanding derived from studies at Earth. The implications of these voltage estimates for the nature of Saturn's magnetospheric dynamics will then be discussed, based on the global picture of Saturn's magnetospheric processes presented by Cowley et al. [2004a,b].

4.2. Observations of the IMF during Cassini's Approach to Saturn

4.2.1. Structure of the Heliosphere During the Declining Phase of the Solar Cycle

The structure of the solar wind outflow and IMF in the heliosphere depends significantly on the phase of the solar activity cycle, [e.g. McComas et al., 2001], which is described in detail in Section 1.3 of Chapter 1. With reference to Figure 1.2 in Chapter 1, we note that the approach phase of the Cassini spacecraft during 2003-4 took place during the declining phase of the solar cycle, such that the main 4-year orbital tour which began with Saturn orbit insertion in 1 July 2004 will encompass the late declining phase and solar minimum. Under such conditions, we expect the Sun's magnetic field to take the form of a dipole tilted with respect to the spin axis [see e.g. Gosling and Pizzo, 1999, and references therein]. Thus, the equatorial heliosphere will be highly structured by the compressions and rarefactions associated with 'corotating interaction regions' (CIRs) [e.g. Gosling and Pizzo, 1999; Crooker et al., 1999], (and explained in Section 1.4 of Chapter 1), with the implication that the interaction of Saturn with the interplanetary medium will be highly variable too. As previously discussed, we anticipate an IMF consisting of 2 sectors per solar rotation, where the sector boundaries (HCS crossings) are embedded within two CIR compression regions, separated by plasma and field rarefactions.

By way of confirmation of our expectation of the appropriateness of this picture to the interval considered here (August 2003 to March 2004), in Figure 4.1 we show a 'source surface' solar magnetic map which is typical of the whole interval, derived from photospheric magnetic field data obtained at the Wilcox Solar Observatory (WSO). Specifically we show the map for Carrington rotation 2008, spanning the interval from 26 September to 23 October 2003. This shows contours of the estimated radial field at 2.5 solar radii, plotted versus heliographic latitude and longitude, where the dashed lines show contours of the radial field directed toward the Sun, while the solid lines show contours of the radial field directed away. The heavy solid line which separates the two regions then indicates the location of the HCS. It can be seen that the field pattern is consistent with a near-dipole field whose axis is tilted at ~40° with respect to the Sun's spin axis, similar to that indicated schematically in Figure 1.6 in Chapter 1. This angle is expected to fall to smaller values as solar minimum is approached (towards the end of 2006 or the beginning of 2007 according to Figure 1.2 in Chapter 1), though the CIR-related picture presented here should still prevail in modified form due to warping of the solar magnetic equator, which is always present to some degree.

4.2.2. Cassini Magnetic Field Data

We now consider the magnetic field data obtained by the Cassini spacecraft during the approach phase to Saturn. Specifically, we consider the 6.5-month interval from mid-August 2003, when magnetic field data acquisition started to become reasonably continuous, to early March 2004, an interval which encompassed eight full solar rotations as observed by the spacecraft. During this interval the heliocentric distance of the spacecraft increased from ~8.5 to ~8.9 AU, at a heliographic latitude of ~3.5°S. The medium sampled by the spacecraft is thus expected to be representative of that which impinged on Saturn at ~9 AU with a propagation delay typically of a few tens

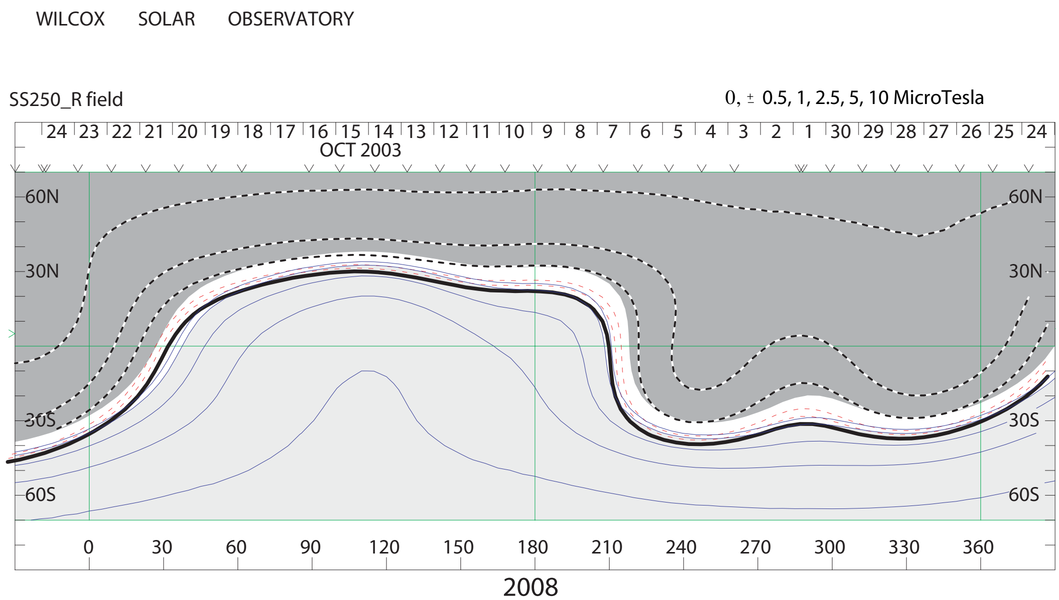

Figure 4.1: Contour map in heliographic co-ordinates of the radial solar magnetic field at 2.5 solar radii during Carrington rotation 2008 (spanning 26 September to 23 October 2003), derived from photospheric field data obtained at the Wilcox Solar Observatory (WSO), courtesy of Dr JT Hoeksema. The central heavy solid line indicates the location of the HCS, separating fields directed toward the Sun north of the line (dashed contours), from fields directed away from the Sun south of the line (solid contours).

of hours. The data used throughout were derived from the Vector Helium Magnetometer (VHM) sensor on the spacecraft, the operation of which is explained in Chapter 3.

We begin in Figure 4.2 by showing a typical 26-day segment of IMF data spanning (slightly more than) a full solar rotation at the spacecraft, specifically for the interval from day 276 to day 301 (inclusive) of 2003 (3 to 28 October). During this interval the heliocentric distance of the spacecraft increased from 8.74 to 8.79 AU. The four panels of the figure show the components of the magnetic field in RTN co-ordinates at 1 min resolution, together with the total field strength in the bottom panel. RTN is a right-handed spherical polar system referenced to the Sun's spin axis, in which B_R (top panel) is positive radially outward from the Sun, B_T (second panel) is the azimuthal component positive in the direction of planetary motion, and B_N (third panel) is the 'minus theta' component positive northward in the solar equatorial plane. It can be seen from the B_T trace that the IMF consisted of two principal sectors, as anticipated in the above discussion, separated by crossings of the HCS on days 282 and 290, indicated by the vertical dashed lines marked 'HCS' at the top of the plot. The first of these, on day 282, marks a transition from predominantly negative to predominantly positive B_T, corresponding to a transition from 'away' fields connected to the region south of the current sheet to 'towards' fields connected north of the current sheet. The second, on day 290, then corresponds to the reverse transition. The ~8-day positive B_T sector is thus considerably shorter than the ~17-day negative B_T sector during this solar rotation. It can also be seen that the HCS crossings occurred ~1-2 days after sudden enduring increases in the total field strength, which we thus identify as the forward waves of CIR compression regions within which the HCS is embedded, as discussed in detail in Section 1.4 of Chapter 1. These are indicated by the vertical dashed lines marked 'FW'. Identification of the compression region reverse waves is perhaps less obvious due to the variability of the field within the compression regions, but these have been tentatively identified with the sudden decreases in field strength indicated by the vertical dashed lines marked 'RW'. The main point we wish to illustrate with these data, however, is that due to the evolution of the CIR structures in the heliosphere, the IMF in Saturn's vicinity is highly structured in time during the solar rotation. Extended several-day intervals

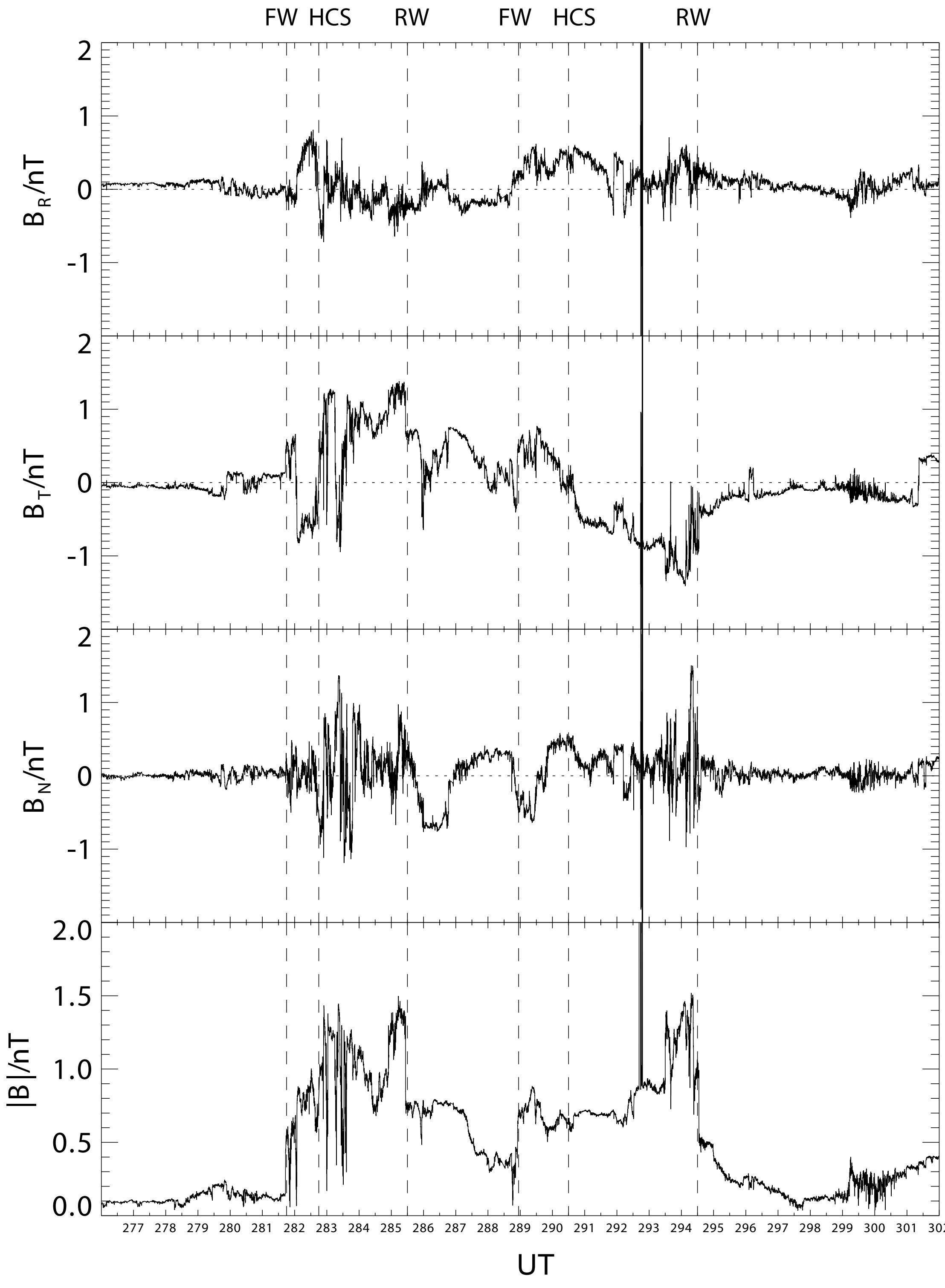

Figure 4.2: Cassini VHM magnetic field data at 1 min resolution for the interval from day 276 to 301 (inclusive) of 2003 (3 to 28 October), spanning a full solar rotation. The top three panels show the components of the field in RTN coordinates, while the bottom panel shows the total field strength. Crossings of the heliospheric current sheet are shown by the vertical dashed lines marked 'HCS', while the dashed lines indicate the probably locations of the forward and reverse waves ('FW' and 'RW' respectively) which bound the compression region within which the HCS is embedded. During this interval the heliocentric distance of the spacecraft increased from 8.74 to 8.79 AU, at a heliographic latitude of 3.5°S.

occur during which the field strength remains very low, typically a few tenths of a nT, but sometimes ~0.1 nT or less (see below), which we take to correspond to solar wind rarefaction regions. Such intervals are then followed by few-day intervals of much higher field strength, ~0.5-1.5 nT, which we take to correspond to CIR compression regions, and which are thus preceded and followed by the compressive and expansive effects of the CIR forward and reverse (shock) waves. We thus infer that the reconnection-mediated interaction of Saturn's magnetosphere with the interplanetary medium will generally undergo substantial CIR-related modulation during each solar rotation, and that this modulation will occur together with a concurrent related pattern of compression-expansion effects associated with the changing dynamic pressure of the solar wind.

A consistent feature of the field data which is potentially significant for the reconnection-mediated interaction with Saturn's magnetosphere is that in the regions of particularly high peak field strength, such as those occurring in the two compression regions around days 282 and 294 in Figure 4.2, the field is seen to be highly variable in magnitude and direction. Similar levels of relative fluctuation can occur in weak field regions too, but the properties of the high-field regions are of special relevance to reconnection-related magnetospheric dynamics. The field behaviour in such regions is examined further in Figure 4.3, where we show magnetic field data for days 293 and 294 during the second compression region on an expanded time base. It can be seen that the region of high field strength contains substantial fluctuations in the direction of the field, especially in the N-T plane transverse to the radial vector. The north-south field component B_N, in particular, fluctuates irregularly between large positive and large negative values on a range of time scales from tens of minutes up to a few hours. Assuming that these are essentially convected structures in the solar wind (or slowly-propagating waves), the implied spatial scale in the radial direction for a typical solar wind flow speed of ~500 km s^{-1} is from ~1 to ~6 million km, which corresponds to ~15 to ~90 R_S. Given that the spatial dimension of Saturn's magnetosphere is of a comparable order (e.g. the distance from the planet to the subsolar magnetopause is typically ~20 R_S), the implication is that the magnetosphere will generally be immersed in a rather

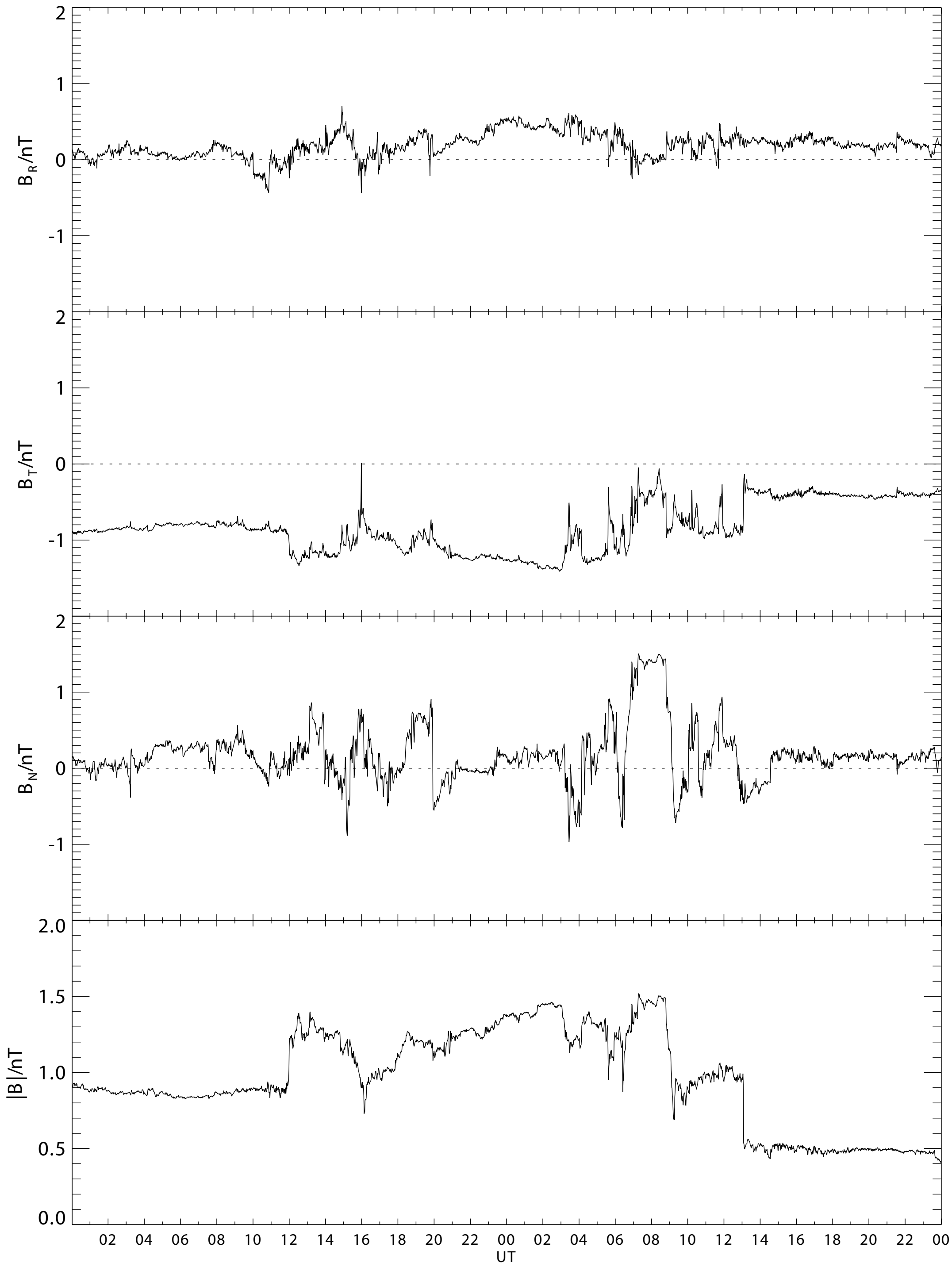

Figure 4.3: Cassini VHM magnetic field data shown in the same format as Figure 4.2., but plotted on an expanded time-base spanning days 293 and 294 in 2003 (20 and 21 October).

inhomogeneous magnetic medium, at least in the radial direction. The spatial scales in the transverse direction, however, may be significantly larger.

An overview of the magnetic field data over the ~6.5 month interval considered here is presented in Figure 4.4, where we show a stacked plot of the total interplanetary field strength in 25.5 day segments, for the interval from day 225 of 2003 (13 August) to day 63 of 2004 (3 March). Each of the eight data segments then corresponds to essentially one solar rotation, where the Carrington longitude of the spacecraft decreased from very nearly 360° at the left-hand edge of each panel to very nearly 0° at the right-hand edge. The solar rotation discussed in detail above and shown in Figure 4.2 corresponds to that shown in the third panel from the top. Clear crossings of the HCS are marked by vertical arrows, with the inclusion of a horizontal bar indicating an interval of time over which a slow reversal or multiple reversals of B_T polarity occur. The polarity of the reversal is indicated by the plus and minus symbols, with '-/+' indicating a change in sign from negative to positive B_T, i.e. from south to north of the current sheet, and vice versa for '+/-'. It can be seen that with the principal exception of the fourth panel of the figure, the basic two-sector structure is retained throughout, with modestly varying phase during each solar rotation. The crossings of the HCS are generally seen to be embedded within compression regions of enhanced field strength. However, the pattern of field strength variation does change somewhat from one solar rotation to the next. In some rotations two separated intervals of high field strength occur which are of roughly equal amplitude, such as in the second and third panels of the figure. In others, the two field enhancements are very unequal in amplitude, such that in effect only one major field enhancement occurs during the rotation, such as in the sixth and seventh panels. In yet others, the field is better described as remaining of roughly constant intermediate amplitude for a significant fraction of the rotation, followed by an extended interval of exceptionally weak fields, as seen in the first and eighth panels. Overall, however, it can be seen that major modulations of the interplanetary field strength during each solar rotation (and consequent reconnection-related dynamics) will be the norm at Saturn during the declining phase of the solar cycle, varying from several-day intervals where

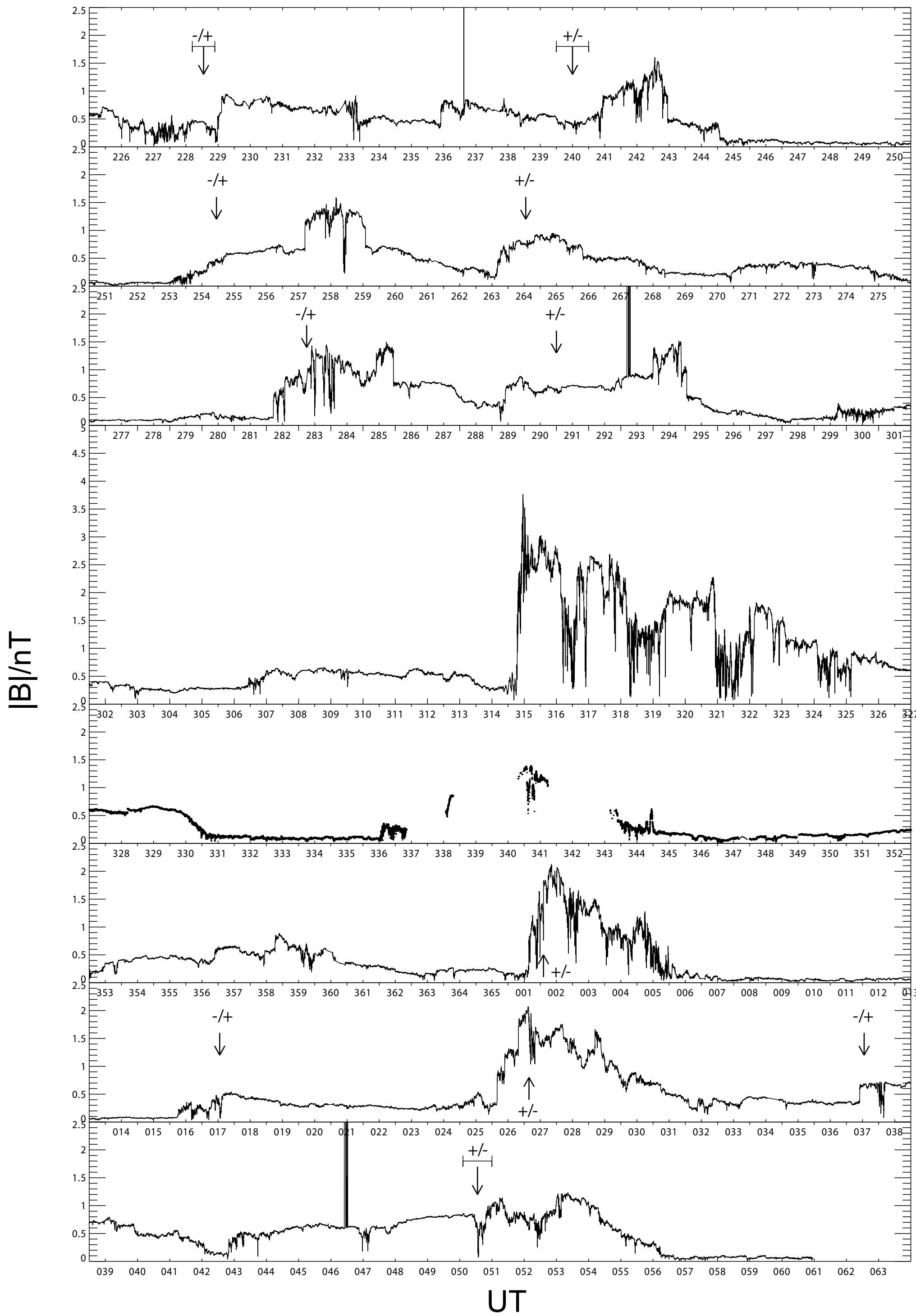

Figure 4.4: Interplanetary field strength measured by Cassini during the interval from day 225 of 2003 (13 August) to day 63 of 2004 (3 March), plotted versus time in a stacked plot of eight 25.5-day intervals, each corresponding to essentially one solar rotation. Clear crossings of the HCS are shown by the arrows, together with a horizontal line in cases where either a gradual reversal or closely-spaced multiple reversals in the sign of BT took place. Note that multiple reversals in B_T took place during the disturbed interval in the fourth panel, and that some HCS crossings were missed in major data gaps due to spacecraft operations. Such data gaps occur in the central region of the fifth panel, and at the end of the interval in the eighth panel.

the field strength can remain as small as ~0.1 nT or less, to few-day compression regions where the field strength peaks at ~1 to ~2 nT.

A major exception to the CIR-related picture, however, occurs in the data in the fourth panel of the figure, where significantly higher field strengths occur than elsewhere, peaking at ~3.8 nT at the end of day 314 (10 November) of 2003, and remaining intermittently high to beyond the end of that solar rotation. The typical pattern of B_T sign reversals was also disrupted during this interval. These disturbances clearly relate to the interval of extremely high solar activity that occurred at the end of October and early November 2003 (principally between days 292 and 307 (19 October to 3 November)), which involved several X-class flares and the emission of associated fast (~1000-2000 km s^{-1}) coronal mass ejections (CMEs) [Lopez et al., 2004]. Clearly such intermittent solar activity will also strongly modulate the interplanetary medium at Saturn's orbit, and thus Saturn's magnetospheric dynamics, with regard to both reconnection-related and compressive effects.

4.3. Open Flux Production at Saturn's Magnetopause

4.3.1 Simple Empirical Model

We now employ the Cassini data presented in Section 4.2 to make a first quantitative estimate of the reconnection-mediated interaction between the solar wind and Saturn's magnetosphere, empirically based on previous experience at Earth. Specifically, we estimate the rate of open flux production at Saturn's dayside magnetopause, which is a primary parameter governing the excitation of solar wind-driven convection and the growth of the magnetospheric tail. These results will then be used in Section 4.4 to discuss the consequent nature of the reconnection-related dynamics of Saturn's magnetosphere.

Observations at Earth have demonstrated that the primary mode of interaction between the magnetosphere and the interplanetary medium takes place via magnetic reconnection at the dayside magnetopause (e.g. Cowley et al. [2003c] and references therein). When the IMF at Earth points to the south, opposite to the northward equatorial planetary field, reconnection at the low-latitude dayside magnetopause produces 'open' magnetic flux tubes which connect from the planet's polar regions into the solar wind. These open flux tubes are then carried by the solar wind flow towards the nightside, and are stretched into a long magnetic tail, from which the magnetic flux eventually returns during sporadic intervals of tail reconnection (principally substorms). When the IMF at Earth points to the north, however, along the equatorial planetary field, open flux production is much reduced, though reconnection can then migrate to the high latitude tail lobe magnetopause [e.g. Reiff and Burch, 1985; Kessel et al., 1996; Øieroset et al., 1997]. Such 'lobe' reconnection does not change the amount of open flux in the system (if reconnection for a given IMF field line occurs at only one lobe as will generally be the case), but may lead to a solar wind-induced circulation of open flux in the polar region. The primary parameter governing the nature and strength of the solar wind interaction, and thus much of magnetospheric dynamics in the terrestrial case, is thus the IMF vector. At Saturn, much of the magnetospheric physics of the interior region may be related to corotational dynamics as indicated in Section 4.2, which may be significantly modulated by solar wind-induced compressions and expansions of the magnetosphere [Southwood and Kivelson, 2001; Cowley and Bunce, 2003a]. It nevertheless seems reasonable to suppose that the reconnection-mediated interaction at the magnetopause boundary at Saturn may follow similar lines to those observed at Earth. Here we propose that this is so, and estimate on this basis the rate of open flux production at Saturn's magnetopause using the Cassini IMF data and an empirical model adapted from Earth. We do not attempt to map the Cassini measurements to Saturn, as such, but instead simply consider the observed field to be representative of that which is present at the planet. We then ask what the rate of open flux production at Saturn's dayside magnetopause would be if the planet were immersed in an interplanetary medium having the same properties as those sampled by the spacecraft, specifically having a field with the same RTN components.

The rate of open flux production is equal to the voltage along the segment of the magnetopause reconnection line where open flux is produced, not counting possible regions of 'lobe' reconnection for IMF orientations directed along the planetary equatorial field. In principle, this voltage can be written as

$$\Phi = V_{SW} B_{\perp} L \quad , \tag{4.1}$$

where V_{SW} is the velocity of the solar wind, taken to a sufficient approximation to be directed radially outward from the Sun, $B_{\perp}$ is the strength of the IMF perpendicular to the velocity vector (i.e. in the T-N plane), and L is a length. The quantity $V_{SW} B_{\perp}$ is the motional electric field in the solar wind in the planet's rest frame, and L is the width of the solar wind channel in the T-N plane (perpendicular to the $\boldsymbol{B}_{\perp}$ vector) in which the IMF reconnects with closed planetary field lines. The principal issue then concerns how length L depends on the properties of the IMF. In the simplest models, which we pursue here, L is taken to depend on the 'clock angle' θ of the magnetic field, that is the angle that vector $\boldsymbol{B}_{\perp}$ makes with respect to the magnetic axis of the planet projected onto the T-N plane. That is, we take $L = L_{o} f(\theta)$, where L_{o} is a constant length to be determined empirically. For Earth, it is traditional to measure the clock angle from the northern magnetic axis, such that open flux production is high for clock angles greater than ~90° (i.e. for IMF vectors directed 'southward'), and weakens for clock angles less than ~90° (i.e. for IMF vectors directed 'northward'). Various functional forms for this dependence have been proposed. One is the 'half-wave rectifier' function advanced e.g. by Aubry and McPherron [1971] and Burton et al. [1975], in which we take $f(\theta) = -\cos\theta$ for θ greater than 90° (such that $B_{\perp} f(\theta)$ is then just $-B_z$), and $f(\theta) = 0$ for θ less than 90°. For a given value of $\boldsymbol{B}_{\perp}$, open flux production is then maximum for a pure southward field, and switches off entirely for northward components of the IMF. However, more recent studies have demonstrated that while terrestrial dayside reconnection is certainly much weaker for northward than for southward IMF, it does not switch off entirely until the clock angle falls below ~30° [Sandholt et al., 1998; Grocott et al., 2003]. A somewhat more gentle dependence of f on θ is therefore indicated, such as the function $f(\theta) = \sin^4(\theta/2)$ employed by Perrault and Akasofu [1978]. This function is identical to the half wave rectifier function in the vicinity of $\theta \approx 180^{\circ}$ to lowest order in $(180^{\circ} - \theta)$, falls to $f(\theta) = 0.25$ at $\theta = 90^{\circ}$, and then to zero at $\theta = 0^{\circ}$. The value at $\theta = 30^{\circ}$ is ~0.004, which is essentially zero. Here we thus adapt the latter function to Saturn, and again measuring the clock angle from the northern axis, we employ

$$\Phi = V_{SW} B_{\perp} L_{o} \cos^{4}(\theta/2) \quad , \tag{4.2}$$

where 'sin' has been changed to 'cos' because for Saturn the dipole axis points to the north, such that the planetary equatorial field points to the south. Open flux production will therefore be stronger for northward IMF, and weaker for southward IMF in this case. The precise definition of the angle θ employed in Eq. (4.2) is indicated in Figure 4.5. This figure shows the T-N plane transverse to the radius vector from the Sun locally at Saturn. Vector $\hat{\boldsymbol{S}}_{\perp}$ shows the unit vector along Saturn's spin axis projected onto this plane, at angle θ_S to the N axis. This direction also represents the northern magnetic axis, since the magnetic axis is closely aligned (within ~1°) with the spin axis at Saturn [e.g., Davis and Smith, 1990]. The angle θ in Eq. (4.2) is thus determined as the angle between $\boldsymbol{B}_{\perp}$ and $\hat{\boldsymbol{S}}_{\perp}$ in the T-N plane, taken positive in the clockwise sense as shown (and defined over the full range between 0° and 360°), using the T and N components measured at the spacecraft as representative of those impinging on Saturn. We note that the planet's spin (and magnetic) axis angle θ_S, measured positive clockwise from the N axis as shown in Figure 4.5, increased from 0.9° to 5.0° over the interval considered here, corresponding to a period just after northern winter solstice.

We now consider the value of the length parameter L_{o} in Eq. (4.2). Clearly, no direct empirical knowledge exists of the value appropriate to Saturn. Here we therefore simply scale values appropriate to the terrestrial case, according to the size of the respective magnetospheres. In a recent study, Milan et al. [2004] have examined the value specifically appropriate to the production of open flux in the terrestrial magnetosphere, by examining the expansion in the region of open flux in the Earth's ionosphere using radar, auroral, and particle precipitation data during non-substorm intervals. The results

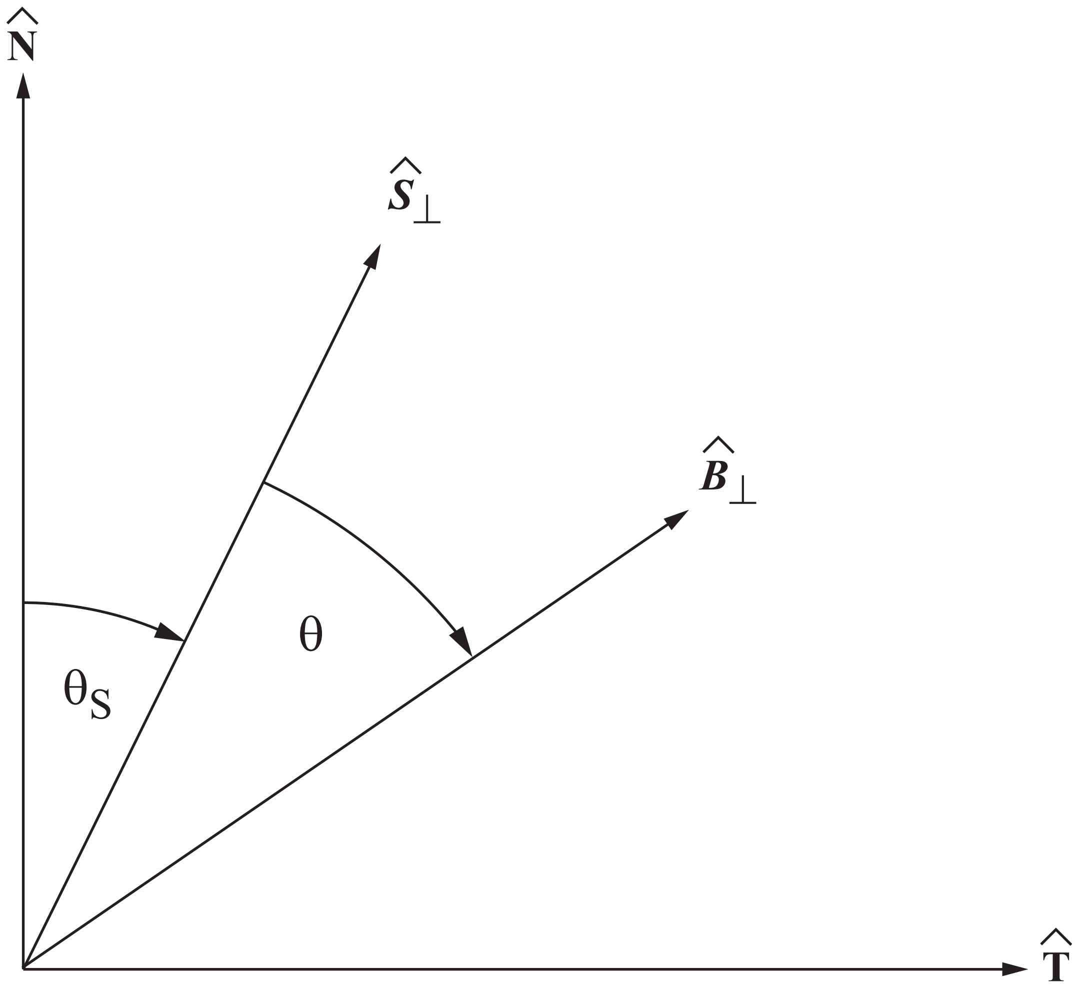

Figure 4.5: Diagram showing the definition of the clock angle θ of the magnetic field employed in Eq. (4.2) for the dayside reconnection voltage. We show the T-N plane locally at Saturn, together with Saturn's spin axis vector projected onto that plane, $\hat{S}_\perp$, at angle θ_S to the N axis. The latter vector also represents the direction of Saturn's magnetic axis projected onto the T-N plane. The clock angle is then taken as the angle between the projected spin/magnetic axis and the field in the T-N plane measured at Cassini, $B_\perp$, the latter being taken as representative of the fields that will impinge locally upon Saturn. Angle θ is measured positive clockwise in the plane as shown, over the full range 0° to 360°.

indicate that the appropriate length in this case is $L_o \approx 5\ R_E$, where R_E is Earth's radius. The subsolar radius of the Earth's magnetosphere, taken to define its scale size, is ~10 R_E, compared with ~20 R_S for Saturn as indicated above. For Saturn we thus take $L_o \approx 10\ R_S$ in Eq. (4.2).

We finally note that the voltage given by Eq. (4.2) is also directly proportional to the solar wind speed V_{SW}, measurements of which, as indicated above, are unavailable for most of the interval studied here. In this situation which have simply used a fixed representative value of 500 km s^{-1} throughout. While this represents an approximation, of course, the important point to note is that the most significant modulation of the RHS of Eq. (4.2) by far will usually arise from variations of the IMF strength and direction, rather than from variations in the solar wind speed. Observations of the CIR-modulated solar wind by the Ulysses spacecraft in the vicinity of Jupiter's orbit at ~5 AU indicate speeds which vary typically over the range from ~350 to ~750 km s^{-1} [e.g. Gosling and Pizzo, 1999], though during the November 'solar storm' interval the speeds may have been significantly higher. Typically, however, the wind speed lies in a range a factor of ~1.5 on either side of our nominal 500 km s^{-1} value. By comparison, changes in the IMF vector result in modulations about mean values typically by an order of magnitude in either direction, as will be demonstrated below. Most of the variability of the estimated open flux production rate will therefore be captured by employing the IMF alone together with a typical value of the solar wind speed.

4.3.2. Voltage Estimates Based on Cassini IMF Data

We now present our estimates of the dayside reconnection voltage at Saturn derived from the Cassini IMF data using Eq. (4.2) and the assumptions and approximations discussed above. Results will be shown for the same intervals as those in Figures 4.2-4.4, so that direct comparison can be made with the field data. We thus begin in Figure 4.6 by showing results for the 26-day interval from day 276 to day 301 of 2003 encompassing essentially one solar rotation, as in Figure 4.2. The top panel shows the

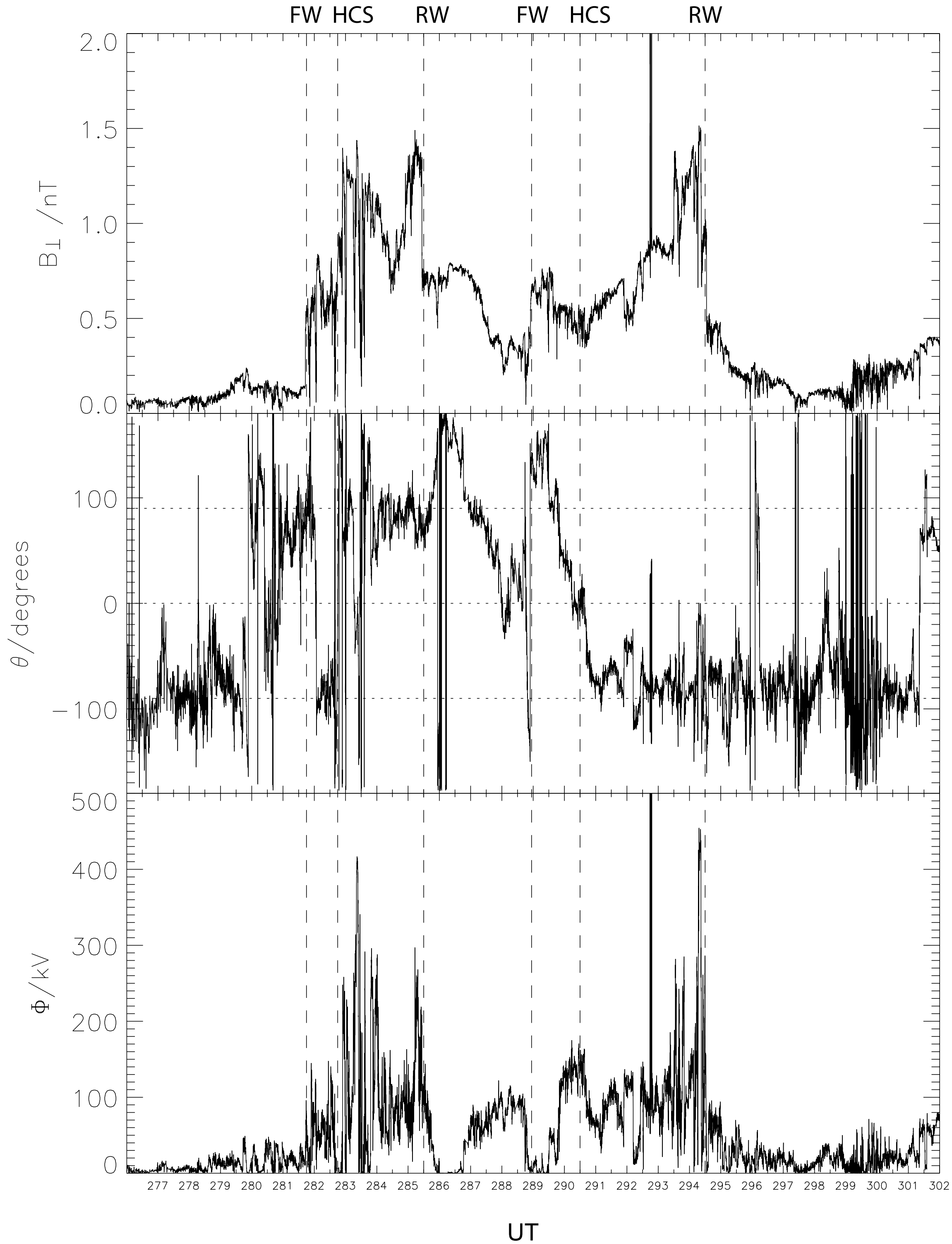

Figure 4.6: Magnetic field and voltage parameters for the interval from day 276 to 301 (inclusive) of 2003, spanning a full solar rotation, corresponding to Figure 4.2. The top panel shows the field strength $B_\perp$ perpendicular to the radial direction from the Sun, while the second panel shows the clock angle θ of the field relative to Saturn's north magnetic axis as defined in Figure 4.5. The bottom panel shows the dayside reconnection voltage Φ associated with open flux production estimated from Eq. (4.2) using the assumptions and approximations discussed in the text.

perpendicular field strength that appears in Eq. (4.2), $B_{\perp} = \sqrt{B_T^2 + B_N^2}$, which is generally very similar to the total field strength shown in Figure 4.2, since B_R is usually a modest component. The second panel then shows the clock angle of the field, θ, defined as indicated in Figure 4.5. This shows a basic pattern of behaviour associated with the sector structure (fields in the positive and negative B_T directions lying essentially at θ values of +90° and -90° respectively), upon which is superposed considerable short-term variation in both strong (as noted above) and weak field regions. The third panel then shows our estimate of the dayside reconnection voltage associated with open flux production, Φ, derived from Eq. (4.2). Broadly speaking, the voltage values follow the behaviour of the strength of the interplanetary field, with additional superposed variations due to fluctuations in the field direction.

As a consequence of the strongly varying field strength during the solar rotation, therefore, the voltage values also show strongly varying behaviour. It can be seen, for example, that there are periods of several days corresponding to rarefaction regions where the voltages remain very small indeed, ~10 kV or less, due to the presence of very weak fields. For example, over the 3-day period from day 276 to day 278 at the beginning of the interval in Figure 4.6, the averaged perpendicular field strength $B_{\perp}$ was 0.06 nT, associated with an averaged voltage of ~7 kV. More typically, however, the field strengths were somewhat higher, around a few tenths of a nT. Such values are associated with voltages of a few tens of kV, which are typically rather variable on time scales of hours and days due to changes in field strength and direction. During the 7-day period from day 295 to day 301 following the second compression interval, for example, the averaged $B_{\perp}$ was 0.19 nT, with an averaged voltage of ~21 kV. There are also few-day intervals in compression regions where the field strengths and voltages are typically much higher, the field strengths being ~0.5 to ~1.5 nT, with voltages peaking in the range ~100 to 400 kV. For example in the period from day 282 to day 284 the averaged $B_{\perp}$ was 0.81 nT, with an averaged voltage of ~94 kV. It should be noted, however, that the voltage values in the regions of highest field strength are characteristically highly variable due to the directional fluctuations noted above.

In Figure 4.7 we thus show results in the same format as Figure 4.6, but on an expanded time base for the 2-day interval corresponding to Figure 4.3, namely days 293-294 of 2003. It can be seen that the estimated voltages during this interval are typically ~100 kV, but are modulated by the field direction between values of essentially zero when the field points toward the south (i.e. when θ deflects towards -180° in the middle panel), and peaks of ~200-400 kV when the field points toward the north (i.e. when θ deflects towards zero). The time scale for such major variations is seen to be typically ~0.5-2 h, associated primarily with the variations of B_N in Figure 4.3. It can therefore be seen that the dayside magnetopause reconnection rate at Saturn will be strongly modulated in time during strong field intervals due to this effect.

In Figure 4.8 we summarise our results by showing a stacked plot of voltage values over eight solar rotations, in the same format as Figure 4.4. This plot shows a pattern of behaviour that derives basically from the pattern of IMF strength seen in Figure 4.4, but where the voltage values are now usually also strongly modulated on shorter time scales by directional field fluctuations, even in rarefaction regions where the strength of the field itself is often relatively steady. It can firstly be seen that several-day intervals of very low voltages associated with very low field strengths occur in some rarefaction regions, for example, the 4-day interval from day 247 to day 250 in the top panel where the averaged voltage is ~11 kV. Similar behaviour can also be observed from days 10 to 13 in the sixth panel, where the averaged voltage is ~4 kV, and on days 58 and 59 in the eighth panel, where the averaged estimated voltage had the extremely low value of ~1.5 kV. More usually, however, outside of the main compression regions the voltages are typically several tens of kV, often fluctuating widely with the field direction over the range ~0-100 kV on time scales of hours and days. For example, in the 5-day interval from day 225 to day 229 in the first panel, the voltage values fluctuate from essentially zero to a maximum of ~180 kV, with an averaged value of ~49 kV. Similarly, in the 4-day interval from day 353 to day 356 in the sixth panel, the voltages vary between essentially zero and ~120 kV, with an average of ~28 kV. The largest voltages then occur in the main field compression regions, though as indicated above, the values are

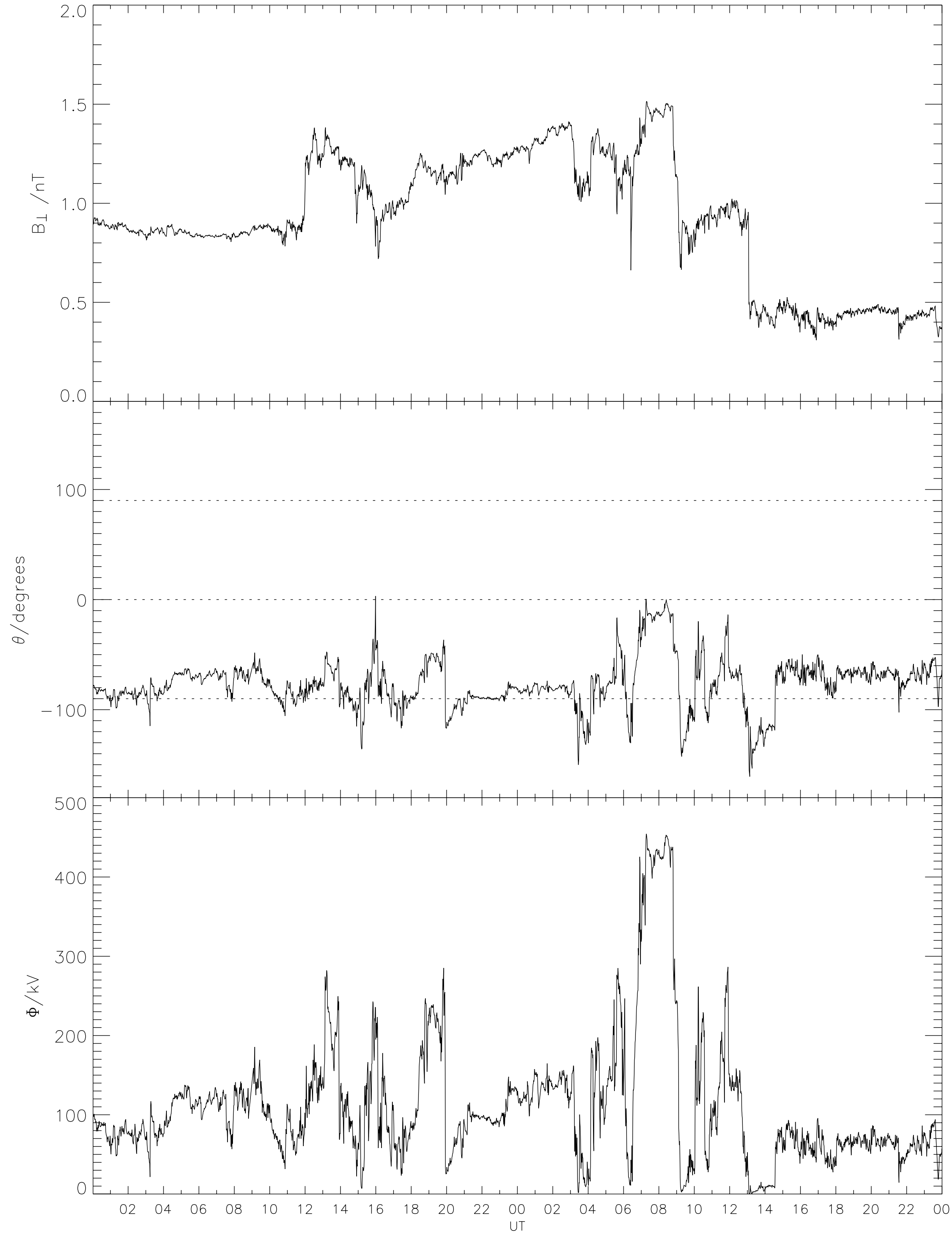

Figure 4.7: Magnetic field and voltage parameters in the same format as Figure 4.6, but plotted on an expanded time-base spanning days 293 and 294 in 2003, corresponding to Figure 4.3.

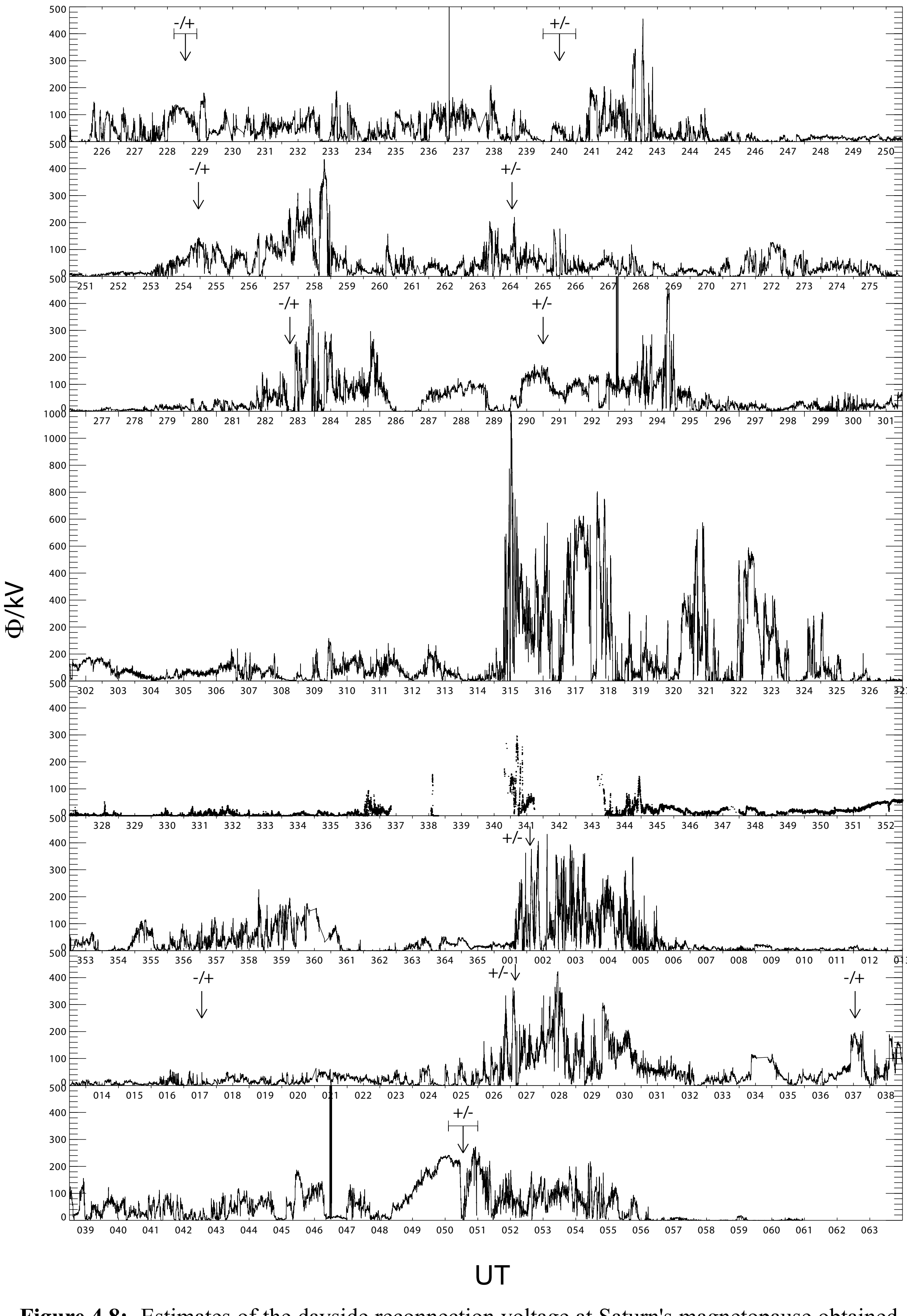

Figure 4.8: Estimates of the dayside reconnection voltage at Saturn's magnetopause obtained using Eq. (4.2) are shown versus time for the interval from day 225 of 2003 to day 63 of 2004 in a stacked plot of eight 25.5-day intervals, each corresponding to one solar rotation, in the same format as Figure 4.4.

also strongly variable in these regions due to fluctuating field directions. Values in these regions typically peak at up to ~400 kV. An example can be seen in the seventh panel of Figure 4.8, in the 4-day interval from day 26 to day 29. Here the voltages vary from small values up to ~420 kV, with an average of ~130 kV. Strong highly variable voltages are also associated with the interval of solar magnetic disturbance seen in the fourth panel of Figure 4.8. The peak voltage value during this period is ~1 MV shortly following the leading shock wave at the end of day 314, while more typically our estimated voltages peak at ~400-600 kV during the period from day 315 to day 322. However, these values are likely to be under-estimates, as the voltages were calculated from Eq. (4.2) based on a constant solar wind speed of 500 km s^{-1}, while CMEs were observed to be ejected from the Sun with speeds of ~1000-2000 km s^{-1} as indicated above. The average estimated voltage over the disturbed interval from day 315 to day 322 is ~180 kV.

Overall, we thus conclude from the results shown in Figure 4.8 that the highly structured IMF at Saturn's orbit, due both to CIRs and solar activity, will thus lead to a similarly highly structured interaction between the interplanetary medium and the planetary magnetosphere, unlike the rather more continuous IMF-modulated behaviour that occurs at Earth. Even aside from the effects of strong solar activity, however, the CIR-related variations are nevertheless seen to change in form from one solar rotation to the next. For example, sometimes only one main interval of high voltage and strong magnetospheric reconnection-associated driving occurs in a given solar rotation, as seen in the seventh panel of Figure 4.8. In other solar rotations two such intervals occur as in the sixth panel, while at other times rather more continuous behaviour is observed over a significant portion of the rotation, as in the first and eighth panels.

We conclude this section by presenting in Figure 4.9 information on the distribution of estimated voltage values obtained from Eq. (4.2). Specifically we plot histograms of the probability of obtaining voltage values in 10 kV bins between zero and 500 kV. The histogram shown by the solid line was derived from the voltage values shown in Figure 4.8 over those solar rotations for which the magnetic data are almost complete, and which show what we take to be typical behaviour, that is for panels 1-3 and 6-8,

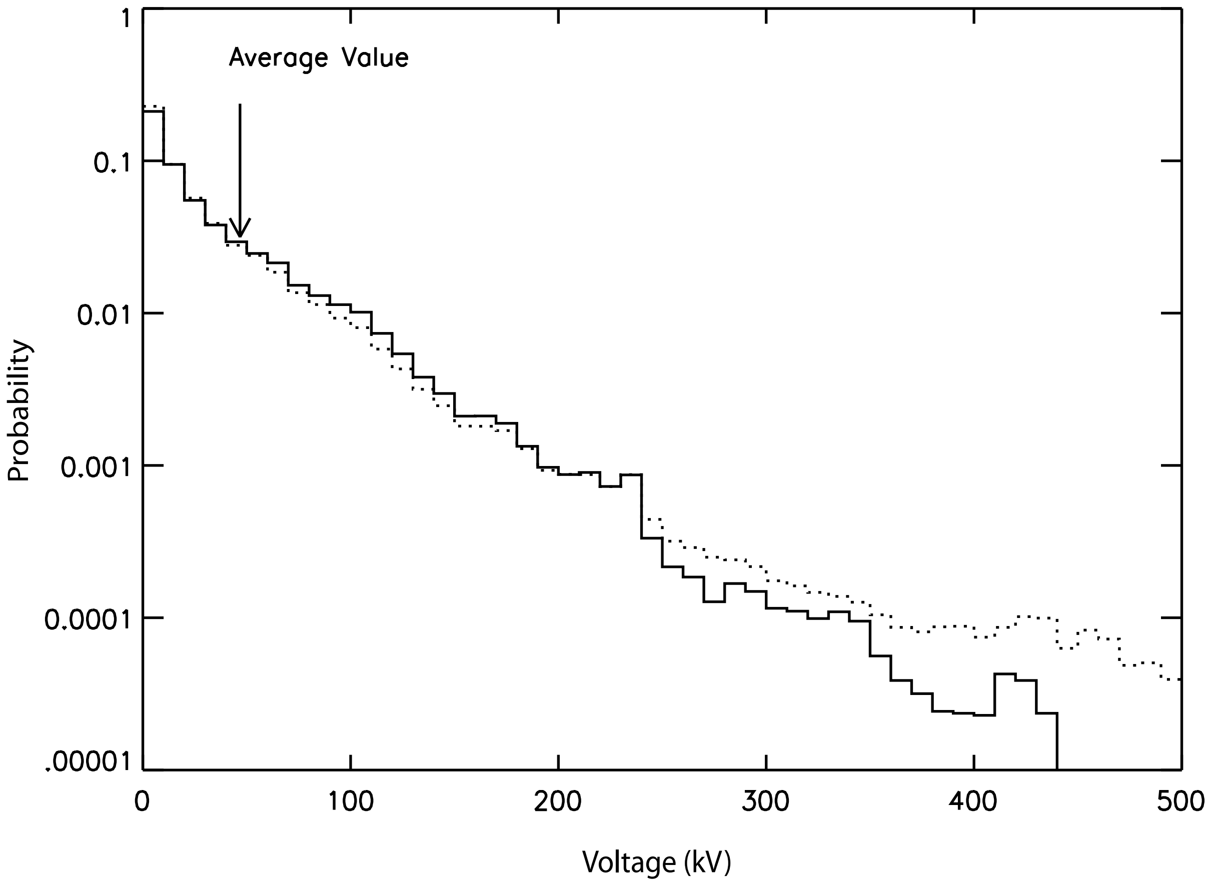

Figure 4.9: Probability histogram of dayside reconnection voltage values obtained from Eq. (4.2), shown in 10 kV bins of voltage from zero to 500 kV. The solid line includes the data shown in panels 1-3 and 6-8 of Figure 4.8, which we take to represent typical behaviour, excluding the data in panels 4 and 5. The vertical arrow shows the average of these data, equal to 46.8 kV. The dashed line then shows the histogram using all of the data from Figure 4.8, now including those shown in panels 4 and 5. The average of these data is 48.5 kV.

omitting panels 4 and 5 (the former containing the interval of solar activity and the latter large data gaps that may bias the statistics). This distribution shows an essentially monotonically decreasing probability with increasing voltage, with a peak of ~20% probability for the bin from 0 to 10 kV, and an extended high-voltage 'tail' reaching to ~400 kV. The averaged voltage over this 'typical' distribution is 46.8 kV, marked by the vertical arrow. The dashed line then shows the distribution including all the data in Figure 4.8, including that from the interval of solar activity in panel 4. The effect of the inclusion of these data is such as to elevate and extend the high-voltage tail of the distribution, above voltage values of ~250 kV. The average value over this complete data set is modestly increased to 48.5 kV.

4.4. Implications for Saturn's Magnetospheric Dynamics

4.4.1. Structure of Saturn's Magnetosphere and Typical Behaviour

In discussing the implications of the above results for Saturn's magnetospheric dynamics, we refer to the theoretical discussion of Chapter 2 which is based on the models of Cowley et al. [2004a,b]. To consider the magnetospheric implications of our voltage values, we first estimate the amount of open flux typically present in Saturn's magnetosphere, and the consequent size of the open flux region in the ionosphere. Open flux estimates have been obtained using Voyager measurements both from tail lobe magnetic field data [Ness et al., 1981], and from the closed flux content of the dayside magnetosphere out to the magnetopause [Cowley and Bunce, 2003b]. These indicate that the open flux in each tail lobe is typically ~35 GWb, such that the open-closed field line boundary maps in the ionosphere to a co-latitude of ~13° in the north and ~14° in the south if the boundary co-latitude is taken for simplicity to be independent of local time. We note that the mapping estimates made here employ the full axi-symmetric SPV model of the planetary magnetic field [Davis and Smith, 1990], such that the inter-hemispheric difference is due to the quadrupole term of the planetary field. We also assume that the operative ionospheric 'surface' lies 1000 km above the 1 bar reference spheroid of the planet [Trauger et al., 1998]. The above co-latitude values are consistent with the size of the open region depicted in Figure 2.9 of Chapter 2. They are also consistent with the typical poleward boundary of the UV aurorae, though the compilation of Hubble Space Telescope images presented by [Gérard et al., 2004], and the results of Clarke et al. [2005] and Grodent et al. [2005], indicate some variability, as not unexpected on the above physical picture.

It is interesting first of all to use the estimated size of the open flux region to also estimate the speed of anti-sunward flow on open field lines in Saturn's ionosphere (See Figure 2.9 in Chapter 2). Applying the averaged reconnection voltage of ~50 kV found above across this region, we find ionospheric transpolar flows of only ~25-50 m s^{-1}, with a transit time across the open region of ~8 (Earth) days. The reconnection-driven flows on open field lines are thus typically much slower than the rotational flows on open field lines driven by ion-neutral collisions, which correspond to ~30% of rigid corotation as indicated in Chapter 2. These rotational flows thus increase from small values near the pole to ~700 m s^{-1} at the open field boundary in the inertial frame, with a rotation period of ~1.5 days. Correspondingly, the ~300 kV voltage associated with this rotational flux transport is rather larger than that of the average Dungey-cycle flow. Typically, therefore, the Dungey-cycle flow produces only a modest modulation of the main rotational motion on open field lines. A theoretical model of such modulated flow will be presented in Chapter 6. The results derived here show that Dungey-cycle flow becomes directly competitive with the rotational flow only at the peaks of the estimated reconnection voltage of ~200-400 kV. Such voltages are associated with transpolar flows of ~100-400 m s^{-1}, and transpolar transit times of ~1-2 days (though we note from the above results that voltages typically remain at such levels only for a few hours at a time). In the interval studied here, the only interval in which Dungey-cycle flow becomes the dominant polar flow is associated with the interval of major solar activity shown in panel 4 of Figure 4.8. Peak Dungey-cycle voltages of (at least) ~1 MV during that interval produce transpolar flows of ~500-1000 m s^{-1}, and a transit time of ~10 h.

We can also use the open flux estimate above to comment on the overall nature of the substorm cycle at Saturn, based on empirical knowledge at Earth. Of course it remains uncertain at present whether impulsive substorm-like behaviour occurs at Saturn, though some indications are given in the results presented in Chapter 5. Here we will take it as a working hypothesis that this is the case. At Earth, the open flux typically present in the tail prior to expansion phase onset is a few tens of percent higher than the average amount, while tail reconnection during the substorm closes some ~40-70% of this flux [e.g. Milan et al., 2003]. If we apply these percentages to the typical ~35 GWb of open flux estimated above for Saturn, we infer that the open flux present at substorm onset will typically be ~45 GWb (corresponding to a boundary co-latitude of ~15° in the north and ~16° in the south), while the amount of open flux closed in each substorm will be ~20-30 GWb. The average time between substorms is then the average time required to accumulate such an amount of open flux in the tail, which with an average dayside voltage of ~50 kV is ~5-7 days. On this basis we thus expect 3-5 substorms to occur during each solar rotation.

A more detailed evaluation of open flux production and subsequent closure can be made with the aid of Figure 4.10, which shows the cumulative amount of open flux produced during each of the solar rotations studied above, obtained by integrating the estimated reconnection voltage values with time. These are shown in a stacked plot in a similar format to Figures 4.4 and 4.8, in which the cumulative open flux is re-set to zero at the start time of each panel. It can be seen that the estimated open flux produced during each solar rotation is almost constant at ~100 GWb, this corresponding to the averaged voltage value of ~50 kV indicated above. The estimated open flux produced during each solar rotation thus corresponds to about three times the total amount of open flux typically contained in the tail, estimated to be ~35 GWb above, such that with the above percentages of open flux closed during each substorm we typically expect ~3-5 substorms to occur during each 25.5 day rotation. The main exception occurs in the fourth panel following the interval of solar disturbance, where we estimate that ~150 GWb of open flux was produced (probably an under-estimate due to the use of the fixed solar wind speed in Eq. (4.2)). This flux corresponds to about 4 times the typical amount of open flux in the tail, and thus to 4-8 substorms, most of which apply to the disturbed interval.

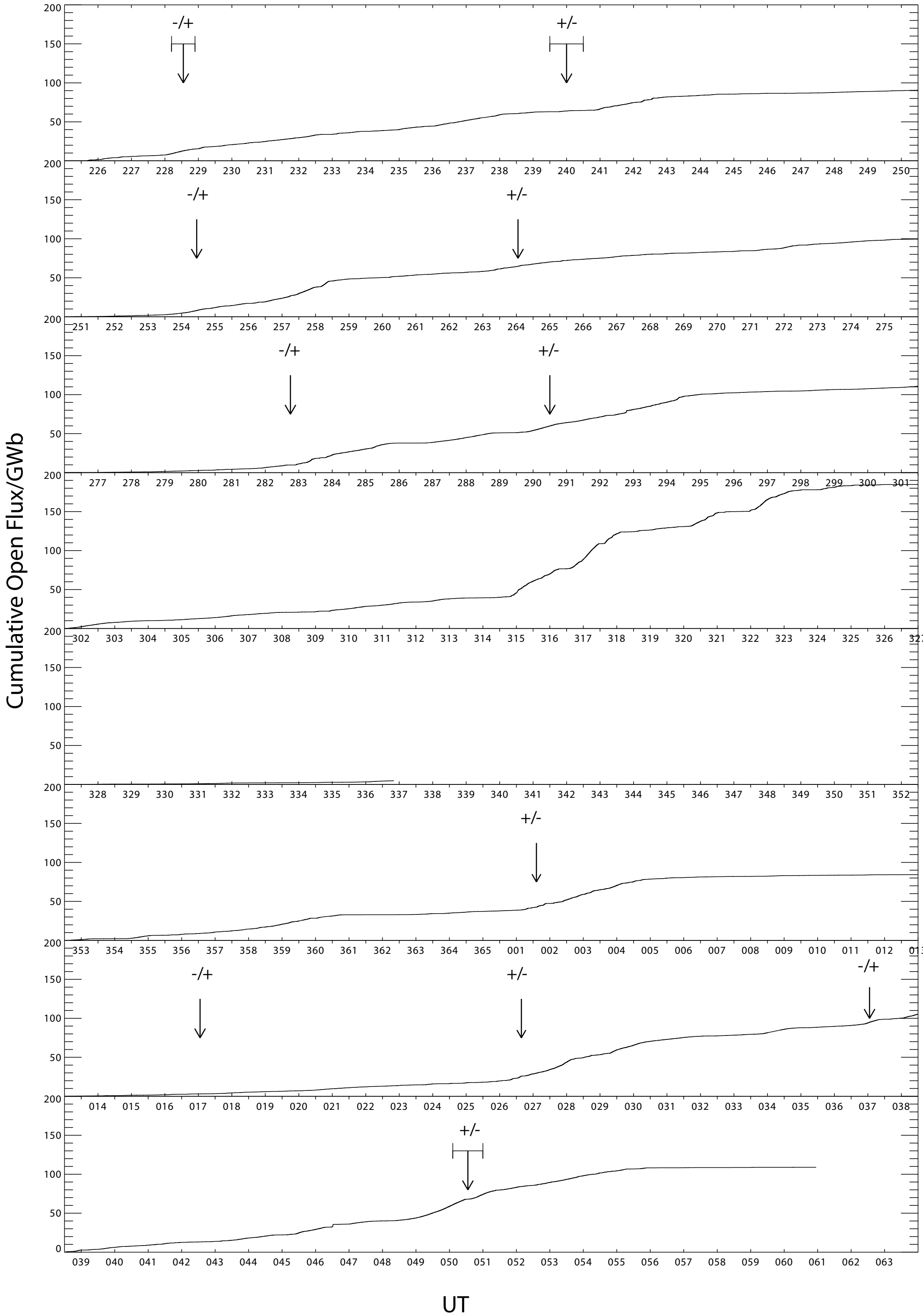

Figure 4.10: Cumulative open magnetic flux produced by reconnection at the dayside magnetopause during each solar rotation, shown in a stacked-plot format similar to that of Figures 4.4 and 4.8. The cumulative open flux is obtained by integration over the estimated reconnection voltage values obtained from Eq. (4.2) and shown in Figure 4.8. The cumulative value is re-set to zero at the start time of each solar rotation panel.

4.4.2. Variability of Solar Wind-Driven Magnetospheric Processes

In addition to this global behaviour, the results in Figures 4.8 and 4.10 also show that the dynamics of Saturn's magnetosphere will vary substantially over several-day intervals due to the strongly varying character of the interplanetary medium resulting from CIRs and solar disturbance. In the following we thus outline our expectations for the various types of interplanetary interval observed.

4.4.2.1. Weak IMF Intervals

It can firstly be seen that extended intervals occur during which the addition of open flux is essentially negligible. These correspond to the rarefaction region intervals in Figure 4.4 where the interplanetary field strength is very low, ~0.1 nT or less, such that the estimated voltages in Figure 4.8 are ~10 kV or less. An example of this behaviour occurs in the 8-day interval from days 245 to 252 of 2003 (first and second panels of Figures 4.4, 4.8, and 4.10). During this interval the averaged IMF field strength was only ~0.07 nT, resulting in an estimated voltage of only ~10 kV. The total open flux created during the whole 8-day interval is thus estimated to be only ~7 GWb (i.e. ~10 kV times 8 days). This represents a very modest inflation of the open flux content of the tail over the interval, corresponding to ~20% of the typical total content estimated above. If this flux were to be added to the above typical content (35 GWb), it is sufficient to cause the boundary to expand equatorward by only ~1.2° in the north and ~1.4° in the south over the whole interval. These estimates represent upper limits, of course, because tail reconnection could still occur at some low rate, thus simultaneously reducing the amount of open flux present. A second similar example is found in the 8-day interval from days 7 to 14 of 2004 (panels 6 and 7 of Figures 4.4, 4.8, and 4.10). In this case the averaged IMF field strength was ~0.06 nT, with an averaged estimated reconnection voltage of ~6 kV. The estimated open flux production during the interval is thus only ~5 GWb in this case, leading to a maximum boundary expansion relative to typical latitudes of ~0.9° in the north and ~1.0° in the south.

During such low-field intervals we thus expect Saturn's outer magnetosphere and tail to become quiescent with regard to Dungey-cycle processes, such that the Vasyliunas-cycle may then dominate in these regions. The amount of open flux in the system and the consequent size of the polar cap will remain almost fixed (if Dungey-cycle tail reconnection also dies away to small values), and with it the size of the auroral oval. Discrete aurorae are still expected around the open-closed field line boundary if the flow shear across it is maintained, but no dawn-dusk asymmetry will be generated by the Dungey-cycle flow in the manner mentioned above [Cowley et al., 2004a], since the latter flows will generally be negligible within the region of open flux (of order ~10 m s^{-1}). See Chapter 6 for further in-depth theoretical discussion of this. In the essential absence of magnetopause reconnection, we also expect there will be an absence of specific cusp-associated auroral phenomena near noon (see further below). It remains possible that tail reconnection could occur at modest rates during such intervals, if for example driven by open flux production during an earlier period. This would cause the region of open flux and surrounding aurorae to contract with time, signalled by an auroral enhancement and poleward motion on the nightside. However, the occurrence of substorms driven by the low-level trickle of open flux into the tail lobes during such intervals seems unlikely from the above flux estimates.

4.4.2.2. Intervals of Intermediate IMF Strength

Although intervals of very low field strength and very low reconnection voltage are not uncommon during the ~6.5 month period studied here, it can be seen from Figures 4.4 and 4.8 that field strengths are more commonly rather higher, say typically in the range ~0.2-0.8 nT. Such values apply to a number of intervals which follow major compression regions, as well as to some of the intervals surrounding HCS crossings in which the field strengths were not strongly elevated. The estimated reconnection voltages associated with open flux production during such intervals typically fluctuate strongly on time scales of hours and days as the field direction changes, from small values when the field points south, to peaks of ~150 kV when the field points north. Overall, however, Figure 4.10 shows that such intervals are associated with a steady significant accumulation of open flux in the system, with averaged estimated voltages of several tens of kV. For example, if we consider the 8-day interval from day 231 to 238 in the first panel of Figures 4.4, 4.8, and 4.10, we find an averaged field strength of ~0.60 nT, and an averaged reconnection voltage of ~56 kV, a little higher than the overall average value. This then implies the production of ~41 GWb of open flux during the interval, a little larger than the typical total open flux content of the system, and sufficient to drive ~2 substorms according to the above estimates. If such an amount of open flux were to be added to the typical value of ~35 GWb without exciting tail reconnection, it would cause the open-closed field line boundary to expand equatorward very noticeably from ~13° to 19° co-latitude in the north, and from 14° to 21° in the south. As a second example we may take the 8-day interval from day 40 to 47 of 2004 (bottom panel of the figures), in which the averaged field strength is ~0.55 nT, and the averaged estimated voltage is ~49 kV. The latter value implies a total estimated production of open flux of ~34 GWb during the interval, a little less than in the previous example, but which would again result in a substantial expansion in the region of open flux if no substorms occur, from ~13° to 18° co-latitude in the north and from 14° to 20° in the south.

Overall, we thus expect such intervals of intermediate IMF strength will be characterised by intermittent excitation of Dungey-cycle flow driven from the dayside, which Figure 4.8 indicates will last typically for intervals of a few hours to a few days, depending on the directional variations of the IMF. Ionospheric flow speeds on open field lines will typically be ~25-50 m s^{-1} (giving a transpolar transit time of ~8 days as indicated above), peaking at ~75-150 m s^{-1}, thus now producing some dawn-dusk modulation of the circulatory flow driven by ion-neutral collisions, and with it, dawn-dusk modulation of the boundary auroral currents. In addition, we also expect that magnetopause reconnection will produce localised flow perturbations near the open-closed field line boundary on the dayside, which will also modulate the boundary currents (See Chapter 6). The upward current will be enhanced in the pre-noon sector and reduced or reversed in the post-noon sector, thus producing specific auroral features associated with the dayside 'cusp', as recently discussed for Jupiter by Bunce et al. [2004], and for Saturn by Bunce et al. [2005c]. This description applies to intervals when the IMF points northward, such that the cusp is associated with open flux production and the excitation of 'normal' Dungey-cycle flow, as shown in Figure 2.9 of Chapter 2. During intervals of southward IMF, however, when the estimated reconnection voltage associated with open flux production given by Eq. (4.2) is small, lobe reconnection may then occur at rates which may not be dissimilar, as mentioned in Section 4.3.1, and as also modelled by Bunce et al. [2005c]. This will superpose 'reverse' Dungey-cycle flow (and related field-aligned currents) on the circulation within the region of open flux, such that cusp emission may then appear just inside the boundary near noon, as observed at Earth [Øieroset et al., 1997; Milan et al., 2000]. In addition to these auroral effects, the loading of the system with open flux during northward IMF intervals at overall rates corresponding to several tens of kV is also expected to lead to the excitation of tail dynamics on few-day intervals. With averaged reconnection voltages of ~50 kV, we would expect one substorm every 5-7 days if each is associated with the closure of ~20-30 GWb as estimated above.

4.4.2.3. Strong-field IMF Compression Regions

The third type of interval which is commonly present corresponds to the high-field intervals associated with CIR compression regions. These have shorter durations than those discussed above, typically 2-4 days, but contain stronger fields in the range ~0.5-2 nT, which produce larger reconnection voltages leading to rapid accumulation of open flux in the system. As pointed out in Section 4.2.2, however, these high fields also fluctuate strongly in direction on times scales of several tens of minutes to a few hours, thus producing voltage values which similarly fluctuate strongly during the few-day strong-field intervals, from small values up to peaks of ~400 kV. In some cases the highest field strengths and voltages span the interval containing the crossing of the HCS, it being noticeable in Figure 4.10 that the HCS crossings often occur near the beginning of an interval of rapidly increasing open flux. In other cases the highest fields occur in the few-day intervals following the crossing. An example of the latter behaviour occurred following the HCS crossing on day 254 of 2003 in the second panel of Figure 4.4. If we then take the 4-day interval from day 255 to 258 following the crossing, we find an averaged field strength of ~0.9 nT, and an averaged voltage of ~109 kV. The total open flux produced during the interval is thus estimated to be ~38 GWb, as seen in Figure 4.10, similar to the open flux produced during the 8-day intervals of intermediate field strength discussed above, and comparable to the total open flux typically contained within the tail. A second example, in which the region of high field strength straddled the HCS crossing, occurred in the 4-day interval from day 01 to day 04 of 2004 (sixth panel of Figures 4.4, 4.8, and 4.10). The averaged field strength during the interval in this case was ~1.1 nT, with an averaged reconnection voltage of ~115 kV, such that the open flux added to the tail over the 4-day interval is estimated to be ~40 GWb.

Typically, therefore, we find that the averaged voltages during these compression intervals are twice to three times the global average, leading to typical ionospheric Dungey-cycle flows in the region of open flux of 50-100 m s^{-1}, peaking at ~200-400 m s^{-1}, sufficient to produce significant dawn-dusk modulation of the auroral currents at the open-closed field line boundary, as examined in Chapter 6. Pronounced ‘cusp’ auroral signatures of dayside reconnection are also expected in the vicinity of noon during these intervals, as described above. The open flux produced over their ~4-day durations is comparable to that generated over the above 8-day intervals of intermediate field strength, as modelled by Bunce et al. [2005c], and corresponding approximately to the typical total open flux content of the tail, and about a third to a half of that produced during the whole of one solar rotation. As previously indicated, addition of such quantities of open flux to the tail lobes is sufficient to create a significant expansion of the open-closed field line boundary over the interval, and to excite one or two substorms.

4.4.3. Synchronism of Reconnection-Related and Compressive Effects

The above sub-sections summarise our inferences drawn directly from the Cassini measurements of the IMF. It should not be forgotten, however, that the CIR-related variations in the IMF will be accompanied by related changes in the solar wind dynamic pressure as indicated in Section 4.2.1, producing synchronised compressions and expansions of the magnetosphere that may also play a role in the solar wind-driven magnetospheric dynamics. We note in particular that the intervals during which the field strengths and reconnection voltages are the highest are initiated by the forward shocks of CIR compression regions, across which the dynamic pressure of the solar wind is expected to strongly increase, resulting in a sudden compression of the magnetosphere.

At Earth, such compressions have been found to give rise to a number of significant magnetospheric effects, including major enhancements in particle precipitation and currents [e.g. Zhou and Tsurutani, 2001; Liou et al., 2003], and the stimulation of rapid flux closure in the tail [e.g. Petrinec and Russell, 1996; Boudouridis et al., 2003; Milan et al., 2004]. In the interval studied by Milan et al. [2004], for example, a shock-induced compression of the terrestrial magnetosphere was found to be followed by a large substorm in which very nearly all of the open flux in the system was closed over a ~1 h interval. If such events are triggered by the CIR-related forward shocks at Saturn, as discussed by Cowley et al. [2005a] in relation to the HST auroral data obtained by Clarke et al. [2005], then they will also act to modulate the amount of open flux in the system, and to synchronise the pattern of growth and collapse of the tail to the interplanetary CIR structure. Suppose, for example, that the sudden compression associated with the forward shock of a CIR results in the rapid closure of a significant proportion of the open flux in the magnetosphere, thus causing the aurorae to contract significantly poleward. According to the above estimates, the dayside reconnection occurring during the subsequent ~4-day strong-field region is then generally sufficient to re-inflate the open flux in the tail back to typical values, thus expanding the auroral oval back to its typical size. If the IMF strength subsequently drops to very low values (e.g ~0.1 nT or less), as it does in some of the following rarefaction regions discussed above, then open flux production will effectively cease irrespective of the direction of the IMF. The subsequent propensity for tail reconnection and substorms may also be reduced by the concurrent drop in solar wind dynamic pressure and consequent magnetospheric expansion. In such circumstances the open flux in the system will then remain essentially constant and the auroral oval of fixed size until the next compression event, unless low-level tail reconnection causes slow contraction. If, on the other hand, the compression region is followed by an extended interval of intermediate IMF strengths (e.g. a few tenths of a nT), as also commonly occurs, then the tail will continue to inflate after the compression interval at a reduced but still significant rate, until 'internally-driven' (i.e. non-shock induced) substorms occur. Typically we may expect substorms to occur every ~5-7 days under such circumstances. The next compression region may then trigger another sudden reduction in open flux, thus re-initialising the sequence.

4.4.4. Effects Associated with Strong Solar Activity

We finally comment briefly on the effects produced by solar activity, as observed here during the ~10-day interval between days 315 and 324 of 2003. We note, however, that the related solar flares and CMEs were of unusually large intensity during this interval, such that the observed effects may not represent typical behaviour. It can be seen from Figure 4.4 that the interval identified was characterised by almost continuously enhanced interplanetary field strengths, leading to the strongly enhanced voltages seen in Figure 4.8. As can be seen in Figure 4.10, the open flux produced during the interval is thus estimated to have exceeded ~140 GWb, this representing four times the typical total amount of open flux in the tail, sufficient to drive an expansion in the region of open flux in the ionosphere from small values to a co-latitude of ~30°. Clearly we expect that major magnetopause and magnetotail dynamics were excited during this interval.

4.5. Summary

In this chapter we have examined the IMF data obtained by the Cassini spacecraft during its approach to Saturn in the second half of 2003 and early 2004, and have used them to infer the nature of the reconnection-mediated interaction between the interplanetary medium and Saturn's magnetosphere at a heliospheric distance near 9 AU. Unlike the data obtained in this vicinity by previous fly-by spacecraft, which encountered the planet during the maximum phase of the solar activity cycle, these data encompass eight solar rotations during the declining phase of the solar cycle. As expected from previous observations under these conditions, particularly by the Ulysses spacecraft at distances out to ~5 AU, it is found that the near-equatorial IMF at ~9 AU is a strongly variable medium, being highly modulated during each solar rotation by CIR-related compression and rarefaction regions. Specifically, the observed IMF pattern consisted of two sectors, with the HCS crossings usually embedded within higher-field compression regions typically of few-day duration at the spacecraft, separated by lower-field rarefaction regions lasting typically for longer several-day intervals. This pattern is as expected for the declining phase of the solar cycle, associated with a tilted dipole field structure at the Sun. However, during November 2003 the usual CIR-related pattern was found to be disrupted by a period of intense solar activity.

We have then employed these data to estimate the strength of the reconnection-mediated interaction between the interplanetary medium and Saturn's magnetosphere. Specifically we have estimated the reconnection voltage at Saturn's dayside magnetopause associated with open flux production, using an empirical formula adapted from related studies at Earth. The results indicate that the structuring of the IMF into several-day intervals of strongly differing field strength will produce corresponding temporal structuring in the interaction between the interplanetary medium and Saturn's magnetosphere, forming several-day intervals with very different types of behaviour. Within these intervals, considerable sub-structuring also occurs on time scales ranging from tens of minutes to hours and days, due to the strong north-south variability in the direction of the field. Integration over these variations shows that the open flux produced in one few-day compression region with field strengths ~0.5 to ~2 nT is ~30-40 GWb, comparable to the typical total amount of open flux estimated to be present in Saturn's magnetosphere. Similar amounts of open flux can also be more slowly accumulated over several-day intervals during which IMF strengths remain at more typical values of a few tenths of a nT. However, several-day intervals can also occur in rarefaction regions in which the field strength remains ~0.1 nT or less. In this case only small amounts of open flux will be produced, of order a few GWb. Overall, the open flux produced in each ~25 day solar rotation is estimated to be ~100 GWb, about three times the typical total amount of open flux present in Saturn's magnetosphere, and corresponding, for example, to the flux produced in two few-day compression regions, plus one several-day region of intermediate field strength, plus one several-day rarefaction region of low field strength. We would emphasise, however, that not all solar rotations are structured in this way, and that some are more highly structured in terms of variable field strength and voltage than others.

The total estimated open flux produced over each solar rotation is nevertheless found to remain roughly constant at ~100 GWb, corresponding to an averaged reconnection-associated voltage of ~50 kV. Assuming that substorms occur in Saturn's tail, and that each one closes ~20 GWb of open flux (~60% of the amount typically present), the implication is that about five substorms occur during each solar rotation, at an averaged interval of ~5-7 days. However, we also point out that the dynamic pressure of the solar wind will be strongly correlated with the interplanetary field strength, thus producing a pattern of magnetospheric compressions and expansions which are synchronised with the field variations. Sudden shock-related compressions at Earth are known to induce the onset of tail reconnection, leading to the rapid closure of open tail lobe flux. If the same happens at Saturn, then sudden reductions in open flux may typically occur at the passage of the forward shocks which lead the subsequent regions of compressed interplanetary field. The open flux produced during the subsequent compression regions may then serve to re-inflate the open field region back to its typical size. In the subsequent rarefaction region after the compression, the interplanetary field may then drop to very low values such that reconnection-driving becomes negligible, and the magnetosphere enters a quiescent state dominated by internally-driven processes until the next shock compression. On other occasions, however, the interplanetary field strength may remain at higher values following the main compression region, leading possibly to a series of substorms at several-day intervals prior to the next shock-induced interval of flux closure. Estimates of open flux production during the period of major solar activity indicate the excitation of major solar-wind induced magnetospheric dynamics during the interval.

Chapter 5

Interplanetary conditions and magnetospheric dynamics during the interval spanning the Cassini orbit insertion fly-through of Saturn's magnetosphere

5.1. Introduction

Prior to the arrival at Saturn of the Cassini spacecraft on 1 July 2004, the primary source of information concerning the dynamics of Saturn's magnetosphere and its interaction with the solar wind has been from remote sensing studies of the planet's radio emissions, specifically of Saturn kilometric radiation (SKR). SKR is discussed in detail in Section 2.8 of Chapter 2. Variations in the emissions can be used as a remote diagnostic of both rotational and solar wind driven dynamics.

In January 2004, a campaign of simultaneous Hubble Space Telescope (HST) UV imaging of Saturn's aurora and Cassini spacecraft measurements of the interplanetary medium upstream of Saturn was undertaken. This included concurrent measurements of the solar wind and interplanetary magnetic field (IMF), together with observations of SKR emissions. The results of this study are outlined in Section 2.7 of Chapter 2, and show that Saturn's aurorae respond strongly to the magnetospheric perturbations associated with corotating interaction region (CIR) compressions in the interplanetary medium [Clarke et al., 2005; Crary et al., 2005; Grodent et al., 2005; Bunce et al., 2005b]. Following a compression, the auroral oval at dawn was observed to expand significantly poleward via the intrusion of bright emissions into the polar region, after which the aurorae evolved over ~30 h into a bright 'spiral' form extending from the nightside via dawn into the post-noon sector. Bursts of SKR were also shown to be associated with these compression-induced auroral effects [Kurth et al., 2005], thus corresponding to the solar wind dynamic pressure modulation found previously by Desch [1982] and Desch and Rucker [1983]. A theoretical description of these auroral and SKR effects is given in Cowley et al. [2005a], and outlined in Chapter 2 in some detail.

The principal purpose of this chapter is to discuss observations of magnetic fields and SKR emissions which were obtained during the first 'Saturn orbit insertion' (SOI) fly-through of Saturn's magnetosphere by the Cassini spacecraft in June-July 2004. First, however, we examine data from a portion of the January 2004 HST-Cassini campaign interval, specifically that showing the response of the SKR emissions and UV aurorae to a CIR-related compression region and embedded heliospheric current sheet (HCS) crossing. We next examine the IMF data preceding and following the SOI fly-through and study the pattern of compressions and rarefactions, calculating the total amount of open flux produced per solar rotation from the empirical formula for the reconnection voltage outlined in Chapter 4. We next show that a CIR compression region and HCS crossing of a similar nature to that in January is expected to have impinged on Saturn at some time during the fly-through. The anticipated HCS crossing is confirmed by examination of the IMF data surrounding the fly-through. We then examine the SOI fly-through data itself and show that similar SKR bursts were observed on the outbound pass as were observed during the HST campaign interval, which we thus link to the arrival of the expected CIR compression at Saturn. Finally, we make an initial examination of magnetic field data observed in the pre-dawn nightside magnetosphere concurrently with the first major burst of SKR, and show that the field signature is consistent with the injection of hot plasma at the spacecraft, presumably originating further down the tail. We discuss the implications of these results in relation to the January 2004 HST campaign data, and theoretical ideas on Saturn's solar wind-driven magnetospheric dynamics proposed by Cowley et al. [2005a].

5.2. SKR and IMF Measurements During the January 2004 HST-Cassini Campaign

We begin with an overview of a portion of the data from the January 2004 HST-Cassini campaign, which shows the response of the SKR emissions and Saturn's aurorae to a CIR compression region and embedded HCS crossing. The discussion given here extends and complements that provided previously by Clarke et al. [2005], Crary et al. [2005], and Kurth et al. [2005].

Figure 5.1 spans the interval from day 24 to 30 of 2004. The bottom panel shows the magnitude of the magnetic field measured by the Vector Helium Magnetometer (VHM) instrument on Cassini, as discussed in detail in Chapter 3. During the interval shown, the spacecraft was located ~0.2 AU upstream of Saturn in the radial direction, and was also displaced from the planet-Sun line by ~0.5 AU toward dawn. At the beginning of the interval, the IMF strength was relatively low at a few tenths of a nT, corresponding to a CIR rarefaction region. At ~16 UT on day 25 a sudden increase in the field strength was observed, indicative of the arrival at the spacecraft of the forward shock of a CIR compression region, marked in the lower panel by the vertical arrow labelled 'S'. At ~15 UT on day 26 a crossing of the HCS took place, indicated by the vertical arrow marked with a '+/-' symbol. This indicates the time of an enduring reversal of the B_T (azimuthal) component of the IMF in RTN co-ordinates, from positive to negative. For the present solar cycle, the '+/-' symbol represents a crossing of the HCS from a 'toward' to an 'away' sector, which is, as usual, embedded within an early interval of the compression region, as described in Section 1.4 of Chapter 1. The declining phase of this compression began on day 28, such that by day 30 the field was almost back to rarefaction region conditions with IMF strengths of ~0.5-0.7 nT. Overall, the compression region was of ~4 days duration.

The top two panels of Figure 5.1 provide information about the SKR emissions obtained from the Radio and Plasma Wave Science (RPWS) instrument on Cassini, the specifics of which are discussed in detail in Chapter 3. The SKR data in the top panel show the sum of the powers in left-hand (LH) and right-hand (RH) circularly polarised radio waves in two frequency bands, namely 100-300 kHz (solid line) and 4-1000 kHz (dashed line), though for the present data set the power is strongly dominated by LH emissions. LH polarisation corresponds to cyclotron emission from the southern polar region of the planet, which was directed towards the Sun and Cassini during the period of interest. The power detected at the spacecraft has been corrected for distance from Saturn using an inverse square law, assuming for simplicity a source at the centre of the planet. The power is then shown in the form of radio power per steradian (W sr^{-1}) in the top panel of Figure 5.1, using a log scale. The power has also been averaged (at 10 min resolution) over a sliding 1 h window. The second panel shows a frequency-time spectrogram over the same interval, covering the frequency band from 4 kHz to 1 MHz, colour-coded according to the scale to the right of the plot.

To understand the relationship between the SKR and IMF data, the propagation delays to and from the planet must first be considered. While the SKR propagation time from the planet to Cassini is only a few minutes at the speed of light, and is thus insignificant, appreciable propagation delays occur for the interplanetary medium. Specifically, using an average solar wind speed of 500 km s^{-1}, the radial propagation delay from Cassini to Saturn is ~17 h. As discussed previously by Crary et al. [2005], this timing is unavoidably uncertain to within a few hours, due particularly to non-radial propagation effects and the separation of the spacecraft and planet in heliographic longitude. For disturbances aligned along the nominal Parker spiral direction, for example, the expected propagation delay would be of order ~12 h. However 17 h is used here for simplicity and commonality with previous discussion [Clarke et al., 2005; Crary et al., 2005; Bunce et al., 2005b].

At the beginning of the interval, the SKR conditions were quiet, the data showing modulations near the planetary rotation period, as observed previously by Voyager [e.g., Kaiser et al., 1984]. To demonstrate this, we have marked the initial peaks observed in the power plot and spectrogram by vertical arrows in the middle panel, separated by fixed intervals of 10.75 h (the SKR period according to Gurnett et al. [2005]), and have

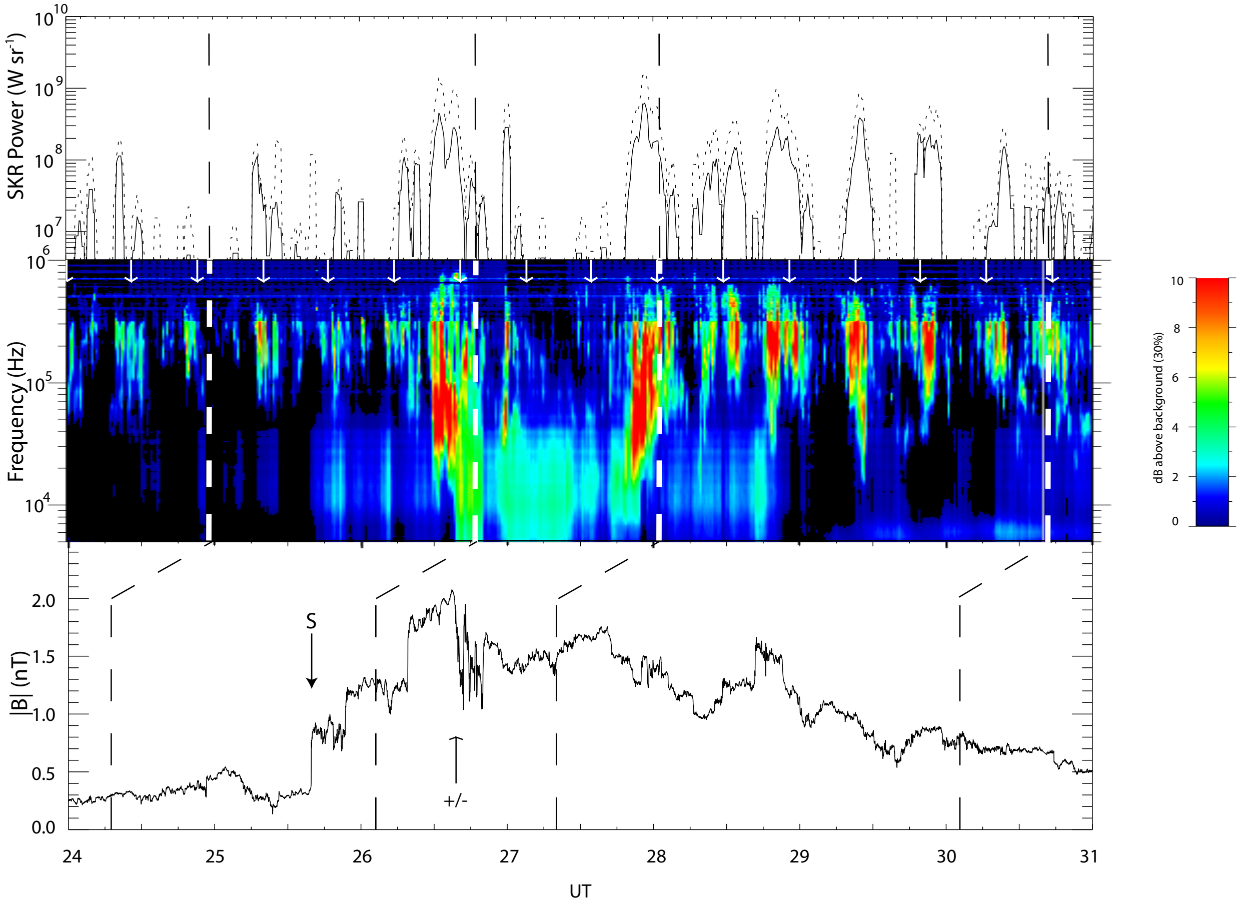

Figure 5.1: Concurrent Cassini SKR and magnetic field data from a portion of the HST-Cassini campaign in January 2004, for the interval from 24 to 30 January. The top panel shows the inverse-square corrected power of the sum of LH and RH circularly polarized radio waves, where the solid line shows the power in the 100-300 kHz frequency band and the dashed line shows the power in the 4-1000 kHz band. The data are computed every 10 min but are averaged over a 1 hour sliding window. The middle panel shows the corresponding frequency-time spectrogram covering the whole frequency band from 4 to 1000 kHz, colour-coded according to the bar on the right-hand side. The vertical arrows are shown at fixed intervals of 10.75 h and phased with respect to the peaks in the periodic emission observed near the beginning of the interval. The bottom panel shows the simultaneous magnitude of the IMF strength observed by Cassini. The vertical dashed lines in the top 2 panels correspond to the times of the HST images in Figure 5.2, with a 64 min shift to account for the time of light travel from Saturn to Cassini (SKR) and to the HST (auroral images). The dashed lines in the bottom panel have then been shifted by 17 h to represent the nominal solar wind propagation delay from Cassini to Saturn.

continued this across the full width of the plot in order to examine the phasing of the subsequent bursts of emission. On day 26 at ~12 UT, however, the onset of intense SKR emissions was observed with a spectrum that spreads to lower frequencies, and with peak powers reaching ~1×10^{9} W sr^{-1} [Kurth et al., 2005]. We note from the vertical arrows that this sudden onset occurred at a time when a minimum in power was expected according to the previous phasing of the planetary modulation. This burst occurred ~3 h after the expected arrival of the forward shock of the CIR compression at Saturn according to the above 17 h time delay. Following this burst, the usual planetary modulation as observed by Cassini was disrupted for at least two cycles. A brief burst was observed at the end of day 26, some ~40 h after the arrival of the shock, and again near an anticipated minimum, following which the SKR power remained continuously weak for an interval of ~19 h, i.e. for almost two planetary rotations. This interval straddles the initial compression region interval containing the HCS crossing. Kurth et al. [2005] note, however, that the Unified Radio and Plasma wave experiment onboard the Ulysses spacecraft detected SKR during this interval of apparently weak emissions. They suggest that the beaming was disrupted in some way after the first strong burst, such that the following emissions could not be seen by Cassini. A second burst of high SKR power as observed by Cassini then began at ~19 UT on day 27, again extending to low frequencies, with peak powers of ~1.5×10^{9} W sr^{-1} (over the full frequency band), and lasting for ~8 h. This burst again began near the time of an anticipated SKR minimum according to the phasing of the previous modulation, and occurred towards the end of the main high-field compression region interval. Following this second intense burst, the SKR power and frequency range subsequently diminished, while the planetary modulation re-emerged with the same phasing (but higher power) as that observed prior to the CIR-related disruption, as indicated by the arrows in the middle panel. This interval corresponded to the declining phase of the CIR compression.

We now examine four concurrent images of Saturn's UV aurora, (*i*) to (*iv*), taken by the Space Telescope Imaging Spectrograph (STIS) on the HST (the operation of which is described in Chapter 3), shown in Figure 5.2. In these images the entire southern auroral oval is visible, due to the 26° tilt of Saturn at this epoch. These frames have been generated by combining individual images obtained on a given HST orbit in the RGB colour system. For each date, the frame includes clear images (blue), F25-SRF$_2$ filtered images (red), and the mean of all images (green), with a total exposure time of ~50 min (the centre times being given in the figure caption). This leads to nearly 30° of rotational blurring for any feature that rigidly corotates with the planet, but distinguishes auroral emissions from reflected sunlight from the disc and rings by their respective blue and red colours. Each frame has a log stretch in intensity, identical for each day, with the upper threshold set to a value of ~20 kR to emphasize the faint emissions.

The vertical dashed lines through the top two panels of Figure 5.1 indicate the timing of the four auroral images relative to the SKR data. The time taken for light to travel between Saturn and Cassini during this interval was ~4 min, and between Saturn and the HST ~68 min, and the lines have been shifted to earlier times accordingly. Similarly, in the bottom panel, the timing relative to the IMF is indicated by a further shift of 17 h. It can thus be seen that HST image (*i*) relates to the rarefaction conditions seen at the beginning of the bottom panel of Figure 5.1, during the interval of weak planetary-modulated SKR. It shows a 'quiet' auroral oval, with some enhancement in intensity on the dawn (left-hand) side. Image (*ii*), taken ~9 h after the expected arrival of the shock at Saturn, and towards the end of the first intense burst of SKR, shows the effect of the onset of the CIR compression on the aurora. The auroral power had increased by a factor of three from the mean over 8-24 January, with the dawn side oval being completely filled with bright UV emissions, implying active precipitation over the entire dawn side of the polar cap [Clarke et al., 2005]. According to Cowley et al. [2005a], this is an early effect of the onset of tail reconnection triggered by the sudden CIR compression of the magnetosphere. HST image (*iii*) corresponds to an interval ~40 h after the arrival of the shock, still within the main compression region, but some hours after the peak fields had arrived at Saturn, and towards the end of the second intense SKR burst. The image shows a pronounced spiral form which is brighter in the dawn sector, and with a central roughly circular dark region. According to Cowley et al. [2005a], such forms result from the rotational transport around the planet of hot plasma injected into the outer nightside magnetosphere from the tail. The final image, (*iv*), corresponds to an interval towards the

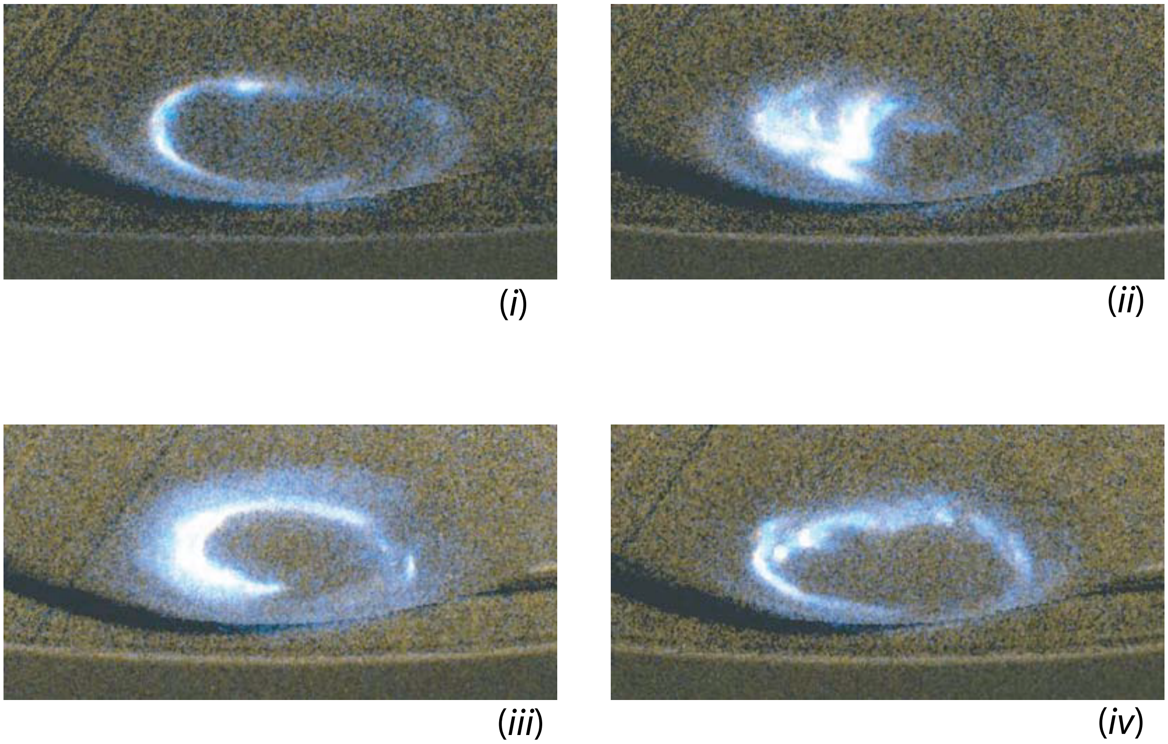

Figure 5.2: Four UV images of Saturn's southern polar aurora obtained by the STIS instrument on the HST during the interval shown in Figure 5.1. The noon-midnight meridian is near the centre of each frame with noon toward the top, dawn to the left, and dusk to the right. Clear and filtered images from a given HST orbit have been combined in the RGB colour system, the total integration time in each frame being ~50 min. The approximate midtimes of the intervals are as follows: (i) 2351 UT on 24 January, (ii) 1903 UT on 26 January, (iii) 0128 on 28 January, and (iv) 1902 UT on 30 January.

end of the compression region where we note that a near-continuous auroral oval had reformed with a central dark polar region, expanded compared with image (*iii*), and with considerable brightness variations in the dawn sector. Overall, we note from this data that in response to a CIR-related compression of Saturn's magnetosphere we observe high-power bursts of SKR that disrupt the pre-existing pattern of planetary-modulated emission, the latter gradually being re-established over the following 2-3 days. Bright auroral displays are observed simultaneously, which are indicative of hot plasma production in the nightside magnetosphere, followed by rotational transport around the outer magnetosphere via dawn to the dayside and beyond.

5.3. Cassini IMF Data Surrounding the SOI Fly-Through

We now wish to consider the interplanetary conditions which prevailed during the Cassini SOI fly-through of Saturn's magnetosphere. However, we begin by considering the structure of the heliosphere in the months while Cassini was approaching the planet, and then in the solar rotations surrounding SOI.

5.3.1. Structure of the Heliosphere During the Approach Phase to Saturn

The structure of the heliosphere during the Cassini approach phase to Saturn has been discussed in Chapter 4, based on observations of the IMF obtained upstream from Saturn during a 6.5 month interval from August 2003 (when magnetic data-taking became almost continuous) to March 2004. It is useful here to consider the subsequent 5 month interval from March to August 2004, encompassing a further six solar rotations. This interval spanned the Cassini SOI fly-through of Saturn's magnetosphere, which occurred on 1 July 2004 [e.g., Dougherty el al., 2005].

Results for the IMF strength, reconnection voltage, and cumulative open flux are shown in Figs. 5.3-5.5, respectively, each consisting of a stacked plot of six panels, with each panel corresponding to one 25.5 day solar rotation. Carrington longitude decreased from ~360° at the beginning of each panel to ~0° at the end. The overall interval covered in each figure is days 64-216 in 2004 (4 March-3 Aug), thus immediately following the interval discussed in Chapter 4, and encompassing SOI and one solar rotation after it. The format is the same as in Chapter 4, so that results can be simply compared. At the beginning of the first panel, the spacecraft was inbound towards the planet at a radial distance of 3,719 R_S and a local time of 8.4 h. The Cassini Saturn fly-through occurred in the fifth panel, with closest approach to the planet on day 183 (1 July) marked by the light vertical dashed line. Intervals containing bow shock and magnetopause encounters are indicated by the horizontal lines labelled 'BS' and 'MP' in the fifth and sixth panels. However, data in regions identified as magnetosheath and magnetosphere have been omitted from these plots. By the end of the interval shown in the sixth panel, the spacecraft had receded to a distance of 132 R_S on its outbound trajectory at a local time of ~5.5 h. The vertical arrows in the plots show crossings of the HCS, with horizontal bars indicating where either a gradual or multiple crossing took place. These were determined by examining the vector field in RTN co-ordinates, and show specifically where reversals in the B_T field component took place, from positive to negative (+/- symbol), or from negative to positive (-/+ symbol).

Returning to Fig. 5.3, it can thus be seen that, as in the interval studied in Chapter 4, the IMF generally consisted of two principal sectors during this interval, consistent with a tilted solar dipole, with HCS crossings generally embedded within few-day higher-field compression regions, and with several-day lower-field rarefaction regions occurring between. These data thus confirm that the structure of the interplanetary medium during the interval spanning the first Cassini fly-through of Saturn's magnetosphere was similar to that discussed in Chapter 4, consistent with expectations for the declining phase of the solar cycle. The phasing of the HCS crossings with respect to Carrington longitude also remained similar, particularly for the (-/+) crossings observed in the first half of each rotation, though the subsequent (+/-) crossings occurring in the second half were generally several days later in the data examined here than in the earlier interval. In addition, during the last solar rotation studied here, shown in the sixth panel, a significant

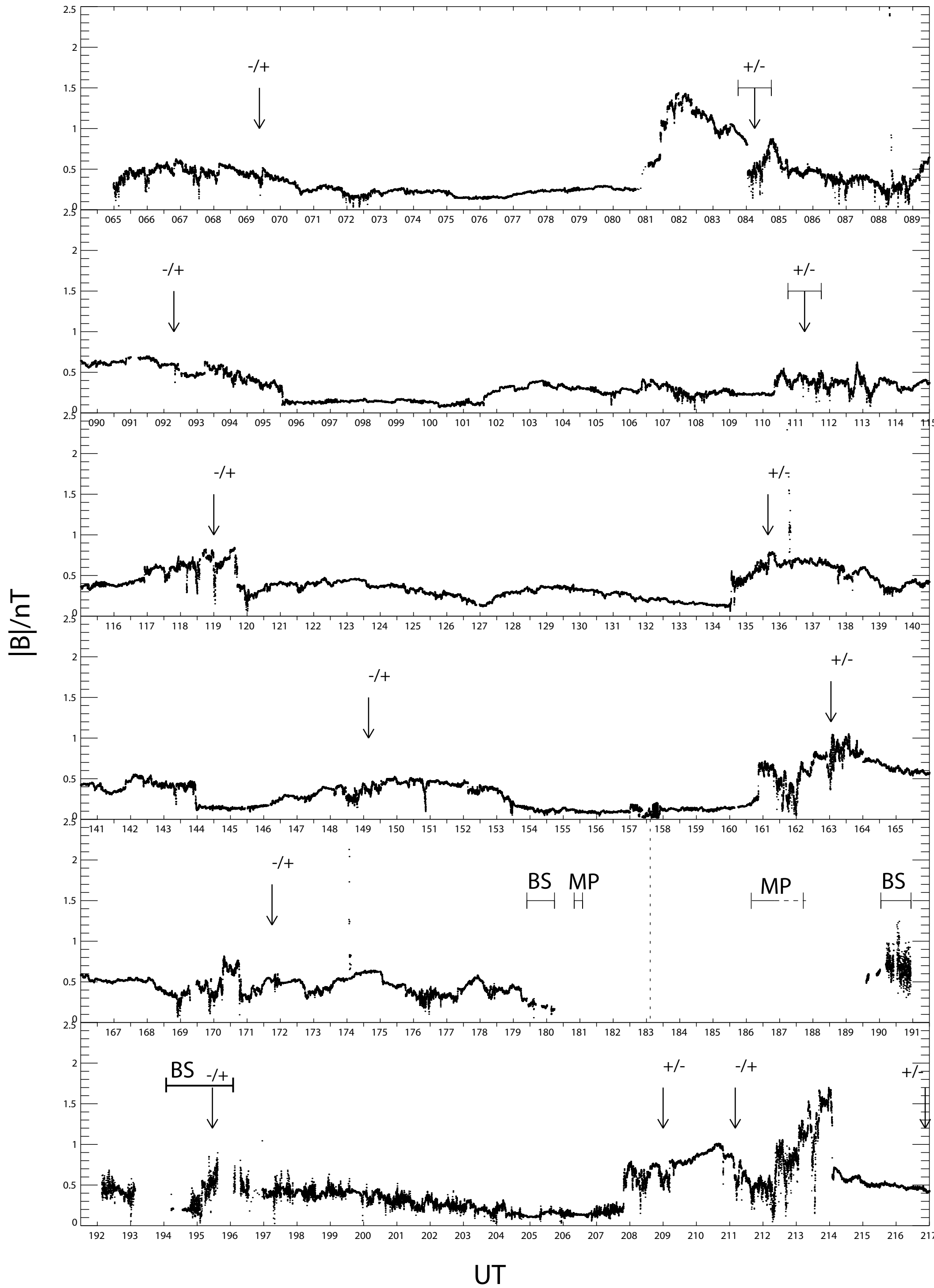

Figure 5.3: IMF strength measured by Cassini during the interval from day 64 (4 March) to day 216 (3 August) of 2004, plotted versus spacecraft event time (UT) in a stacked plot of six 25.5-day intervals, each corresponding to essentially one solar rotation.

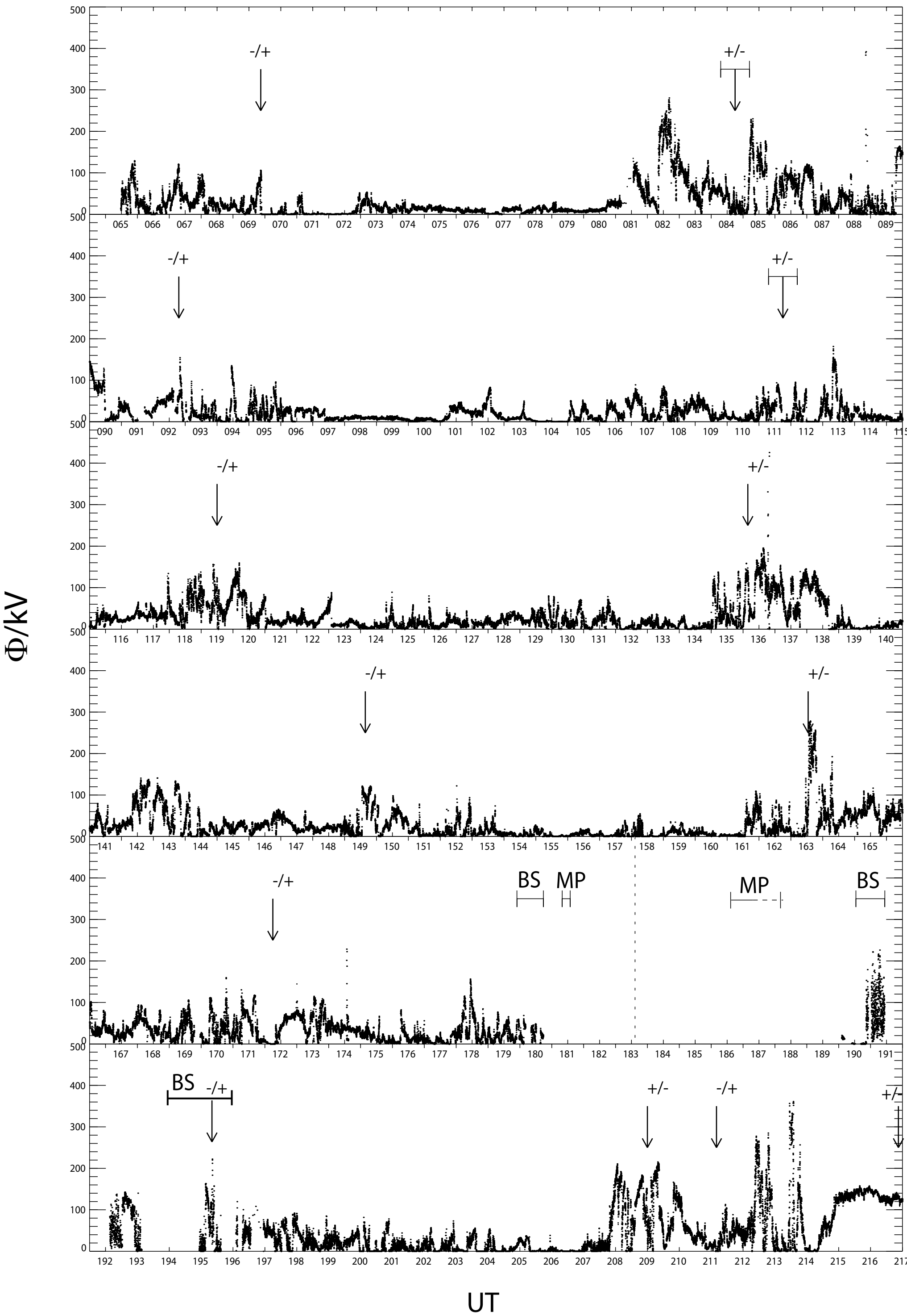

Figure 5.4: Estimates of the dayside reconnection voltage at Saturn's magnetopause obtained using Eq. (4.2) are shown versus spacecraft event time for the interval from day 64 to 216 of 2004 in a stacked plot.

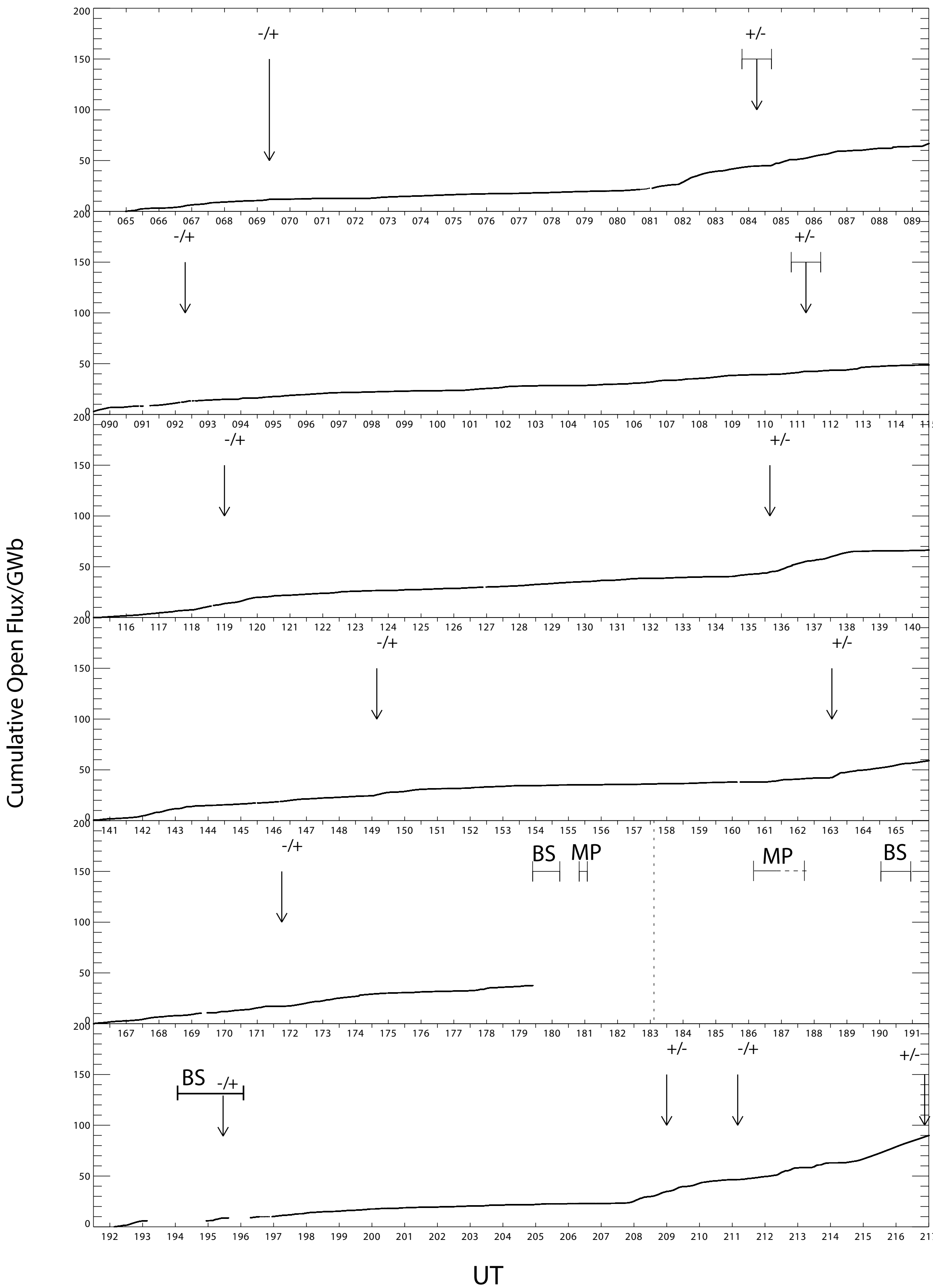

Figure 5.5: Cumulative open magnetic flux produced by reconnection at the dayside magnetopause during each solar rotation, shown in a stacked plot in a similar format to Figs. 5.3 and 5.4. The cumuative open flux is obtained by integration of the estimated reconnection voltage values obtained from Eq. 4.2 and shown in Fig. 5.4. The cumulative value is re-set to zero at the start time of each solar rotation panel.

interval of mainly positive B_T intruded into a usually negative B_T region, as indicated by the arrows shown on the right hand side of the panel. The IMF strengths in Fig. 5.3, in the interval preceding the fly-through, were also generally smaller than in the earlier interval studied in Chapter 4, by a factor of about two. For example, the fields in major compression regions in the earlier interval typically peaked at ~2 nT as indicated above, while in the first four solar rotations shown in Fig. 5.3, the peak field only significantly exceeded 1 nT in the first panel. This feature is significant for overall magnetospheric dynamics during these intervals (as estimated from Eq. (4.2) in Chapter 4), because open flux production over a solar rotation is often concentrated in the high-field compression regions. It can also be seen in Fig. 5.3, however, that some recovery in IMF strength took place during the solar rotation following the first fly-through, shown in the sixth panel.

Figure 5.4 shows voltage values derived using Eq. (4.2), while Fig. 5.5 shows the cumulative open flux produced during each solar rotation obtained by integrating the voltage with time, with the flux being re-set to zero at the start of each panel. Since solar wind velocity data are only very intermittently available during the interval, we have simply used a fixed typical value $V_{SW} = 500 \text{ km s}^{-1}$ in Eq. (4.2), as in Chapter 4. However, modulation of Eq. (4.2) by the IMF vector is generally much larger than that due to the solar wind speed, so this does not represent a significant limitation. Overall, the voltage values in Fig. 5.4 follow the variations in the field strength in Fig. 5.3, but are also strongly modulated on shorter time-scales by fluctuations in the north-south component of the IMF, as found previously. However, the generally weaker fields follow through to weaker overall reconnection voltages and to smaller cumulative open flux production. In the first four panels of Fig. 5.5, for example, the estimated open flux produced during each solar rotation is ~60 GWb, compared with ~100 GWb found for the solar rotations discussed in Chapter 4. On the basis of the above arguments, this implies 2-3 hypothetical Saturn substorms per solar rotation, at intervals of 9-12 days, compared with 3-5 substorms per solar rotation, at intervals of 5-8 days, as indicated above. The corresponding averaged reconnection voltage is ~30 kV, compared with ~50 kV obtained in Chapter 4. These results thus indicate the presence of a rather less active magnetosphere in the pre-fly-through interval than in the previous interval studied in

Chapter 4. In the post-fly-through interval shown in the sixth panel, however, the overall field strengths and voltages recover to values similar to those reported in the previous chapter, with a total estimated cumulative open flux production of just less than ~100 GWb, and a related averaged reconnection rate of ~45 kV. It thus remains unclear whether the more or less active conditions apply to the immediate fly-through interval itself. This chapter will go on to investigate the SOI fly-through interval in more detail to probe the magnetospheric dynamics.

5.3.2. Cassini IMF Data Surrounding the SOI Fly-Through

Next, we look specifically at the two solar rotations immediately preceding the SOI fly-through, the fly-through itself, and two solar rotations immediately afterwards, with the benefit of the in-depth knowledge of the pattern in the previous months. In Figure 5.6 we thus show a stacked plot of Cassini IMF and SKR data for a 4-month interval spanning the SOI fly-through, specifically from day 115 (24 April) to day 242 (29 August) of 2004. The SKR data in the figure will be discussed in section 5.4 below. Each pair of panels show data from one solar rotation of length 25.5 days, in which the Carrington longitude of the spacecraft decreased from ~360° at the left-hand border of each panel to ~0° at the right-hand border. The data thus encompass five solar rotations at the spacecraft, as indicated by the numbered bars on the right side of the plot. At the beginning of the interval the spacecraft was located at a radial range from Saturn of ~580 R_S (Saturn's radius R_S is taken as 60,330 km), at a local time of ~7.5 hr. Cassini was thus located in the solar wind ~230 R_S upstream from the planet, and displaced ~530 R_S from the planet-Sun line towards dawn. With a nominal solar wind speed of ~500 km s^{-1}, the propagation delay between spacecraft and planet for purely radial propagation at the solar wind speed was thus ~7.5 hr, reducing to ~5.5 hr for disturbances aligned along the nominal Parker spiral direction. These estimated delays decreased approximately linearly with time as the planet was approached, with closest approach occurring at 0239 UT on day 183 (1 July) at a radial distance of ~1.3 R_S. This time is marked by the vertical dashed line in the central IMF panel. At the end of the interval

Cassini had receded to a radial range of ~150 R_S from the planet at a local time of ~6.5 hr, almost on the dawn meridian. The delay for purely radial propagation from the Sun was then less than 0.5 hr, or smaller in magnitude than -0.5 hr for disturbances aligned along the spiral (the minus indicating that such disturbances would arrive at the planet before arriving at the spacecraft). Overall, the interplanetary propagation delay between the spacecraft and the planet during the whole of the interval is thus expected to be no more than a few hours, which is thus small compared with the solar rotation time scale of the figure.

The lower panels of each pair in Figure 5.6 show the magnitude of the IMF. Data are omitted during the SOI interval, principally in rotation 3, when the spacecraft was located in either the magnetosheath or magnetosphere of Saturn, though the IMF may be somewhat disturbed by upstream waves in the vicinity of the planetary bow shock [Dougherty et al., 2005]. Intervals during which bow shock crossings were observed are indicated in rotations 3 and 4 by the horizontal bars marked 'BS', while intervals containing magnetopause crossings are similarly indicated by the horizontal bars marked 'MP'. As in Figs. 5.3-5.5, the vertical arrows marked with the '+/-' and '-/+' symbols indicate crossings of the HCS, from 'toward' to 'away' and vice versa, respectively. It can thus be seen that the IMF structure generally consisted of two sectors per solar rotation throughout the interval, which, as indicated above, had been the case since (at least) August 2003. Comparison with the results in Chapter 4 and in Section 5.3.1 above also shows that the phasing in heliographic longitude of the crossings had remained roughly constant over the interval.

The magnetic field data in Figure 5.6 show that the HCS crossings are generally embedded in several-day regions of higher field strength, peaking typically at ~0.75 to ~1.5 nT, which we take to correspond to CIR-related regions of solar wind compression (Cassini solar wind plasma data are not routinely available during the interval considered here). The '+/-' crossings in the right-hand portions of the panels, in particular, all have a well-marked sharp increase in field strength preceding the crossing, which we take to correspond to the 'forward' shock of the following CIR compression region, of the same

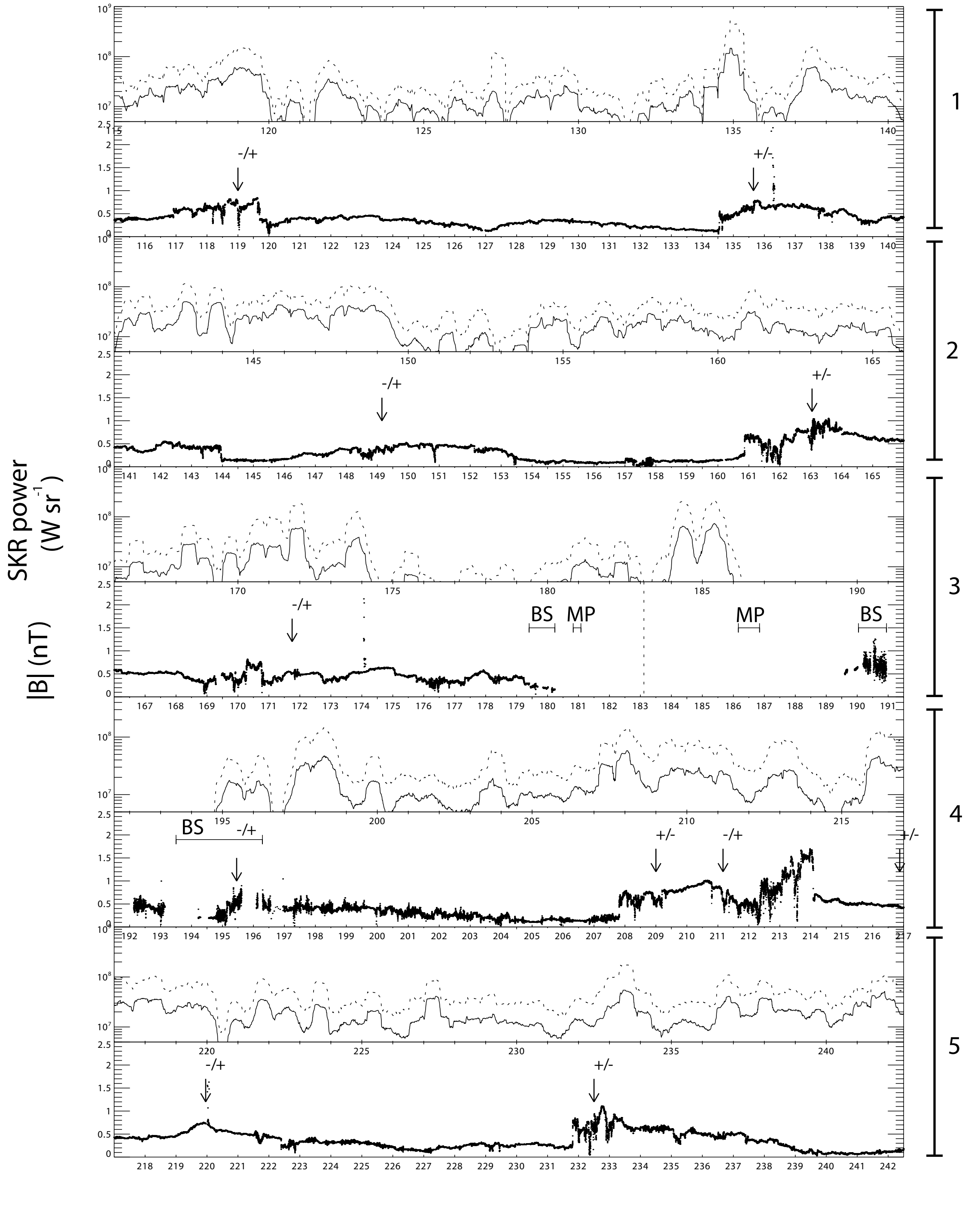

Figure 5.6: Stacked plot of Cassini IMF and SKR data obtained from day 115 (24 April) to day 242 (29 August) of 2004, shown as 5 double panels of 25.5 days duration. The top panel of each pair shows SKR data, while the bottom panel shows the corresponding IMF data for that solar rotation.

general character as the shock marked 'S' in Figure 5.1. Between the compression regions the field strength then falls typically to values of a few tenths of a nT, corresponding to the intervening solar wind rarefaction regions.

5.3.3. Implications for Solar Wind Conditions During the Cassini SOI Fly-Through

We now compare the phasing of the CIR-related structures observed during the solar rotations shown in Figure 5.6 with the timing of the SOI fly-through indicated by the bow shock and magnetopause markers in the IMF panel of rotation 3. The comparison immediately shows that the CIR compression region associated with the '+/-' crossing of the HCS is expected to have arrived at Saturn's magnetosphere at some time during the SOI fly-through. Judging from the times of the 'earliest' and 'latest' arrivals of the sharp field increase occurring prior to the HCS crossing in the two preceding and two following solar rotations, it seems probable that the forward shock of the CIR arrived some time between days 181 (29 June) to 185 (3 July) inclusive, a period that brackets essentially the whole of the fly-through interval when Cassini was inside the magnetosphere. The IMF data obtained prior to the final inbound bow shock crossing on day 180 (28 June) show that the compression region had not arrived at that time, such that the initial period of entry to the Saturn system, at the least, occurred during the weak field conditions of a solar wind rarefaction region. This is consistent with the expanded condition of the bow shock and magnetopause observed during the inbound pass [Dougherty et al., 2005]. On exit, however, the IMF strength was elevated to values comparable with those following the compression regions observed during the previous and following solar rotations, indicating that the compression region had indeed arrived while Cassini was inside the magnetosphere. This is also consistent with the relatively compressed condition of the magnetopause and bow shock observed initially on the outbound pass [Dougherty et al., 2005], as indicated in the third IMF panel of Figure 5.3. However, further bow shock crossings were observed at rather larger distances on days 194-196 (12-14 July), as marked in the IMF panel during rotation 4, indicative of declining solar wind dynamic pressure and a corresponding expansion of the magnetosphere and bow shock during this interval.

The magnetic field data in Figure 5.6 thus strongly indicate that a CIR compression region associated with a '+/-' HCS crossing impinged on Saturn at some point during the interval when Cassini was inside the magnetosphere. If so, we should then find that the sense of the B_T field component in the IMF and magnetosheath should have reversed from positive on the inbound pass to negative on the outbound pass. In Figure 5.7 we show magnetic field observations in RTN coordinates for two 5 day intervals, the first (Figure 5.7a) spanning the inbound interval from the first crossing of the bow shock to the last crossing of the magnetopause (days 177 to 181 respectively), while the second (Figure 5.7b) spans the outbound interval from the first crossing of the magnetopause to the seventh crossing of the bow shock (days 186 to 190 respectively). Crossings of the bow shock and magnetopause are indicated by the dashed vertical lines during intervals marked as 'BS' and 'MP' at the top of the figure. The 'MP' interval on the outbound pass is indicated partially by a dashed line, however, since the absence of a large magnetic shear between the internal and external field during days 187 and 188 renders the timing of the final magnetopause encounter(s) unclear [Dougherty et al., 2005]. In addition, plasma and other science data (excepting magnetometer data) that might contribute to an identification were not obtained on the outbound pass from days 186 to 194, due to a temporary suspension of science commanding for reasons of spacecraft health and safety. Nevertheless, the magnetometer data in Figure 5.4 show that the B_T field component in the solar wind and magnetosheath was consistently positive during the inbound pass up to the last magnetopause encounter on day 181, and was consistently negative during the outbound pass from the first magnetopause encounter on day 186. These data thus prove that a '+/-' crossing of the HCS took place during the intervening interval when Cassini was located continuously inside the magnetosphere, with the further implication that the associated CIR compression also impacted on the system at some time during this interval. These data do not, however, provide an otherwise more detailed indication of the expected timing of the event, and of the associated SKR and auroral effects that should then follow.

5.4. SKR Data and its Implications for Magnetospheric Dynamics During the SOI Fly-Through

It has been seen from the discussion of the Cassini-HST campaign data in section 5.2 that SKR emissions are strongly modulated by the arrival at Saturn of CIR-compressions in the interplanetary medium, as anticipated from the earlier Voyager results of Desch [1982] and Desch and Rucker [1983]. The primary purpose of this section is thus to examine the SKR data obtained during the SOI interval for related effects, which may thus provide insight into interplanetary-modulated magnetospheric dynamics during the fly-through. We begin, however, by giving an overview of the emissions observed during the interval surrounding the fly-through, which provides a wider context.

5.4.1. SKR Observations Surrounding the SOI Fly-Through

The upper panels in Figure 5.6 show the inverse-square corrected power in SKR emissions observed over the ~4 month (5 solar rotation) interval surrounding the SOI fly-through, which we compare with the IMF data shown in the same figure, discussed in the previous section. We recall from section 5.3.2 that the solar wind propagation time from the spacecraft to the planet is at most a few hours, while the light propagation time from the planet to the spacecraft is at most a few minutes, such that the two data sets may be considered to be essentially simultaneous on the time scale of this plot. As in Figure 5.1, the solid line shows the sum of the powers in the LH and RH polarised emissions in the 100-300 kHz frequency band, while the dashed line shows that in the 4-1000 kHz band. The value is again shown in the form of radio power per steradian (W sr^{-1}), using a log scale. The power has also been averaged over a 10.75 h sliding window in order to smooth the variations associated with the planetary rotation period.

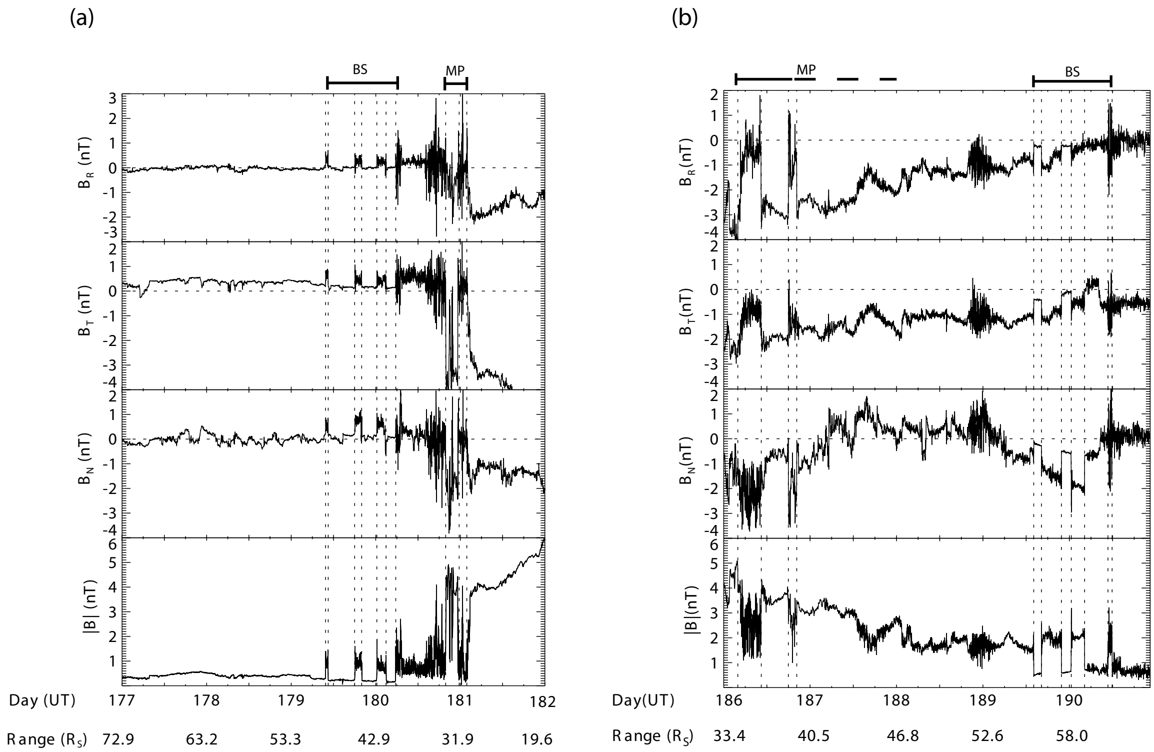

Figure 5.7: Cassini magnetic field data for two 5-day intervals spanning solar wind, magnetosheath, and magnetosphere regions on the inbound and outbound passes of the SOI fly-through. From top to bottom, the panels shows the B_R, B_T, and B_N components of the field in RTN co-ordinates and the total field strength |B|. Vertical dotted lines show the positions of magnetopause and bow shock crossings, as indicated by the horizontal lines marked "MP" and "BS" at the top of the plots.

(a) Shows the interval from days 177 to 181 on the inbound pass, spanning the whole interval from the first bow shock crossing on day 179 to the last magnetopause crossing on day 181. The radial distance of the spacecraft decreased from ~73 to ~20 R_S over the interval, at a local time of ~7.5 hours.

(b) Shows the interval from days 186 to 190 on the outbound pass, spanning the interval from the first magnetopause crossing on day 186 to the seventh bow shock crossing on day 190. Further shock crossings occurred on days 194-196. The line marked "MP" at the top of the plot is shown partly dashed because magnetopause encounters occurring on days 187 and 188 remain unclear in the absence of sharp field shears and concurrent plasma data. The radial distance of the spacecraft increased from ~33 to ~63 R_S over the interval, at a local time of ~5 hours.

If we first compare the SKR and magnetic field data in Figure 5.6 when Cassini was in the solar wind, it can be seen that there is a general correspondence between high field strength intervals with embedded HCS crossings and high-power SKR emissions, as anticipated from the results shown previously in Section 5.2 and those of Desch [1982] and Desch and Rucker [1983]. If we examine the pair of panels corresponding to solar rotation 1, for example, it can be seen that intervals of high SKR power accompany the high field region and HCS crossing on days 118-119, and also the sharp field strength increase associated with the forward shock of the CIR compression occurring on day 134. There is also a further interval of high SKR power during the high-field region following the latter shock, centred on day 137. In rotations 2, 4, and 5 we also note in particular that an interval of stronger SKR emission is again associated with the compression region occurring in the second half of each solar rotation, during which the '+/-' HCS crossing took place. The emissions start on day 160 in rotation 2, 207 in rotation 4, and 232 in rotation 5. We note that it was this 'same' compression region that caused the major SKR and UV auroral effects which were observed during the Cassini-HST campaign discussed in Section 5.2, such that it seems reasonable to infer from these data that similar magnetospheric and auroral effects were produced during its subsequent appearances in the following solar rotations. This is also the compression that impinged on Saturn during the SOI fly-through, as inferred above, such that related dynamics were also presumably in progress at some point during the fly-through.

We therefore now turn to the SKR data observed during the SOI pass during solar rotation 3 in Figure 5.6. We note that a major SKR data gap occurred on the outbound pass from days 186 to 194, due to the spacecraft problem noted above, when no science data were obtained other than magnetometer data. This SKR data gap thus spans the interval from near the first outbound magnetopause crossing to near the final outbound bow shock. Fortunately, however, full data coverage extends over nearly all of the magnetosphere traversal up to the first outbound magnetopause crossing on day 186, and thus through all of the interval during which the arrival of the CIR compression appears likely from the contextual magnetic field data discussed in Section 5.3. Examining the SKR data in this panel, it can first be seen that an interval of high-power SKR bursts occurred from days 170 to 173, associated with the disturbed-field region surrounding the '-/+' HCS crossing that occurred on day 171. Following this, however, an extended interval of very low power SKR emission began on day 174 during the approach to the planet, and continued in the low-field rarefaction region leading up to entry into the Saturn system on day 180. Somewhat higher normalised powers were then observed during the inbound pass through the magnetosphere and during closest approach on days 181-183, though remaining overall of modest normalised amplitude. We note in passing that the SKR power calculations were modified during closest approach because the method of power calculation employed at larger distances, which used a planet-centred source, is inadequate in the region very close to the planet. Specifically, during the interval from day 182.5 to the end of day 183, the powers were derived using the RPWS instrument as a circularly polarized goniometer (assuming no linear polarization), such that the varying source direction, as well as the power, was obtained directly from the data. Bursts of high-power SKR emission were then observed on days 184 and 185, comparable in normalised magnitude to the highest observed at other times during the interval shown in Figure 5.6, before the beginning of the data gap starting on day 186. In view of the HST-Cassini campaign results discussed in Section 5.2, it seems reasonable to suppose that these bursts are related to auroral events of a similar nature to those shown in Figure 5.2, associated with the anticipated CIR-compression of the magnetosphere. Of course we do not know precisely how the onset of the auroral and SKR events relate to the time of arrival of the CIR compression, but we suppose that they must generally be coincident to within a few hours. Noting from the results of Chapter 2 and Section 5.3.1 above, and from Figure 5.1 that compression regions typically last for several days following the arrival of the initial forward shock, we may then expect compressive effects to be present from day 184 throughout the remainder of the outbound pass and into the SKR data gap, but to relax towards the end of solar rotation 3 in Figure 5.6, consistent with the outbound boundary locations observed in the magnetometer data [Dougherty et al., 2005].

5.4.2. SKR Observations During the SOI Fly-Through

With the HST-Cassini campaign data as background, we now consider the magnetic field and SKR observations obtained during the SOI fly-through interval in more detail. In Figure 5.8 we show these data in the same format as Figure 5.1, over the interval from day 180 to 186. These data thus span the interval from the bow shock crossings and magnetopause crossings observed inbound on days 180 and 181 (shown by the vertical arrows marked 'BS' and 'MP' respectively), to the first magnetopause crossings observed outbound on day 186 (marked similarly). Closest approach to the planet occurred at 0239 UT on day 183. The major distinction between Figures 5.1 and 5.8, therefore, is that the magnetic field data in the lower panel of Figure 5.1 shows the IMF upstream of Saturn, while that in Figure 5.8 generally corresponds to Saturn's magnetospheric field. We note that, as in Figure 5.1, the SKR power values in the upper panel have generally been derived using an assumed source at the centre of the planet, except for the near-planet interval on days 182.5-183 when the goniometer method was employed as mentioned above.

If we first examine the SKR data in the top two panels, it can be seen that planetary-modulated SKR emissions spanning the frequency range from ~40 to ~600 kHz are present throughout the inbound pass. As in Figure 5.1, a series of vertical arrows has been drawn in the middle panel, separated from each other by fixed intervals of 10.75 h and adjusted to coincide with peaks in the emission on the inbound pass (account being taken also of data from earlier intervals than that shown). An ~8 h gap in observed SKR emissions then spanned the interval of closest approach, while waves in the in situ plasma medium intruded into the band at frequencies below the upper hybrid resonance, reaching ~100 kHz near closest approach [Gurnett et al., 2005]. A short (~1.5 h) interval of very intense noise was also observed near closest approach, extending from low frequencies to several tens of kHz, which was associated with the firing of the rocket motor which placed Cassini into orbit around Saturn. Power in these non-SKR emissions is efficiently excluded from the values shown in the upper panel through examination of their polarisation characteristics. Observations of SKR emissions were resumed ~4 h after closest approach, these being of similar normalised amplitude and frequency range as those observed on the inbound pass. They also appear initially to be modulated in phase with the inbound pass, though the considerable structure observed in the emissions renders this conclusion somewhat uncertain. Voyager observations have previously established, however, that the phase of SKR modulations does not depend on the spacecraft longitude, between the inbound and outbound passes [e.g., Kaiser et al., 1984]. A major burst of SKR emission then started at the beginning of day 184, extending to frequencies below 4 kHz, peaking in intensity at $\sim 5\times10^{8}$ W sr^{-1} (over the full 4-1000 kHz frequency band), and lasting for ~14 h. We note from the arrows in the middle panel of Figure 5.5 that this burst occurred essentially in anti-phase with the previous planetary modulation, such that relative minima in power occurred near expected maxima at the start and end of the burst, while peak powers were observed near an expected minimum. Following this burst an ~11 h interval of low SKR-band power was then observed at Cassini, before further structured high-power bursts were observed on day 185, which were again not generally in phase with the inbound planetary modulation.

Comparison of these SKR observations with those for 24-30 January 2004 in Figure 5.1 shows a number of similarities. In both cases a prior interval of relatively low-power planetary-modulated SKR emission was disrupted by several-hour bursts of high-power emission which extend to lower frequencies than before, and which do not observe the prior planetary phasing. Also in both cases, the initial high-power burst was followed by a several-hour interval of low SKR power prior to the occurrence of further high-power bursts. As indicated by the January 2004 Ulysses observations mentioned in section 5.2, however, the observation of low powers by Cassini does not necessarily imply a global lull in emission, but perhaps only a significant change in the beaming pattern of the radiation [Kurth et al., 2005]. In the January 2004 interval the subsequent bursts eventually resumed the prior planetary phasing ~2 days after onset, a feature that cannot be followed in the SOI interval due to the extended data gap that followed. Planetary-modulated emissions were again present, however, when science data collection was resumed on day 195. In the January interval we know that these disturbed SKR emission features were associated with a CIR compression of the magnetosphere, and related

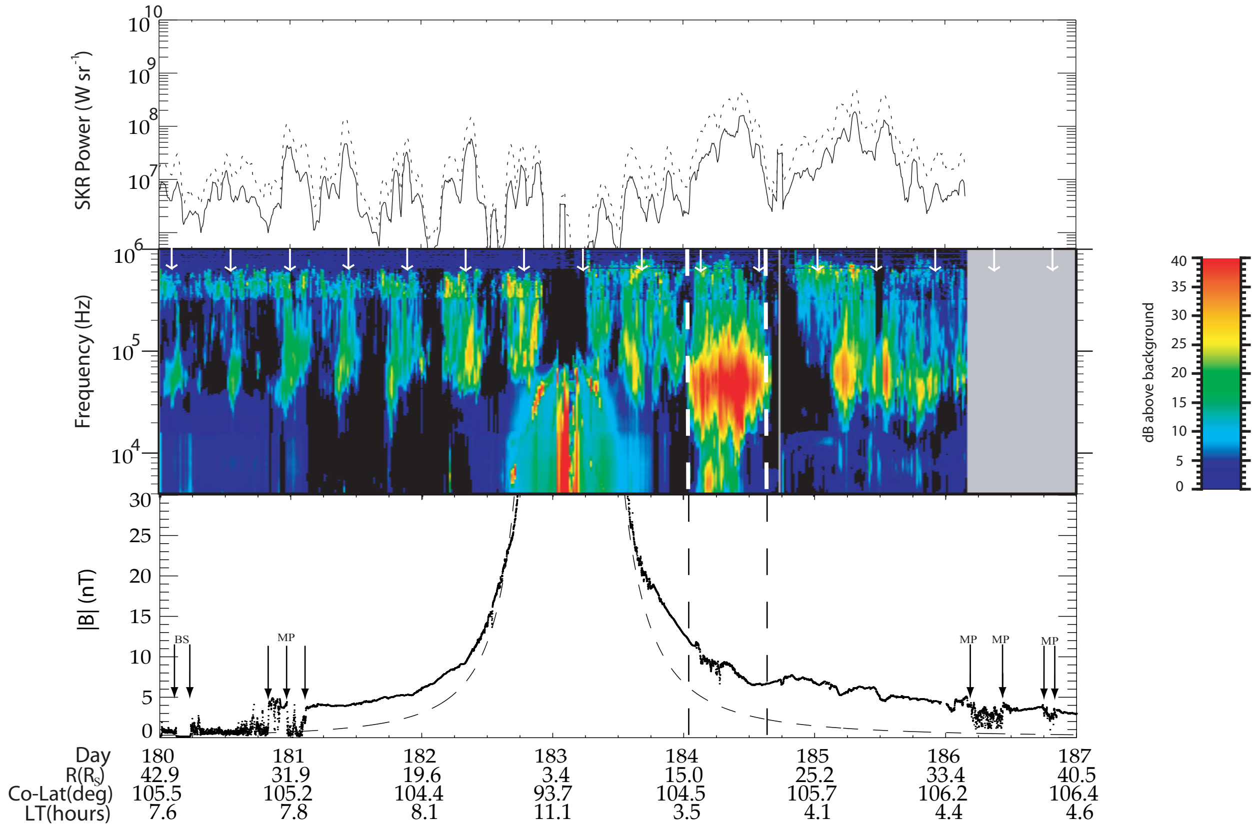

Figure 5.8: Cassini SKR and magnetic field data for days 180-186, encompassing the SOI fly-through of Saturn's magnetosphere. The top and middle panels are similar to Figure 5.1, though with a data gap for much of the final day. The bottom panel shows the magnitude of the magnetic field strength over the same interval, with the dashed curve showing the strength of the internal field of the planet from the SPV model. Vertical dashed lines indicate the interval of the first major burst of SKR observed on the outbound pass. In the bottom panel the vertical arrows marked "BS" and "MP" indicate bow shock and magnetopause crossings, respectively. Information on spacecraft position is given at the bottom, specifically the distance from the planet (R_S), the co-latitude relative to the magnetic and spin axis (degrees), and the local time (hours).

major auroral disturbances illustrated in Figures 5.1 and 5.2. In view of the similarities noted above, it thus seems reasonable to suppose that the SKR burst events observed on the outbound pass in Figure 5.8 were related similarly to the anticipated CIR compression during the SOI fly-through. We thus infer that the inbound pass took place before the arrival of the compression region and in the absence of major auroral disturbance, while the outbound pass, certainly after the beginning of day 184, took place during conditions of compression, and in the presence of auroral and SKR disturbance of a similar nature to that observed during the HST-Cassini campaign shown in Figure 5.1.

5.5. Magnetic Field Observations During the SOI Fly-Through

As shown in Section 5.2 and previously by Clarke et al. [2005] and Kurth et al. [2005], the CIR-related SKR disturbances observed during the January 2004 HST-Cassini campaign were accompanied by bright auroral displays that are indicative of the injection of hot plasma into the nightside-dawn outer magnetosphere, followed by sub-corotation around the planet via dawn to noon and beyond [Cowley et al., 2005a; Grodent et al., 2005]. Given this scenario, it is of interest to examine whether related features were observed in situ by Cassini as it traversed the pre-dawn magnetosphere during the interval of SKR disturbance on its outbound pass. We thus examine the magnetospheric magnetic field strength data shown in the lower panel of Figure 5.8 to determine whether such features were observed. The dashed line in this panel also shows the magnitude of the internal field alone determined from the Saturn-Pioneer-Voyager (SPV) model of Davis and Smith [1990], for purposes of comparison. Information on the position of the spacecraft during the fly-through is indicated at the bottom of figure, showing the distance from the planet (R_S), the co-latitude relative to the magnetic and spin axis (deg), and the local time (h). It can be seen that the spacecraft approached the planet from a radial range of ~43 R_S at the start of the interval, at a local time of ~7.6 h in the post-dawn sector, and receded to a radial range of ~41 R_S at the end of the interval, at a local time of ~4.5 h in the pre-dawn sector. With the exception of a short interval near closest approach, the spacecraft was also consistently located south of the planet's equatorial plane, at a latitude of ~-15°.

If we first examine the magnetic field data from the inbound pass, no evidence can be seen that would suggest the occurrence of a sudden magnetospheric compression during the interval, at least up to the second half of day 182. Such a compression would be expected to result in an increase in field strength of a few nT over an interval of several tens of minutes, and clearly none is evident. After the first half of day 182, however, the rapid rise in field strength to large values near closest approach would render such an effect very hard to discern. Overall, however, these data are consistent with the conclusions of section 5.4 above, that the inbound pass took place prior to the arrival of the CIR compression.

Turning therefore to the data from the outbound pass, we note that near the middle of day 183, when the field magnitude returned to within the range of the plot, the spacecraft was located at a radial distance of ~9 R_S within a region of warm corotating plasma in which the density decreased slowly with increasing distance [Young et al., 2005]. The presence of this warm middle magnetosphere plasma is indicated in the magnetic field data by the small-scale variations that occurred in the field strength, as is also evident in the corresponding region of the inbound pass [Dougherty et al., 2005]. At 21:30 UT on day 183 the spacecraft then passed into a low-density region of quiet field at a radial distance of ~13.6 R_S, which we take from an examination of the spacecraft location and the field direction to correspond to the tail lobe. Mapping of model field lines from the spacecraft into the polar ionosphere yields a co-latitude of ~15° at this time, which is plausibly close to the boundary of open and closed field lines, as inferred from prior auroral data. At ~03 UT on day 184, however, at a radial distance of ~16.5 R_S, the magnetic field data indicate that the spacecraft was again engulfed by hot plasma. This is indicated by a sudden reduction in the field strength, and subsequent rapid variations in the field indicative of the presence of a high-beta plasma. Comparison with the SKR data in the upper panels of Figure 5.8 shows that these effects occurred in direct temporal correspondence with the large burst of SKR emission that began at the start of day 184, bracketed by the vertical dashed lines in Figure 5.8.

The magnetic field data spanning the SKR burst are shown on an expanded time base in the lower panel of Figure 5.9, together with the SKR power data in the upper panel. It can be seen that a small sudden increase in the field strength occurred shortly after 02 UT on day 184, which might represent the effect of a sudden magnetospheric compression. Following this, the field underwent a large sudden reduction in strength centred on ~03 UT, from a peak of ~11.5 nT to a trough of ~9.5 nT, this representing a reduction in the magnetic pressure by ~30%. Following this the field underwent large irregular variations in strength over the following ~4 h, after which the field fluctuations continued but at diminishing amplitudes. These data thus clearly indicate the sudden appearance of hot plasma at the spacecraft at and after ~03 UT, in association with the SKR burst shown in the upper panel. We suggest the most likely scenario is that the hot plasma was formed by tail dynamics (e.g. possibly reconnection) at larger distances down the tail, and was then injected along the previously open field lines towards the planet, where it was observed by the spacecraft in the relatively near-planet pre-dawn magnetosphere. This scenario is consistent with the picture suggested by Cowley et al. [2005a], who proposed that the CIR-related auroral disturbances observed during the HST-Cassini campaign in January 2004, discussed in section 5.2, were due to compression-induced reconnection in the magnetospheric tail which closed a significant fraction of the previously open magnetic flux. Bunce et al. [2005a] conducted a multi-instrument study of the SOI interval. Ion and electron observations on the outbound pass show that the spacecraft is engulfed by a hot, tenuous plasma population and thus suggest that following the shock-compression, the magnetosphere underwent a significant reconfiguration, exemplified by a relaxation of the field and an injection of hot plasma. They propose, in agreement with the theory of Cowley et al. [2005a] that this behaviour is indicative of a major episode of tail reconnection, triggered by the impact of the compression region on Saturn's magnetosphere. We finally note in Figure 5.8 that further variations of the tail field were also observed on day 185, after the initial SKR-related event discussed here, and that these too appear to be temporarily related to the subsequent high-power SKR bursts that were observed on this day.

5.6. Summary

In this chapter we have employed concurrent magnetic field and SKR emission data from the Cassini spacecraft to discuss the nature of the interplanetary conditions during the SOI fly-through of Saturn's magnetosphere, and their probable connection with dynamic phenomena observed inside the magnetosphere during the pass. Examination of the IMF data before and after the fly-through shows that a CIR compression region and embedded HCS crossing is expected to have impinged on Saturn's magnetosphere at some time during the 5-day pass (between days 181 and 186), though these contextual data do not provide a more detailed indication of the expected event timing. Investigation of the direction of the field observed in the inbound and outbound magnetosheath and solar wind does confirm however, that a crossing of the HCS of appropriate sign (from a 'towards' to an 'away' sector) did indeed occur during the interval the spacecraft was located inside the magnetosphere, thus providing strong corroborative evidence that a CIR compression impinged on the magnetosphere at some time during the fly-through. This inference is also supported by the observed locations of the bow shock and magnetopause, which were relatively expanded on the inbound pass and compressed (at least initially) on the outbound pass, relative to expectations at the local times concerned [Dougherty et al., 2005].

Given these inferences, we have then overviewed the results obtained during the HST-Cassini campaign in January 2004, when detailed observations were made of the SKR and auroral emissions associated with the arrival at Saturn of a CIR compression region. These observations show that high-power bursts of radio emission followed the arrival of a CIR compression, as discussed previously by Kurth et al. [2005]. These bursts disrupted the pre-existing pattern of planetary-modulated emission, which was then gradually re-established after an interval of 2-3 days. During this event, two ~8 h bursts

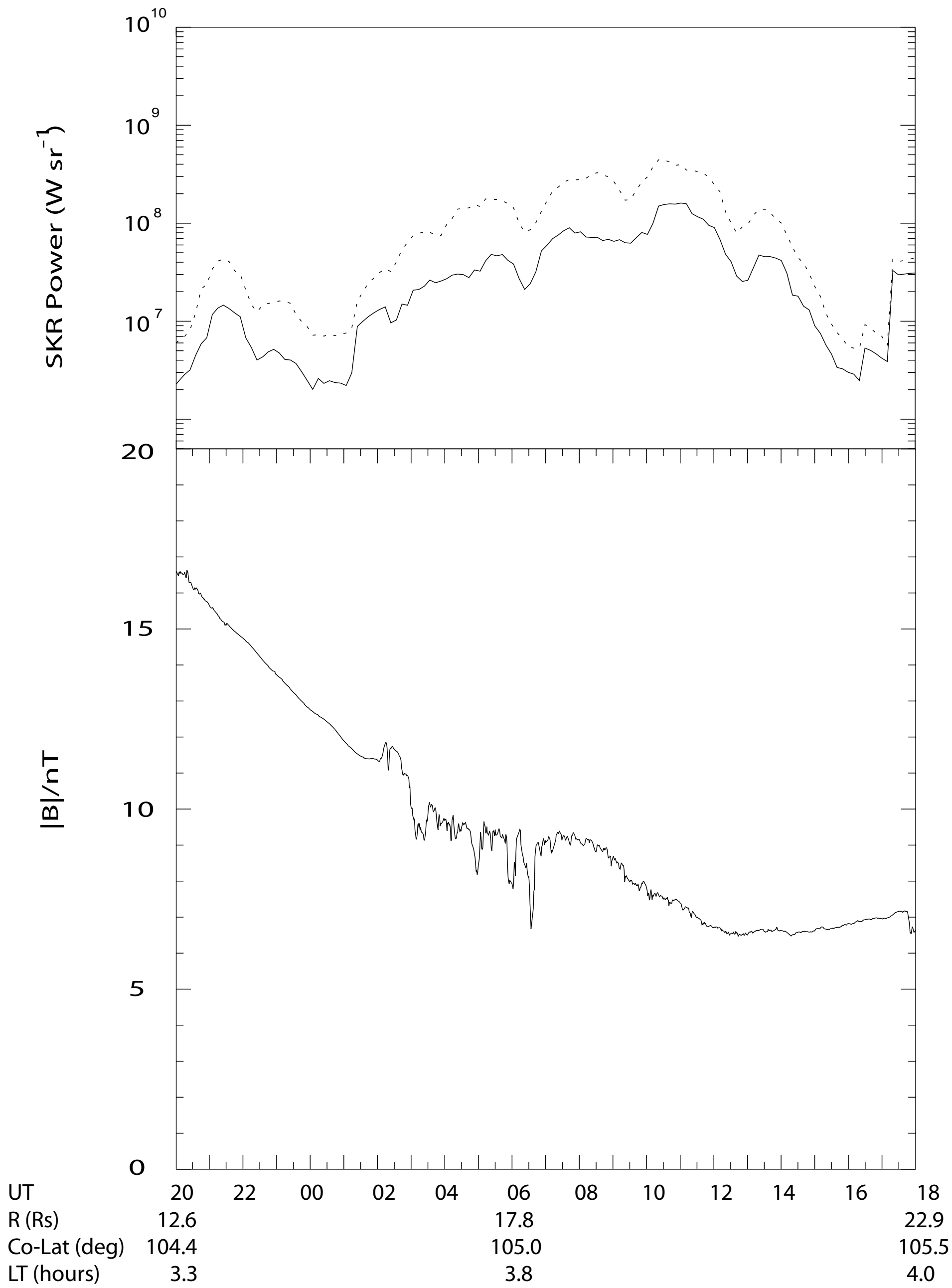

Figure 5.9: Cassini SKR and magnetic field strength data as in Figure 5.5 but plotted on an expanded time base for the interval from 2000 UT on day 183 to 1800 UT on day 184. Spacecraft position data are given at the bottom of the plot.

of high SKR power were observed, each characteristically extending to lower frequencies than before, and separated by a ~23 h interval (i.e. two planetary rotations) of relative SKR quiet as seen at Cassini. In view of the continued observation of SKR by Ulysses during this interval, however, this relative quiet could be due to an alteration in the beaming pattern, rather than to an overall absence of SKR. The concurrent HST observations show that the burst intervals were associated with intense UV auroral activity at Saturn, involving the poleward expansion of bright emissions into the dawn sector, followed by rotation to noon and later local times, forming a spiral pattern. Cowley et al. [2005a] have suggested that this morphology is produced by a CIR compression-induced interval of rapid open flux closure in the tail leading to hot plasma injection in the nightside magnetosphere, followed by flow around the planet in the dawn sector produced by magnetosphere-ionosphere coupling in the presence of rapid planetary rotation. Examination of concurrent SKR and IMF data from several solar rotations surrounding the SOI fly-through shows that such SKR enhancements usually occur in association with CIR compressions, in conformity with prior Voyager results, such that we associate them generally with the type of auroral activity observed during the January 2004 HST-Cassini campaign.

We have then examined data from the SOI fly-through interval in some detail. We find that a HCS crossing from an ‘away’ to a ‘towards’ sector occurred ~9 days prior to entry into Saturn’s magnetosphere, such that rarefaction region conditions following this interval prevailed at the time of entry. The SKR emissions, which were modulated at the planetary period, were correspondingly very weak during this period, and continued to be relatively weak during the inbound and early outbound passage through the magnetosphere, up until the beginning of day 184. We thus infer that the inbound pass, at least, occurred under conditions of SKR and auroral quiet, prior to the arrival of the compression. There is certainly no evidence in the in situ magnetospheric magnetic field data for the occurrence of a sudden increase in field strength that might accompany a compression of the outer magnetosphere during this interval. However, the expected in situ magnetic signature is made difficult to discern due to the large and rapidly changing field at the spacecraft during the close-approach interval.

Bursts of high-power SKR emission were then observed during the outbound pass, the most notable of which was a burst lasting ~14 h which began near the start of day 184. Such bursts are of a similar character to those observed during the 24-30 January HST-Cassini campaign event, which we thus infer were related similarly to the arrival of the anticipated CIR compression region. Specifically, the main SKR bursts had comparable power to those observed during the January interval, extended to significantly lower frequencies than before, and disrupted the pre-existing pattern of planetary modulation, with a significant interval of quiet (as seen by Cassini) following the initial burst. Comparison with the in situ field data in the pre-dawn magnetosphere also clearly indicates that these emissions were related to concurrent variations in the nightside magnetic field. Specifically, the major SKR burst on day 184 occurred together with the appearance of hot plasma at the spacecraft, clearly indicated in the magnetic field data as an interval of depressed and highly variable magnetic field strength, following the prior interval during which the spacecraft was located in the quiet field of the southern tail lobe. Such behaviour is suggestive of the onset of a major episode of tail reconnection, which resulted in the injection of hot plasma along previously open field lines into the dawn-sector magnetosphere. Plasma data for the interval confirm that the spacecraft was engulfed by a hot, tenuous plasma population. We suggest that this represents an in situ signature directly related to the CIR-associated auroral dynamics observed by the HST during the January 2004 campaign. The observations are consistent with the interpretive scenario suggested by Cowley et al. [2005a], in which the CIR compression induces an interval of rapid reconnection in the tail, which injects hot plasma into the nightside magnetosphere, and from thence around the planet via dawn. We also suggest that the outbound SKR bursts were associated with the same CIR-related tail dynamics, whose timing overrode that of the unknown process that usually modulates the SKR emission near the planetary period. The extension of the SKR emission to lower frequencies in such events could then result from the enhanced field-aligned currents flowing between the magnetosphere and ionosphere, which cause the discrete auroral acceleration regions to move to higher altitudes, and hence to smaller gyro-frequencies, in order to enhance the precipitating magnetospheric electron flux. We believe that these data thus provide the first evidence of a specific link between SKR emission features and in situ dynamics inside Saturn's magnetosphere.

Chapter 6

A model of the plasma flow and current in Saturn's polar ionosphere under conditions of strong Dungey cycle driving

6.1 Introduction

Recent theoretical interest in the dynamics of Saturn's magnetosphere has been stimulated by new data from the Cassini Saturn orbiter space mission [e.g. Dougherty et al., 2005; Krimigis et al., 2005; Young et al., 2005], by ground-based IR Doppler measurements of ionospheric flows [Stallard et al., 2004], and by studies of the planet's aurorae using the Hubble Space Telescope (HST) [e.g. Gérard et al., 1995, 2004; Cowley et al., 2004a; Prangé et al., 2004; Grodent et al., 2005]. Coordinated HST and Cassini interplanetary observations, as discussed in Chapters 2 and 5, have shown in particular that the aurorae respond strongly to upstream conditions, particularly the dynamic pressure of the solar wind [Clarke et al., 2005; Crary et al., 2005; Grodent et al., 2005; Bunce et al., 2005b], thus reflecting related behaviour observed in Saturn kilometric radiation (SKR) emissions [e.g. Desch, 1982; Desch and Rucker, 1983; Kurth et al., 2005], also discussed further in Chapter 5.

These studies indicate that the solar wind interaction is important at Saturn, as it is at Earth (see e.g. the review by Cowley et al. [2003]). At the same time, it is believed that internal dynamics are also significant, driven by the rapid ~11 h planetary rotation and the internal sources of plasma formed by Saturn's and Titan's atmosphere and the surfaces of icy moons and ring material [e.g. Richardson et al., 1998; Saur et al., 2004, and discussed in Section of 2.3 Chapter 2]. Recently, a qualitative picture of the overall plasma flow and electric current system in Saturn's coupled solar wind-magnetosphere-ionosphere system has been discussed by Cowley et al. [2004a], and outlined in Chapter 2. This picture contains co-existing elements related both to internally-driven processes and the solar wind interaction, and forms the basis of the theoretical model of the flow and current in Saturn's polar ionosphere developed here. A related quantitative model based on this picture was presented previously by Cowley et al. [2004b]. However, for simplicity of initial discussion, this model assumed axi-symmetry of the system, such that only the basic latitudinal variations of the azimuthal flow were represented. A related axi-symmetric model of Jupiter's ionospheric flow and currents has also been proposed [Cowley et al., 2005b]. When internally-driven and solar wind-related processes are both active in the magnetosphere, however, significant dawn-dusk asymmetries will also generally be present, as discussed qualitatively by Cowley et al. [2004a]. In this chapter we present a more realistic model of Saturn's polar ionospheric flows and currents when both solar wind and internally-driven processes are active, thus generalising the initial axi-symmetric model of Cowley et al. [2004b]. Specifically, we choose to model conditions of strong steady solar wind driving, that are most applicable to few-day strong-field interplanetary compression regions, as discussed in Chapter 4.

6.2 Physical picture

As indicated above, the theoretical model developed here is based on the qualitative picture discussed by Cowley et al. [2004a], which contains co-existing features associated with both internally-driven processes and the solar wind interaction. The overall physical picture that forms the motivation for this model was discussed in Sections 2.5 and 2.6 of Chapter 2, where the plasma flows in the magnetospheric equatorial plane and northern polar ionosphere under various conditions were described.

We now consider the flux transport in these processes. In Chapter 4, estimates for the flux transport in the Dungey cycle at Saturn were presented. Cassini measurements of the upstream IMF were used, and an algorithm validated at Earth [e.g. Milan et al., 2004] was modified to kronian conditions. While the average Dungey-cycle voltage was estimated to be ~50 kV (corresponding to a flux transport of ~50 kWb s^{-1} by Faraday's law), the results indicate a very variable interaction overall, modulated by CIR structures in the solar wind. Here we choose to model compression-region conditions when the Dungey cycle is the most active, and have thus employed a Dungey-cycle voltage of 200 kV in the illustrative model to be presented below (see also Badman et al. [2005]). The flux transport in the Vasyliunas cycle at Saturn is not known at present, but for definiteness we assume it here to be comparable in magnitude to that of the active Dungey cycle, as will be discussed further below.

In Sections 2.5.2 and 2.6.2 of Chapter 2, the plasma flows in the ionosphere were detailed with and without the effect of Dungey cycle driving. Here we now briefly consider the ionospheric and field-aligned current systems that are implied by these flows, and the relationship of the latter to Saturn's aurorae. The generally sub-corotating plasma flow in the ionosphere drives currents which are proportional to the degree of sub-corotation (i.e. to the electric field in the rest frame of the neutral atmosphere), the Pedersen currents flowing equatorward and the Hall currents eastward. While the Hall currents are thus expected to close in the ionosphere as a first approximation, the Pedersen currents instead close in the magnetosphere via rings of field-aligned current which are determined by the plasma angular velocity profile.

Beginning with the case where Dungey cycle driving is absent, these upward and downward-directed currents are indicated by the circled dots and crosses respectively in Figure 2.7. Four main regions of current are implied. At highest latitudes, distributed downward-directed field-aligned current is expected within the polar cap, associated with the twisting of the tail lobe field lines, that feeds the equatorward-directed ionospheric Pedersen current which grows with distance from the rotation axis. Much of this current then returns up the field lines in a narrow layer at the open-closed field line boundary, where the plasma angular velocities suddenly increase from about a third of rigid corotation on open field lines to an angular velocity significantly closer to rigid corotation on closed field lines in the outer magnetosphere, thus suddenly reducing the equatorward ionospheric Pedersen current. Assuming a current layer of a few hundred km width in the ionosphere as observed (i.e. some fraction of a degree of latitude), the peak upward current densities are estimated to be ~50-200 nA m^{-2} by Cowley et al. [2004a,b], sufficient to require downward acceleration of magnetospheric electrons through field-aligned voltages of a few tens of kV, resulting in the formation of UV aurorae of several tens of kR intensity. On this basis Cowley et al. [2004a,b] proposed that the 'main oval' aurorae at Saturn [e.g. Gérard et al., 1995, 2004; Trauger et al., 1998] are associated with the boundary between open and closed field lines. In the situation depicted in Fig. 2.9, when the effect of the Dungey cycle is taken into account, the flow shear across the boundary is greater at dawn than at dusk, such that the upward current at the boundary and the aurorae will also be stronger at dawn than at dusk. It is the representation and quantification of these dawn-dusk effects that is the principal focus of the present chapter. As mentioned in the introduction, and described in Chapter 2, dawn-dusk asymmetries are a commonly observed but not ubiquitous feature of Saturn's aurorae.

At lower latitudes within the outer magnetosphere region the field-aligned current then reverses once more to downward, particularly at its equatorward boundary at dawn where the angular velocity is expected to drop with increasing co-latitude into the middle magnetosphere, thus implying an increase in the equatorward Pedersen current. These downward currents will be less significant at dusk, however, where the shear in the flow between the outer and middle magnetosphere regions is expected to be less. Finally, at lower latitudes in the middle magnetosphere, the field-aligned current once more becomes directed upward as the plasma angular velocities increase toward rigid corotation and the Pedersen current falls with increasing co-latitude. This middle magnetosphere current system was modelled by Cowley and Bunce [2003b] and Cowley et al. [2004b] based on Voyager plasma angular velocity profiles, showing that for an ionospheric Pedersen conductance of ~1 mho, the large-scale upward current density peaks at ~10-15 nA m^{-2} at ~20° co-latitude. Such current densities are too low to require downward acceleration of hot magnetospheric electrons into the ionosphere, such that these currents are not expected to be associated with strong auroral emissions. Smaller-scale flow features are also observed in some of the Voyager data which may be associated with larger amplitude but more localised current systems. However, modelling of these features by Cowley and Bunce [2003b] still led only to weak precipitation and aurorae in this lower-latitude region. These considerations do not, therefore, alter our previous conclusion that Saturn's aurorae are associated with the open-closed field line boundary, and hence with the solar wind interaction, rather than the middle magnetosphere and internal dynamics. At Jupiter, however, the equivalent middle magnetosphere 'corotation breakdown' currents are more intense by at least an order of magnitude [e.g. Cowley et al., 2005b], and are believed to be associated with accelerated electron precipitation that produces the bright 'main oval' auroral emissions in that case [Bunce and Cowley, 2001; Cowley and Bunce, 2001; Hill, 2001; Southwood and Kivelson, 2001; Grodent et al., 2003].

6.3 Basic theory

In this section we present the basic theory which underlies our model of plasma flow and currents in Saturn's ionosphere. Three basic ingredients are required. The first is the choice of the geometry of the ionospheric layer where the horizontal currents flow, and of the planetary magnetic field that threads through it. The second is the flow of plasma and neutral atmosphere in this layer, from which the horizontal and field-aligned currents can be calculated. The third is the model basis on which auroral parameters are calculated from the field-aligned currents. Each of these topics will now be discussed in turn. The specifics of the model will then be given in Section 6.4.

6.3.1 Geometry and magnetic field model

With regard to the first of these topics, the models presented by Cowley and Bunce [2003b] and Cowley et al. [2004b] employed a spheroidal ionospheric layer following the flattened figure of the planet, the full SPV model of the planetary magnetic field which is axially symmetric about the planet's spin axis [Davis and Smith, 1990], and a modest correction for the consequent fact that the magnetic field does not then pass exactly normally through the ionospheric current layer. Here, however, we relax these features in order to incorporate more complex local-time dependent flows into the model while retaining simplicity of calculation. Specifically, we first take the polar ionospheric layer to be at a fixed radial distance of $R_i = 55{,}364$ km, corresponding to an altitude of 1000 km above the 1 bar reference spheroid of the planet at the pole [e.g. Trauger et al., 1998]. This value compares with a corresponding equatorial ionospheric radius of 61,268 km, and the conventional (1 bar) Saturn radius $R_S = 60{,}330$ km, as used throughout this thesis. Using the full spheroidal geometry, the increase in ionospheric radius between the pole and 20° co-latitude, bounding the main region of interest here, is only ~1%, so this does not represent a major simplification. Second, we also assume that the planetary magnetic field is purely radial through this spherical surface, and thus neglect the correction for non-vertical magnetic fields. We note that the tilt of the SPV field to the ionospheric normal varies from zero at the pole to a maximum of ~18° at 20° co-latitude. However, the latter tilt changes the horizontal current by only ~5%, so that this is also a modest effect. Third, although we could here take any axi-symmetric radial field varying with co-latitude without changing the principle of the calculations, for full simplicity we have taken the polar field to be of constant strength B_i over the whole region of interest. In the SPV model, the radial field in the northern hemisphere decreases from ~75,600 nT at the pole to ~66,400 nT at 20° co-latitude, while in the southern hemisphere it varies from ~62,400 to ~55,500 nT over the same range. Here, therefore, for general calculations we have taken the polar radial field strength to be $B_i = 64{,}000$ nT as a round value representative of both polar hemispheres. Inter-hemispheric differences can still be investigated in principle, however, by using differing field strengths for the two polar regions.

It is also useful to introduce the flux function of the field, F, which for an axi-symmetric field is related to the field components (in spherical polar co-ordinates) by $\boldsymbol{B} = (1/r\sin\theta)\nabla F \times \hat{\boldsymbol{\varphi}}$. The properties of the flux function are such that $F = \text{const}$

defines a flux shell mapping from the northern to the southern hemisphere via the equator, thus allowing easy field line mapping between these regions, and that the amount of magnetic flux contained between the shells of flux functions F_1 and F_2, integrated in azimuth around the axis, is $2\pi(F_2 - F_1)$. For a spherical ionosphere and a constant radial field, the above expression relating the flux function to the field is readily integrated to give the ionospheric flux function as

$$F(\theta_i) = B_i R_i^{\,2}(1 - \cos\theta_i) \quad , \tag{6.1}$$

where we have taken F to be zero on the magnetic axis.

6.3.2 Plasma flow and current

We now briefly give the basic equations which govern the plasma flow and current in our model calculations. The convective plasma flow, which applies to electrons throughout the ionosphere and also to ions above the layer where ion-neutral collisions occur (and where the ionospheric currents consequently flow), may be specified by defining either the ionospheric plasma velocity in the inertial frame, $\mathbf{V}_i$, or equivalently the corresponding electric field $\mathbf{E}_i$. These are related by

$$\mathbf{V}_i = \frac{\mathbf{E}_i \times \mathbf{B}_i}{\mathrm{B}_i^{\,2}} = \frac{\mathbf{E}_i \times \hat{\mathbf{r}}}{\mathrm{B}_i} \qquad \text{or} \qquad \mathbf{E}_i = -\mathbf{V}_i \times \mathbf{B}_i = \mathrm{B}_i \, \hat{\mathbf{r}} \times \mathbf{V}_i \quad , \tag{6.2a,b}$$

where the second expressions are valid specifically in the northern ionosphere where $\mathbf{B}_i$ points radially outward. Since the ionospheric magnetic field is essentially incompressible, the curl of $\mathbf{E}_i$ must be zero by Faraday's law, so the electric field can also be expressed as the gradient of a scalar potential Φ_i

$$\mathbf{E}_i = -\nabla\Phi_i \quad . \tag{6.3}$$

The motion of the ionospheric plasma can thus be determined by specifying either $\mathbf{V}_i$, $\mathbf{E}_i$, or Φ_i. Substitution of Eq. (6.3) into Eq. (6.2a) shows that the streamlines of the ionospheric flow are the equipotentials $\Phi_i = \text{const}$, where the magnetic flux per unit time transported between streamlines of potentials Φ_1 and Φ_2 is $(\Phi_2 - \Phi_1)$ Wb s^{-1}.

While the above quantities are defined in the inertial frame, the horizontal ionospheric Pedersen and Hall currents are determined by the electric field in the rest frame of the neutral atmosphere in the ionospheric current layer, $\mathbf{E}_i'$. Specifically, the height-integrated current intensities are given by

$$\mathbf{i}_P = \Sigma_P \mathbf{E}_i' \qquad \text{and} \qquad \mathbf{i}_H = \Sigma_H \hat{\mathbf{r}} \times \mathbf{E}_i' \quad , \tag{6.4a,b}$$

where Σ_P and Σ_H are the Pedersen and Hall conductances (the conductivities integrated in height through the ionosphere) respectively. This electric field is related to the value in the inertial frame $\mathbf{E}_i$ by

$$\mathbf{E}_i' = -(\mathbf{V}_i - \mathbf{V}_n) \times \mathbf{B}_i = \mathbf{E}_i + \mathbf{V}_n \times \mathbf{B}_i \quad , \tag{6.5}$$

where $\mathbf{V_n}$ is the velocity of the neutral atmosphere in the inertial frame. We further assume for simplicity that the neutral atmosphere rigidly corotates with the planet at speed $\mathbf{V}_{RC} = R_i \Omega_S \sin\theta_i \hat{\varphi}$ in the inertial frame (where Ω_S is Saturn's angular velocity equal to 1.638×10^{-4} rad s^{-1}), except for a wind driven by ion drag which is a constant factor *k* times the ion velocity in the corotating frame (see e.g. Huang and Hill [1989] and Millward et al. [2005] for discussions in a jovian context). That is, we assume $\mathbf{V}_n = \mathbf{V}_{RC} + k(\mathbf{V}_i - \mathbf{V}_{RC})$, so that $\mathbf{V}_i - \mathbf{V}_n = (1-k)(\mathbf{V}_i - \mathbf{V}_{RC})$. Substitution into Eq. (6.5) then yields

$$\mathbf{E}_i' = (1-\mathrm{k})\left(\mathbf{E}_i + \mathrm{B}_i \mathrm{R}_i \Omega_S \sin\theta_i \,\hat{\theta}\right) \,, \tag{6.6}$$

so that from Eq. (6.4) the ionospheric currents become

$$\mathbf{i}_P = \Sigma_P^* \left(\mathbf{E}_i + \mathrm{B}_i \mathrm{R}_i \Omega_S \sin\theta_i \,\hat{\theta}\right) \quad \text{and} \quad \mathbf{i}_H = \Sigma_H^* \left(\hat{\mathbf{r}} \times \mathbf{E}_i + \mathrm{B}_i \mathrm{R}_i \Omega_S \sin\theta_i \,\hat{\varphi}\right) \,, \tag{6.7a,b}$$

where $\Sigma_P^* = (1-k)\Sigma_P$ and $\Sigma_H^* = (1-k)\Sigma_H$ are the 'effective' Pedersen and Hall conductivities, respectively, reduced from the true values by 'slippage' of the neutral atmosphere from rigid corotation. The field-aligned current density is then determined from the horizontal current intensity by current continuity as $\mathrm{j}_{\|i} = -\mathrm{div}(\mathbf{i}_P + \mathbf{i}_H)$. For simplicity we take Σ_P^* and Σ_H^* to be constants in our model over the whole polar ionosphere. In this case we find that $\mathrm{div}\,\mathbf{i}_H = 0$, such that the Hall current closes wholly in the ionosphere, and the field-aligned current is determined only by the divergence of the Pedersen current. From Eq. (6.7a) we have

$$\mathrm{j}_{\|i} = -\mathrm{div}\,\mathbf{i}_P = -\Sigma_P^* \,\mathrm{div}\left(\mathbf{E}_i + \mathrm{B}_i \mathrm{R}_i \Omega_S \sin\theta_i \,\hat{\theta}\right) = \Sigma_P^* \left(\nabla^2 \Phi_i - 2\mathrm{B}_i \Omega_S \cos\theta_i\right) \,. \tag{6.8}$$

In accordance with the results discussed in Section 6.2 and the previous studies by Cowley and Bunce [2003b] and Cowley et al. [2004b], here we will take Σ_P^* to have a value of 1 mho.

6.3.3 Auroral parameters

Having determined the field-aligned currents, we are then interested to consider their consequences for auroral precipitation. Specifically we are interested in the regions of upward field-aligned current which are expected to be carried mainly by precipitating magnetospheric electrons, and whether these currents require field-aligned acceleration of the 'source' populations. To determine this, we compare the model values of the field-aligned current density with the maximum that can be carried by magnetospheric electrons without acceleration. This is given by

$$j_{\|i0} = eN\left(\frac{W_{th}}{2\pi\, m_e}\right)^{1/2} \quad , \tag{6.9}$$

where the magnetospheric electron population has been assumed to be an isotropic Maxwellian of density N and thermal energy W_{th} (equal to $k_B T$ where T is temperature and k_B is Boltzmann's constant), and e and m_e are the electron charge and mass respectively. This expression corresponds to the case of a full downward-going loss-cone, and an empty upward-going loss-cone. If the model current density is higher than that given by Eq. (6.9), then according to Knight's [1973] kinetic theory a field-aligned voltage must exist along the field lines which accelerates magnetospheric electrons into the ionosphere to produce the required current. The minimum value of this voltage is given by

$$\Phi_{\|} = \frac{W_{th}}{e}\left[\left(\frac{j_{\|i}}{j_{\|i0}}\right) - 1\right] \quad , \tag{6.10}$$

this value being appropriate if the 'top' of the voltage drop is located at a radial distance well above the minimum value given by

$$\left(\frac{r_{min}}{R_i}\right) \approx \left(\frac{j_{\|i}}{j_{\|i0}}\right)^{1/3} \quad . \tag{6.11}$$

In Eq. (6.11) we have assumed as a sufficient approximation that the field strength drops as the inverse cube of the radial distance along the polar field lines, corresponding to the planetary dipole field. Equation (6.10) also assumes that the voltage drop is sufficiently compact along the field lines that no electrons mirror before they have experienced the full voltage drop. Following Lundin and Sandahl [1978], the enhanced precipitating energy flux of the electrons is then given by

$$E_f = \frac{E_{f0}}{2}\left[\left(\frac{j_{\|i}}{j_{\|i0}}\right)^2 + 1\right] \ , \tag{6.12}$$

where E_{f0} is the unaccelerated electron energy flux corresponding to Eq. (6.9), given by

$$E_{f0} = 2NW_{th}\left(\frac{W_{th}}{2\pi\, m_e}\right)^{1/2} \ . \tag{6.13}$$

These expressions will be used below to estimate the field-aligned voltages, energy fluxes, and consequent UV auroral luminosities associated with the upward-directed currents in the model.

6.4 Model of the plasma flow and current

6.4.1 Form of the plasma velocity model

The model of the ionospheric flow presented here represents a development of the axi-symmetric models of Cowley and Bunce [2003b] and Cowley et al. [2004b], constructed to provide a quantitative representation of the asymmetric ionospheric flow pattern depicted in Fig. 2.9 of Chapter 2. Here we begin by providing an overview of the basis on which the model has been developed. We first assume for simplicity that the Vasyliunas cycle and the Dungey cycle return flow combine to produce an outer magnetosphere region which forms a symmetrical ring of closed flux centred on the pole, though containing faster flows at dawn than at dusk, as in Fig. 2.9 of Chapter 2. If so, the polar cap region of open flux is also circular, and centred on the pole. The resulting concentric ring geometry of the flow regions then greatly simplifies the mathematics of the model. In our analysis we will denote quantities associated with the polar cap region by subscript 'PC', the outer magnetosphere ring by 'OM', and the middle magnetosphere region at lower latitudes by 'MM'.

Briefly, for theoretical convenience, the flow model is taken to consist of the sum of two components. The first is a rotational flow (denoted by subscript 'RO') which is essentially similar to the axisymmetric model presented previously by Cowley et al. [2004b]. That is, with increasing latitude on closed field lines, the plasma angular velocity falls from near-rigid corotation in the inner magnetosphere to ~55% of rigid corotation at the outer boundary of the middle magnetosphere, and then increases to 75% of rigid corotation in the outer magnetosphere ring, these variations being in accord with the large-scale behaviour of the Voyager plasma velocity measurements [e.g. Richardson, 1986, 1995; Richardson and Sittler, 1990]. In view of the previous results of Cowley and Bunce [2003b] mentioned in Section 6.2, here we do not include representation of the smaller-scale flow features observed in some of those measurements. On open field lines the angular velocity then falls to 30% of rigid corotation, in accordance with the observations of Stallard et al. [2004] and the theory of Isbell et al. [1984] (for an effective ionospheric conductance of 1 mho). Flow asymmetry is then introduced by vectorially adding a second component consisting of a sun-aligned twin-vortex (denoted by subscript 'TV'), which provides anti-sunward flow across the polar cap at a rate determined by the Dungey-cycle voltage, and return sunward flow via dawn and dusk which is confined to the outer magnetosphere ring. As indicated in Section 6.2, this voltage is chosen to be equal to 200 kV corresponding to interplanetary compression region conditions, based on estimates presented in Chapter 4, and by Badman et al. [2005]. For simplicity, the twin-vortex is chosen to be symmetrical about the noon-midnight meridian. The sunward 'return' flow is thus the same at dawn and dusk, but adds vectorially to the rotational flow in the outer magnetosphere region to produce a combined flow which, though directed consistently eastward, is increased to close to rigid corotation at dawn, but reduced to near outer middle magnetosphere values (~55% of rigid corotation) at dusk. Specifically, we choose the width of the outer magnetosphere ring such that the averaged angular velocity of the twin vortex flow at dawn and dusk corresponds to 20% of rigid corotation. If the flow associated with the rotational component is then 75% of rigid corotation, as indicated above, the combined flow in the outer magnetosphere ring will average to 95% of rigid corotation at dawn and 55% at dusk, in conformity with the above discussion. With regard to the middle magnetosphere at lower latitudes, we note that (as indicated above) the return flow of the twin-vortex is confined wholly to the outer magnetosphere ring, so that only the rotational flow component contributes in this region.

Having thus outlined the nature of the flow, we now consider the location of the boundaries between the three flow regions, specified by the choice of boundary flux function values, related to co-latitude through Eq. (6.1). The boundary of the polar cap (denoted by subscript 'BPC') is first chosen to correspond to flux function $F_{BPC} = 1530$ nT R_S^2, essentially the same as employed previously by Cowley et al. [2004b]. The amount of open flux contained within the polar cap is then $2\pi F_{BPC} \approx 35\ \mathrm{GWb}$, a value consistent with in situ magnetic field data obtained from the Voyager spacecraft [Ness et al., 1981; Cowley et al., 2004b], and with the results of Badman et al. [2005] derived from HST images. From Eq. (6.1) the co-latitude of the polar cap boundary is then $\theta_{i\,BPC} \approx 13.68°$. As indicated above, the location of the boundary of the outer magnetosphere region (denoted by subscript 'BOM'), where it interfaces with the middle magnetosphere, is then chosen so that the averaged angular velocity within this region associated with the twin-vortex flow is 20% of rigid corotation. Since the total amount of magnetic flux in the outer magnetosphere ring is $2\pi(F_{BOM} - F_{BPC})$, it is easy to show that the flux per unit time transported by an azimuthal plasma flow of angular velocity ω in the inertial frame is just $\omega(F_{BOM} - F_{BPC})$, equal to the voltage associated with the electric field across the ring in that frame. Since the voltage associated with the 'return' flow of the twin vortex at both dawn and dusk is just half the Dungey-cycle voltage Φ_{DC} (the voltage associated with the antisunward transport across the polar cap), we thus have

$$\left(F_{BOM} - F_{BPC}\right) = \frac{\Phi_{DC}}{2\langle\omega\rangle_{TV}} \quad , \tag{6.14}$$

where Φ_{DC} is chosen to be 200 kV as indicated above, and the averaged angular velocity associated with the twin-vortex return flow is chosen to be $\langle\omega\rangle_{TV} = 0.2\,\Omega_S$. From Eq. (6.14) we then find $F_{BOM} \approx 2368.67\ \mathrm{nT\ R_S}^2$, corresponding to a co-latitude of $\theta_{i\,BOM} \approx 17.05°$, such that the amount of closed flux in the outer magnetosphere ring is ~19 GWb. We note that the flux function value of the corresponding feature in the axisymmetric Cowley et al. [2004b] model based solely on Voyager data is 2200 nT Rs^2, similar to the value employed here.

We can now also derive the value of the voltage (flux transport) associated with the Vasyliunas cycle in the model. On a similar basis to the above, the voltage across the outer magnetosphere ring associated with the rotational flow component is $\Delta\Phi_{RO\,OM} = \omega_{OM}\left(F_{BOM} - F_{BPC}\right)$, where $\omega_{OM} = 0.75\,\Omega_S$ is the angular velocity associated with this flow component in this region, as above. Substituting from Eq. (6.14) we then find

$$\Delta\Phi_{RO\,OM} = \frac{\omega_{OM}}{2\langle\omega\rangle_{TV}}\Phi_{DC} \quad , \tag{6.15}$$

so that with the above numbers we have $\Delta\Phi_{RO\,OM} = 375\ \mathrm{kV}$. The combined voltage at dusk, equal to the voltage in the Vasyliunas cycle, is then

$$\Phi_{VC} = \Delta\Phi_{RO\,OM} - \frac{\Phi_{DC}}{2} = 275\ \mathrm{kV} \quad , \tag{6.16}$$

comparable with, but slightly larger than the Dungey-cycle voltage. The combined voltage at dawn is similarly $\Delta\Phi_{RO\,OM} + (\Phi_{DC}/2) = 475\ \mathrm{kV}$, equal to the sum of the Dungey-cycle and the Vasyliunas-cycle voltages (see Fig. 2.9 of Chapter 2).

The above discussion has thus provided an overview of how the flow model is constructed, and how its major parameters have been determined. Below we provide a systematic quantitative description of its components, and begin with the rotational flow.

6.4.2 Rotational flow model

The rotational flow is specified by defining the plasma angular velocity as a function of the flux function, $\omega_{RO} = \omega_{RO}(F)$. In conformity with the discussion above we choose for the polar cap

$$\omega_{RO}(F) = \omega_{PC} = 0.3\,\Omega_S \quad , \tag{6.17a}$$

while for the outer magnetosphere

$$\omega_{RO}(F) = \omega_{OM} = 0.75\,\Omega_S \quad , \tag{6.17b}$$

and for the middle magnetosphere

$$\omega_{RO}(F) = \Omega_S - (\Omega_S - \omega_{BMM})\frac{\left(1 + (F_{BOM}/F_{MM})^n\right)}{\left(1 + (F/F_{MM})^n\right)} \quad . \tag{6.17c}$$

The last expression is based on the overall plasma angular velocity profiles observed during the Voyager fly-bys, as employed previously by Cowley and Bunce [2003b] and Cowley et al. [2004b], and is such that the angular velocity in the middle magnetosphere at the BOM boundary is $\omega_{RO}(F_{BOM}) = \omega_{BMM}$, and then increases to rigid corotation,

$\omega_{RO} = \Omega_S$, as F becomes large. The change from sub-corotation at angular frequency ω_{BMM} to rigid corotation takes place in the vicinity of $F \approx F_{MM}$, and the change is increasingly sharp as the exponent n increases. The specific values employed here are $\omega_{BMM} \approx 0.587\,\Omega_S$, $F_{MM} = 3600\,\mathrm{nT\,R_S}^2$, and $n = 8$ [Cowley et al., 2004b]. The value of ω_{BMM} has been chosen so that there is no discontinuity in the combined flow (rotational plus twin vortex) at the dusk 'BOM' boundary between the outer and middle magnetosphere.

The associated ionospheric plasma velocity and electric field in the inertial frame (Eq. (6.2b)) are then

$$\mathbf{V}_{\boldsymbol{i\,RO}} = \boldsymbol{R_i} \sin\theta_i \omega_{\boldsymbol{RO}} \hat{\boldsymbol{\varphi}} \qquad \text{and} \qquad \mathbf{E}_{\boldsymbol{i\,RO}} = -\boldsymbol{B_i}\boldsymbol{R_i} \sin\theta_i \omega_{\boldsymbol{RO}} \hat{\boldsymbol{\theta}} \quad , \tag{6.18a,b}$$

while from Eq. (6.3) the electrostatic potential, assumed zero on the axis, is

$$\Phi_{RO}(F) = \int_0^F \omega(F')dF' \quad , \tag{6.19}$$

a form which is generally valid for an axi-symmetric field and flow. Due to the constant values of plasma angular velocity in the polar cap and outer magnetosphere assumed above, the expressions for the electrostatic potential in these regions are especially simple. For the polar cap we have

$$\Phi_{RO}(F) = \omega_{PC} F \quad , \tag{6.20a}$$

while for the outer magnetosphere

$$\Phi_{RO}(F) = \omega_{OM}(F - F_{BPC}) + \omega_{PC} F_{BPC} \quad . \tag{6.20b}$$

With the above values, the voltage across the polar cap associated with the rotational flow in the inertial frame is thus ~273.6 kV, comparable to the Dungey- and Vasyliunas-cycle values, while that across the outer magnetosphere is 375 kV as previously indicated.

6.4.3 Twin-vortex flow model

The twin-vortex flow is described by specifying an electrostatic potential as a function of co-latitude θ_i and azimuthal angle φ_i on the ionospheric sphere, $\Phi_{i\,TV}(\theta_i, \varphi_i)$, which, when added to the rotational potential given by Eq. (6.20), gives the total potential, and hence the electric field and flow of the model. Azimuth φ_i increases with local time, and is defined such that $\varphi_i = 0°$ points towards the Sun. In common with previous derivations of related twin-vortex flows in the terrestrial system (see below), we look for potentials which are solutions of Laplace's equation on a spherical surface

$$\nabla^2 \Phi_{i\,TV} = \frac{1}{R_i^{\,2} \sin^2 \theta_i} \left[\sin\theta_i \frac{\partial}{\partial \theta_i} \left(\sin\theta_i \frac{\partial \Phi_{i\,TV}}{\partial \theta_i} \right) + \frac{\partial^2 \Phi_{i\,TV}}{\partial^2 \varphi_i} \right] = 0 \quad . \tag{6.21}$$

Physically acceptable solutions are obtained separately for the polar cap and the outer magnetosphere, where the outer boundary of the latter region is taken to be an equipotential (i.e. a streamline), such that the twin-vortex flow does not extend into the middle magnetosphere at lower latitudes as previously stated. The solutions in the polar cap and outer magnetosphere regions are then joined by specifying a common distribution of potential around the polar cap (BPC) boundary. We note from Eq. (6.8) that the effect of these assumptions is to confine the field-aligned currents associated with the twin-vortex flow to sheet currents lying on the BPC and BOM boundaries. Following the formulation of Freeman and Southwood [1988] and Freeman et al. [1991], to solve Eq. (6.21) we change variable from θ_i to x_i given by

$$x_i = \log_e\left(\tan\frac{\theta_i}{2}\right) \qquad \text{so that} \qquad \sin\theta_i\frac{\partial}{\partial\theta_i} \equiv \frac{\partial}{\partial x_i} \quad , \tag{6.22a,b}$$

and look for separable solutions. The required solutions are as follows. For $x_i \le x_{i\,BPC}$ in the polar cap we have

$$\Phi_{i\,TV}(x_i,\varphi_i) = \sum_{m=1}^{\infty}(a_m \sin m\varphi_i + b_m \cos m\varphi_i)\exp\left(m\left(x_i - x_{i\,BPC}\right)\right) \quad , \tag{6.23}$$

while for $x_{i\,BPC} \le x_i \le x_{i\,BOM}$ in the outer magnetosphere

$$\Phi_{i\,TV}(x_i,\varphi_i) = \sum_{m=1}^{\infty}(a_m \sin m\varphi_i + b_m \cos m\varphi_i)\frac{\sinh\left(m\left(x_{i\,BOM} - x_i\right)\right)}{\sinh\left(m\left(x_{i\,BOM} - x_{i\,BPC}\right)\right)} \quad . \tag{6.24}$$

In these expressions $x_{i\,BPC}$ and $x_{i\,BOM}$ are the values of x_i on the BPC and BOM boundaries, respectively, defined by the flux function values of the boundaries, F_{BPC} and F_{BOM}, and the corresponding co-latitudes of the boundaries, $\theta_{i\,BPC}$ and $\theta_{i\,BOM}$ obtained from Eq. (6.1). The expressions are such that on the BOM boundary we have $\Phi_{i\,TV}\left(x_{i\,BOM},\varphi_i\right) = 0$ for all φ_i, as required (i.e. the BOM boundary is an equipotential), while on the BPC boundary Eqs. (6.23) and (6.24) both give

$$\Phi_{i\,TV}\left(x_{i\,BPC},\varphi_i\right) = \sum_{m=1}^{\infty}(a_m \sin m\varphi_i + b_m \cos m\varphi_i) \quad , \tag{6.25}$$

which expresses the boundary potential as a Fourier series in φ_i. We can then choose any single-valued function for the distribution of potential around the boundary, $\Phi_{i\,TV}\left(x_{i\,BPC},\varphi_i\right)$, and solve for the required coefficients a_m and b_m through the usual Fourier integrals

$$a_m = \frac{1}{\pi}\int_{-\pi}^{\pi} d\varphi_i \; \Phi_{i\,TV}\left(x_{i\,BPC},\varphi_i\right)\sin m\varphi_i \quad \text{and} \qquad b_m = \frac{1}{\pi}\int_{-\pi}^{\pi} d\varphi_i \; \Phi_{i\,TV}\left(x_{i\,BPC},\varphi_i\right)\cos m\varphi_i \quad . \tag{6.26a,b}$$

(Note that the arbitrary zero of potential has been chosen so that the averaged value of $\Phi_{i\,TV}\left(x_{i\,BPC},\varphi_i\right)$ around the boundary is zero. Any common constant potential value can be added to those given by Eqs. (6.23)-(6.25) if this is not the case.) Equations (6.23) and (6.24) then give the required solutions in the polar cap and outer magnetosphere for the given distribution of potential on the BPC (open-closed field line) boundary.

We thus now consider the potential on this boundary, and derive the corresponding Fourier coefficients. We first note from Eq. (6.26b) that if the twin-vortex flow is symmetric about the noon-midnight meridian, as will be assumed here, then the b_m coefficients are zero for all m. Furthermore, if the pattern is also symmetric about the dawn-dusk meridian, as will also be assumed for simplicity, then the only non-zero a_m are those with m odd. The simplest choice would be to take $a_1 = \Phi_{DC}/2$, where Φ_{DC} is the total twin-vortex voltage across the polar cap driven by the Dungey cycle, with all other a_m zero, giving a very broad distribution of flow into and out of the polar cap about noon and midnight respectively. More realistically, however, the flow into (and out of) the polar cap may be more restricted in local time about noon (and midnight), giving rise to a 'merging gap' flow configuration. Here we therefore take for the 'afternoon' quadrant $0 \le \varphi_i \le \pi/2$

$$\Phi_{i\,TV}\left(\theta_{i\,BPC},\varphi_i\right) = \frac{\Phi_{DC}}{2}\left\{\begin{array}{ll} \sin\left(\dfrac{\pi\varphi_i}{\varphi_{MG}}\right) & \text{for } \; 0 \le \varphi_i \le \dfrac{\varphi_{MG}}{2} \\ \\ 1 & \text{for } \; \dfrac{\varphi_{MG}}{2} \le \varphi_i \le \dfrac{\pi}{2} \end{array}\right\} , \tag{6.27}$$

with corresponding expressions for the other quadrants. With Eq. (6.27), flow takes place across the boundary only in azimuthal sectors of total angular width φ_{MG} about noon (and midnight), and is zero (the boundary is 'adiaroic') elsewhere. The functional form chosen avoids a discontinuity in the first derivative of the potential (i.e. in the azimuthal component of the electric field and hence the north-south flow) at the junction between the merging gap and the adiaroic section of the boundary. Introducing Eq. (6.27) into Eq. (6.26a) then yields for m odd

$$a_m = \frac{4}{\pi}\int_0^{\pi/2} d\varphi_i \; \Phi_{i\,TV}\left(\theta_{i\,BPC}, \varphi_i\right)\sin m\varphi_i = \left(\frac{2\Phi_{DC}}{\pi}\right)\cos\left(\frac{m\varphi_{MG}}{2}\right)\left[\frac{1}{m} + \frac{m}{\left((\pi/\varphi_{MG})^2 - m^2\right)}\right] \quad , \tag{6.28}$$

with other coefficients being zero as indicated above. The angular extent of the merging gap has been somewhat arbitrarily set as $\varphi_{MG} = 45°$, so that inflow (and outflow) of open flux into the polar cap is restricted to one quarter of the angular extent of the dayside (and nightside) boundaries. We also take $\Phi_{DC} = 200\text{ kV}$ as previously indicated.

The above equations thus define the potential associated with the twin-vortex flow. The electric field and flow components are then given by

$$E_{i\,TV\,\theta} = -B_i V_{i\,TV\,\varphi} = -\frac{1}{R_i \sin\theta_i}\frac{\partial \Phi_{i\,TV}}{\partial x_i} \tag{6.29a}$$

and

$$E_{i\,TV\,\varphi} = B_i V_{i\,TV\,\theta} = -\frac{1}{R_i \sin\theta_i}\frac{\partial \Phi_{i\,TV}}{\partial \varphi_i} \quad , \tag{6.29b}$$

so that in the polar cap we have (in general)

$$E_{i\,TV\,\theta} = -B_i V_{i\,TV\,\varphi} = -\frac{1}{R_i \sin\theta_i}\sum_{m=1}^{\infty} m\left(a_m \sin m\varphi_i + b_m \cos m\varphi_i\right)\exp\left(m\left(x_i - x_{i\,BPC}\right)\right) \tag{6.30a}$$

and

$$E_{i\,TV\,\varphi} = B_i V_{i\,TV\,\theta} = -\frac{1}{R_i \sin\theta_i} \sum_{m=1}^{\infty} m\left(a_m \cos m\varphi_i - b_m \sin m\varphi_i\right) \exp\left(m\left(x_i - x_{i\,BPC}\right)\right) \ , \qquad (6.30b)$$

while in the outer magnetosphere

$$E_{i\,TV\,\theta} = -B_i V_{i\,TV\,\varphi} = \frac{1}{R_i \sin\theta_i} \sum_{m=1}^{\infty} m\left(a_m \sin m\varphi_i + b_m \cos m\varphi_i\right) \frac{\cosh\left(m\left(x_{i\,BOM} - x_i\right)\right)}{\sinh\left(m\left(x_{i\,BOM} - x_{i\,BPC}\right)\right)}$$

(6.31a)

and

$$E_{i\,TV\,\varphi} = B_i V_{i\,TV\,\theta} = -\frac{1}{R_i \sin\theta_i} \sum_{m=1}^{\infty} m\left(a_m \cos m\varphi_i - b_m \sin m\varphi_i\right) \frac{\sinh\left(m\left(x_{i\,BOM} - x_i\right)\right)}{\sinh\left(m\left(x_{i\,BOM} - x_{i\,BPC}\right)\right)} \ .$$

(6.31b)

6.4.5 Ionospheric and field-aligned currents

Using the electric fields and potentials of the rotational and twin-vortex flows described above, we can now determine both the horizontal ionospheric Pedersen current from Eq. (6.7a), and the consequent field-aligned current from Eq. (6.8). Hall currents are not considered, since with the assumptions given above these close wholly in the ionosphere as previously indicated. Adding the contributions from the twin-vortex and the rotational flows, we find from Eqs. (6.7a) and (6.18b) the total Pedersen current to be given by

$$\boldsymbol{i}_P = \Sigma_P^* \left(\boldsymbol{E}_{i\,TV} + B_i R_i \sin\theta_i \left(\Omega_S - \omega_{RO}(F)\right)\hat{\boldsymbol{\theta}}\right) \ . \qquad (6.32)$$

Substituting into Eq. (6.8) to find the field-aligned current density, we find that the term associated with the twin vortex flow drops out due to the assumption in Eq. (6.21) as previously indicated, such that the distributed field-aligned current density is associated only with the rotational component of the flow, given by

$$j_{\|i} = -\frac{\Sigma_P^* B_i}{\sin\theta_i}\frac{d}{d\theta_i}\left[\sin^2\theta_i\left(\Omega_S - \omega_{RO}(F)\right)\right] \quad . \tag{6.33}$$

The distributed field-aligned current in the model is thus axi-symmetric. For the polar cap region we find

$$j_{\|i} = -2\Sigma_P^* B_i\left(\Omega_S - \omega_{PC}\right)\cos\theta_i \quad , \tag{6.34a}$$

while for the outer magnetosphere

$$j_{\|i} = -2\Sigma_P^* B_i\left(\Omega_S - \omega_{OM}\right)\cos\theta_i \quad . \tag{6.34b}$$

The distributed field-aligned currents in these regions are thus directed downward into the ionosphere, vary slowly with co-latitude, and are larger in the polar cap than in the outer magnetosphere if ω_{OM} is closer to rigid corotation than is ω_{PC} as assumed here. For the middle magnetosphere we also find from Eq. (6.17c)

$$j_{\|i} = -\Sigma_P^* B_i\left(\Omega_S - \omega_{RO}(F)\right)\left(2\cos\theta_i - \frac{\sin^2\theta_i}{\left(1-\cos\theta_i\right)}\frac{n}{\left(\left(F_{MM}/F\right)^n + 1\right)}\right) \quad , \tag{6.34c}$$

where F is given by Eq. (6.1). This function is such that the field-aligned current density is negative (downward) at the BOM boundary, then reverses to positive with increasing co-latitude, before peaking and falling to small values as the plasma angular velocity approaches rigid corotation, as will be shown in the results below. These properties are essentially the same as those in the axi-symmetric model of Cowley et al. [2004b].

In addition to these distributed field-aligned currents, sheet field-aligned currents also flow at the circular BPC and BOM boundaries due to discontinuities in the co-latitudinal Pedersen currents. These discontinuities are driven by shears in the azimuthal flow across the boundaries, with contributions being provided both by the rotational and the twin-vortex flow components. The contribution from the rotational flow component is independent of local time, while the twin-vortex flow provides dawn-dusk asymmetries as discussed above. From Eqs. (6.17a,b) and (6.32), the contribution at the polar cap boundary (BPC) from the rotational flow component is

$$i_{\| i\,RO} = \Sigma_P^* B_i R_i \sin\theta_{i\,BPC}\left(\omega_{OM} - \omega_{PC}\right) \ , \tag{6.35a}$$

where a positive value indicates an upward-directed current, while using Eqs. (6.17b,c) at the outer magnetosphere boundary (BOM) we have

$$i_{\| i\,RO} = -\Sigma_P^* B_i R_i \sin\theta_{i\,BOM}\left(\omega_{OM} - \omega_{BMM}\right) \ . \tag{6.35b}$$

Similarly from Eqs. (6.30a), (6.31a), and (6.32), the contribution at the polar cap boundary from the twin vortex flow is (in general)

$$i_{\| i\,TV} = -\frac{2\Sigma_P^*}{R_i \sin\theta_{i\,BPC}} \sum_{m=1}^{\infty} m\left(a_m \sin m\varphi_i + b_m \cos m\varphi_i\right) \frac{1}{\left(1 - \exp\left(-2m\left(x_{i\,BOM} - x_{i\,BPC}\right)\right)\right)} \ , \tag{6.36a}$$

while at the outer magnetosphere boundary we have from Eq. (6.31a) and recalling that the twin vortex flow is taken to be zero in the middle magnetosphere

$$i_{\| i\,TV} = \frac{2\Sigma_P^*}{R_i \sin\theta_{i\,BOM}} \sum_{m=1}^{\infty} m\left(a_m \sin m\varphi_i + b_m \cos m\varphi_i\right) \frac{1}{\sinh\left(m\left(x_{i\,BOM} - x_{i\,BPC}\right)\right)} \ . \tag{6.36b}$$

This completes the mathematical description of our model of the flows and currents in Saturn's polar ionosphere. We now proceed to present the results derived on this basis.

6.5 Results

6.5.1 Flow streamlines

We begin our discussion by presenting an overview of the overall pattern of ionospheric plasma flow in our model. This is illustrated in Fig. 6.1, where we show the streamlines of the flow in polar plots, obtained by contouring the associated electrostatic potential, Φ_i . In Figs. 6.1a to 6.1c we show separately the streamlines of the rotational flow, the twin vortex flow, and the combined flow, respectively. In each plot the contours are shown at fixed voltage intervals, such that their spacing gives an impression of the relative speed of the flow in the various model regions. The direction toward the Sun (i.e. noon, corresponding to $\varphi_i = 0°$) is at the bottom of each diagram, dusk ($\varphi_i = 90°$) is to the right, and dawn ($\varphi_i = 270°$) to the left. The region from the pole to 20º co-latitude is shown, marked at 5º intervals by the dotted circles. The circles shown by the blue dashed lines then indicate the 'polar cap boundary' (BPC), the interface between the open flux region and the outer magnetosphere, and the 'outer magnetosphere boundary' (BOM), the interface between the outer and middle magnetosphere, located at ~13.68º and ~17.05º co-latitude respectively.

Figure 6.1a shows a plot of the streamlines for the eastward-directed rotational flow only, given by Eqs. (6.17)-(6.20). The contours of potential in this case are shown at 100 kV intervals, from zero at the pole at the centre of the plot, to 1000 kV at the outermost contour shown. It can be seen that the potential increases relatively slowly within the polar cap region of open field lines, indicative of the relatively slow rotation of the plasma, reaching ~274 kV at the polar cap boundary. The azimuthal flow then increases in the outer magnetosphere ring, as indicated by the more closely-spaced streamlines in this region, such that the potential rises to ~649 kV at the outer magnetosphere boundary. Beyond this, in the middle magnetosphere, the azimuthal velocities initially fall somewhat, before increasing again at lower latitudes as the plasma angular velocity increases towards near-rigid corotation with the planet.

Figure 6.1b shows a plot of the flow streamlines for the twin vortex flow only, given by Eqs. (6.23), (6.24) and (6.27). This plot has been derived using 25 terms in the Fourier series in Eqs. (6.23) and (6.24) (from $m = 1$ to $m = 51$ with m odd only), as is the case for all the plots shown in this section. The format is the same as for Fig. 6.1a, except that the spacing between the contours has been reduced to 20 kV. It can be seen that the twin vortex provides a roughly uniform anti-sunward flow across the polar cap, though with somewhat higher speeds near the boundary at noon and midnight, compared with dawn and dusk, due to the confined 'merging gap' nature of the flow across the open-closed field line boundary. These streamlines then close wholly in the outer magnetosphere ring at lower latitudes, symmetrically between dawn and dusk. The potential contours are much more closely spaced in this region, indicating faster flows directed almost azimuthally via dawn and dusk. The twin vortex flow terminates at the outer magnetosphere boundary (outer blue long-dashed circle), and does not extend into the middle magnetosphere region at lower latitudes.

The streamlines of the combined flow, obtained by adding the potentials contoured in Figs. 6.1a and 6.1b, are shown in Fig. 6.1c, where the streamlines are again shown with 100 kV between each contour, as in Fig. 6.1a. It can be seen that two types of streamline are now present in the region of open field lines, reflecting the contrasting behaviours in Figs. 6.1a and 6.1b. On the dusk side of the polar cap, streamlines pass between the dayside and nightside 'merging gaps', corresponding to an anti-sunward motion driven by the solar wind, combined with a strongly sub-corotational circulation. These streamlines are then closed in the outer magnetosphere ring via dawn, within the region bounded by the red dot-dashed line. The red line thus marks the boundary between the Dungey-cycle flow in the polar region and the Vasyliunas-cycle flow at lower latitudes, and is at a potential of ~373.6 kV. On the dawn side of the polar cap, however, streamlines close wholly within the region of open field lines. Although the existence of closed flow streamlines contained within the polar cap may initially seem counterintuitive, Milan et al. [2005] have recently discussed how the plasma rotation within the polar cap promotes the closure of more recently opened field lines in the tail, as implied by Fig. 6.1c, while others may remain within the tail for longer intervals, thus

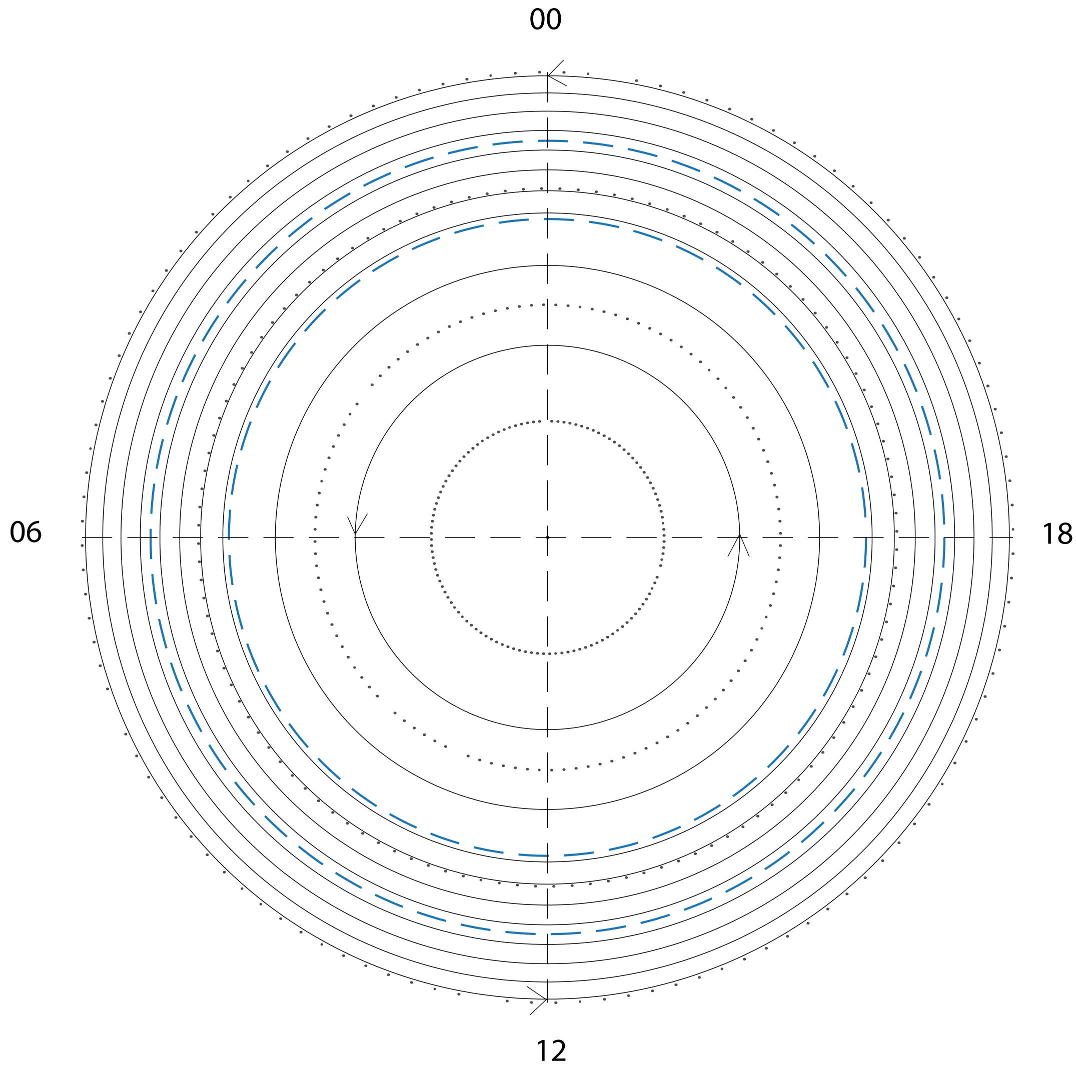

Figure 6.1a: Streamlines of the model ionospheric flow in the inertial frame, obtained by contouring the electrostatic potential, on a polar grid. The direction to the Sun is at the bottom of the diagrams, dusk to the right, and dawn to the left. The region from the pole to 20º co-latitude is shown, marked at 5º intervals by dotted circles. Inner and outer circles shown by the blue dashed lines indicate the boundary of the polar cap (BPC) and the boundary of the outer magnetosphere (BOM), respectively. Long dashed lines indicate the noon-midnight and dawn-dusk meridians. (a) Shows contours of the potential for the rotational flow component only, at consistent 100 kV intervals from zero at the pole to 1000 kV at the outermost contour at ~20º co-latitude.

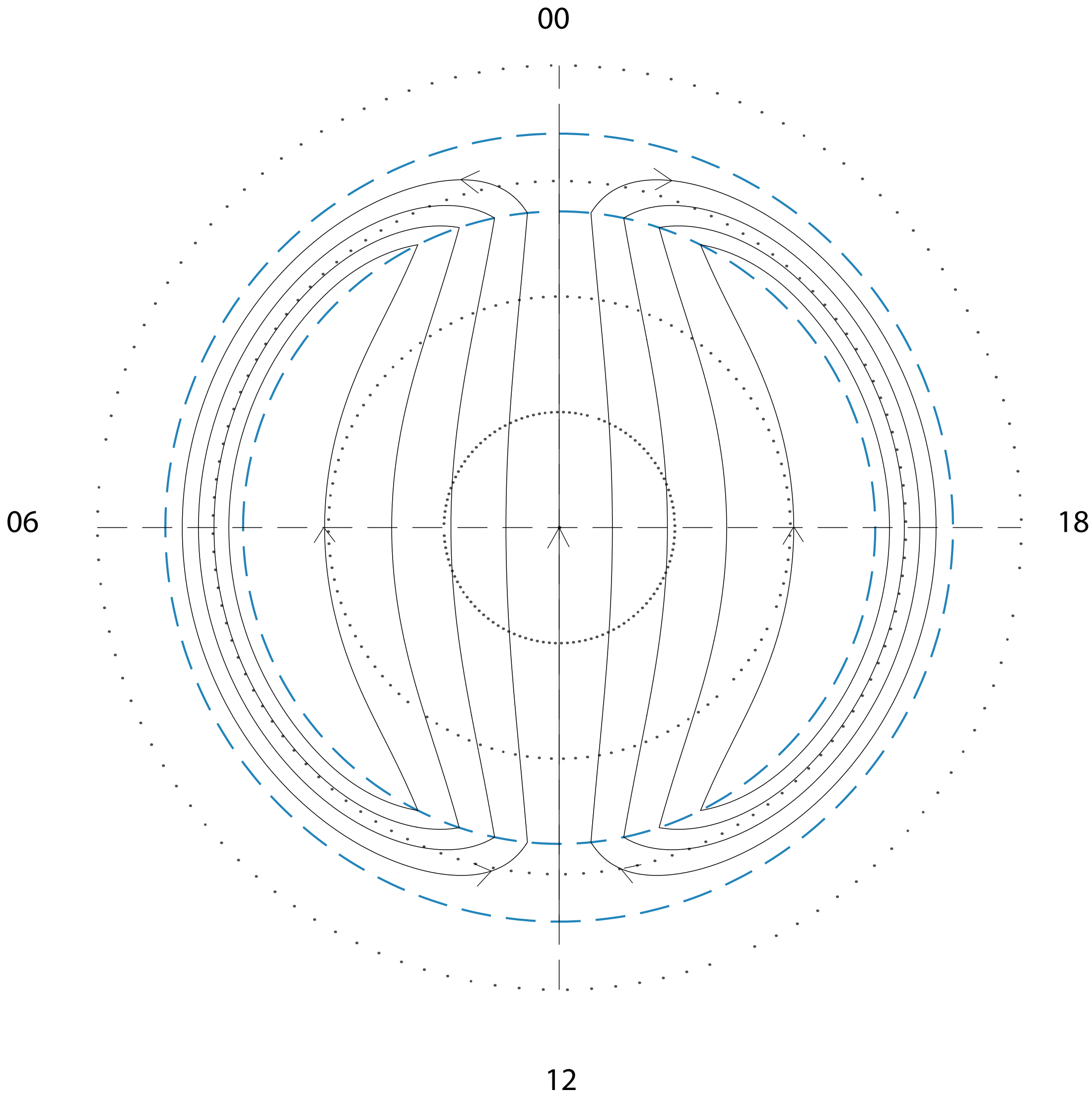

Figure 6.1b: Shows contours of the potential for the twin vortex flow only, in a similar format to Fig. 6.1a, except that contours are shown at intervals of 20 kV.

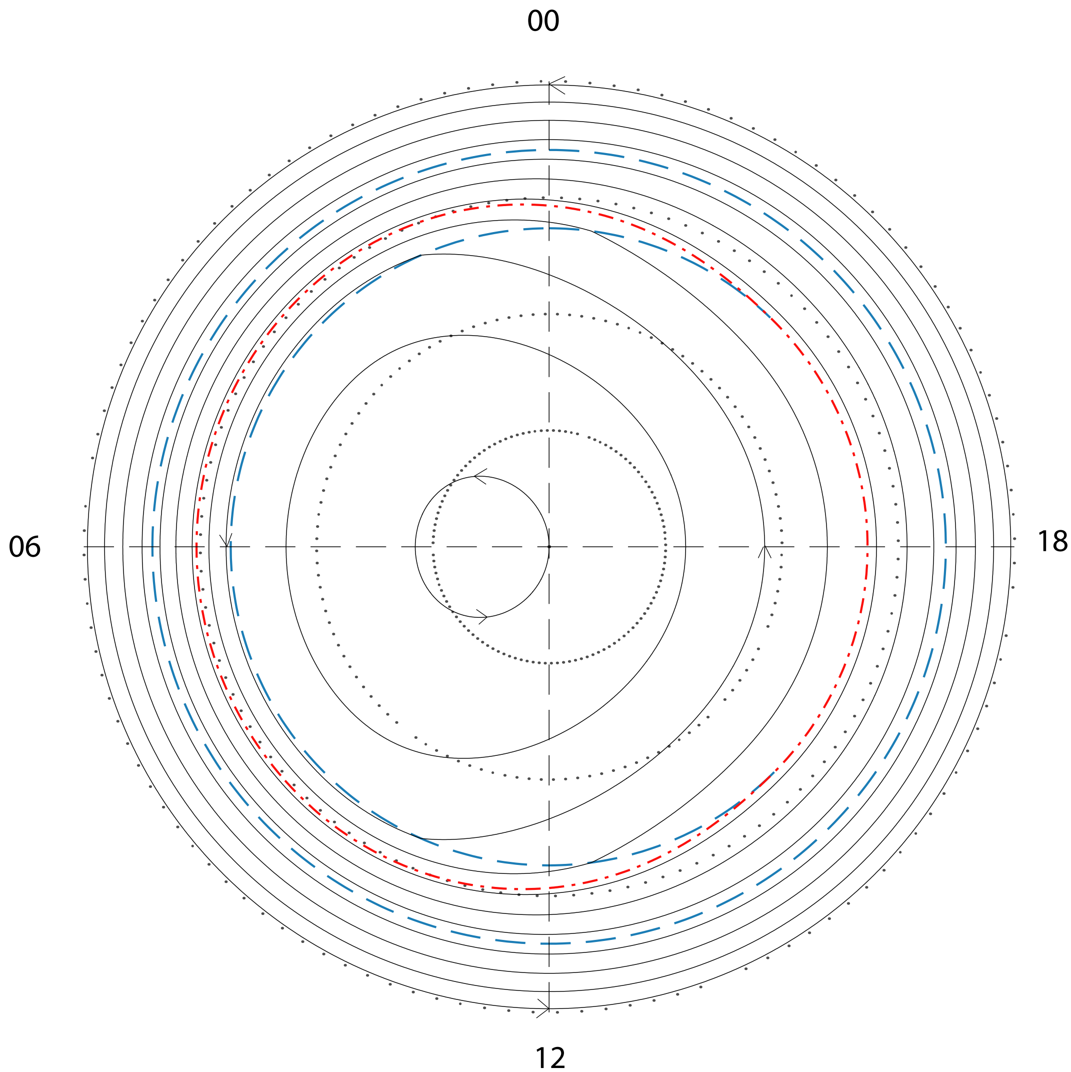

Figure 6.1c: Shows contours of potential for the combined rotational and twin vortex flow (i.e. the potentials shown in (6.1a) and (6.1b) added together), with contours of potential again being shown at 100 kV intervals. The red dot-dashed line marks the boundary between the regions of Dungey-cycle and Vasyliunas-cycle flow in the outer magnetosphere, at a potential of ~373.6 kV.

forming a very extended tail of connected open field lines. Eventually, however, such regions of open flux will become closed again, during episodes of strong tail reconnection that reach to very high latitudes [e.g. Cowley et al., 2005a].

The overall dawn-dusk asymmetry effects introduced by adding the twin vortex flow to the rotational flow (the latter being essentially the flow in the axi-symmetric model of Cowley et al. [2004b]), can thus be seen qualitatively by comparison of Figs. 6.1a and 6.1c. In the polar cap, the twin vortex flow reduces the eastward flow at dawn, and enhances it at dusk. In the outer magnetosphere region, on the other hand, the twin vortex flow enhances the eastward flow at dawn (where the flow corresponds to the sum of the Vasyliunas cycle and the Dungey-cycle return flow), and reduces it at dusk (where the flow corresponds to the Vasyliunas cycle alone). Consequently, the addition of the twin vortex enhances the flow shears at both the polar cap and outer magnetosphere boundaries at dawn, and hence also the sheet field-aligned currents, while reducing them at both boundaries at dusk. In the following sections we now examine these asymmetry effects more quantitatively.

6.5.2 Plasma velocities

In Figs. 6.2 and 6.3 we show co-latitude profiles of the azimuthal flow from the pole to 30º co-latitude on the principal local time meridians, in two complementary formats. In Fig. 6.2 we show the plasma angular velocity ω of the combined flow normalized to Ω_S, where ω is defined simply by

$$\omega = \frac{V_{i\varphi}}{R_i \sin\theta_i} \quad , \tag{6.37}$$

where $V_{i\varphi}$ is the total plasma azimuthal velocity. This format lends itself to discussion of departures of the plasma flow from rigid corotation. In Fig. 6.3 we show the total

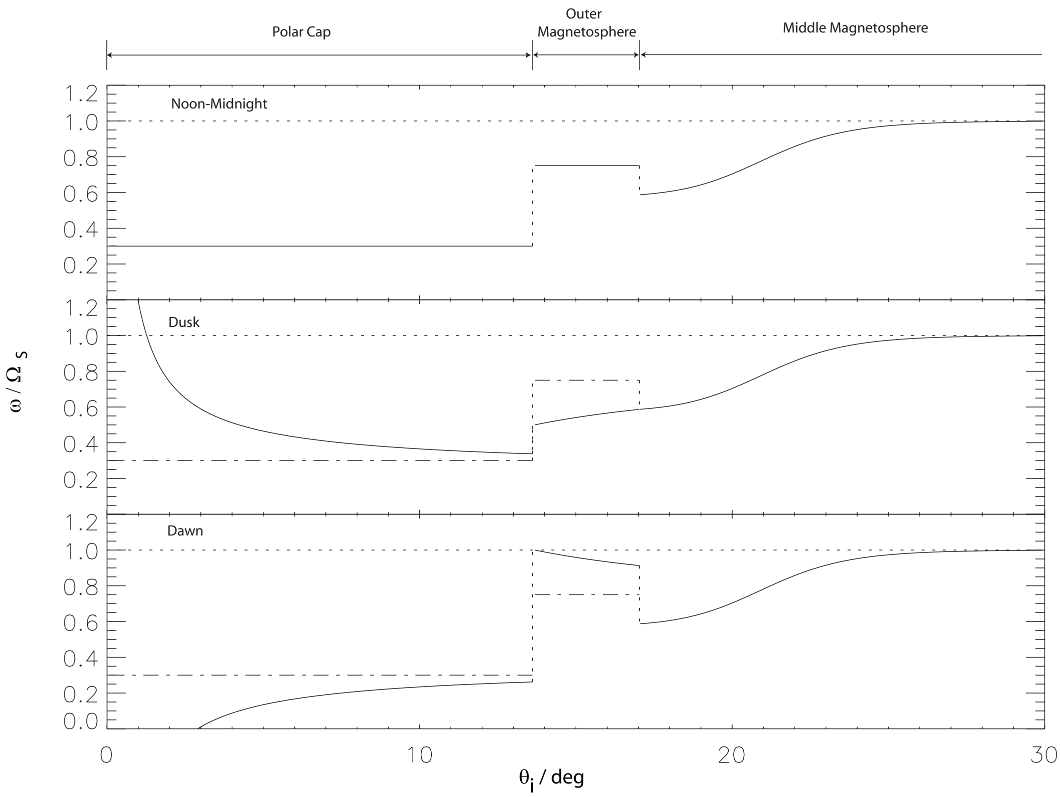

Figure 6.2: Plot of the total plasma angular velocity in the model, ω, defined by Eq. (6.37), normalized to Saturn's angular velocity, Ω_S, shown versus co-latitude angle θ_i on the principal meridians. The horizontal bars at the top of the figure indicate the regions of co-latitude that map to the polar cap, the outer magnetosphere, and the middle magnetosphere regions. The solid line in the upper panel shows the plasma angular velocity on the noon and midnight meridians, which results from the rotational flow component only. The horizontal dotted line shows rigid corotation. The middle panel similarly shows the total plasma angular velocity on the dusk meridian, shown by the solid line, while for comparison the dot-dashed line shows the rotational flow component only, as on the noon-midnight meridian in the upper panel. The solid line in the lower panel then shows the total plasma angular velocity on the dawn meridian, while the dot-dashed line again shows the rotational flow component only.

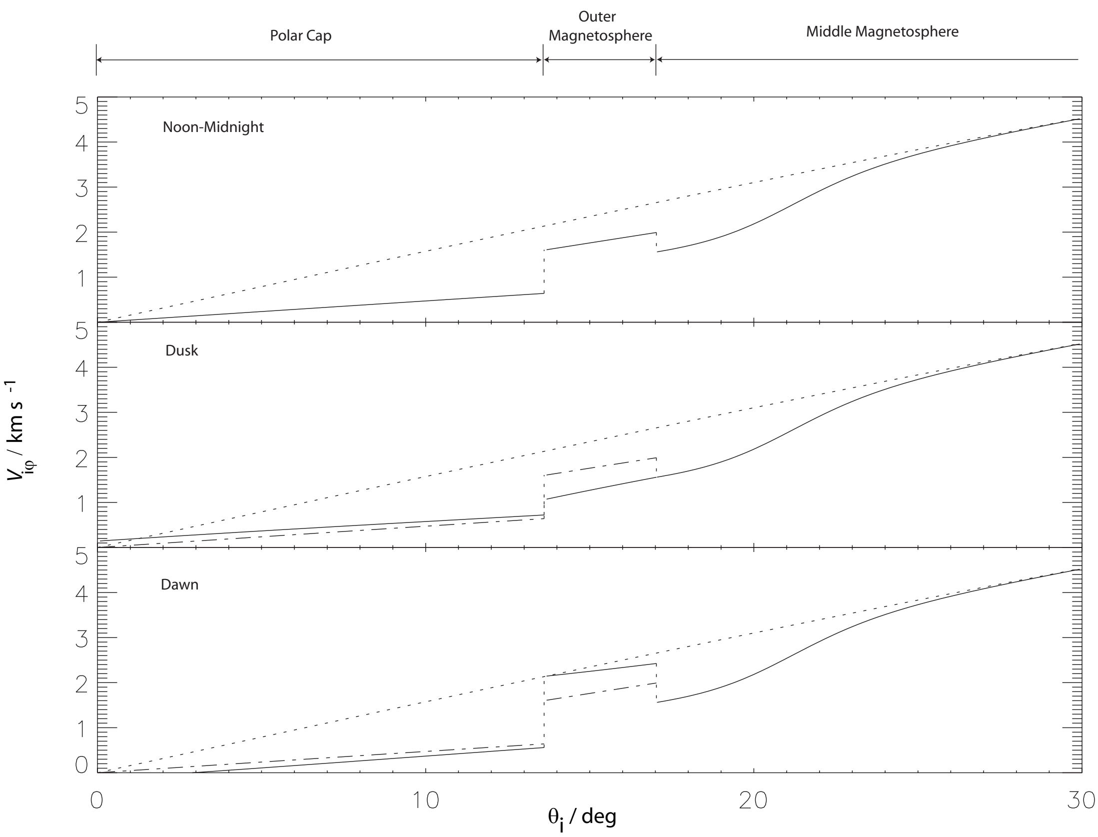

Figure 6.3: Plot of the total plasma azimuthal velocity versus co-latitude angle θ_i on the principal meridians, given by the sum of the twin vortex flow component $V_{iTV\varphi}$ from Eqs. (6.30a) and (6.31a), and the rotational flow component V_{iRO} in Eq. (18a). The format follows that of Fig. 6.2. The solid line in the upper panel thus shows the azimuthal velocity in km s^{-1} on the noon and midnight meridians, given by the rotational flow component only, while the long dotted line shows the azimuthal velocity corresponding to rigid co-rotation with the planet (as in all panels of the figure). The middle panel then shows the total azimuthal velocity profile on the dusk meridian in a similar format, where the dot-dashed line shows for comparison the contribution of the rotational component only, as in the upper panel. The lower panel then shows the azimuthal velocity on the dawn meridian in the same format.

azimuthal velocity, which is proportional to the ionospheric electric field, and is directly related to the ionospheric currents. The upper panel in each figure shows the azimuthal plasma flow on the noon and midnight meridians, where the twin vortex flow makes no contribution (its velocities are purely meridional at these local times). These flows therefore correspond to the rotational flow component only, similar to the axi-symmetric model of Cowley et al. [2004b]. The two lower panels then show the asymmetries at dusk and dawn introduced in the model developed here.

Considering first the noon-midnight meridian in the upper panels, the plasma angular velocity in Fig. 6.2 remains at a fixed value of 0.3 Ω_S within the polar cap region, while increasing to 0.75 Ω_S in the outer magnetosphere. It then falls to a local minimum of ~0.59 Ω_S in the middle magnetosphere region, before increasing once more to approach near-rigid corotation (horizontal dotted line) at ~30º co-latitude. The corresponding plasma azimuthal velocities in Fig. 6.3 show an approximately linear increase in the polar cap, with a jump from ~0.64 km s^{-1} to ~1.61 km s^{-1} at the polar cap boundary. The velocity then increases again in the outer magnetosphere region before falling from ~1.99 km s^{-1} to a local minimum of ~1.56 km s^{-1} across the boundary of the outer magnetosphere. The azimuthal velocity profile then increases once more, to ~4.52 km s^{-1} in the near-rigidly corotating region at 30º co-latitude. The dotted line in this panel (and those below) again indicates the azimuthal velocity for rigid corotation.

The middle panels of Figs. 6.2 and 6.3 then show the azimuthal flows on the dusk meridian, where the dot-dashed lines correspond to the rotational flow component only, as in the upper panels, for purposes of comparison. Here, the effect of the twin vortex is to increase the plasma angular velocity within the polar cap region, to ~0.34 Ω_S at the polar cap boundary (the singularity at the pole itself is simply due to the finite anti-sunward flow of the twin vortex at this point). However, the effect in the outer magnetosphere region is to reduce the angular velocity to ~0.50 Ω_S at its poleward edge, such that the jump in angular velocity across the polar cap boundary is now strongly reduced compared with that on the noon-midnight meridian shown in the upper panel of Fig. 6.2. The jump in the azimuthal velocity at the polar cap boundary in Fig. 6.3 is similarly reduced, now increasing from ~0.72 km s^{-1} in the polar cap to ~1.07 km s^{-1} in the outer magnetosphere. Beyond the polar cap boundary the angular velocity (and the azimuthal velocity) then monotonically increase with co-latitude, the velocity step at the outer magnetosphere boundary being (by design) reduced to zero at this meridian.

The lower panels of Figs. 6.2 and 6.3 similarly show the effects on the dawn meridian. It can be seen that the effect of the twin vortex is now such as to decrease the plasma angular velocity in the polar cap region, while increasing it in the outer magnetosphere region. The effect is thus to enhance the jumps in flow at both boundaries. At the polar cap boundary the angular velocity increases from ~0.26 Ω_S in the polar cap to approximately rigid corotation in the outer magnetosphere. This corresponds to an increase in azimuthal velocity in the lower panel of Fig. 6.3 from ~0.56 km s^{-1} to ~2.15 km s^{-1}. At the outer magnetosphere boundary the angular velocity then falls from ~0.91 Ω_S to ~0.58 Ω_S, corresponding to a fall in azimuthal velocity from ~2.43 km s^{-1} to ~1.56 km s^{-1}. The flow shears at the dawn boundary are thus enhanced compared with the rotational flow alone on the noon and midnight meridians.

6.5.3 Ionospheric Pedersen currents

The horizontal ionospheric Pedersen current intensity, given by Eq. (6.32), is directly proportional to the electric field in the rigidly corotating frame (through use of the effective ionospheric Pedersen conductance), and hence to the plasma velocity in this frame. The principal meridional (equatorward-directed) component of the current, which can be written as $i_{P\theta} = \Sigma_P^* B_i (R_i \Omega_S \sin\theta_i - V_{i\varphi})$, is thus proportional to the displacement of the azimuthal velocity curves shown in Fig. 4 from the curve for rigid corotation (light dotted lines). Co-latitude profiles of the currents on the principal meridians are shown in Fig. 6.4, in a similar format to Figs. 6.2 and 6.3, for an effective ionospheric Pedersen conductance of 1 mho. The current can then be simply scaled for any other choice of conductivity value.

The upper panel of the figure again shows the meridional Pedersen current on the noon and midnight meridians, where the corresponding azimuthal flow is due just to the rotational flow component. This current profile is thus again essentially similar to the axi-symmetric model of Cowley et al. [2004b]. Within the polar cap, the equatorward current increases near-linearly with distance from the pole, peaking at ~0.096 A m^{-1} at the polar cap boundary. This near-linear rise in the current intensity occurs where the model angular velocity is constant at 0.3 Ω_S, such that the azimuthal plasma velocity in the rigidly corotating frame increases near-linearly with distance from the pole as seen in Fig. 6.3. The current then falls by a factor of ~3 to ~0.034 A m^{-1} in the outer magnetosphere, before slowly growing to ~0.043 A m^{-1} at the equatorward boundary of this region. The current then jumps to a local maximum of ~0.070 A m^{-1} in the middle magnetosphere as the plasma velocity drops once more, before falling to small values at large co-latitudes as the plasma approaches near-rigid corotation. We note that the growth in equatorward current with co-latitude in both the polar cap and outer magnetosphere requires distributed downward-directed field-aligned currents to flow in these regions, given by Eqs. (6.33) and (6.34), while the decreasing current in the middle magnetosphere requires (mainly) an upward-directed field-aligned current in this region. Similarly, the jumps in current at the polar cap and outer magnetosphere boundaries require an upward-directed sheet current at the polar cap boundary, and a downward-directed sheet current at the outer magnetosphere boundary, as given by Eqs. (6.35) and (6.36). These field-aligned currents will be discussed in the following section.

The equatorward Pedersen current on the dusk meridian is then shown in the middle panel of Fig. 6.4. The dot-dashed line represents the contribution of the rotational flow only, as shown in the upper panel, for purposes of comparison. The current in the polar cap is now somewhat reduced compared with noon and midnight, and peaks at ~0.090 A m^{-1} at the polar cap boundary. The current in the outer magnetosphere on the other side of the boundary, however, is increased to ~0.068 A m^{-1}. Consequently, the jump in current at the boundary is now strongly reduced compared with noon and midnight, and hence also the implied magnitude of the upward-directed sheet field-aligned current at the boundary. Beyond this boundary the Pedersen current intensity then remains almost

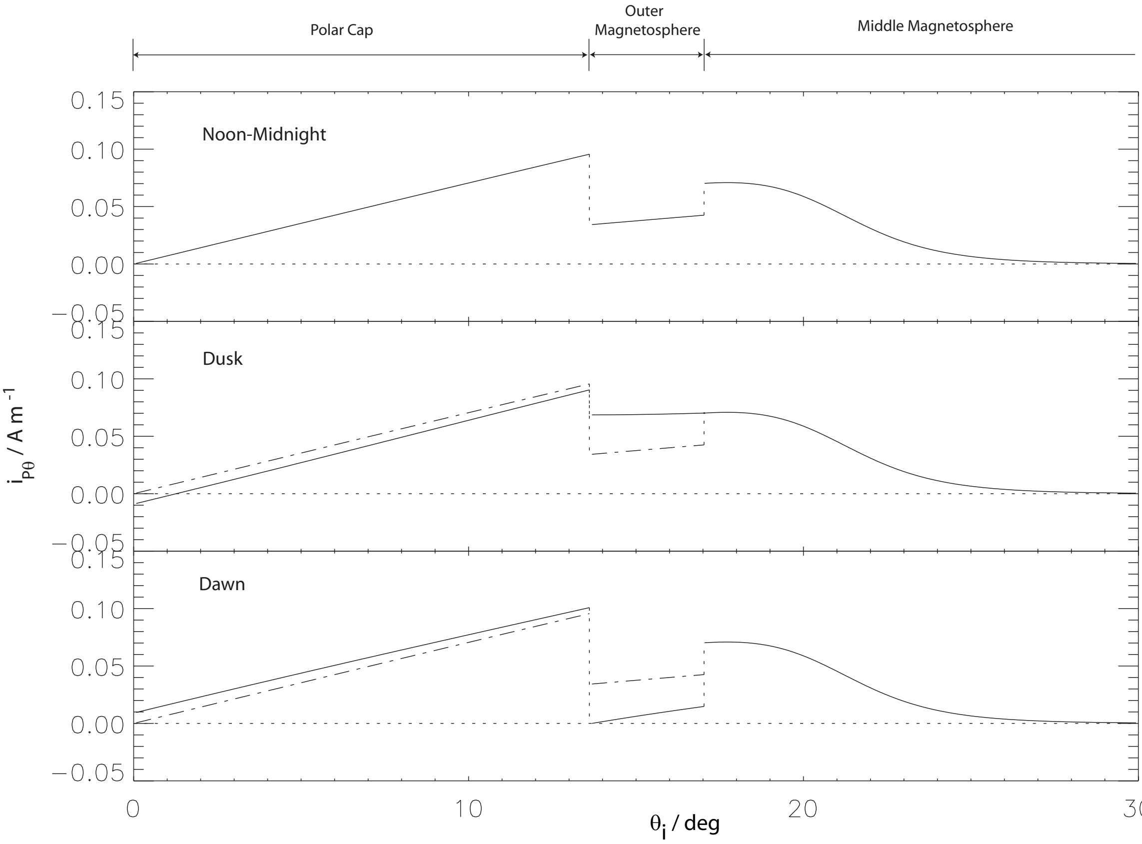

Figure 6.4: Plot of the co-latitudinal component of the horizontal ionospheric Pedersen current intensity, $i_{P\theta}$ given by Eq. (6.32), shown versus co-latitude angle θ_i on the principal meridians, assuming Σ_P*=1 mho. The format follows that of Figs. 6.2 and 6.3. The solid line in the upper panel thus shows the Pedersen current intensity in A m^{-1} on the noon and midnight meridians, associated with the rotational flow component only. The horizontal dotted line indicates the zero level (the current for rigid corotation). The solid line in the middle panel shows the co-latitudinal component of the Pedersen current intensity on the dusk meridian while the dot-dashed line shows for comparison the contribution of the rotational component only, as in the upper panel. The lower panel shows the co-latitudinal component of the Pedersen current intensity on the dawn meridian, in the same format.

constant in value, before falling in the middle magnetosphere as in the upper panel. There is no jump in current (or azimuthal velocity) at the outer magnetosphere boundary in this case, hence the magnitude of the downward-directed sheet field-aligned current at the boundary is locally zero at this meridian.

The lower panel in Fig. 6.4 shows the equatorward-directed Pedersen current at dawn. In this case, the current in the polar cap is somewhat increased compared with noon and midnight, and peaks at ~0.101 A m^{-1} at the polar cap boundary, before falling to near-zero in the outer magnetosphere, where the plasma near-rigidly corotates, as seen in Fig. 6.2. The jump in current at the polar cap boundary is thus significantly increased in this case compared with noon and midnight, and with it the intensity of the sheet field-aligned current at the boundary. At the outer magnetosphere boundary the current then increases from ~0.015 A m^{-1} in the outer magnetosphere to ~0.07 A m^{-1} in the middle magnetosphere, thus also implying a significantly increased downward sheet current at this boundary compared with noon and midnight.

6.5.4 Field-aligned currents

We now discuss the field-aligned currents flowing above the ionosphere which are required by the divergence of the horizontal ionospheric Pedersen current shown in Fig. 6.4. In Fig. 6.5 we begin by showing a co-latitude profile of the distributed field-aligned currents, given by Eqs. (6.33) and (6.34) (for a conductance of 1 mho), which we noted above are related to the rotational flow component only, and are thus independent of local time (azimuth) in the model. Away from the region boundaries, these currents are thus essentially similar to the field-aligned currents in the axi-symmetric model of Cowley et al. [2004b]. Positive values indicate upward-directed currents, and negative values downward-directed currents. As indicated above, the growth of the Pedersen currents with co-latitude in the polar cap implies distributed downward-directed field-aligned currents in this region, with a nearly constant magnitude of ~15 nA m^{-2}. Similarly, in the outer magnetosphere, the currents are again downward-directed with a

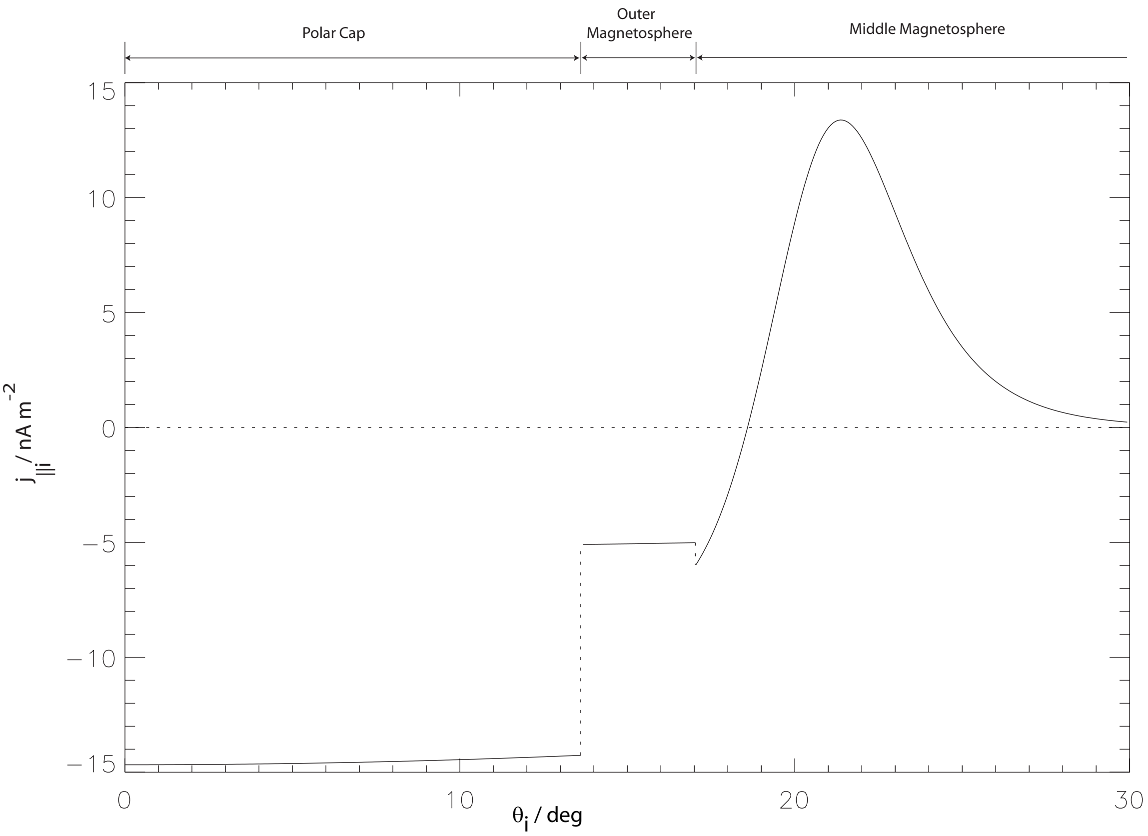

Figure 6.5: Plot of the distributed field-aligned current density $j_{||i}$ obtained from Eq. (6.34) from the rotational flow component only, shown versus co-latitude θ_i. The horizontal bars at the top of the plot indicate the regions of co-latitude that map to the polar cap, the outer magnetosphere, and the middle magnetosphere regions. Positive values indicate currents directed upward out of the ionosphere, negative values indicate currents directed downward into the ionosphere, and the horizontal dotted line indicates the zero level.

reduced magnitude of ~5 nA m^{-2}. The decrease of the Pedersen currents in the middle magnetosphere, however, leads to upward directed field-aligned currents in this region. There is a small region of downward-directed current near the poleward boundary of the middle magnetosphere, but the current subsequently reverses sense and peaks at ~13 nA m^{-2} at ~21.5º co-latitude, before falling to small magnitudes again at lower latitudes. These values are thus very comparable to those of the Cowley et al. [2004b] model. What is not shown in this plot, however, are the sheet field-aligned currents on the region boundaries, directed upward at the polar cap boundary, and downward at the outer magnetosphere boundary. In the Cowley et al. [2004b] model, these sheet currents were resolved into structures of finite width, since the angular velocity model was smoothly-varying with latitude and did not have sharp jumps as in the present case.

In Fig. 6.6 we thus show the intensity of the sheet field-aligned currents on the polar cap and outer magnetosphere boundaries, plotted versus azimuth angle φ_i. As indicated above, φ_i = 0º corresponds to noon, φ_i = 90º to dusk, φ_i = 180º to midnight, and φ_i = 270º to dawn. The solid line shows the total sheet current flowing on the polar cap boundary, where the dot-dashed line shows the axi-symmetric current associated with the rotational flow alone. A strong local time modulation in the current is evident, with upward currents of ~0.10 A m^{-1} at dawn, compared with ~0.022 A m^{-1} at dusk, in conformity with the above discussion. The switch between these values across noon and midnight occurs in the region of the twin vortex 'merging gaps', as indicated at the top of the figure, with localized maxima and minima in the current intensity occurring near their 'ends' due to a localised maximum in the flow vorticity in these regions. The long dashed line similarly shows the total sheet current flowing on the outer magnetosphere boundary, with the short dashed line again showing the value associated with the rotational flow alone. The downward-directed current intensity is near-constant at ~ -0.055 A m^{-1} on the portion of the boundary around dawn, but decreases to near-zero on the corresponding portion of the boundary at dusk, in conformity with the above discussion of Figs. 6.3 and 6.4.

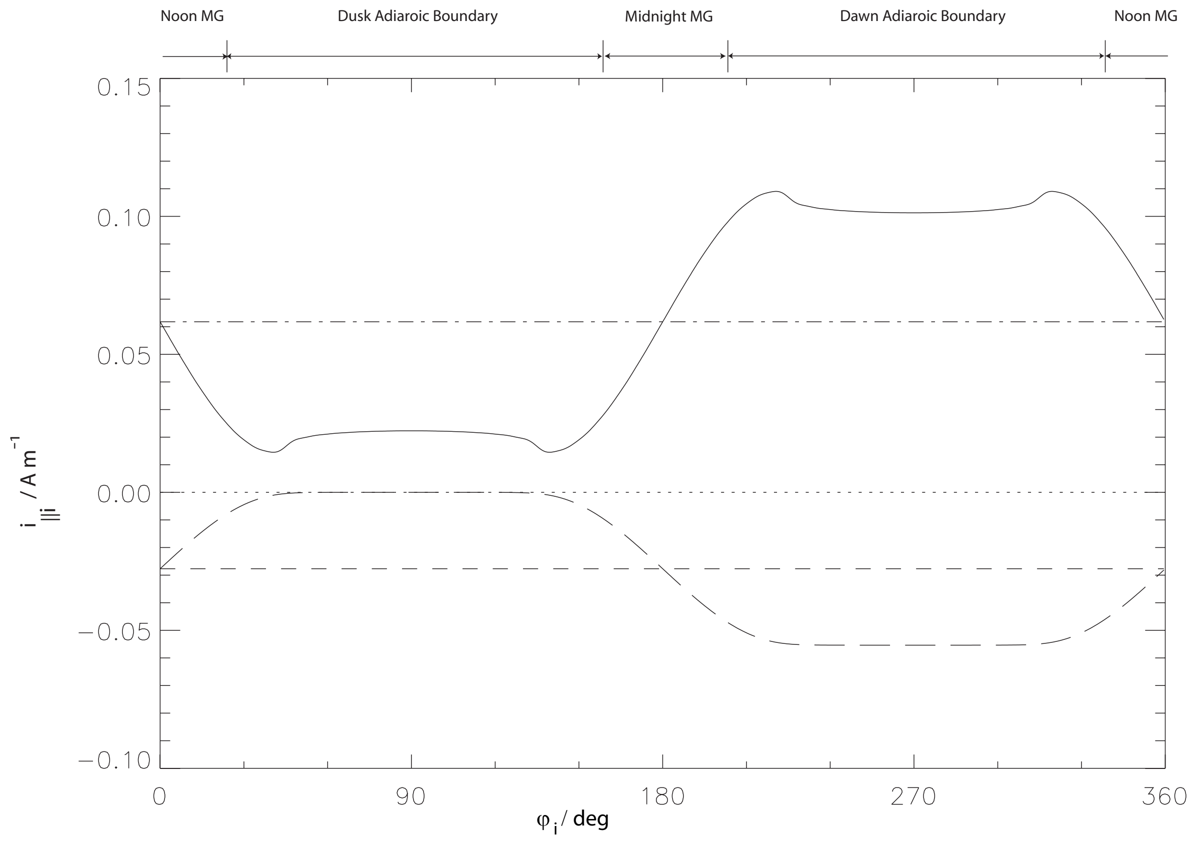

Figure 6.6: Plot of the sheet field-aligned current intensities $i_{||i}$ flowing on the polar cap and outer magnetosphere boundaries, obtained from Eqs. (6.35) and (6.36), shown versus azimuth angle φ_i. The solid line shows the total sheet current intensity flowing on the polar cap boundary (BPC), while the dot-dashed line shows the axi-symmetric current of the rotational flow component only. The long dashed line similarly shows the total sheet current intensity flowing on the outer magnetosphere (BOM) boundary, while the short-dashed line shows the axi-symmetric current of the rotational flow component only. By definition, azimuthal angle $\varphi_i = 0^o$ corresponds to noon, while 90º corresponds to dusk, 180º to midnight, and 270º to dawn. The sections of the polar cap boundary corresponding to the 'merging gaps' (MG) and the adiaroic sections are indicated by the horizontal bar at the top of the plot. Positive values indicate currents directed upward out of the ionosphere, negative values indicate currents directed downward into the ionosphere, and the horizontal dotted line indicates the zero level.

6.5.5 Auroral Parameters

We now consider the implications of the results concerning the upward-directed field-aligned currents for electron acceleration and aurorae. We recall from Section 6.3.3 that field-aligned acceleration of magnetospheric electrons is required if the upward-directed field-aligned current density exceeds the maximum value that can be provided by the unaccelerated magnetospheric electron population, given by Eq. (6.9), which depends on the density and temperature of the source plasma.

We first briefly consider the distributed upward field-aligned current in the middle magnetosphere region, shown in Fig. 6.5. The radial dependence of the density and temperature of the source plasma within the middle magnetosphere has been determined by Richardson [1986, 1995] and Richardson and Sittler [1990], using Voyager plasma data. These data show that the hot plasma electrons that extend along the field lines to low altitudes have a typical number density of ~0.2 cm^{-3} and a thermal energy of ~150 eV in this region, as previously employed by Cowley and Bunce [2003b] and Cowley et al. [2004b]. Substituting into Eq. (6.9), these parameters yield a limiting current density of ~66 nA m^{-2} which is thus much greater than the maximum ~13 nA m^{-2} upward-directed field-aligned current in the middle magnetosphere shown in Fig. 6.5. These currents do not therefore require field-aligned acceleration of magnetospheric electrons, in conformity with the previous conclusions of Cowley and Bunce [2003b] and Cowley et al. [2004b]. We can also compute the energy flux associated with these precipitating electrons, given by Eq. (6.13), which is ~0.020 mW m^{-2}. A simple 'rule of thumb' is that 1 mW m^{-2} of electron energy input into the upper atmosphere results in ~10 kR of auroral UV output [Waite et al., 1983; Rego et al., 1994; Grodent et al., 2001]. Thus electron precipitation with this energy flux would result in an UV emission of only ~0.2 kR, below current ~1 kR thresholds of detectability. We do not exclude the possibility of weak structured aurorae occurring in this region, however, associated with smaller-scale flow features mentioned above and investigated by Cowley and Bunce [2003b], but which are not included here.

We thus now consider the aurorae associated with the upward-directed currents on the polar cap boundary. We note, however, that Knight's [1973] auroral acceleration theory outlined in Section 6.3.3 relates to the field-aligned current density, while our model yields only the field-aligned sheet current intensity at the boundary. In this case we simply make an assumption about the width of the current layer based on observations, and then check for model consistency with observed parameters such as the total auroral power. As discussed previously by Cowley et al. [2004a], the aurorae observed around (what is taken to be) the region of open field lines, have typical latitudinal widths of ~300-1000 km. Here we therefore present results for a range of boundary widths, from 250 to 1000 km. In Figure 6.7 we thus show the current density $j_{\|i}$ around the polar cap boundary for this range of widths. The solid line shows the current density for the centre width of 500 km, while for the upper and lower dashed lines the widths are a factor of two smaller (250 km) and larger (1000 km) respectively. The same line format will also be adopted for the auroral parameters shown below in Fig. 6.8. The current densities at dawn and dusk for each of these widths are given in Table 6.1 for easy reference, spanning ~100-400 nA m^{-2} at dawn, and ~20-80 nA m^{-2} at dusk.

These boundary currents may be carried partially in some lower latitude portion by hot electrons from the outer magnetosphere, with a number density of ~0.01 cm^{-3} and a thermal energy of ~1 keV according to Voyager measurements [Richardson, 1986, 1995], and partially in some higher-latitude portion by magnetosheath (cusp) electrons with a number density of ~0.2 cm^{-3} and a thermal energy of ~50 eV [Sittler et al., 1983]. The outer magnetospheric source has a limiting current from Eq. (6.9) of ~8.5 nA m^{-2}, shown in Fig. 6.7 by the horizontal dot-dashed line. The limiting energy flux from Eq. (6.13) is ~0.017 mW m^{-2}, which we again note would by itself produce only a below-threshold auroral UV intensity of ~0.17 kR. The magnetosheath source correspondingly has a limiting current density of ~37.8 nA m^{-2}, shown in Fig. 6.7 by the horizontal dotted line, and an even lower energy flux of ~0.0038 mW m^{-2}. Comparison of these limiting current densities with the model values in Fig. 6.7 shows that auroral acceleration of both sources is required for all current layer widths at dawn. At some points along the dusk adiaroic

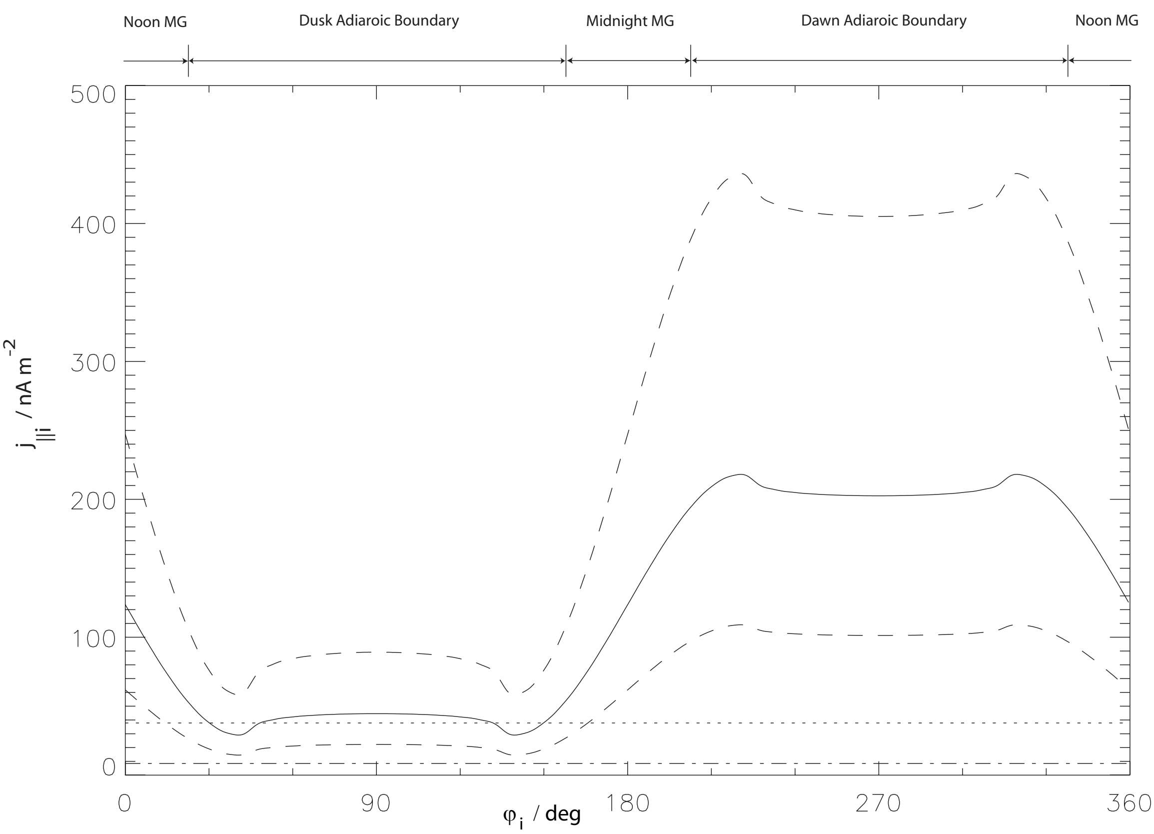

Figure 6.7: Plot of the field-aligned current density flowing on the polar cap boundary for three assumed values of the boundary width, shown versus azimuth angle φ_i. The upper and lower dashed lines correspond to widths of 250 and 1000 km respectively, while the central solid line is for a width of 500 km. The horizontal dotted line shows the limiting current density that can be carried by unaccelerated cool magnetosheath electrons, given by Eq. (6.9) with N=0.2 cm^{-3} and W_{th}=50 eV, while the dot-dashed line similarly shows the limiting current density that can be carried by unaccelerated outer magnetosphere electrons with N=0.01 cm^{-3} and W_{th}=1 keV. When the field-aligned current density exceeds the limiting value, field-aligned acceleration of auroral electrons is required.

Table 6.1. Current density and auroral parameters at dawn and dusk on the polar cap boundary, for three assumed values of the width of the current layer.

Current layer width	250 km		500 km		1000 km	
Local time	Dawn	Dusk	Dawn	Dusk	Dawn	Dusk
Current density						
$j_{\parallel i}$ /nAm^{-2}	400	80	200	40	100	20
Auroral parameters for outer magnetosphere source						
$\Phi_{\parallel}$ / kV	48	10	23	5.0	11	2.0
r_{min} / R_i	3.7	2.2	2.9	1.7	2.2	1.4
E_f / mW m^{-2}	22	1.5	5.0	0.5	1.5	0.2
Auroral parameters for magnetosheath source						
$\Phi_{\parallel}$ / kV	0.5	0.05	0.22	0.01	0.08	0.0
r_{min} / R_i	2.2	1.4	1.7	1.1	1.4	1.0
E_f / mW m^{-2}	0.25	0.01	0.06	0.005	0.02	0.0

boundary however, the current density falls below the threshold for acceleration of magnetosheath electrons for current layer widths of 500 and 1000 km.

We now discuss the implications of these results for field-aligned electron acceleration and aurorae. Figure 6.8a shows the three auroral parameters introduced in Section 6.3.3, computed using the above outer magnetosphere hot electron source, plotted versus azimuth in a similar format to Figure 6.7. The values at dawn and dusk are also given in Table 6.1 for each of the boundary widths. The top panel shows the minimum field-aligned voltage $\Phi_{\|}$ required to produce the upward current, given by Eq. (6.10). The values at dawn are ~10-50 kV, a factor of ~5 larger than those at dusk, which are 2-10 kV. The middle panel shows the minimum radial distance of the top of the accelerating voltage drop, in units of ionospheric radial distance, given by Eq. (6.11). The values are ~2-4 R_S at dawn, and ~1.5-2 R_S at dusk. The bottom panel shows the energy flux associated with the precipitating electrons, given by Eq. (6.12). The dawn-side energy fluxes are ~2-20 mW m^{-2}, sufficient to produce discrete auroral intensities of ~20-200 kR respectively. On the dusk side, however, the energy fluxes are strongly reduced to ~0.2-2 mW m^{-2}, yielding auroral intensities of ~2-20 kR, respectively. These strong variations of the electron energy flux with the width of the current layer, and between dawn and dusk, result from the fact that the energy flux is proportional to the square of the current density in Eq. (6.12).

Figure 6.8b shows the same parameters for the magnetosheath electron source, with values at dawn and dusk again tabulated in Table 6.1. In this case, the values of the accelerating voltage, minimum acceleration region height, and precipitating energy flux are all significantly smaller than for the outer magnetosphere source due to the increased density and decreased temperature of the unaccelerated source electrons. The minimum field-aligned voltages shown in the upper panel peak at ~0.1-0.5 kV at dawn, and are about a factor of ten smaller at dusk. The minimum radial distance of the accelerating voltage drop in the middle panel also shows reduced values, generally below ~2 R_S. Similarly, the energy fluxes shown in the lower panel lie in the range ~0.02-0.2 mW m^{-2} at dawn, yielding auroral emissions in the range ~0.2-2 kR, while on the dusk side the

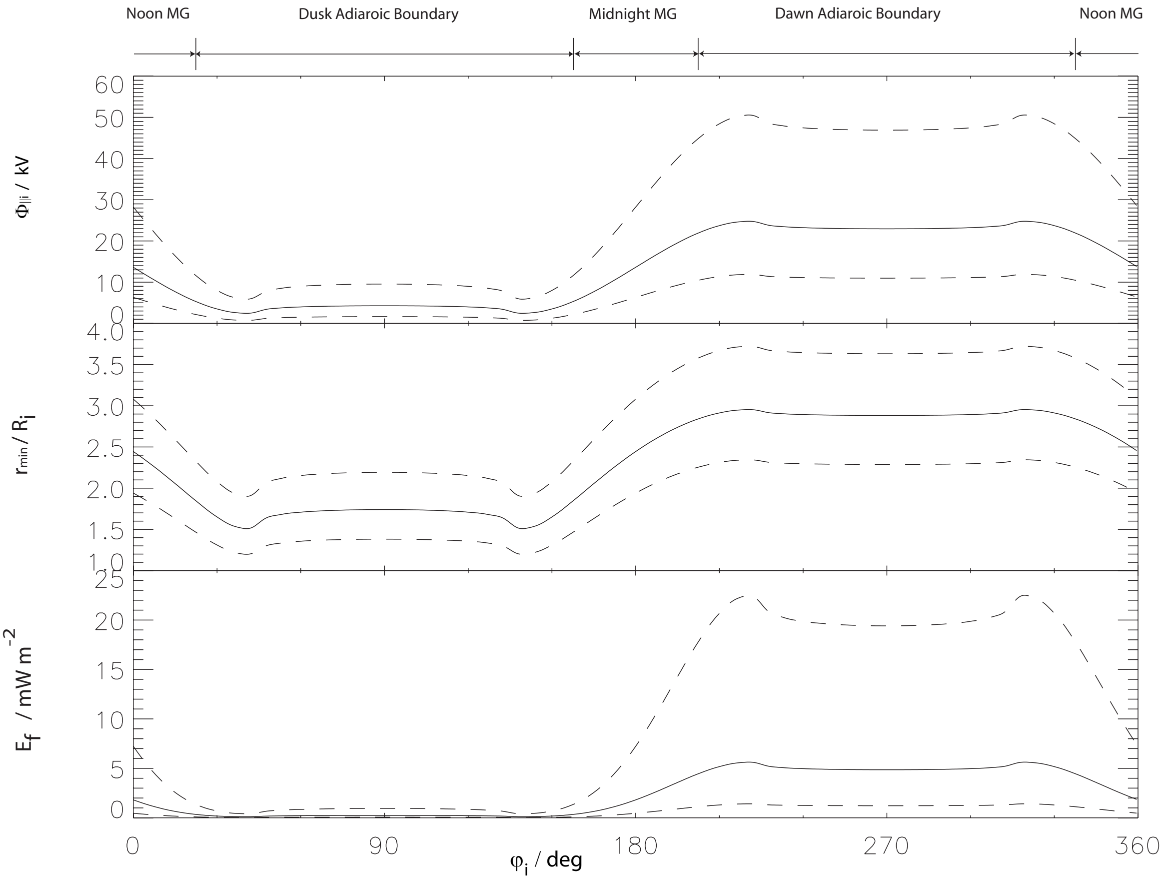

Figure 6.8a: Plot of auroral acceleration parameters for the outer magnetosphere hot electron source plasma, shown versus azimuth angle φ_i. The upper panel of the figure shows the minimum field-aligned voltage required to produce the upward field-aligned current, $\Phi_{||}$, given by Eq. (6.10). As in Fig. 6.7, the central solid line corresponds to an assumed current layer width of 500 km, while the upper and lower dashed lines represent boundary widths of 250 and 1000 km respectively. The middle panel similarly shows the minimum radial distance of the top of the accelerating voltage drop, in units of ionospheric radial distance (essentially the planetary radius), given by Eq. (6.11). The lower panel then shows the energy flux E_f associated with the precipitating accelerated electrons, given by Eq. (6.12). The horizontal bars at the top of the panels indicate the merging gap (MG) and adiaroic regions around the polar cap boundary.

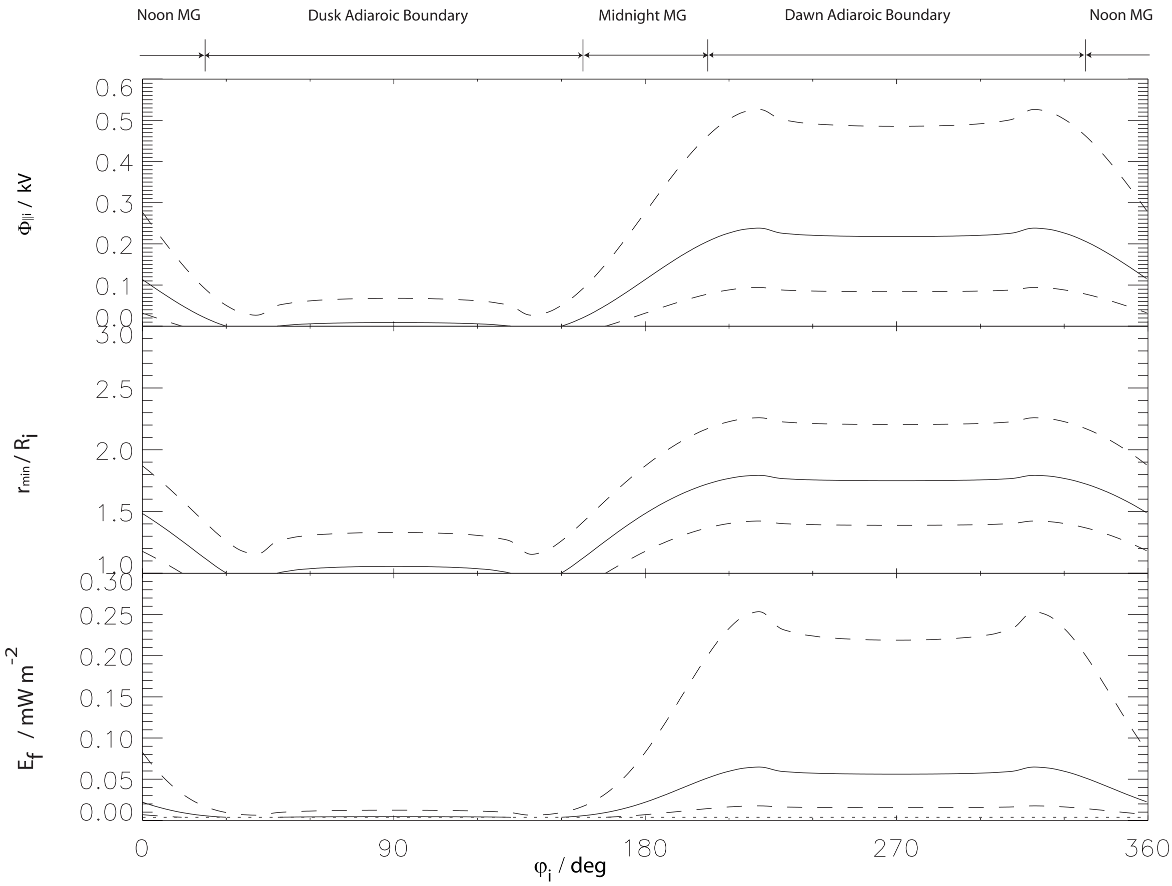

Figure 6.8b: As for Fig. 6.8a, but for the magnetosheath source plasma. The horizontal dotted line in the bottom panel shows the unaccelerated electron energy flux given by Eq. (6.13). This was too small to show in Fig 6.8a.

values are an order of magnitude lower, such that even the largest flux would yield an aurora too faint to be detected above present background levels of ~1 kR. The horizontal dotted line in the bottom panel shows the unaccelerated electron energy flux for the magnetosheath source, ~0.0038 mW m^{-2} as given by Eq. (6.13), that would yield an aurora of only ~0.04 kR.

Combining together the results shown in Figs. 6.8a and 6.8b, and tabulated in Table 6.1, it can be seen that the currents at the polar cap boundary will be associated with bright aurorae in some equatorward portion where the current is carried by outer magnetosphere electrons, typically ~50 kR at dawn and ~5 kR at dusk, with weaker aurorae in some poleward portion where the current is carried by magnetosheath electrons, typically ~1 kR at dawn and decreasing below threshold at dusk. However, since such structure is at the limit of what can presently be spatially resolved, the observed boundary aurorae should clearly be dominated by that produced by the accelerated outer magnetosphere electrons, with the above parameters.

Finally, integration of the energy flux values across the current layer and around the open-closed field-line boundary yields the total power of the electrons precipitating in the boundary region. The total precipitating powers for the three current layer widths and both sources are given in Table 6.2. With 15% energy efficiency, these translate to UV output powers which are also given. For definiteness, the values given in the table assume that the whole of the current is carried by the given source in each case. It can be seen that for the centre width of 500 km the precipitating electron power for the outer magnetosphere source is ~100 GW, while that for the magnetosheath source is only ~1 GW. The corresponding UV output powers are ~15 and ~0.2 GW, respectively. For other widths the powers vary approximately inversely with the width. Clearly, the total powers for the outer magnetosphere source are far greater than those for the magnetosheath, such that the overall power will generally be dominated by the former contribution. For example, if we assume for simplicity that half the current is carried by electrons from the outer magnetospheric source and half by electrons from the magnetosheath, we find total precipitating electron powers of ~103, ~51.9, and ~26.4

Table 6.2. Total precipitating electron power around the polar cap boundary, together with the auroral UV output, for various assumed current layer widths, and two magnetospheric electron source populations. For definiteness, the values given in the table assume that the whole of the current is carried by the given source in each case.

Current layer width	250 km	500 km	1000 km
Outer magnetosphere source			
Precipitating electron power (GW)	204	102	51.6
UV output power (GW)	30.6	15.3	7.75
Magnetosheath source			
Precipitating electron power (GW)	2.32	1.22	0.72
UV output power (GW)	0.35	0.18	0.11

GW for the 250, 500 and 1000 km boundary widths respectively, yielding UV output powers of ~15.5, ~7.79, and ~3.96 GW.

We now briefly consider the relationship of these results to the observed properties of the aurorae at Saturn. In overall terms, observations show that the auroral brightness typically lies in the range ~1-100 kR, while the total auroral output power generally varies from a few GW to a few tens of GW [Gérard et al., 1995, 2004; Trauger et al., 1998; Cowley et al., 2004a; Clarke et al., 2005; Grodent et al., 2005; Badman et al., 2005]. The values derived from our model lie in similar ranges, and are thus in basic accord with the observations. Dawn enhancements of the aurorae compared with dusk are also commonly observed, though not invariably so. Of course, our model has been designed to illustrate particular conditions in which the Dungey cycle is active, specifically compression region conditions in the solar wind when Dungey-cycle driving can reach averaged values of a few hundred kV over a few days, as shown by the results presented in Chapter 4, and by Badman et al. [2005]. Examination of auroral images obtained under such conditions during the joint Cassini-HST campaign in January 2004 (e.g. 'visit 13'), do indeed show a substantial dawn-dusk asymmetry as indicated by our model, with auroral brightnesses of ~10-50 kR, and total auroral output powers of ~15 GW [Clarke et al., 2005; Grodent et al., 2005; Badman et al., 2005]. Our model thus also appears to be in basic agreement with these more specific observations. However, the model is certainly not expected to describe all circumstances, particularly solar wind rarefaction region conditions when the IMF is very weak, such that Dungey-cycle flow may become negligible for extended intervals.

We finally briefly address the issue of why it is that Dungey-cycle driving at Saturn produces a strong dawn-dusk auroral asymmetry, while no such zeroth order effect is observed at Earth where it is known that the Dungey cycle dominates [e.g. Cowley et al., 2003]. Basically, the Dungey cycle twin-vortex flow is associated with field-aligned currents flowing on the open field boundary and on the equatorward boundary of the twin vortex, which are opposite at dawn and dusk, and opposite on the two boundaries. At Earth, these are termed the 'region-1' and 'region-2' field-aligned currents, respectively, and are directed upward at dusk and downward at dawn on the open field boundary, and vice-versa on the equatorward boundary. Discrete aurorae associated with upward field-aligned currents at Earth may thus be present both at dusk ('region-1') and dawn ('region-2'), joined by the upward currents of the Harang discontinuity across midnight, and augmented also by diffuse auroral precipitation from trapped hot plasma on closed flux tubes. At Saturn, these same currents are present, as in our model (though their directions are reversed compared with Earth due to the differing polarity of the planetary magnetic field), but they are now superposed on unidirectional currents flowing at the same boundaries associated with the shears in the rotational flow. These latter currents are directed upward on the open field boundary, and downward on the equatorward boundary, and as we have indicated here, they are sufficiently strong that usually the Dungey-cycle currents may modulate their magnitude but not reverse their sense. In this case discrete aurorae associated with upward currents are confined to the open field boundary, where they are modulated in local time by the Dungey-cycle flow as in our model, while upward currents and discrete aurorae are not expected to occur on the equatorward boundary. Of course, the overall auroral display at Saturn may also include some more uniform contribution from diffuse precipitation of trapped hot plasma on closed flux tubes, in the region just equatorward of the open field boundary.

6.6. Summary

In this chapter we have proposed a simple model of the plasma flow and current in Saturn's polar ionosphere. This builds on the previous quantitative axi-symmetric model of Cowley et al. [2004b], by including the dawn-dusk asymmetries present when both the solar wind and internally driven processes are active, as discussed qualitatively by Cowley et al. [2004a]. The model parameters have been guided by Voyager plasma velocity measurements on closed field lines [e.g. Richardson, 1986, 1995; Richardson and Sittler, 1990], by ground-based IR Doppler measurements of ionospheric flows in the polar cap [Stallard et al., 2004], and by remote sensing studies of the planet's aurorae using the HST [Gérard et al., 1995, 2004; Cowley et al., 2004a; Prangé et al., 2004].

The physical nature of the flow pattern in the model consists of elements which are intended to represent sub-corotational plasma flow in the middle magnetosphere resulting from plasma pick-up and radial transport from internal sources, and the Vasyliunas- and Dungey-cycles of convection at higher latitudes. For theoretical convenience, the overall flow pattern representing these behaviours is expressed as the sum of two components. The first is a sub-corotating purely rotational flow varying with co-latitude, which is essentially similar to the axi-symmetric model of Cowley et al. [2004b]. Dawn-dusk flow asymmetry is then introduced by vectorially adding a second flow component, consisting of a sun-aligned twin vortex, which provides anti-sunward flow across the polar cap, and return sunward flow via dawn and dusk confined to the outer magnetosphere ring. The anti-sunward flow across the polar cap enhances the rotational flow at dusk and diminishes it at dawn, while the return sunward flow in the outer magnetosphere enhances the rotational flow at dawn and diminishes it at dusk. The action of the twin-vortex flow is thus to increase the flow shears at both the polar cap and outer magnetosphere boundaries at dawn, while reducing them at both boundaries at dusk. The voltage associated with the twin vortex is just the Dungey cycle voltage associated with anti-sunward transport across the polar cap. Based on an analysis of upstream interplanetary Cassini data in Chapter 4, this voltage was estimated to have typical values of ~50 kV, with peaks of up to a few hundred kV. Here we have modelled active Dungey cycle conditions such as occur during solar wind compression regions, and have thus chosen a value of 200 kV. The voltage in the Vasyliunas cycle has been chosen to be comparable to the Dungey cycle, equal to 275 kV.

We then consider the height-integrated Pedersen current driven in the polar ionosphere by the plasma flow in the neutral atmosphere rest frame, and the field aligned currents that relate to its divergence. In our calculation we assumed a constant value of the effective height-integrated Pedersen conductivity of 1 mho on the basis of the results of Bunce et al. [2003], such that the currents calculated may be simply linearly scaled to other choices. For uniform conductivity, the Hall current closes wholly in the ionosphere, such that the field-aligned currents are determined only by the divergence of the Pedersen current. The rotational flow component then yields distributed field aligned currents flowing through the region of interest, which are essentially similar to those modelled by Cowley et al. [2004b], except that here the currents flowing on the polar cap and outer magnetosphere boundaries are simplified to sheet currents, rather than being resolved into structures of finite width. The distributed field-aligned currents in the polar cap and outer magnetosphere are downward-directed, and of magnitude ~15 and ~5 nA m^{-2} respectively. The field-aligned current then reverses sense in the middle magnetosphere, with a peak upward-directed current of ~13 nA m^{-2} at ~21.5º co-latitude. The sheet currents associated with the rotational flow are then upward-directed on the polar cap boundary, and downward-directed on the outer magnetosphere boundary. By its construction, however, the twin-vortex flow produces no distributed field-aligned currents, but only sheet currents on the boundaries. On the polar cap boundary these are directed upwards at dawn and downwards at dusk, and vice versa at the outer magnetosphere boundary, thus modulating the axi-symmetric sheet currents of the rotational flow component. The combined upward currents on the polar cap boundary peak at ~0.10 A m^{-1} at dawn, and have a minimum of ~0.02 A m^{-1} at dusk, while the downward currents on the outer magnetosphere boundary peak at ~0.05 A m^{-1} at dawn and fall to zero at dusk.

We finally consider the implications of the upward-directed field aligned currents in the model for electron acceleration and aurorae. Downward-directed field-aligned acceleration of magnetospheric electrons is required if the upward-directed field-aligned current density exceeds the maximum value that can be provided by the unaccelerated electron population. The latter maximum current depends on the density and temperature of the source plasma, which is taken to be the hot electron component in the middle magnetosphere, while at the polar cap boundary we consider two sources, the hot outer magnetosphere electrons and cooler denser electrons of the magnetosheath. We firstly find that the broadly-distributed upward-directed field aligned currents associated with sub-corotation in the middle magnetosphere are too small to require field-aligned acceleration of magnetospheric electrons, in conformity with the prior conclusions of Cowley and Bunce [2003b] and Cowley et al. [2004b], and that the energy fluxes of the unaccelerated electrons are too weak to produce significant aurorae. This does not preclude the existence of weak structured aurorae in this region, however, associated with small-scale flow features not included in our model [Cowley and Bunce, 2003b]. Interest then focuses on the upward-directed currents along the polar cap boundary. Our model only yields the sheet current intensity along this boundary, however, so we need to assume a width of the current layer in order to estimate the current density and resulting auroral accelerations. We chose to model a range of observationally-motivated current sheet widths from 250 to 1000 km, yielding upward current densities of ~100-400 nA m^{-2} at dawn and ~20-80 nA m^{-2} at dusk. These values compare with maximum current densities for the unaccelerated population of ~8.5 nA m^{-2} for the outer magnetosphere source, and ~38 nA m^{-2} for the magnetosheath source. Auroral electron acceleration is thus required at all local times for all boundary widths considered for the outer magnetosphere source, more so at dawn than at dusk, while for the magnetosheath source the current density falls below the maximum that can be carried by the unaccelerated electrons for the larger widths at dusk.

For the outer magnetosphere source the accelerating voltages peak in the dawn sector at ~10-50 kV for the three boundary widths considered, yielding precipitating energy fluxes of ~2-20 mW m^{-2}. The associated auroral intensities are then ~20-200 kR. On the dusk side the corresponding voltage and energy flux values fall to ~2-10 kV and ~0.2-2 mW m^{-2}, yielding auroral intensities of ~2-20 kR. The model thus suggests the presence of substantial dawn-dusk auroral asymmetry under the active Dungey-cycle conditions considered. For the magnetosheath source, the corresponding accelerating voltages and energy fluxes are much less, peaking in the dawn sector, for example, at ~0.1-0.5 kV and ~0.02-0.2 mW m^{-2}. The auroral energy deposited will thus usually be dominated by the portion of the boundary current carried by hot outer magnetosphere electrons. We have also integrated the energy flux values across the current layer and around the open-closed field line boundary, to yield the total UV output power. If we assume for simplicity that half the current is carried by each plasma source, we find total output powers of ~5-15 GW.

Overall we find that the auroral brightnesses and total output powers derived here are in broad agreement with observations. Dawn-dusk asymmetry in the sense indicated is also found to be a common but not invariable feature of Saturn's aurorae. Of course, the model discussed here has been developed to illustrate particular magnetospheric conditions, specifically intervals of steady strong Dungey-cycle driving, such as are likely to occur during solar wind compression regions when the IMF and magnetopause reconnection rates are strong. HST observations obtained under these conditions during the January 2004 campaign appear to be in good overall agreement with the theoretical results derived. However, the model will not apply in detail to other circumstances, such as solar wind rarefaction regions where the IMF is weak, and magnetospheric activity may be confined to episodic intervals of tail reconnection for example. Further development of the model to describe more diverse and time-dependent circumstances is thus warranted.

Chapter 7
Conclusions and Future Work

7.1 Introduction

With its stunning rings and dozens of moons, Saturn has long intrigued observers. The gas giant also has a huge magnetosphere, arising from its internal dynamo-generated magnetic field. This thesis concerns solar wind-magnetosphere coupling at Saturn and the related dynamics, motivated in large part by the availability of data from the Cassini-Huygens mission. Previous missions to Saturn (Pioneer 11, Voyager-1 and -2) have merely flown by, albeit gleaning images and useful data. However, with its 4-year nominal orbital tour and vast suite of instruments, Cassini has enabled us to probe Saturn's magnetosphere in great detail, and unlock many of its secrets, along with posing further questions for us to investigate.

7.2 Structure of the IMF

Before reaching Saturn, Cassini had a 7-year cruise which encompassed two Venus swingbys, plus Earth and Jupiter gravity assists. These served more than to just boost the spacecraft, but also as a useful platform from which to test the instruments. The long cruise also provided an opportunity to sample the interplanetary magnetic field out to the orbits of the giant planets during the declining phase of the solar cycle, in contrast to the other missions that had visited Saturn at solar maximum. This prompted the study presented in Chapter 4. It is known that the gas giant planets have large magnetic fields and extremely rapid rotation rates. As such, this indicates that corotation of the plasma with the planet will be the dominant flow within the magnetospheric cavity. However, this picture does not preclude significant interactions taking place between these magnetospheres and the solar wind. The interactions are of two types, concerned with the stresses exerted in the direction tangential and normal to the magnetopause boundary. The first of these, associated with tangential stress, is expected to be mediated principally by magnetic reconnection at the magnetopause, as at Earth. The reconnection process and its consequences depends significantly on the strength and orientation of the IMF. The second interaction, associated with normal stress, is concerned with the effect of magnetospheric compressions and expansions resulting from variations in the solar wind dynamic pressure. The work in Chapter 4 was mostly concerned with the first of these solar-wind related processes, associated with magnetopause reconnection, though the results suggest that for the outer planets the effects may generally be coupled with those due to compressions and expansions. The chapter investigated the reconnection-driven interaction of the solar wind with Saturn's magnetosphere, and employed the data to estimate the dayside reconnection voltage produced at Saturn's magnetopause associated with the production of open flux. The results have subsequently been used, for example by Badman et al. [2005], along with auroral observations, to deduce tail reconnection rates at Saturn, and adapted by Gérard et al. [2005] to calculate voltages for high-latitude (lobe) reconnection.

7.3 Saturn kilometric radiation

With Saturn orbit insertion on 1 July 2004 looming, the next logical step was to build on the analysis technique developed in Chapter 4 to investigate the structure of the IMF in the solar rotations preceding and including SOI. Knowing the pattern of CIR compressions and rarefactions is useful in aiding prediction of conditions inside the magnetosphere in the absence of an upstream monitor. For the study in Chapter 5, this technique was combined with the use of SKR data as a remote diagnostic of magnetospheric dynamics. The IMF and SKR data were correlated with auroral images from the January 2004 Hubble-Cassini campaign, which showed the effect of the arrival at Saturn of a CIR compression region. Observations of the IMF data preceding SOI suggested that a CIR compression with embedded HCS crossing is expected to have impinged on the magnetosphere at some point during the SOI fly-through. The data during SOI itself were then studied in detail, in the absence of auroral images, but with the knowledge of the response of the SKR emissions to compressions. On the outbound pass, strong bursts of SKR extending to low frequencies were observed, which were not in phase with the previous emissions. The implication is that much of the outbound pass occurred under compressed conditions of SKR and auroral disturbance, probably of the same general character as observed in association with CIR compressions during the HST-Cassini campaign in January 2004. Examination of the in situ magnetic field data showed that the largest emission bursts are associated with concurrent variations in the pre-dawn magnetic field, which are indicative of the injection of hot plasma at the spacecraft. As such, the data presented in Chapter 5 thus provide the first evidence of a specific link between SKR emission features and in situ dynamics inside Saturn's magnetosphere, a very useful tool for future Cassini studies.

7.4 The kronian aurora

The high-latitude far-ultraviolet (FUV) kronian aurora has been observed by a variety of spacecraft and telescopes. Recent high resolution images from the HST have enabled some general auroral characteristics to be established. The motivation behind the theoretical work presented in Chapter 6 was to investigate the processes that cause the aurora, in particular during the few-day intervals each solar rotation where Dungey cycle driving is strong, as described in Chapter 4. The models presented by Cowley et al. [2004a, b], provided initial axisymmetric descriptions of the flows and currents in the polar ionosphere that produce the aurora. The images from the January 2004 Hubble-Cassini campaign presented in 2004, combined with the plethora of in situ instrument data to be obtained during the 4-year Cassini orbital tour, provided strong impetus to design a fully quantitative model of the flows and currents that drive the kronian aurora. By adding a twin vortex flow to the previous purely rotational models, the work presented in Chapter 6 enabled us to study the effect of strong Dungey cycle driving on the flows, and to quantify the commonly-observed dawn dusk asymmetry in the main oval.

7.5 Future questions

A number of issues arise following the work presented in this thesis. First, the empirical formula presented in Chapter 4 can be refined with the benefit of more plasma data from Cassini, and better statistical knowledge of the stand-off distance of the magnetopause (e.g. Achilleos et al. [2006]). However, it should be noted that what is presented in Chapter 4 is a very useful empirical guide, and while the addition of further refinements will change the magnitude of the rate of open flux production, the overall magnetospheric response to varying solar wind conditions will be similar.

As regards the work in Chapter 5, there are still many unanswered questions regarding the SKR emissions. As discussed in Chapter 2, the view of the emissions that has been held for some 25 years has recently been challenged, with the observation of SKR on the nightside of the planet, a finding that is not consistent with a dayside source region. Many uncertainties also remain about the exact rotation period of the planet, as the SKR period has changed by ~1% since the Voyager era, and as such, cannot be indicative of the rotation rate of the core of the planet.

The model presented in Chapter 6 was not intended to provide a global, time-dependent explanation of the auroral morphology, but to serve as the first attempt at quantifying the typical emissions under a particular set of conditions, and to make some comment on how they compare with observation. The model thus has scope for refinement, particularly to take into account varying Dungey cycle driving voltages, as calculated in Chapter 4.

Of course, any mission of discovery can reveal unexpected results, and Cassini has been no different. Recently, the Cassini magnetometer has detected the interaction of the magnetospheric plasma of Saturn with an atmospheric plume at the icy moon Enceladus [Dougherty et al., 2006], a finding which was unanticipated based on knowledge from previous flyby missions. The field results are consistent with local outgassing via a plume from the surface of the moon near the south pole, the source being the “tiger stripes” or cracks in the surface observed in that area. In addition, enhanced ion cyclotron wave activity at the water group gyro-frequency during the flyby points to Enceladus as a major source of ions for the magnetospheric plasma. This significant neutral source from Enceladus may go some way towards answering one of the outstanding questions regarding our understanding of Saturn’s magnetosphere, what is the missing source of the large densities of water and its derivatives that are observed. However, further study in this area is clearly warranted.

Furthermore, Cassini will remain in orbit around Saturn until 2008, with the later stages of the mission incorporating high inclination orbits and a considerable amount of time spent in Saturn’s magnetic tail. There remains a great deal of scope to further probe Saturn’s magnetospheric dynamics during this time, to test the latest theories, and to raise new questions for the future.

References

Achilleos, N. C.S. Arridge, C.M. Jackman, C. Bertucci, M.K. Dougherty, and C.T. Russell: Probabilistic modelling of Saturn's magnetopause boundary, *Geophys. Res. Lett.*, in preparation, 2006.

Acuña, M.H., N.F. Ness, and J.E.P. Connerney: The magnetic field of Saturn: Further studies of the Pioneer 11 observations, *J. Geophys. Res.*, 85, 5675, 1980.

Alfvén, H.: Electric currents in cosmic plasmas, *Rev. Geophys. Space Phys.*, 15, 271, 1977.

Aubry, M.P., and R.L. McPherron, Magnetotail changes in relation to the solar wind magnetic field and magnetospheric substorms, *J. Geophys. Res.*, 76, 4381, 1971.

Badman, S.V., E.J. Bunce, J.T. Clarke, S.W.H. Cowley, J.–C. Gérard, D. Grodent, and S.E. Milan: Open flux estimates in Saturn's magnetosphere during the January 2004 Cassini-HST campaign, and implications for reconnection rates, *J. Geophys. Res.*, 110, A11216, doi:10.1029/2005JA011240, 2005.

Balogh, A., T. J. Beek, R. J. Forsyth, P. C. Hedgecock, R. J. Marquedant, E. J. Smith, D. J. Southwood, and B. T. Tsurutani: The magnetic field investigation on the Ulysses mission: instrumentation and preliminary scientific results, *Astron. Astrophys. Suppl. Ser.*, 92, 221-36, 1992.

Balogh, A., G. Erdos, R.J. Forsyth, and E.J. Smith: The evolution of the interplanetary sector structure in 1992, *Geophys. Res. Lett.*, 20, 21, 2331-2334, 1993.

Barbosa, D.D.: Titan's atomic nitrogen torus: Inferred properties and consequences for the Saturnian aurora, *Icarus*, *72*, 53, 1987.

Baumjohann, W., and R.A. Treumann: Basic space plasma physics, *Imperial College Press*, pg. 189, 1997.

Behannon, K.W., J.E.P. Connerney, and N.F. Ness: Saturn's magnetic tail: Structure and dynamics, *Nature*, 292, 753, doi:10.1038/292753a0, 1981.

Behannon, K.W., R.P. Lepping, and N.F. Ness: Structure and dynamics of Saturn's outer magnetosphere and boundary regions, *J. Geophys. Res.*, *88*, 8791, 1983.

Biermann, L.: Kometschwerfe und solare korpuskularstrahlung, *Z. Astrophys*., 29, 274, 1951.

Boudouridis, A., E. Zesta, L.R. Lyons, P.C. Anderson, and D. Lummerzheim: Effect of solar wind pressure pulses on the size and strength of the auroral oval, *J. Geophys. Res*., *108*(A4), 8012, doi: 10.1029/2002JA009373, 2003.

Boudouridis, A., E. Zesta, L.R. Lyons, P.C. Anderson, and D. Lummerzheim: Magnetospheric reconnection driven by solar wind pressure fronts, *Ann. Geophysicae*, 22, 1367, 2004.

Brice, N.M., and G.A. Ioannidis, The magnetospheres of Jupiter and Earth, *Icarus*, *13*, 173, 1970.

Broadfoot, A.L., B.R. Sandel, D.E. Shemansky, J.B. Holberg, G.R. Smith, D.F. Strobel, J.C. McConnell, S. Kumar, D.M. Hunten, S.K. Atreya, T.M. Donahue, H.W. Moos, J.L. Bertaux, J.E. Blamont, R.B. Pomphrey, and S. Linik: Extreme ultraviolet observations from Voyager 1 encounter with Saturn, *Science*, 212, 206, 1981.

Bunce, E.J.: Large-scale current systems in the Jovian magnetosphere, *PhD thesis*, 2001.

References

Bunce, E.J., and S.W.H. Cowley: Divergence of the equatorial current in the dawn sector of Jupiter's magnetosphere: analysis of Pioneer and Voyager magnetic field data, *Planet. Space Sci.*, 49, 1089, 2001.

Bunce, E.J., S.W.H. Cowley, and J.A. Wild: Azimuthal magnetic fields in Saturn's magnetosphere: Effects associated with plasma sub-corotation and magnetopause-tail current system, *Ann. Geophys.*, 21, 1709, 2003.

Bunce, E.J., S.W.H. Cowley, and T.K. Yeoman, Jovian cusp processes: Implications for the polar aurora, *J. Geophys. Res.*, *109* A09S13, doi:10.1029/2003JA010280, 2004.

Bunce, E.J., S.W.H. Cowley, D.M. Wright, A.J. Coates, M.K. Dougherty, N. Krupp, W.S. Kurth, and A.M. Rymer: In-situ observations of a solar wind compression-induced hot plasma injection in Saturn's tail, *Geophys. Res. Lett.*, 32, L20S04, doi: 10.1029/2005GL022888, 2005a.

Bunce, E.J., S.W.H. Cowley, C.M. Jackman, J.T. Clarke, F.J. Crary, and M.K. Dougherty: Cassini observations of the interplanetary medium upstream of Saturn and their relation to Hubble Space Telescope auroral data, *Adv. Space Res.*, in press, 2005b.

Bunce, E.J., S.W.H. Cowley, and S.E. Milan: Interplanetary magnetic field control of Saturn's polar cusp aurora, *Ann. Geophysicae*, 23 (4), 1405-1431, 2005c.

Burke, B.F., and K.J. Franklin: Observations of a variable radio source associated with the planet Jupiter, *J. Geophys. Res.*, 60, 213-217, 1955.

Burton, R.K., R.L. McPherron, and C.T. Russell: An empirical relationship between interplanetary conditions and D_{st}, *J. Geophys. Res.*, *80*, 4204, 1975.

Carbary, J.F., T.W. Hill, and A.J. Dessler: Planetary spin period acceleration of particles in the Jovian magnetosphere, *J. Geophys. Res.*, 81, 28, 5189-5195, 1976.

Cecconi, B. and P. Zarka: Model of a variable radio period for Saturn, *J. Geophys. Res.*, 110 (A12), A12203, 2005.

Chapmann, S. and V.C.A. Ferraro: A new theory of magnetic storms, *Terrest. Magnetism Atmos. Elec.*, 36, 171, 1931.

Chua, D., G. Parks, M. Brittnacher, W. Peria, G. Germany, J. Spann, and C. Carlson: Energy characteristics of auroral electron precipitation: A comparison of substorms and pressure pulse related auroral activity, *J. Geophys. Res.*, *106*, 5945, 2001.

Clarke, J.T., H.W. Moos, S.K. Atreya, and A.L. Lane: IUE detection of bursts of H Ly α emission from Saturn, *Nature*, *290*, 226, 1981.

Clarke, J.T., J.-C. Gérard, D. Grodent, S. Wannawichian, J. Gustin, J. Connerney, F. Crary, M. Dougherty, W. Kurth, S.W.H. Cowley, E.J. Bunce, T. Hill, and J. Kim: Morphological differences between Saturn's ultraviolet aurorae and those of Earth and Jupiter, *Nature*, *433*, 717, 2005.

Connerney, J.E.P., M.H. Acuña, and N.F. Ness: Saturn's ring current and inner magnetosphere, *Nature*, 292, 724, 1981.

Cowley, S.W.H.: The plasma environment of the Earth, *Contemp. Phys.*, 32, 235-250, 1991.

Cowley, S.W.H., and E.J. Bunce: Origin of the main auroral oval in Jupiter's coupled magnetosphere-ionosphere system, *Planet. Space Sci.*, *49*, 1067, 2001.

Cowley, S.W.H., and E.J. Bunce: Modulation of jovian middle magnetosphere currents and auroral precipitation by solar wind-induced compressions and expansions of the magnetosphere: Initial conditions and steady state, *Planet. Space Sci.*, *51*, 31, 2003a.

Cowley, S.W.H., and E.J. Bunce: Corotation-driven magnetosphere-ionosphere coupling currents in Saturn's magnetosphere and their relation to the auroras, *Ann. Geophysicae*, *21*, 1691, 2003b.

Cowley, S.W.H., J.A. Davies, A. Grocott, H. Khan, M. Lester, K.A. McWilliams, S.E. Milan, G. Provan, P.E. Sandholt, J.A. Wild, and T.K. Yeoman: Solar wind-magnetosphere-ionosphere interactions in the Earth's plasma environment, *Phil. Trans. Roy. Soc. Lond. A*, 361, 113, 2003.

Cowley, S.W.H., E.J. Bunce, and R. Prangé: Saturn's polar ionospheric flows and their relation to the main auroral oval, *Ann. Geophysicae*, 22, 1379, 2004a.

Cowley, S.W.H., E.J. Bunce, and J.M. O'Rourke: A simple quantitative model of plasma flows and currents in Saturn's polar ionosphere, *J. Geophys. Res.*, *109* (A05212), doi: 10.1029/2003JA010375, 2004b.

Cowley, S.W.H., S.V. Badman, E.J. Bunce, J.T. Clarke, J.-C. Gérard, D. Grodent, C.M. Jackman, S.E. Milan, and T.K. Yeoman: Reconnection in a rotation-dominated magnetosphere and its relation to Saturn's auroral dynamics, *J. Geophys. Res.*, *110*, A02201, doi: 10.1029/2004JA010796, 2005a.

Cowley, S.W.H., I.I. Alexeev, E.S. Belenkaya, E.J. Bunce, C.E. Cottis, V.V. Kalegaev, J.D. Nichols, R. Prangé, and F.J. Wilson: A simple axi-symmetric model of magnetosphere-ionosphere coupling currents in Jupiter's polar ionosphere, *J. Geophys. Res.*, 110, A11209, doi: 10.1029/2005JA011237, 2005b.

Cowling, T.J.: The magnetic field of sunspots, *Mon. Not. R. Astron. Soc.*, 94, 39, 1934.

Crary, F.J., J.T. Clarke, M.K. Dougherty, P.G. Hanlon, K.C. Hansen, J.T. Steinberg, B.L. Barraclough, A.J. Coates, J.-C. Gérard, D. Grodent, W.S. Kurth, D.G. Mitchell, A.M. Rymer, and D.T. Young: Solar wind dynamic pressure and electric field as the main factors controlling Saturn's auroras, *Nature*, *433*, 720, 2005.

Crooker, N.U., J.T. Gosling, V. Bothmer, R.J. Forsyth, P.R. Gazis, A. Hewish, T.S. Horbury, D.S. Intrilligator, J.R. Jokipii, J. Kóta, A.J. Lazarus, M.A. Lee, E. Lucek, E. Marsch, A. Posner, I.G. Richardson, E.C. Roelof, J.M. Schmidt, G.L. Siscoe, B.T. Tsurutani, and R.F. Wimmer-Schweingruber: CIR morphology, turbulence, discontinuities, and energetic particles, *Space Sci. Rev*., *89*, 179, 1999.

Davis, L., Jr., and E.J. Smith: A model of Saturn's magnetic field based on all available data, *J. Geophys. Res.*, *95*, 15257, 1990.

Delamere, P.A. and F. Bagenal: Modelling variability of plasma conditions in the Io torus, *J. Geophys. Res*., *108*(A7), 1276, doi: 10.1029/2002JA009706, 2003.

Desch, M.D.: Evidence for solar wind control of Saturn radio emission, *J. Geophys. Res*., *87*, 4549, 1982.

Desch, M.D. and H.O. Rucker: The relationship between Saturn kilometric radiation and the solar wind, *J. Geophys. Res.*, 88, 8999-9006, 1983.

Dougherty, M.K., S. Kellock, D.J. Southwood, A. Balogh, M. Barlow, T. Beek, M.W. Dunlop, R. White, E.J. Smith, L. Wigglesworth, M. Fong, R. Marquedant, B.T. Tsurutani, B. Gerlach, G. Musmann, K.-H. Glassmeier, H. Hartje, M. Rahm, I. Richter, C.T. Russell, D. Huddelston, R.C. Snare, G. Erdos, S. Szalai, F.M. Neubauer, S.W.H. Cowley, and G.L. Siscoe: The Cassini magnetic field investigation, *Space Sci. Rev*., *114*, 331, 2004.

Dougherty, M.K., N. Achilleos, N. Andre, C.S. Arridge, A. Balogh, C. Bertucci, M.E. Burton, S.W.H. Cowley, G. Erdos, G. Giampieri, K-H. Glassmeier, K.K. Khurana, J. Leisner, F.M. Neubauer, C.T. Russell, E.J. Smith, D.J. Southwood, and B.T. Tsurutani: Cassini Magnetometer Observations During Saturn Orbit Insertion, *Science*, 307, 1266, 2005.

Dougherty, M.K., K.K., Khurana, F.M. Neubauer, C.T. Russell, J. Saur, J.S. Leisner, and M.E. Burton: Identification of a dynamic atmosphere at Enceladus with the Cassini magnetometer, *Science*, 311, 5766, 1406, 2006.

Dungey, J.W.: Interplanetary field and the auroral zones, *Phys. Rev. Lett.*, *6*, 47, 1961.

Espinosa, S.A. and M.K. Dougherty: Periodic perturbations in Saturn's magnetic field, G*eophys. Res. Lett.*, 27, 2785, 2000.

Farrell, W.M., M.D. Desch, M.L. Kaiser, A. Lecacheux, W.S. Kurth, D.A. Gurnett, B. Cecconi, and P. Zarka: A nightside source of Saturn's kilometric radiation: Evidence for an inner magnetosphere energy driver, *Geophys. Res. Lett.*, 32, 18107, 2005.

Frank, L.A., B.G. Burek, K.L. Ackerson, J.H. Wolfe, and J.D. Mihalov: Plasma in Saturn's magnetosphere, *J. Geophys. Res.*, 86, 5695, 1980.

Freeman, M.P., and D.J. Southwood: The effect of magnetospheric erosion on mid-latitude and high-latitude ionospheric flows, *Planet. Space. Sci.*, 36, 509, 1988.

Freeman, M.P., J.M. Ruohoniemi, and R.A. Greenwald: The determination of time-stationary two-dimensional convection patterns with single-station radars, *J. Geophys. Res.*, 96, 15735, 1991.

Galopeau, P., P. Zarka, and A. Ortega-Molina: Evidence of Saturn's magnetic field anomaly from Saturnian kilometric radiation high-frequency limit, *J. Geophys. Res.*, 96, 14, 129-14, 140, 1981.

Galopeau, P.H.M. and P. Zarka: Reply to comment on "Evidence of Saturn's magnetic field anomaly from Saturn kilometric radiation high-frequency limit", *J. Geophys. Res.*, 97, 12291-12297, 1992.

Galopeau, P.H.M., P. Zarka, and D. LeQuéau: Source location of Saturn's kilometric radiation: The Kelvin-Helmholtz instability hypothesis, *J. Geophys. Res.*, *100*, 26,397, 1995.

Galopeau, P.H.M. and A. Lecacheux: Variations of Saturn's radio rotation period measured at kilometre wavelengths, *J. Geophys. Res.*, *105*, 13089, 2000.

Gérard, J.-C., V. Dols, D. Grodent, J.H. Waite, G.R. Gladstone, and R. Prangé: Simultaneous observations of the saturnian aurora and polar haze with the HST/FOC, *Geophys. Res. Lett.*, *22*, 2685, 1995.

Gérard, J.-C., D. Grodent, J. Gustin, A. Saglam, J.T. Clarke, and J.T. Trauger: Characteristics of Saturn's FUV aurora observed with the Space Telescope Imaging Spectrograph, *J. Geophys. Res.*, *109*, A09207, doi:10.1029/2004JA010513, 2004.

Giampieri, G., M.K. Dougherty, E.J. Smith, and C.T. Russell: The rotation period of Saturn's planetary magnetic field, in preparation, 2006.

Gosling, J.T.: Corotating and transient solar wind flows in three dimensions, *Ann. Rev. Astron. Astrophys.*, *34*, 35, 1996.

Gosling, J.T., and V.J. Pizzo: Formation and evolution of corotating interaction regions and their three dimensional structure, *Space Sci. Rev.*, *89*, 21, 1999.

Grocott, A., S.W.H. Cowley, and J.B. Sigwarth: Ionospheric flow during extended intervals of northward but B_y-dominated IMF, *Ann. Geophysicae*, *21*, 509, 2003.

Grodent, D., J.H. Waite Jr., and J.C. Gérard: A self-consistent model of the Jovian auroral thermal structure, *J. Geophys. Res.*, 106 (A7), 12933-12952, 2001.

Grodent, D., J.T. Clarke, J. Kim, J.H. Waite Jr., and S.W.H. Cowley: Jupiter's main oval observed with HST-STIS, *J. Geophys. Res.*, 108 (A11), 1389, doi: 10.1029/2003JA009921, 2003.

Grodent, D., J.-C. Gérard, S.W.H. Cowley, E.J. Bunce, and J.T. Clarke: The global morphology of Saturn's southern ultraviolet aurora, *J. Geophys. Res.*, 110, A07215, doi:10.1029/2004JA010983, 2005.

Gurnett, D.A., W.S. Kurth, and F.L. Scarf: Plasma waves near Saturn: Initial results from Voyager 1, *Science*, 212, 235-239, 1981.

Gurnett, D.A., W.S. Kurth, D.L. Kirchner, G.B. Hospodarsky, T.F. Averkamp, P. Zarka, A. Lecacheux, R. Manning, A. Roux, P. Canu, N. Cornilleau-Wehrlin, P. Galopeau, A. Meyer, R. Boström, G. Gustafsson, J.-E. Wahlund, L. Åahlen, H.O. Rucker, H.P. Ladreiter, W. Macher, L.J.C. Woolliscroft, H. Alleyne, M.L. Kaiser, M.D. Desch, W.M. Farrell, C.C. Harvey, P. Louarn, P.J. Kellogg, K. Goetz, and A. Pedersen: The Cassini radio and plasma wave investigation, *Space Sci. Rev.*, *114*, 395, 2004.

Gurnett, D.A., W.S. Kurth, G.B. Hospodarsky, A.M. Persoon, T.F. Averkamp, B. Cecconi, A. Lecacheaux, P. Zarka, P. Canu, N. Cornilleau-Wehrlin, P. Galopeau, A. Roux, C. Harvey, P. Louarn, R. Boström, G. Gustafsson, J.-E. Wahlund, M.D. Desch, W.M. Farrell, M.L. Kaiser, K. Goetz, P.J. Kellogg, G. Fischer, H.-P. Ladreiter, H. Rucker, H. Alleyne, and A. Pedersen: Radio and plasma wave observations at Saturn from Cassini's approach and first orbit, *Science*, *307*, 1255, 2005.

Hanlon, P.G., M.K. Dougherty, R.J. Forsyth, M.J. Owens, K.C. Hansen, G. Toth, F.J. Crary, D.T. Young: On the evolution of the solar wind between 1 and 5 AU at the time of the Cassini Jupiter flyby: Multispacecraft observations of interplanetary coronal mass ejections including the formation of a merged interaction region, *J. Geophys. Res.*, 109 (A9), A09S03, 2004.

Hill, T.H.: Inertial limit on corotation, *J. Geophys. Res.*, 84, 6554-6558, 1979.

Hill, T.W., A.J. Dessler, and C.K. Goertz: Magnetospheric models, in *Physics of the Jovian Magnetosphere* edited by A.J. Dessler, Cambridge Univ. Press, Cambridge, UK, p. 353, 1983.

Hill, T.W.: The jovian auroral oval, *J. Geophys. Res.*, 106, 8101, 2001.

Huang, T.S., and T.W. Hill: Corotation lag of the jovian atmosphere, ionosphere and magnetosphere, *J. Geophys. Res.*, 94, 3761, 1989.

Isbell, J., A.J. Dessler, and J.H. Waite Jr.: Magnetospheric energization by interaction between planetary spin and the solar wind, *J. Geophys. Res.*, 89, 10716, 1984.

Jackman**,** C.M., N. Achilleos, E.J. Bunce, S.W.H. Cowley, M.K. Dougherty, G.H. Jones, S.E. Milan, and E.J. Smith: Interplanetary magnetic field at ~9 AU during the declining phase of the solar cycle and its implications for Saturn's magnetospheric dynamics, *J. Geophys. Res.*, 109, A11203,doi:10.1029/2004JA010614, 2004.

Jackman, C.M., N. Achilleos, E.J. Bunce, B. Cecconi, J.T. Clarke, S.W.H. Cowley, W.S. Kurth, and P. Zarka: Interplanetary conditions and magnetospheric dynamics during the Cassini orbit insertion fly-through of Saturn's magnetosphere, *J. Geophys. Res.*, 110, A10212, doi: 10.1029/2005JA011054, 2005a.

Jackman, C.M., N. Achilleos, E.J. Bunce, S.W.H. Cowley, and S.E. Milan: Structure of the interplanetary magnetic field during the interval spanning the first Cassini fly-through of Saturn's magnetosphere and its implications for Saturn's magnetospheric dynamics, *Adv. Space Res.*, 36, 2120-2126, 2005b.

Jackman, C.M., and S.W.H. Cowley: A model of the plasma flow and current in Saturn's polar ionosphere under conditions of strong Dungey cycle driving, *Ann. Geophysicae*, 24, 1029-1055, 2006.

Judge, D.L., F.M. Wu, and R.W. Carlson: Ultraviolet photometer observations of the Saturnian system, *Science*, *207*, 431, 1980.

Kaiser, M.L., M.D. Desch, J.W. Warwick, and J.B. Pearse: Voyager detection of non-thermal radio emission from Saturn, *Science, 209*, 1238, 1980.

Kaiser, M.L., M.D. Desch, W.S. Kurth, A. Lecacheux, F. Genova, B.M. Pedersen, and D.R. Evans: Saturn as a radio source, in *Saturn*, edited by T. Gehrels and M.S. Matthews, p. 378, The University of Arizona Press, Tucson, 1984.

Kaiser, M.L.: Observations of nonthermal radiations from planets, in *Plasma Waves and Instabilities at Comets and in Magnetospheres, Geophys. Monogr. Ser.,* vol. 53, edited by B.T. Tsurutani and H. Oya pp. 221-237, AGU, Washington, D.C., 1989.

Kaiser, M.L., M.D. Desch, M.H. Acuña, N.F. Ness, and J.E.P. Connerney: Comment on "Rotation rate of Saturn's interior from magnetic field observations" by Giacomo Giampieri and Michele K. Dougherty, *Geophys. Res. Lett.*, 32 (2), L02201, 2005.

Kessel, R.L., S.-H. Chen, J.L. Green, S.F. Fung, S.A. Boardsen, L.C. Tan, T.E. Eastman, J.D. Cravens, and L.A. Frank: Evidence of high-latitude reconnection during northward IMF: Hawkeye observations, *Geophys. Res. Lett*, *23*, 583, 1996.

Khurana, K.K. and M.G. Kivelson: Inference of the angular velocity of plasma in the Jovian magnetosphere from the sweepback of the magnetic field, *J. Geophys. Res.*, 98, 67, 1993.

Kivelson, M.G. and C.T. Russell (editors): Introduction to space physics, Cambridge University Press, 1995.

Knight, S.: Parallel electric fields, *Planet. Space Sci.*, 21, 741, 1973.

Krimigis, S.M., D.G. Mitchell, D.C. Hamilton, N. Krupp, S. Livi, E.C. Roelof, J. Dandouras, T.P. Armstrong, B.H. Mauk, C. Paranicas, P.C. Brandt, S. Bolton, A.F. Cheng, T. Choo, G. Gloeckler, J. Hayes, K.S. Hsieh, W.-H. Ip, S. Jaskulek, E.P. Keath, E. Kirsch, M. Kusterer, A. Lagg, L.J. Lanzerotti, D. LaVallee, J. Manweiler, R.W. McEntire, W. Rasmuss, J. Saur, F.S. Turner, D.J. Williams, and J. Woch: Dynamics of Saturn's magnetosphere from MIMI during Cassini's orbital insertion, *Science*, 307, 1270, 2005.

Kunow, H.: Solar wind: Corotating interaction region, In: *Encyclopedia of Astronomy and Astrophysics*, Institute of Physics Publ., Bristol, Vol. 4, p2825, 2001.

Kurth, W.S., D.A. Gurnett, J.T. Clarke, M.D. Desch, M.L. Kaiser, P. Zarka, B. Cecconi, A. Lecacheux, W.M. Farrell, P. Galopeau, J.-C. Gérard, D. Grodent, M.K. Dougherty, F.J. Crary, and R. Prangé: An Earth-like correspondence between Saturn's auroral features and radio emission, *Nature*, 433, 722-725, doi: 10.1038/nature03334, 2005.

Ladreiter, H.P., P. Zarka, and A. Lecacheux: Direction-finding study of Jovain hectometric and broadband kilometric radio emissions: Evidence for their auroral origin, *Planet. Space Sci.*, 42, 919-931, 1994.

Lebreton, J.P. and D.L. Matson: The Huygens probe: Payload and mission overview: *Space Sci. Rev*., *104*, 59, 2002.

Lebreton, J.P., O. Witasse, C. Sollazzo, T. Blandquaert, P. Couzin, A.M. Schipper, J.B. Jones, D.L. Matson, L.I. Gurvits, D.H. Atkinson, B. Kazeminejad, M. Perez-Ayucar: An overview of the descent and landing of the Huygens probe on Titan, *Nature*, 438, 758-764, 2005.

Lecacheux, A., and F. Genova: Source location of Saturn kilometric radio emission, *J. Geophys. Res*., *88*, 8993, 1983.

Liou, K., P.T. Newell, C.-I. Meng, C.-C. Wu, and R.P. Lepping: Investigation of external triggering of substorms with Polar ultraviolet imager observations, *J. Geophys. Res*., *108*(A10), 1364, doi: 10.1029/2003JA009984, 2003.

Lopez, R.E., D.N. Baker, and J.E. Allen: Sun unleashes Halloween storm, *Eos Trans. AGU*, *85*, 105, 2004.

Lundin, R., and I. Sandahl: Some characteristics of the parallel electric field acceleration of electrons over discrete auroral arcs as observed from two rocket flights, in *Symposium on European Rocket Research*, ESA SP-135, ESA, Noordwijk, The Netherlands, p. 125, 1978.

McComas, D.J., R. Goldstein, J.T. Gosling, and R.M. Skoug: Ulysses' second orbit: Remarkably different solar wind, *Space Sci. Rev*., *97*, 99, 2001.

Meurant, M., J.-C. Gérard, C. Blockx, B. Hubert, and V. Coumans: Propagation of electron and proton shock-induced aurora and the role of the interplanetary magnetic field and solar wind, *J. Geophys. Res*., *109,* A10210, doi: 10.1029/2004JA010453, 2004.

Milan, S.E., M. Lester, S.W.H. Cowley, and M. Brittnacher: Dayside convection and auroral morphology during an interval of northward interplanetary magnetic field, *Ann. Geophysicae*, 18, 436, 2000.

Milan, S.E., M. Lester, S.W.H. Cowley, K. Oksavik, M. Brittnacher, R.A. Greenwald, G. Sofko, and J.-P. Villain: Variations in polar cap area during two substorm cycles, *Ann. Geophysicae*, *21*, 1121, 2003.

Milan, S.E., S.W.H. Cowley, M. Lester, D.M. Wright, J.A. Slavin, M. Fillingim, C.W. Carlson, and H.J. Singer: Response of the magnetotail to changes in the open flux content of the magnetosphere, *J. Geophys. Res.*, 109, A04220, doi: 10.1029/2003JA010350, 2004.

Milan, S.E., E.J. Bunce, S.W.H. Cowley, and C.M. Jackman: Implications of rapid planetary rotation for the Dungey magnetotail of Saturn, J. Geophys. Res., 110, A02201, doi:10.1029/2004JA010716, 2005.

Millward, G., S. Miller, T.S. Stallard, N. Achilleos, and A.D. Aylward: On the dynamics of the jovian ionosphere and thermosphere. IV; Ion-neutral coupling, *Icarus*, 173, 200, 2005.

Ness, N.F., M.H. Acuña, R.P. Lepping, J.E.P. Connerney, K.W. Behannon, L.F. Burlaga, and F.M. Neubauer, Magnetic field studies by Voyager 1: Preliminary results at Saturn, *Science*, *212*, 211, 1981.

Ness, N.F., M.H. Acuña, K.W. Behannon, L.F. Burlaga, J.E.P. Connerney, R.P. Lepping, and F. Neubauer: Magnetic field studies by Voyager 2: Preliminary results at Saturn, *Science*, 215, 558, 1982.

Nichols, J.D., and S.W.H. Cowley: Magnetosphere-ionosphere coupling currents in Jupiter's middle magnetosphere: Effect of precipitation-induced enhancement of the ionospheric Pedersen conductivity, *Ann. Geophysicae*, *22*, 1799, 2004.

Øieroset, M., P.E. Sandholt, W.F. Denig, and S.W.H. Cowley: Northward interplanetary magnetic field cusp aurora and high-latitude magnetopause reconnection, *J. Geophys. Res., 102*, 11349, 1997.

Parker, E.N: Dynamics of the interplanetary magnetic field, *Astrophys. J.*, 128, 664, 1958.

Perrault, P., and S.-I. Akasofu: A study of geomagnetic storms, *Geophys. J. Roy. Astr. Soc*., *54*, 547, 1978.

Petrinec, S.M., and C.T. Russell: Near-Earth magnetotail shape and size as determined from the magnetopause flaring angle, *J. Geophys. Res*., *101*, 137, 1996.

Pizzo, V.J.: Global quasi-steady dynamics of the distant solar wind – I. Origins of north-south flows in the outer heliosphere, *J. Geophys. Res.*, *99*, 4173, 1994a.

Pizzo, V.J.: Global quasi-steady dynamics of the distant solar wind – II. Deformation of the heliospheric current sheet, *J. Geophys. Res.*, *99*, 4185, 1994b.

Pontius, D.H. and T.W. Hill: Departure from corotation of the Io plasma torus: Local plasma production, *Geophys. Res. Lett.*, 12, 1321-1324, 1982.

Pontius, D.H.: Radial mass transport and rotational dynamics, *J. Geophys. Res.*, *102*, 7137, 1997.

Prangé, R., L. Pallier, K.C. Hansen, R. Howard, A. Vourladis, R. Courtin, and C. Parkinson: A CME-driven interplanetary shock traced from the Sun to Saturn by planetary auroral storms, *Nature*, *432*, 78, 2004.

Rego, D., R. Prangé, and J.-C. Gérard: Lyman α and H_2 bands from the giant planets: 1. Excitation by proton precipitation in the Jovian aurorae, *J. Geophys. Res.*, 99, 17,075, 1994.

Reiff, P.H., and J.L. Burch: IMF B_y-dependent plasma flow and Birkeland currents in the dayside magnetosphere: 2 A global model for northward and southward IMF, *J. Geophys. Res.*, *90*, 1595, 1985.

Richardson, J.D.: Thermal ions at Saturn: Plasma parameters and implications, *J. Geophys. Res.*, 91, 1381, 1986.

Richardson, J.D., and E.C. Sittler Jr.: A plasma density model for Saturn based on Voyager observations, *J. Geophys. Res.*, 95, 12019, 1990.

Richardson, J.D.: A new model for plasma transport and chemistry at Saturn, *J. Geophys. Res.*, 97, 13705, 1992.

Richardson, J.D.: An extended plasma model for Saturn, *Geophys. Res. Lett.*, *22*, 1177, 1995.

Richardson, J.D., A. Eviatar, M.A. McGrath and V.M. Vasyliunas: OH in Saturn's magnetosphere: Observations and theory, *J. Geophys. Res.*, 103, 20245, 1998.

Sandel, B.R., and A.L. Broadfoot: Morphology of Saturn's aurora, *Nature*, *292*, 679, 1981.

Sandel, B.R., D.E. Shemansky, A.L. Broadfoot, J.B. Holberg, G.R. Smith, J.C. McConnell, D.F. Strobel, S.K. Atreya, T.M. Donahue, H.W. Moos, D.M. Hunten, R.B. Pomphrey, S. Linicks: Extreme Ultraviolet Observations from the Voyager-2 encounter with Saturn, *Science*, 215 (4532), 548-553, 1982.

Sandholt, P.E., C.J. Farrugia, J. Moen, and S.W.H. Cowley: Dayside auroral configurations: responses to southward and northward rotations of the interplanetary magnetic field, *J. Geophys. Res.,* 103, 20279-20295, 1998.

Saur, J., B.H. Mauk, A. Kassner, and F.M. Neubauer: A model for the azimuthal plasma velocity in Saturn's magnetosphere, *J. Geophys. Res.*, *109*, A05217, doi: 10.1029/2003JA010207, 2004.

Scarf, F.L., D.A. Gurnett, W.S. Kurth, and R.L. Poynter: Voyager 2 plasma wave observations at Saturn, *Science*, 215, 587, 1982.

Shemansky, D.E., and J.M. Ajello: The Saturn spectrum in the EUV – Electron excited Hydrogen, *J. Geophys. Res.*, 88, 459-464, 1983.

Sigwarth, J.B., L.A. Frank, and N.J. Fox: The effect of a dynamic pressure pulse in the solar wind on the auroral oval, total open magnetic flux of the polar cap and the auroral ionosphere (abstract), *33rd COSPAR Scientific Assembly*, Warsaw, Poland, 2000.

Sittler, E.C. Jr., K.W. Ogilvie, and J.D. Scudder: Survey of low-energy plasma electrons in Saturn's magnetosphere: Voyagers 1 and 2, *J. Geophys. Res.*, 88, 8847, 1983.

Smith, E.J., L. Davis, Jr., D. Jones, P.J. Coleman, Jr., D.S. Colburn, P. Dyal, and C.P. Sonnett: Saturn's magnetic field and magnetosphere, *Science*, 207, 407, 1980.

Southwood, D.J., and M.G. Kivelson: A new perspective concerning the influence of the solar wind on Jupiter, *J. Geophys. Res.*, 106, 6123, 2001.

Stallard, T.S., S. Miller, L.M. Trafton, T.R. Geballe, and R.D. Joseph: Ion winds in Saturn's southern auroral/polar region, *Icarus*, 167, 204, 2004.

Stevensen, D.J.: Reducing the non-axisymmetry of a planetary dynamo and an application to Saturn, *Geophys. Astrophys. Fluid dyn.*, 113, 1982.

Trauger, J.T., J.T. Clarke, G.E. Ballester, R.W. Evans, C.J. Burrows, D. Crisp, J.S. Gallagher III, R.E. Griffiths, J.J. Hester, J.G. Hoessel, J.A. Holtzman, J.E. Krist, J.R. Mould, R. Sahai, P.A. Scowen, K.R. Stapelfeldt, and A.M. Watson: Saturn's hydrogen aurora: Wide field and planetary camera 2 imaging from the Hubble Space Telescope, *J. Geophys. Res.*, 103, 20237, 1998.

Vasyliunas, V.M.: Plasma distribution and flow, in *Physics of the Jovian Magnetosphere,* edited by A.J. Dessler, 395 pp., Cambridge Univ. Press, New York, 1983.

Waite, J.H. Jr., T.E. Cravens, J. Kozyra, A.F. Nagy, S.K. Atreya, and R.H. Chen: Electron precipitation and related aeronomy of the Jovian thermosphere and ionosphere, *J. Geophys. Res.*, 88, 6143, 1983.

Warwick, J.W., J.B. Pearce, D.R. Evans, T.D. Carr, J.J. Schauble, J.K. Alexander, M.L. Kaiser, M.D. Desch, M. Pedersen, A. Lecacheux, G. Daigne, A. Boischot, and C.H. Barrow: Planetary radio astronomy observations from Voyager-1 near Saturn, *Science*, 212 (4491), 239-243, 1981.

Warwick, J.W., D.R. Evans, J.H. Romig, J.K. Alexander, M.D. Desch, M.L. Kaiser, M. Aubier, Y. Leblancy, A. Lecacheux, and B.M. Pedersen: Planetary radio astronomy observations from Voyager-2 near Saturn, *Science*, 215 (4532), 582-587, 1982.

Webb D.F. and R.A. Howard:The solar-cycle variation of coronal mass ejections and the solar-wind mass flux, *J. Geophys. Res.*, 99, 4201, 1994.

Woodgate, B.E., R.A. Kimble, C.W. Bowers, S. Kraemer, M.E. Kaiser, A.C. Danks, J.F. Grady, J.J. Loiacono, M. Brumfield, L. Feinberg, T.R. Gull, S.R. Heap, S.P. Maran, D. Lindler, D. Hood, W. Meyer, C. VanHouten, V. Argabright, S. Franka, R. Bybee, D. Dorn, M. Bottema, R. Woodruff, D. Michika, J. Sullivan, J. Hetlinger, C. Ludtke, R. Stocker, A. Delamere, D. Rose, I. Becker, H. Garner, J.G. Timothy, M. Blouke, C.L. Joseph, G. Hartig, R.F. Green, E.B. Jenkins, J.J. Linsky, J.B. Hutchings, H.W. Moos, A. Boggess, F. Roesler, and D. Weistrop: The Space Telescope Imaging Spectrograph Design, *Pub. Astro. Soc. Pac.*, 110, 1183, 1998.

Wu, C.S. and L.C. Lee: A theory of terrestrial kilometric radiation, *Astrophys. J.*, 230, 621-626, 1979.

Young, D.T., J.-J. Berthelier, M. Blanc, J.L. Burch, S. Bolton, A.J. Coates, F.J. Crary, R. Goldstein, M. Grande, T.W. Hill, R.E. Johnson, R.A. Baragiola, V. Kelha, D.J. McComas, K. Mursula, E.C. Sittler, K.R. Svenes, K. Szegö, P. Tanskanen, M.F. Thomsen, S. Bakshi, B.L. Baraclough, Z. Bebesi, D. Delapp, M.W. Dunlop, J.T. Gosling, J.D. Furman, L.K. Gilbert, D. Glenn, C. Holmlund, J.-M. Illiano, G.R. Lewis, D.R. Linder, S. Maurice, H.J. McAndrews, B.T. Narheim, E. Pallier, D. Reisenfeld, A.M. Rymer, H.T. Smith, R.L. Tokar, J. Vilppola, and C. Zinsmeyer: Composition and dynamics of plasma in Saturn's magnetosphere, *Science*, *307*, 1262, 2005.

Zarka, P.:Auroral radio emissions at the outer planets: Observations and theories, *J. Geophys. Res.*, *103*, 20159, 1998.

Zarka, P., and W.S. Kurth: Radio wave emission from the outer planets before Cassini, *Space Science Reviews*, 116, 371-397, doi: 10.1027/s11214-005-1962-2, 2005.

Zhou, X., and B.T. Tsurutani: Interplanetary shock triggering of nightside geomagnetic activity: Substorms, pseudobreakups, and quiescent events, *J. Geophys. Res.*, 106, 18957, 2001.